Development of a Radiopaque Infiltration Resin for Early Enamel Carious Lesion

MALIHE MOEINIAN

Thesis submitted in fulfilment of the requirements for the degree of Doctor of Philosophy in the Faculty of Medicine, Queen Mary University of London

April 2018

Centre for Oral Growth and Development Institute of Dentistry,

Barts and The London School of Medicine and Dentistry

Queen Mary University of London

Barts and The London
School of Medicine and Dentistry

Declaration regarding plagiarism

I declare that the coursework material attached herewith is entirely my own work and that I have attributed any brief quotations both at the appropriate point in the text and in the bibliography at the end of this piece of work.

I also declare that I have not used extensive quotations or close paraphrasing and that I have neither copied from the work of another person, nor used the ideas of another person, without proper acknowledgement.

Name: Malihe Moeinian Course: PhD

Title of work submitted:

Development of a Radiopaque Infiltration Resin for Early Enamel Carious Lesion

Examination: A thesis submitted for the degree of Doctor of Philosophy, University of London

Signature: Date: May 2017

Acknowledgements

I would like to thank my academic supervisors, Prof Ferranti Wong and Prof Robert Hill, for their supervision, sharing their expertise, patient guidance, encouragement and helping me to become an independent researcher. I have been extremely lucky to have supervisors who cared so much about my work, and who responded to my queries all way in this research.

I am thankful to Prof Allan Boyde, for his invaluable insights and kind support in this study.

I am deeply grateful to Dr Mangala Patel, for her constant encouragement and support throughout this study.

I would like to thank Dr Graham Davis, Dr David Mills, Dr Andy Bushby and Dr Simon Rawlinson, for all their help and support.

My PhD journey would not have been as enjoyable without all my colleagues in the Dental Physical Science Unit. A special thanks to Huda Al-Mandil, Maryam Abdollahyan and Arian Gederi for their genuine friendship, all the fun, memorable times and support over this journey.

Last but not least, my immense gratitude goes to my parents, Maryam and Davood, my siblings, Mahsa and Mahdi. There are not enough words to describe how thankful I am to them. Being apart from them has made me realise how much they mean to me. Thanks them for their endless amounts of love. Thanks them for all the support, no matter what. Thanks them for being such a wonderful family.

Abstract

A white spot lesion (WSL) is defined as enamel porosity, which could be due to an enamel defect or an initial carious lesion. ICON® resin is a resin infiltrant that penetrates into the enamel porosity and seals the lesion, thus inhibiting the progression of caries. This method is micro-invasive; however, the resin is radiolucent and the clinician cannot detect the material using radiographs. In order to develop a radiopaque resin, understanding the pore size and pore structure in WSLs is helpful. Therefore, the aim of this study was to characterise: (1) the pore size and structure, (2) the incorporation of radiopaque agents into ICON® resin.

Brunauer–Emmett–Teller (BET) and focused ion beam-scanning electron microscopy (FIB-SEM) were used to characterise the porosity in WSLs. The data showed the enamel prisms become more pronounced in the advanced areas of the WSLs and demineralisation occurs within or/and between the enamel prisms. The pore size could be as small as an enamel crystallite, 28x48nm.

Nano-strontium hydroxyapatite (non-coated and coated) and strontium bioglass were made as radiopaque fillers and characterised using different techniques including fourier transform infrared spectroscopy (FTIR), BET, transmission electron microscopy (TEM), X-ray diffraction (XRD) and particle size measurements. The radiopaque fillers had micron-sized particles, which made them unsuitable for infiltration into WSLs despite their possible ability to remineralise the WSLs. Radiopaque monomers including bromine-methacrylate and tin-methacrylate were able to make ICON® resin radiopaque and they showed a similar viscosity, wettability and biocompatibility compared to ICON® resin. The X-ray microtomography (XMT) showed that the experimental radiopaque resins were able to infiltrate into the WSLs, artificial and natural lesions, and they could be detected using image subtraction. Backscattered electron (BSE) imaging after each step of application of materials showed that the etching pattern and etchant gel could be barriers for a successful infiltration of the resins into WSLs.

Table of Contents

Figure Index

Table Index

Equation Index

List of abbreviation

ADA	American Dental Association
ADSA	Axisymmetric Drop Shape Analysis
Al	Aluminum
ART	Atraumatic Restorative Treatment
ATP	Adenosine Triphosphate
Ba	Barium
BET	Brunauer-Emmett-Teller
BG	Bioactive Glass
Bis-GMA	Bis-Glycidyl Dimethacrylate
BO	Bridging Oxygen
Br	Bromine
BrM	Bromine-methacrylate
BSE	Backscatter Electron
Ca	Calcium
CA	Contact Angle
CCD	Charge-couple Device
CEJ	Cemento-Enamel Junction
CHFS	Continuous Hydrothermal Flow Synthesis
CPFS	Continuous Plastic Flow System
CPP-ACP	Casein Phosphopeptide Amorphous CalciumPhosphate
CT	Computed Tomography
CVD	Chemical Vapour Deposition
DC	Degree of Conversion
DMAEM	Dimethylaminoethyl Methacrylate
DMAM	Dimethyl Amino Ethyl Methacrylate
DMFT	Decayed, Missing, Filled teeth
DMSO	Dimethyl Sulfoxide
DNA	Deoxyribonucleic Acid
DS	Drift Suspension
EDJ	Enamel Dentine Junction
EDTA	Ethylene diaminetetraacetic Acid
EDX	Energy Dispersive X-ray
EEC	Early Enamel Caries
FDA	The Food and Drug Administration
FIB-SEM	Focused Ion Beam- Scanning Electron Microscopy
FTIR	Fourier Transform Infrared
FWHM	Full Width Half Maximum
GIC	Glass Ionomer Cement
HA	Hydroxyapatite

HCl	Hydrochloric Acid
HEMA	2-Hydroxyethyl Methacrylate
HPLC	High Performance Liquid Chromatography
ICDAS	International Caries Detection and Assessment System
IR	Infra Red
ISO	International Standards Organisation
IUPAC	International Union of Pure and Applied Chemistry
KOH	Potassium Hydroxide
LAC	Linear Attenuation Coefficient
LD	Lesion Depth
MAC	Mass Attenuation Coefficient
META/MMA	Methacryloxyethyl Trimellitate Anhydride/Methyl Methacrylate
MHDP	methylhydroxidiphosphonate
MI	Minimally Invasive
MMA	Methyl Methacrylate
MMA/TBB	Methyl Methacrylate/ Tributylborane
MTT	3-[4,5-dimethylthiazol-2-yl]-2,5- diphenyltetrazolium bromide
NADH	Nicotinamide Adenine Dinucleotide-hydrogen
NADPH	Nicotinamide Adenine Dinucleotide Phosphate
NaF	Sodium Fluoride
NaOCl	Sodium Hypochlorite
NaOH	Sodium Hydroxyapatite
NBO	Non-bridging Oxygen
NMR	Nuclear Magnetic Resonance
OCT	Optical Coherence Tomography
PBS	Phosphate Buffered Saline
PC	Penetration Coefficient
PD	Penetration Depth
PE	Primary Electron
PF	Plaque Fluid
PMMA	Poly(methyl methacrylate)
PP	Penetration Potential
PTFE	Poly(tetrafluoroethylene)
RI	Refractive Index
RPM	Revolution Per Minute
SBF	Stimulated Body Fluid
SD	Standard Deviation
Se	Standard Error
SE	Secondary Electron
SEM	Scanning Electron Microscopy

SnM	Tin-methacrylate
SNR	Signal to Noise Ratio
Sr	Strontium
SrBG	Strontium Bioactiveglass
SrHA	Strontium Hydroxyapatite
TBBO	Tri-n -butylborane Oxide
TEG-DMA	Triethylene Glycol Dimethacrylate
TEM	Transmission Electron Microscope
WHO	World Health Organisation
WSL	White Spot Lesion
XMT	X-ray Microtomography
XRD	X-ray Diffraction

Chapter 1- General Introduction, Aims and Objectives

1.1 Background

Dental caries is the most common global disease in adults and children (Petersen *et al.* 2005). Caries is a disease of the dental hard tissue initiated by acid demineralisation from plaque bacteria, resulting in the formation of spaces (reported as pores in literature) within the enamel structure. When these pores are filled with air, they have an opaque appearance compared to the more translucent mineralised enamel and are termed white spot lesions (WSLs) clinically. It should be mentioned that the WSL could also result from a hypomineralised lesion due to enamel developmental defects.

The WSL is a sub-surface demineralised lesion with an intact superficial layer. It is considered to be reversible through remineralisation, especially in the presence of fluoride (Robinson *et al*. 2000; Featherstone 2008). Recently, an infiltration technique using a low viscosity resin (ICON®) was proposed to treat these lesions. The infiltrant was shown to infiltrate into the lesion and seal the porosity, thus arresting the progression of the caries process (Meyer-Lueckel and Paris 2008). Although there is some evidence of clinical success, ICON® is radiolucent and cannot be visualised clinically and radiographically. This leads to concerns including difficulties in assessing and monitoring the infiltrant in the lesion clinically. Furthermore, secondary caries beneath the lesion will not be detectable since both the resin and caries are radiolucent.

The aims of this study are to explore various techniques in making infiltrant resin radiopaque and to assess the ability of the chosen radiopaque resin to infiltrate into the white spot lesions (Figure 1.1). In the current study, WSLs only include lesions produced by early enamel caries (EEC).

The structure of this thesis is divided into 4 parts:

Part 1- Introduction, General Aims and Objectives (Chapter 1),

Part 2- Literature Review (Chapter 2-5)

Part 3- Experiments, Results and Discussion. For each experiment, there will be an introduction on the techniques, specific aims and objectives, results, discussion and conclusion (Chapters 6-13),

Part 4 – General Discussion, conclusion and future works (Chapter 14).

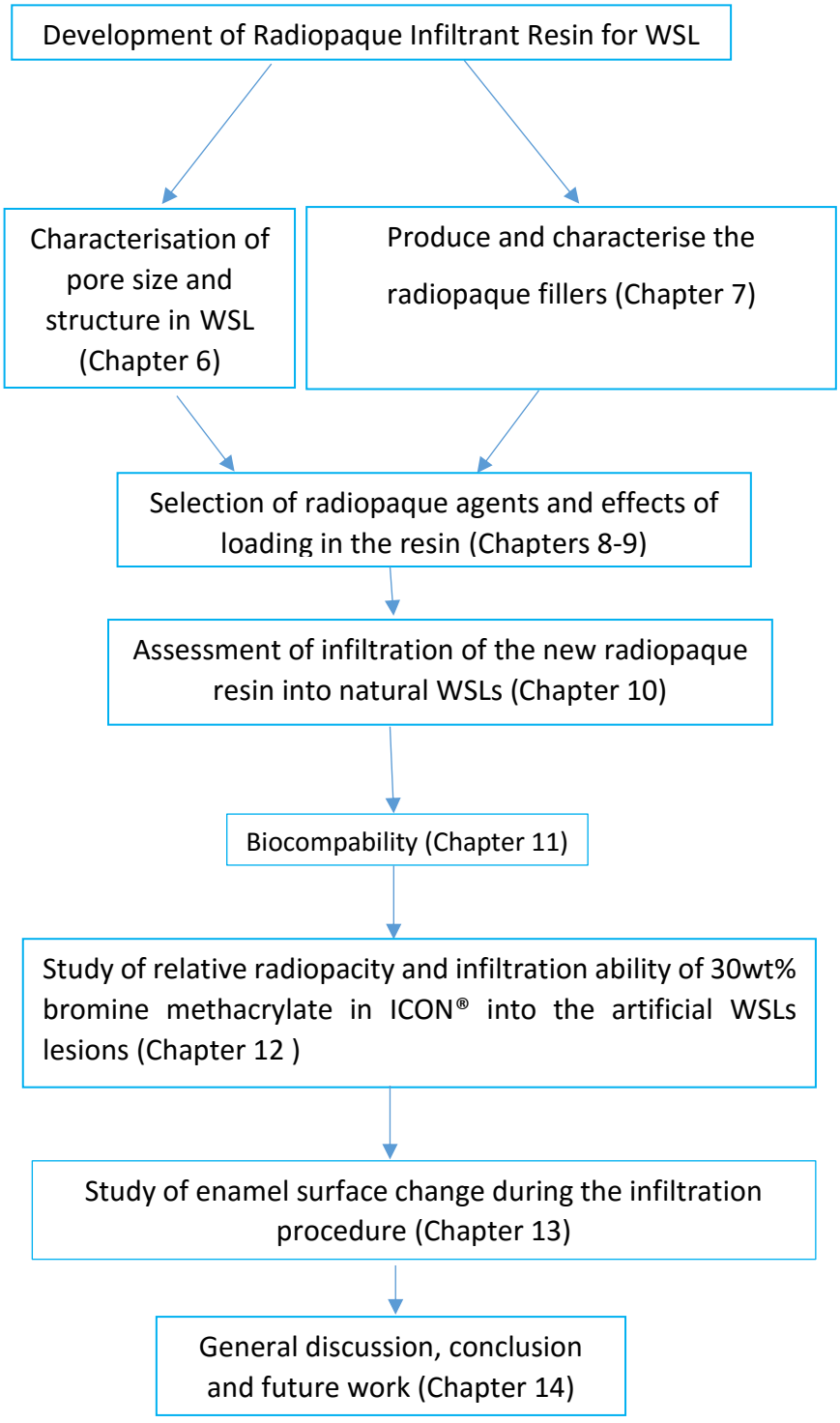

Figure1.1 A diagram showing the structure of the current study.

1.2 Aims and Objectives

The aims are:

- To explore various techniques to investigate the pore size and structure in white spot lesion;
- To develop and characterise radiopaque fillers for infiltrant resin in terms of:
    - Composition,
    - Particle size,
    - Crystal size.
- To incorporate the radiopaque agents into ICON® resin;
- To characterise the radiopaque resins in terms of:
    - Curing ability,
    - Radiopacity,
    - Consistency,
    - Viscosity,
    - Wettability,
    - Infiltrating ability,
    - Biocompatibility.
- To measure and compare the linear attenuation coefficient (LAC) changes and penetration depth of the designed radiopaque resin with ICON® in natural and artificial carious lesions;
- To investigate the enamel surface change during infiltration procedure.

The Objectives are:

- To use Brunauer–Emmett–Teller (BET) technique to estimate the pore size and structure within the WSL;
- To use Focused Ion Beam-Scanning Electron Microscopy (FIB-SEM) to study the structure of WSL and measure the pore size directly;
- To synthesise and characterise nano size strontium hydroxyapatite (nano-SrHA);
- To synthesis and characterise strontium bioactive glass (SrBG);
- To incorporate radiopaque fillers (nano-SrHA / SrBG) and radiopaque monomers (tin methacrylate / bromine methacrylate) into ICON® resin;
- To measure the radiopacity of experimental materials according to ISO-4049 standard;
- To investigate the dispersion of radiopaque agents in experimental materials;
- To measure and compare the viscosity of experimental radiopaque resins with ICON®. Null hypothesis will be formulated to test their differences;
- To measure and compare the contact angle (wettability) of experimental radiopaque resins with ICON®. Null hypothesis will be formulated to test their differences;
- To choose the most appropriate experimental radiopaque resins for infiltration in natural WSLs;
- To use clinical photographs and dental digital radiographs for visual assessments and compare changes before and after application of the selected experimental radiopaque resins in natural WSLs;
- To use X-ray microtomography (XMT) to measure and compare radiopacities before and after application of the selected experimental radiopaque resins in natural WSLs. Null hypothesis will be formulated to test their differences;

- To use X-ray microtomography (XMT) to measure and compare the penetration depth, before and after application of the selected experimental radiopaque resins in natural WSLs;
- To use DNA fluorometric and MTT assays to measure and compare the cell cytotoxicity of experimental radiopaque resins with ICON®;
- To choose the most appropriate experimental radiopaque resin in order to infiltrate the artificial white spot lesion;
- To use XMT to measure and compare the radiopacities of the chosen radiopaque experimental resin with ICON® after infiltration in artificial white spot lesions created by static demineralisation technique. Null hypothesis will be formulated to test their differences;
- To use XMT to measure and compare the radiopacities of the chosen radiopaque resin with ICON® after infiltration in artificial white spot lesions created by dynamic demineralisation technique. Null hypothesis will be formulated to test their differences;
- To use X-ray microtomography (XMT) to measure and compare the penetration depth, before and after application of the selected experimental radiopaque resins in artificial WSLs;
- To use Scanning Electron Microscopy (SEM) to investigate the enamel surface changes during the infiltration procedure according to ICON® manufacturer.

Literature Review

Chapter 2- Tooth Structure and Dental Enamel

2.1 Basic tooth structure

Teeth are considered as the most characteristic and long-lasting feature of mammalian species. Human teeth are small but important, as they are the first point of contact with food and drink. They break down food through cutting and crushing it, mechanically and prepare it for swallowing and digestion. They are able to withstand a wide range of imposed loads and physiological stress while retaining their structural strength, shape and integrity.

The human tooth is divided into the crown and root. The crown is part of the tooth in the oral environment and the root is inside the alveolar bone. Each mature human tooth consists of several different parts including enamel, dentine, cementum and pulp (Figure 2.1).

Enamel is the first outer layer of the crown. It is whitish, translucent and a highly-mineralised tissue. It is very hard and made of crystalline material. It is resistant to grinding, abrasion, acid and chemical attacks and acts as a protective shell for the tooth against the outside environment. However, enamel has a very rigid and brittle structure that leads it to fracture easily. Therefore, it is supported by dentine.

Dentine is made of collagen-apatite with a tougher and less mineralised structure in comparison with enamel. It consists of millions of tubules, extending from the crown to the root. It helps to retain enamel integrity and protects the pulp. The interface between the dentine and enamel structure is called enamel-dentine junction (EDJ).

The pulp is the structure in the middle of the tooth filled with connective tissue including nerves and blood vessels.

Cementum is the outer layer of the root. It is approximately 45% inorganic material (mainly, hydroxyapatite), 33% organic material (mainly, collagen) and 22% water. It is yellowish and it is softer than dentine and enamel. The main role of cementum is attaching the periodontal ligaments to the tooth for stability. The interface between the cementum and the enamel is called cemento-enamel junction (CEJ) (Berkovitz *et al.* 2009).

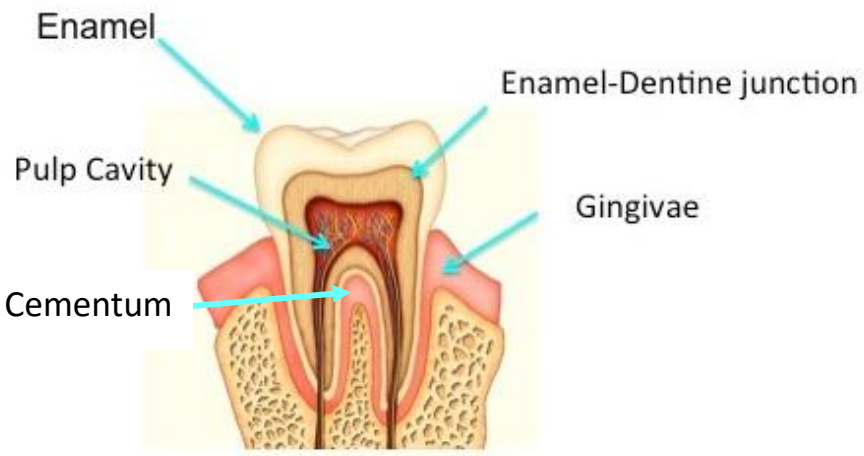

Figure 2.1 A schematic structure of a human tooth including the crown and the root. The crown is made of the enamel, dentine and pulp while the root is made of cementum, dentine and the pulp (http://beta.classmint.com, accessed on 12/06/2016).

Human beings have two sets of dentition during their lifetime, primary and permanent. The primary (deciduous or milk) and permanent teeth erupt between the ages of 6 to 24 months and 6 to 12 years old, respectively. This age range does not include the third molars. Primary (deciduous or milk) dentition consists of incisors, canines and molars while the permanent dentition also includes premolars (Atkinson and White 1992).

2.2 Enamel

2.2.1 Mature dental enamel structure

Enamel is a calcified tissue layer, which is hard, very thin and translucent, covering the crown completely (Elliott 1997).

Fully formed enamel is the most highly mineralised extracellular matrix. It consists of approximately 98wt% non-stoichiometric hydroxyapatite (HA), ~2wt% non-collagenous protein and water (Elliott 1997).

The organic components comprise enamel-specific proteins with a high potential of binding to the hydroxyapatite (HA) crystals. The inorganic content of enamel is a

crystalline calcium phosphate hydroxyapatite ($Ca_{10}(PO_4)_6(OH)_2$) substituted with carbonate ions (Fincham *et al*. 1999).

Hydroxyapatite crystals can be best defined as a series of hexagonal plates (Kerebel *et al*. 1979) arranged one on top of another, with 60° rotation in relation to immediate neighbours to form a column (Figure 2.2). Each plate has a hydroxyl ion in the centre, surrounded by a triangle of calcium ions (Ca^{2+}), enclosed by a triangle of phosphate ions rotated out of phase by 60°, all within a hexagon of calcium ions (Kay *et al.* 1964). The enamel's crystalline regions grow by deposition of ions on the crystal faces a, b and c (Figure 2.2) defined as the crystallographic axes of the HA structure. Rapid elongation of crystalline appears in the c-axis direction (Omelon and Grynpas 2008), from the build-up of ions in the plane followed by an increase in crystallite width (b-axis) and the thickness (a-axis) increases at a slower rate (Simmer and Fincham 1995).

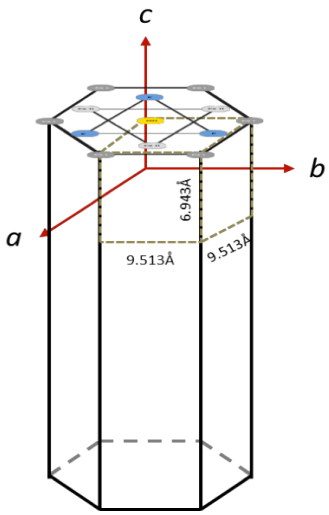

Figure 2.2 A schematic image of an enamel HA crystallite, presenting the arrangement of ions in the hexagonal plate (Siddiqui 2014).

Each atomic site within the HA crystals can be replaced by ions. Calcium in the apatite structure can be replaced by a variety of metal cations, e.g. Na^+, K^+, Mg^{2+}, Sr^{2+}; the phosphate ions may be replaced partially by carbonate; and the OH site could be substituted by F^- or Cl^- (Robinson *et al.* 1995).

2.2.2 Enamel microstructure

The mineral part of enamel is made of apatite with a hierarchy of structural levels from the atomic to the microscopic level (Boyde 1989). The enamel prism with a 3-6µm thickness and up to 3mm length is the largest structural unit of enamel and it is perpendicular to the enamel-dentine junction (EDJ). It has been discovered that the number of prisms in a tooth ranges from 5 to 12 million in the lower lateral incisor and upper first molar, respectively (Robinson *et al.* 1995). Each individual prism shows a "key-hole" structure including a head and a tail at a cross-section view of demineralised enamel (Figure 2.3). The heads and tails are directed toward the crown of the tooth, and the cemento-enamel junction (CEJ) throughout enamel, respectively. The appearance of a key-hole structure is more evident due to the presence of the space between the prisms, which is called inter-prism enamel (Scott *et al.* 1974).

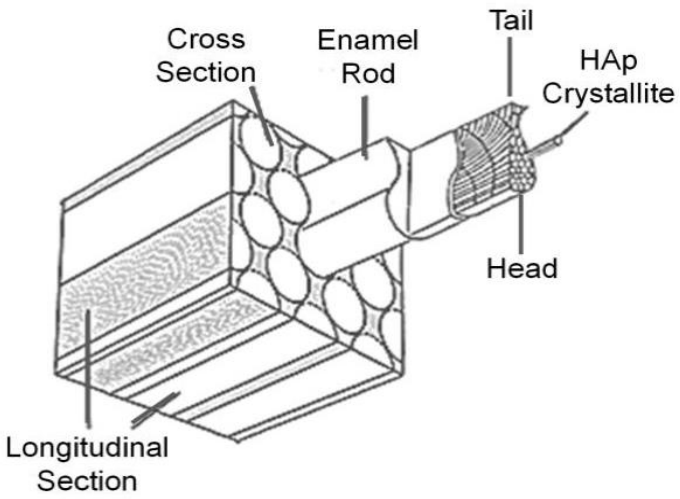

Figure 2.3 A schematic image of an enamel and HA key-hole structure. The key-hole structure includes head and tail for each enamel prism. Each enamel prism is packed with elongated HA crystallite (www.studyblue.com, accessed on 12/06/2016).

Each prism is composed of elongated carbonated apatite crystallites arranged in a distinctive pattern (Figure 2.3). In sound enamel, these crystallites are almost 40nm and 23-1000nm in diameter and length, respectively (Jongebloed *et al.* 1975). Robinson and his colleagues stated that the crystallites represent elongated and irregular hexagons in cross-sections (Robinson *et al.* 1995). These crystallites exist

at divergent angles at the prism junctions or boundaries leading to discontinuities in the structure. These areas acquire a more concentrated organic matrix through maturation, mainly a protein matrix of enamelins (enamel-specific-proteins). Both sites become “crack stoppers” and “crack propagation” tracks in the adult tissue (Boyde 1989).

The crystals in the enamel prisms and inter-prism enamel have similar composition but with different orientation. This gives rise to enamel pores, 1-10nm in diameter with a polygonal cross-section in the enamel structure. These pores, 1-5 volume% of enamel, are the inter-crystalline spaces occupied with water and organic materials. Areas close to the EDJ have shown a higher number of pores in the enamel structure, with smaller and extensively distributed crystals containing a higher amount of proteins (Weatherell *et al.* 1968).

When there are deficiencies in the packing of enamel crystallites at the enamel prism junctions, or boundaries, the number of porosities would increase in these areas (Hamilton *et al*. 1973).

2.2.3 Enamel physical properties

Enamel has special mechanical properties including great hardness with significant resilience due to its unique structural organisation. Since enamel is very rigid and dense, it would be very brittle without the presence of underlying softer dentine.

Although the composition of enamel is considered as equivalent to HA with a mineral density of 3.15 g/cm^3, Elliott confirmed that enamel is HA with multiple impurities. These impurities could include of carbonate ions which have a significant impact on the enamel density by reducing it to 2.99-3.02g/cm^3 compared to the density of pure HA (Elliott 1997).

It should be noted that enamel pores have a great influence on the physical properties of the enamel. Quantitative microradiography studies showed that enamel has a wide range of mineral content and porosity (Weidmann *et al*. 1967). The mineral content decreases from the outer surface of enamel compared to that nearer the EDJ while the pore volume is significantly greater in inner enamel

compared to the enamel surface. This gives rise to an increase in enamel permeability to ions, water and small organic molecules (Lowe *et al*. 1971).

2.2.4 Enamel chemical gradients

The lattice parameters, crystallinity (reflecting crystal size and crystal strain), stoichiometry (Ca/P molar ratio) and the chemical stability of the apatite crystal can be affected by the presence of imported ions. This leads to an inevitable change in chemical behaviour of enamel through the depth of enamel in the tooth structure (Elliott 1997).

The trace minerals in hydroxyapatite contribute to the crystals' lattice (Fincham *et al*. 1999) and their concentration affects the enamel solubility. The carbonate content increases from the enamel surface (1wt%) to the EDJ (4wt%), by substituting the phosphate and hydroxyl ions due to the metabolic activity of cells during enamel formation (Robinson *et al*. 1995). A high carbonate content increases solubility and makes enamel more prone to dissolution. However, the hydroxyl ions could be replaced by a similar sized ion, such as fluoride (high electronegativity and symmetrical charge distribution), and then the structure becomes more stable against dissolution. Fluoride in mature enamel is present in higher concentrations near to the surface. This may be due to the presence of fluoride in toothpastes. Its presence not only inhibits demineralisation, but also promotes remineralisation. On the other hand, magnesium substituting calcium ions will result in less stable crystals and therefore more soluble crystals, facilitating demineralisation (Robinson *et al*. 2000).The susceptibility of the crystals to dissolution by acid provides the chemical basis of dental caries (Nanci 2007).

In this study, the goal is to develop a radiopaque resin, which is able to infiltrate in the pores in early enamel carious lesions. The infiltration ability of the resin infiltrant depends on the capillary reaction in pores. Each tooth has a specific morphology and anatomy according to the tooth type, function and its location in the jaw (Berkovitz *et al*. 2009). Furthermore, enamel presents a vulnerable structure chemically, due to the natural variability in its chemical composition. This variation could be noted between teeth and within the tooth itself due to environmental and developmental factors (Dowker *et al.* 1999). All these factors result in various pore

sizes and structures in natural early enamel carious lesions, which can affect the ability of experimental radiopaque resins to infiltrate the lesions.

Chapter 3- Dental Caries

3.1 Dental caries

Dental caries, known as tooth decay, is a chronic multifactorial dental disease (Figure 3.1). It is caused by chemical imbalances in the oral environment. Dental decay is a complex process that involves bacteria, dietary sources of fermentable carbohydrates and salivary components over a period of time (Featherstone 2008).

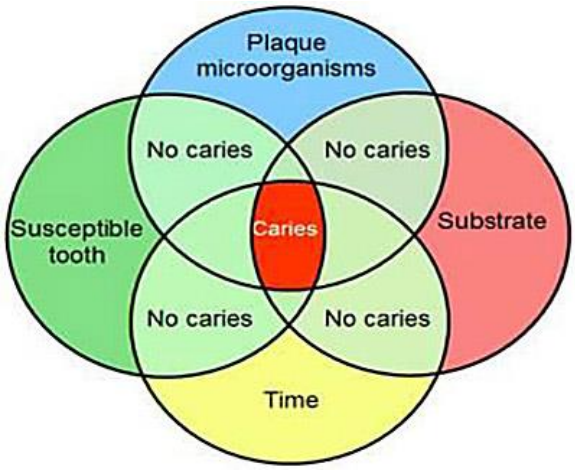

Figure 3.1 A schematic diagram showing the aetiological factors that develop caries. It is necessary to have all four factors together to develop dental caries (http://www.tankonyvtar.hu, accessed on 14/09/2016).

Microbial communities in the oral cavity are polymicrobial and mainly set up as a biofilm on various surfaces such as the teeth, dental materials and mucosa. Acquired pellicle is a salivary- or dietary-derived proteinaceous layer, which forms on the tooth surface. Then, the initial colonisers adhere to that, which affect the subsequent sequence of microbial colonisation. Oral biofilm consists of a microbial species community embedded in a matrix of bacterial components, salivary proteins, peptides and also food debris (Marsh 2004).

The basic mechanism of dental caries is demineralisation through acid attack. The microorganisms existing in the dental plaque can produce organic acids such as lactic acid, formic acid, acetic acid and propionic acid from the fermentable dietary carbohydrates. These acids penetrate through the plaque and into the enamel porosity. This dissolves carbonated hydroxyapatite (HA) crystals leading to the

release of Ca^{2+} and PO_4^{3-} ions from the tooth structure out into plaque fluid and saliva (Figure 3.2). On the other hand, remineralisation is the reverse process, where the ions (e.g. Ca^{2+}) in saliva will diffuse back into the tooth surface. There is a dynamic process between demineralisation and remineralisation in the oral environment (Figure 3.3). If the rate of demineralisation exceeds the rate of remineralisation, the tooth mineral dissolves step-by-step, while the overall structural integrity of the tooth is largely preserved. However, if the dissolution of mineral continues the enamel prisms would lose their alignment. This gives rise to the weakening of the overall structure, thus resulting in the collapse of the remaining tissue and formation of a dental cavity (Featherstone 1999).

Demineralisation occurs on three types of dental tissues including the enamel, dentine and cementum. Dental caries develops in areas for example that are difficult to clean properly, or where the level of saliva is very low at that site (Robinson *et al*. 2000; Deng *et al*. 2004).

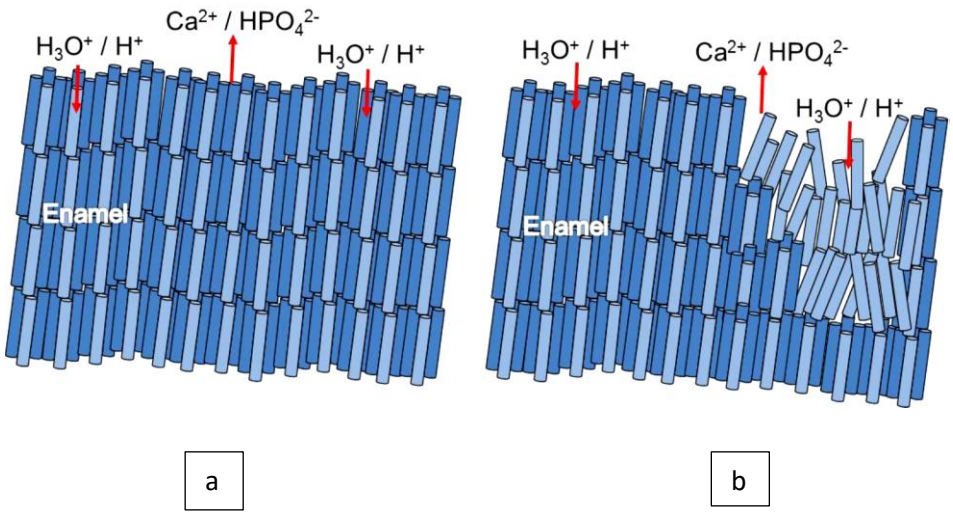

Figure 3.2 Schematic illustration of enamel prism microstructure: (a) sound enamel, (b) demineralised enamel (Mohammed 2014).

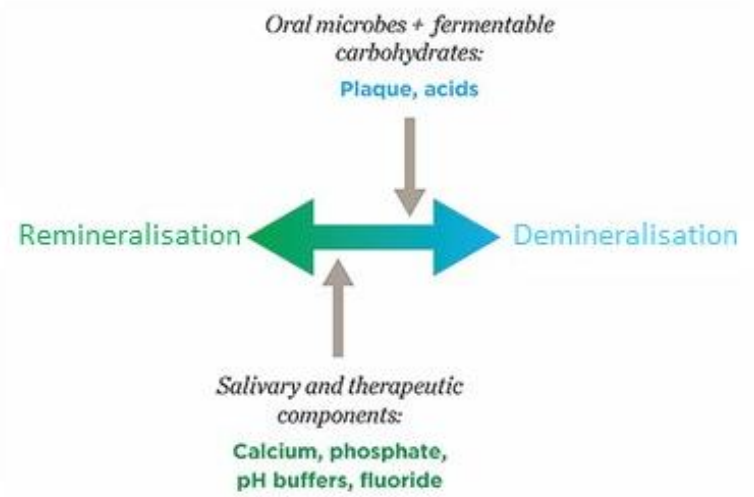

Figure 3.3 A diagram showing the oral equilibrium between demineralisation and remineralisation and their relevant supporting factors; green represents remineralisation and blue represents demineralisation (https://cced.cdeworld.com, accessed on 14/09/2016).

3.1.1 Prevalence of dental caries

Dental caries is one of the most common oral disease. The United States Department of Health and Human Services in 2000 reported that dental caries is 5 times more common than asthma and seven times more common than hay fever among children. Epidemiological studies reported a significant reduction in dental caries worldwide, which continues in populations (Bagramian *et al.* 2009).

Based on studies from 190 countries in the World Health Organisation (WHO) region, the average of decayed, missing or filled teeth (DMFT) index for 12 years old children was 2.11 and 0.3 worldwide and the UK, respectively (Virdi 2012).

The survey conducted by the NHS Dental Epidemiology Programme for England stated 30.9% and 33.4% in 5 and 12 years old children have at least one decayed, missing or filled tooth, respectively (Hilliard 2010; Rooney *et al.* 2010).

3.1.2 Cost of dental caries

WHO estimates that dental caries is the fourth most expensive disease to cure globally and the dental care expenditure is usually 6% of oral health expenditure. This number does not include preventive measures. The cost of dental care as a

percentage of total health cost varies between 0.5% in Mongolia to 8% in the US (more than US$ 100 billion on oral health care in 2009). Furthermore, there are indirect costs, such as absence from school and work leading to negative long-term economic impact on individuals and societies (Fisher *et al.* 2012).

3.2 Histological features of enamel caries

Enamel caries is initiated with partial demineralisation. Initial caries consists of a relatively sound surface layer of enamel (2-50µm thick) and a demineralised area underneath, where the main part of the mineral loss occurs (Figure 3.4). Initial caries appears to the naked eye as a "white spot lesion" clinically, which is an early sign of caries (Featherstone 2008).

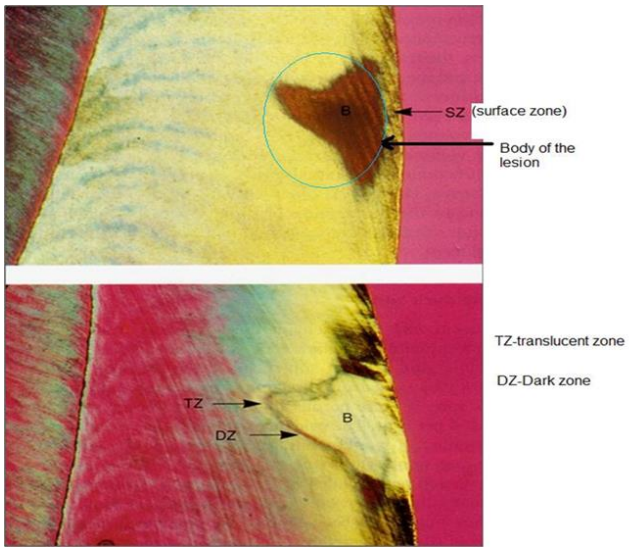

Figure 3.4 The histological features of initial enamel caries lesion called "White Spot Lesion". It has an intact surface layer and a demineralised area underneath (www.dentallecnotes.blogspot.com, accessed on 12/09/2016).

The enamel carious lesion has been categorised into four zones based on the histological changes. These zones are surface zone, body of the lesion, dark zone and translucent zone (Darling 1961; Silverstone 1968). This is in terms of the porosity level and amount of mineral loss in the lesion observed under polarized light microscopy (Figure 3.5).

The surface layer and body of the lesion are best seen after imbibition of the section in water, while the dark and translucent zones are best seen after imbibition of sections in quinoline. The dark zone and surface layer characterise remineralisation areas, while the translucent and body of the lesion zones represent demineralisation areas (Carton *et al.* 2007).

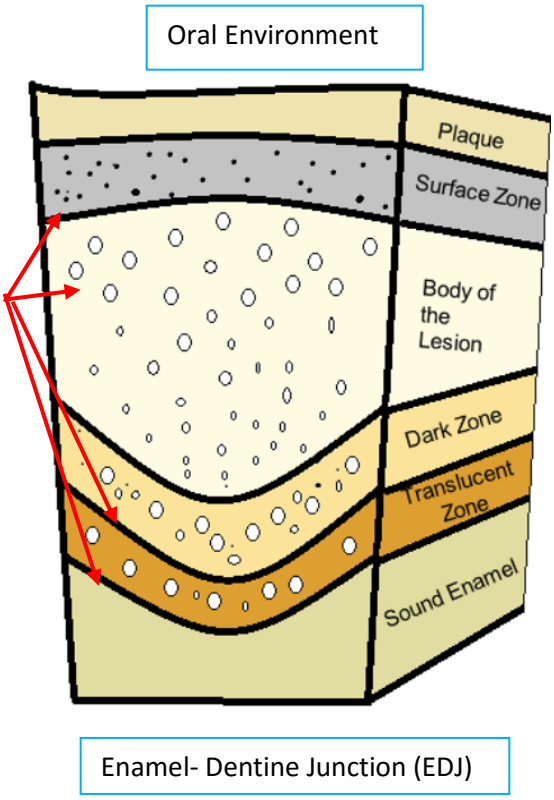

Figure 3.5 A schematic representation of enamel caries with four zones starting from the outer enamel surface layer towards the enamel-dentine junction (EDJ) and the relevant porosity level and the pore size (red arrows), modified from (Mohammed 2014).

- ***Surface zone***

The surface zone (layer) is the outermost layer of initial enamel caries. It is very similar to sound enamel and it has 1-2% porosity, 1% mineral loss and 40µm thickness (Silverstone 1968). This is predominantly due to dissolution of carbonate and magnesium elements in the enamel surface followed by the re-deposition of a

fluoride-enriched mineral. The presence of the fluoride makes the surface more resistant to acid attack. Furthermore, the enamel pellicle (organic material with 0.1-1µm in thickness) on the surface of the tooth is a selective barrier leading to a decrease in mineral loss at the surface.

- ***Body of the lesion***

Body of the lesion with 5-25% pore volume is the final stage of enamel destruction as it forms the continuous enlargement of the pore size and the collapse of enamel structure.

- ***Dark zone***

Dark zone is very similar to the translucent zone with smaller pores. The mineral loss is 5-10%. Since it is suggested that there is remineralisation occurring in this region, the dark zone represents both remineralisation and demineralisation.

- ***Translucent zone***

Translucent zone is the first detectable carious change in the enamel forming a surface layer. The mineral loss is about 1-2%. This zone has a small number of relatively large pores (Mohammed 2014) .

3.3 Dissolution of enamel and degradation of hard tissue

In a neutral environment in the mouth (pH of 6.5-7), there is an equilibrium between the enamel hydroxyapatite and the saliva which provides free calcium and phosphate ions. This results in normal saturation and tooth stabilisation (Silverstone 1968). At a critical pH (~5.5), a thermodynamic process under-saturation in the oral environment occurs, where the tooth tissue begins to dissolve and dental caries is formed (Robinson *et al.* 2000).

At, or below the critical pH, H^+ ions, produced by the bacterial metabolites, react with the phosphate groups of the enamel crystals resulting in $(HPO_4)^{2-}$ ion formation. This phenomenon, commences in the dissolution of the surface of enamel and is termed as demineralisation, which is the beginning of early enamel

caries. Demineralisation occurs due to prolonged and/or frequent cycling of low pH that is below the threshold value (Larsen 1990).

The non-cavitated enamel lesion is due to a dynamic balance between demineralisation and remineralisation. Whether the balance tips one way or the other depends on the oral environment, which is influenced markedly by an individual or, in the case of a child, the individual and carers (Featherstone 2008).

Despite the substantial body of work over the last four decades, there is still no clear consensus regarding the dissolution mechanism of dental enamel. Recently, Dorozhkin reviewed the literature on the various mechanisms involved in enamel demineralisation, yet none of the described mechanisms was able to provide a general answer for how this process occurs (Dorozhkin 2012), although clues are provided to help explain this phenomena.

3.4 White Spot Lesion (WSL)

A white spot lesion (WSL) is defined is defined as subsurface enamel porosity from carious demineralisation on the smooth surfaces of the tooth. It appears as a milky white opaque region (Bishara and Ostby 2008). In other words, WSL is the loss of enamel mineral while the surface of the lesion is relatively intact (Arends and Christoffersen 1986).

Formation of these lesions occurs quickly, as first clinical signs can be revealed as early as two weeks after initial biofilm formation (Holmen *et al*. 1987). They include an intact surface layer followed by the more porous lesion body underneath. The early attack of enamel caries is believed to be affected by decalcifying agents passing through the more resistant enamel surfaces. After these agents gain access to the subsurface enamel, they spread easily in all directions. White spot lesion formation may also progress inwards from the surface following the outlines of enamel prisms. This path of invasion affects the inter-prismatic area more than the prisms and tends to follow the striae of Retzius. Accordingly, WSLs are areas of early enamel demineralisation characterised by increased porosity. They are produced by enlargement of the intercrystalline spaces, which may subsequently become filled by amorphous organic material in the prism and inter-prism areas.

It should be mentioned that the pores within the body of the lesion allow diffusion of both acids and minerals through them, thus permitting the demineralisation of enamel to occur (Fejerskov *et al.* 2003). White spot lesions become more demineralised and ultimately form a cavity.

The shape of white spot lesion depends on the shape of the biofilm and the direction of the enamel prisms. For example, the lesion on the proximal surface is a kidney-shaped area between the contact facet and the gingival margin, while it is conical in shape in the cross section (Figure 3.6).

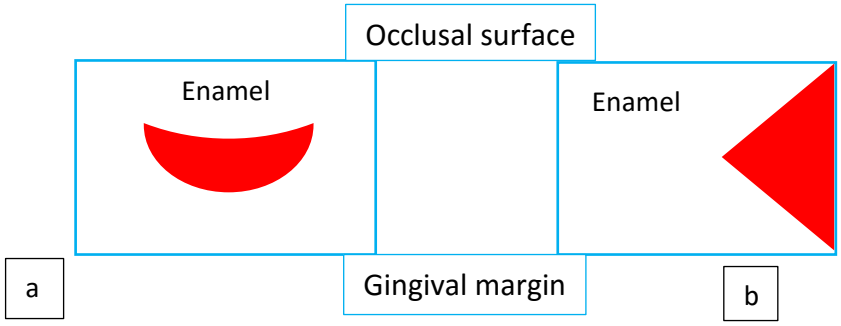

Figure 3.6 A schematic representation of caries (red areas) in (a) proximal and, (b) cross-section views of the tooth.

The intact surface layer plays a key role as a protective layer on the surface of the early enamel caries lesion due to its thickness and similar mineral density to the normal enamel. This layer may form due to high extrinsic fluoride ion deposition on the surface of the enamel lesion (Banerjee *et al.* 2011). Various studies have shown a range of surface layer thickness for natural and artificial lesions. Silverstone (Silverstone 1968) reported 30µm surface layer thickness covering the WSL, while other researchers (Groeneveld and Arends 1975) reported a range between 27 to 44µm thickness on artificial early caries lesion. Meyer-Lueckel *et al*. (2007) and Cochrane *et al*. (2012) reported a larger range of surface thickness, ranging between 10 to 160µm and between 35 to 130µm, respectively. In addition, the latter two studies reported 90 to 92% of the mineral content compared to that in sound enamel (Meyer-Lueckel *et al.* 2007; Cochrane *et al.* 2012). The differences in thickness of the intact layer may be due to the techniques that were used to define

the surface layer. Therefore, it is crucial to remove or perforate the surface layer in order to infiltrate the resin into the lesion fully (Paris *et al*. 2007).

The chalky, opaque appearance in an established white spot lesion is produced by an optical phenomenon, which is dependent on the pore volume of the lesion body of the WSLs. During demineralisation of the enamel, the pore volume of the WSLs increases; therefore, the refractive index (RI) of the lesion is changed. The resulting difference in the refractive indices between the sound enamel and the carious lesions is observed as a WSL, as it is visually distinguished from the surrounding sound enamel (Kim *et al.* 2011). Hence, WSL is more noticeable when a tooth is dry than wet because the difference in the refractive indices between sound enamel (1.63) and air (1.0) is more than that between enamel and water (1.33). The refractive index difference affects the light scattering and the lesion appears opaque. If the lesion is only visible on a dry tooth surface, the depth is probably in the outer enamel, whereas a visible lesion on a wet tooth surface will indicate that the lesion has progressed more into the enamel and possibly, into dentine (Kidd and Fejerskov 2004). Radiography and electrical resistance (Ricketts *et al.* 1996) are some of the other caries detection techniques that are based largely on enamel porosity. However, the mineral content of enamel is also a main factor on the manifestation of the WSL (Kidd and Fejerskov 2004).

A white spot lesion might occur due to an enamel defect or the early stage of enamel caries. Regardless of the aetiology, there appears to be no evidence documenting the differences in the porosities seen in the two types of WSLs. In this study, the focus is on white spot lesions as early enamel caries lesions. Furthermore, the terms white spot lesion and early enamel caries lesion have been used as interchangeable phrases in the present study.

3.4.1 Characterisation of WSL

WSL has an intact surface layer and a porous lesion body underneath (Arends and Christoffersen 1986) as previously mentioned (Arends and Christoffersen 1986). Suga (1988) obtained a contact microradiograph image from WSL showing a radiopaque outermost surface and a radiolucent subsurface due to remineralisation and demineralisation, respectively (Figure3.7) (Suga, 1988).

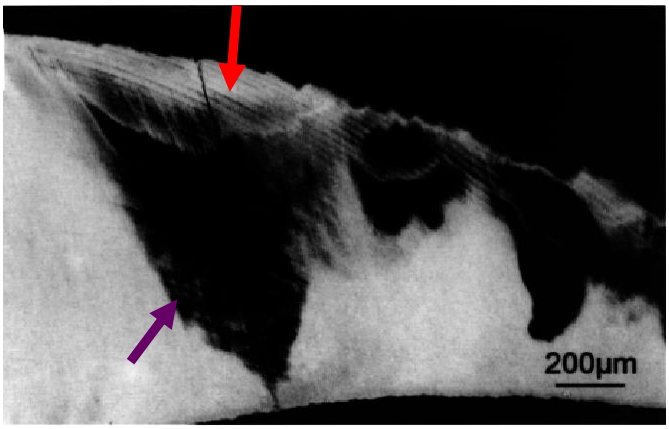

Figure 3.7 A contact microradiograph image of early enamel carious lesion showing a radiopaque surface layer (red arrow) and a radiolucent body lesion (purple arrow) (Yanagisawa and Miake 2003).

WSLs are prevalent lesions and play a key role in operative dentistry. However, there is still no clear consensus on their aetiology, structure and mineral gradient densities in the literature. The following studies carried out to characterise the white spot lesions.

- Featherstone and colleagues studied the chemical and structural changes of in-vitro carious lesions (Figure 3.8). They used two protocols including methylhydroxidiphosphonate (MHDP) and non-MHDP systems, as basic references for future studies in this field. They stated non-MHDP system represent the pure acidic environment whereas MHDP system involves the possible effect of dissolution inhibitors such as salivary proteins. They found a gradual increase in porosity of the outer 30µm of the enamel surface in the first few hours of experiment in both groups with preferential dissolution of calcium. The relevant mechanism is not clear but might be due to chemical reaction, calcium-deficient sites in the enamel crystal lattice or combination of the both (Featherstone *et al.* 1979; Ingram and Silverstone 1981).

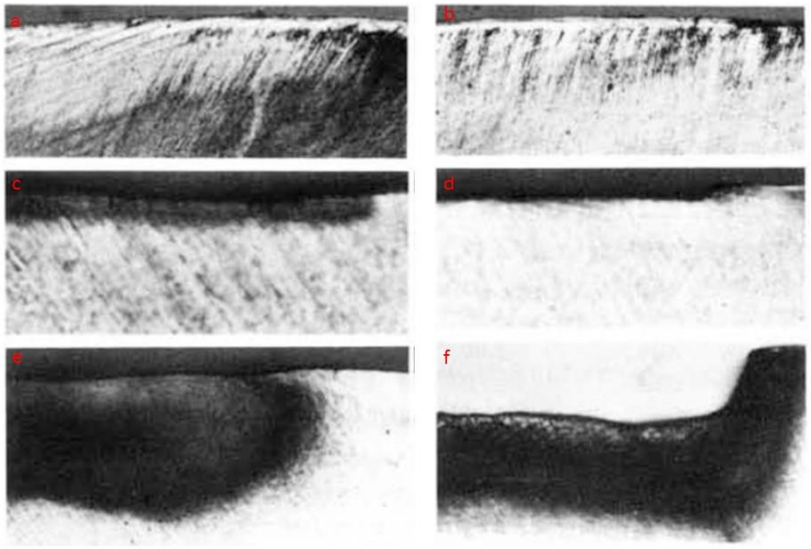

Figure 3.8 Ground sections of in-vitro enamel carious lesions in polarized light: (a)1-hour lesion produced with methylhydroxidiphosphonate **(**MHDP).x10; (b) 1-hour lesion produced without MHDP.x10; (c) 8-hour lesion produced with MHDP.x25; (d) 8-hour lesion produced without MHDP.x25; (e) 5-day lesion produced with MHDP.x25; (f) 5-day lesion produced without MHDP.x25; (a) and (b) examined in quinoline and the rest examined in water.

- Holmen and colleagues (1985) investigated the chemical, histological and ultrastructural changes on the enamel surface at false plaque retentive sites in-vivo in periods of 1, 2, 3 and 4 weeks using scanning electron microscopy (SEM). Their findings on the early enamel caries stages are summarised as follows (Figure 3.9):
    - Week 1: A dissolution of microstructure is visible and intercrystalline space was evident;
    - Week 2: The intercrystalline space increases and there is complete dissolution of individual HA crystals. Also, some scratches appear due to preferential dissolution or uniform intercrystalline space enlargement;
    - Week 3: The removal of perikymata occurs and underlying enamel is exposed;
    - Week 4: The intercrystalline space enlargement and dissolution of individual crystals are more evident (Holmen *et al.* 1985).

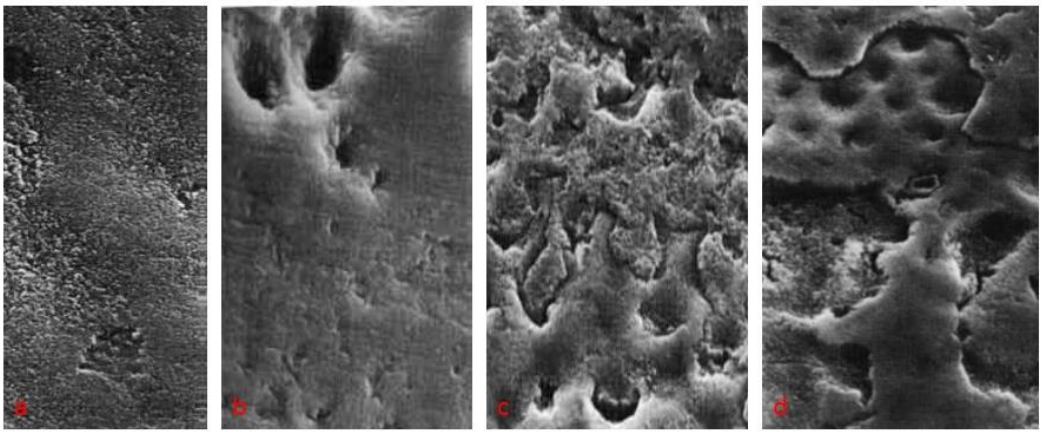

Figure 3.9 Microradiograph illustration of surface features after 1 (a), 2(b), 3(c) and 4 (d) weeks of in-vivo enamel carious lesion showing: (a) evident intercrystalline space.x1,000; (b) focal holes and multiple scratches. x1,000; (c) removal of perikymata.x1,000; (d) loss of larger part of perikymata.x2,000 (Holmen *et al*. 1985).

- Transmission electron microscopy (TEM) was used to investigate the changes at crystal level in early enamel carious lesions. They showed the development of etch pits in the central region of the enamel rods during the initial stages of enamel dissolution and the preferential dissolution of enamel crystallites in the central rod areas (Figure 3.10) (Featherstone *et al.* 1979; Yanagisawa and Miake 2003). Following the prolonged acid attack, enamel showed 'hollowing' of the rod structure (Neel *et al.* 2016) leading to form porosities in enamel carious lesion.

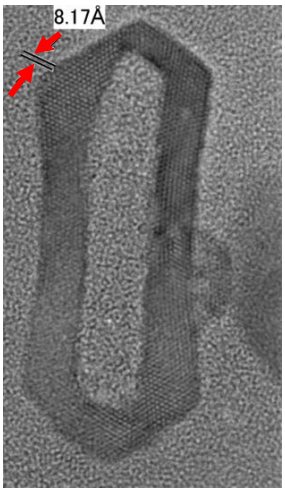

Figure 3.10 TEM image of enamel crystal showing dissolution at the centre of the crystal (Yanagisawa and Miake 2003).

- Cochrane and colleagues (2012) used quantitative x-ray microtomography technique at a 15-µm voxel size to determine the mineral content and depth in the surface layer of early enamel carries lesions. They found that the thickness of intact layer varied from 35 to 130 µm and its mineral content ranged from 74% to 100% for sound enamel. There were no significant differences in these measurements between clinically active and inactive lesions. Furthermore, they reported that the surface layers in active lesions were more porous than the inactive lesions (Cochrane *et al.* 2012).

Studies in the literature using scanning electron microscopy (SEM), indentation, backscattered SEM, and confocal laser scanning microscopy used to characterise the WSL are beneficial. These methods however are destructive as they require a section of the lesion, sometimes even at a particular stage of the caries dynamic cycle leading to loss of information between these sections.

3.5 Management of early enamel caries

3.5.1 Minimally invasive management

The understanding of caries has advanced impressively over recent years and it is now understood that caries is a dynamic process with phases of demineralisation and remineralisation (Featherstone and Doméjean 2012). Depending on the balance between these two processes a carious lesion may either regress, progress or stay static. If all the dental plaque is removed or the carious lesion is isolated from the biofilm, then caries will arrest.

Since the dentine-pulp complex is capable of repair and enamel can remineralise, the management of dental caries moves towards the biological approach rather than restorative treatment. Therefore, the concept of minimal intervention dentistry is introduced, which is defined as holistic patient care on early detection of disease, patient assessment, clinical assessment including dental history, biofilm status and staging of the carious lesions present at diagnosis, and prevention of disease progression with regular recall appointment (Banerjee 2013; Tellez *et al.* 2013). On the other hand, an untreated WSL, in particular in high caries risk patients, might progress to carious cavitation, which needs a dental restoration in order to

prevent further infection such as an abscess. Therefore, WSL prevention, diagnosis and treatment are very important to prevent tooth cavity formation (Featherstone 2008).

Several approaches have been introduced as non-invasive management of initial caries lesions (ranging from the first signs of demineralisation to a dentine lesion without cavitation) such as preventive regimes, including diet intervention and regular tooth brushing with fluoridated tooth paste twice daily. Furthermore, minimally invasive approaches are available to treat early enamel carious lesions (Kim *et al.* 2011). This latter approach aims to provide a material barrier either on top or within the lesion (Dorri *et al.* 2015).

3.5.1.1 Remineralisation

Fluoride and casein phosphopeptide amorphous calcium phosphate (CPP-ACP) play a key role in both enhancing remineralisation and caries arrest. Remineralisation of the lesion could be improved by the patient's oral hygiene and local fluoridation application (Kidd and Van Amerongen 2003).

The use of fluoride mouthwash and fluoride varnishes applied professionally will increase the oral fluids and biofilm fluoride level, which makes it supersaturated with respect to fluorapatite and enhances the white spot enamel lesion remineralisation (Botelho *et al*. 2009). Remineralisation by topical fluoride application requires multiple visits and long-term follow-up including patient cooperation, which is often difficult to obtain. Moreover, monitoring systems to assess the lesions status over time are still being studied, and are hard to apply in every day clinical practice (Dorri *et al.* 2015). Cochrane proposed CPP-ACP, a saliva biomimetic, that stabilises the calcium and phosphate ions in the same way as statherin and proline-rich proteins in saliva (Cochrane and Reynolds 2012). CPP-ACP is soluble in saliva (Shen *et al.* 2011) and is able of creating a diffusion gradient allowing calcium and phosphate ions to localise in supra-gingival plaque. It will then diffuse into the lesion and remineralise it either by an intact complex or by release of the ions (Cochrane and Reynolds 2012). In particular, deeper lesions do not remineralise completely because of the hypermineralised surface layer formation (Ten Cate and Duijsters 1983). Hence remineralisation is unpredictable in these

lesions, treatment should start early and performed regularly. Moreover, the success depends on patients' adherence (Beerens *et al.* 2010).

3.5.1.2 Resin infiltration

Sealants prevent the diffusion of bacterial acids into the lesion and they were first used to seal the pits and fissures of teeth. They were considered to be a very effective caries preventive measure (Ahovuo-Saloranta *et al.* 2013). Furthermore, resin infiltration (caries infiltration), the main focus of this research, is an approach to treat the initial caries lesion on proximal surfaces (Dorri *et al.* 2015).

Resin infiltration as a minimally invasive approach occludes the pores within the lesion body and inhibits further demineralisation of existing lesions efficiently. It helps to strengthen the enamel mechanically and prevents the breakdown of the enamel surface (Paris *et al.* 2007). We believe that resin infiltration is able to seal off the bacteria in WSL porosities and therefore, inhibits bacteria's activity in the lesion.

Robinson *et al.* (1976) proposed resorcinol-formaldehyde resin for caries infiltration (Robinson *et al.* 1976). However, it is unsuitable due to the toxic nature of the material and the hazardous effect on vital dentine and pulp tissue. This concept has been modified and commercially developed in Germany for early carious lesion management. In contrast to the sealing of a carious lesion that depends upon the external occlusion of the lesion with the sealant material, caries-inhibiting potential of the infiltrant depends on the occlusion of the pores within the body of the lesion. Other indications for infiltrant are amelogenesis imperfecta, molar incisor hypomineralisation and fluorosis (Muñoz *et al.* 2013).

Meyer-Lueckel and his colleagues carried out a randomised controlled trial assessing the progression of infiltrated non-cavitated proximal carious lesion radiographically (Meyer-Lueckel *et al.* 2012). The study reported that only 4% of the test lesions progressed against 42% of control lesions. Martignon *et al.* (2006) reported that 32% of caries progression was noted on the test lesions in comparison to 70% for the control lesions for the same period of time (Martignon *et al.* 2006).

3.5.2 Conventional invasive treatment (Restoration)

Conventional invasive treatment (restorative technique) involves rotary burs and hand instruments to remove caries and restore the cavity with a filling (e.g. composite). As the prevalent area for the proximal surface caries is below the contact area, therefore, there is a need to remove the marginal ridge of the tooth to gain access, even for a small carious lesion on the proximal surface. In other words, conventional cavity preparation may provide excellent cosmetic results but requires the substantial loss of dental hard tissue and further weakening of the tooth structure. Furthermore, it is simply inevitable to cause iatrogenic damage to the teeth.

It should be mentioned that while restoring the tooth, the patient may experience the effects of the local anaesthetic, caries removal with hand and rotary instruments and restoration placement. In other words, the tooth will enter the re-restoration cycle, with replacement restorations getting even larger until they eventually compromise the tooth in the long term (Brantley *et al.* 1995). Therefore, if the tooth is restored unnecessarily, the patient might experience all these discomforts unnecessarily.

Based on the above reasons, the removal of decalcified enamel lesion should only be considered as a last option when other options fail and the benefits of restoring the tooth outweigh the destructive effects of removing the sound enamel structure. Since due to the reversible nature of WSL, less invasive treatments should be preferred (Ardu *et al.* 2007; Dorri *et al.* 2015).

Chapter 4- ICON® Resin Infiltration

4.1 Resin Infiltration

4.1.1 Background

Treating tooth surfaces after eruption to decrease the incidence of dental caries involves the following two main approaches:

- To provide a physical barrier

Materials in this category, such as varnishes and sealants are beneficial in enamel fissures or in the most susceptible region of the dentition to accumulate the cariogenic bacteria (Buonocore 1972; Maiwald and Geiger 1973).

- To enhance the natural resistance of sound enamel

In this category, products such as solutions, pastes, or gels containing fluorides play a key role to reduce the enamel surface susceptibility to caries (Buonocore and Gwinnett 1967; Vrbic and Brudevold 1970; Mellberg and Nicholson 1974).

Robinson *et al.* (1976) proposed that there is a possibility for components of topical prophylactic materials to penetrate and accumulate in the porous enamel in early enamel carious lesions, which will lead to the arrest or even reversal of the demineralisation process. This is due to fact that the carious dental tissue is more porous in comparison with sound enamel resulting in greater accessibility. In their study, they suggested that ideal topical prophylactic material should: 1) be hydrophilic, as fissures and the porous enamel of the lesion are usually moist; 2) have a low viscosity, as the material should be able to spread over the tooth surface rapidly and penetrate into the pores of early enamel lesion; 3) be bactericidal or bacteriostatic; 4) be biocompatible; 5) be able to polymerise into a solid phase and support the physically weakened enamel mechanically; and 6) be cosmetically acceptable. They found that resorcinol-formaldehyde resin fulfilled the mentioned criteria, in particular the first, third and fifth points. However, the material was shown to have the possible adverse effect on vital dentine and pulp. Furthermore, resorcinol-formaldehyde resin produced the dark-red colour due to oxidation, which made it cosmetically unacceptable. As a result, Robinson and colleagues (1976) stated that although the suitability of the resorcinol-formaldehyde resin as a caries prophylactic material was questionable, the concept of this type of treatment

or technique could be a feasible approach to treat early enamel caries (Robinson *et al.* 1976). In 2006, the ICON® resin infiltrant was developed in Germany, at the Charite University Hospital in Berlin and marketed under the brand name of ICON® (DMG America Company, Englewood, NJ) (Robinson *et al*. 1976; Mueller *et al.* 2006).

Resin infiltration is an approach to treat the non-cavitated carious lesions on smooth surfaces of primary and permanent teeth. It can also improve the aesthetic appearance of the WSLs on labial surfaces. This technique has advantages including being non-invasive, preserving of the tooth structure and being able to be completed in a single visit (Paris and Meyer-Lueckel 2009).

Resin infiltration improves the aesthetic of WSL as the infiltrated WSLs appear to be similar to the surrounding sound enamel. However, it is unclear whether it is because of the small difference in the refractive indices between the sound enamel (RI= 1.63) and the infiltrant (RI=1.46), or the reduced susceptibility to subsequent extrinsic staining that gives rise to the improved aesthetics (Kim *et al.* 2011). Furthermore, resin infiltration, a very low viscosity resin, is used to prevent further progression of caries in WSLs by occluding pores of the lesion body, which act as a cariogenic acid pathway (Meyer-Lueckel and Paris 2008). Martignon and colleagues showed that the progression of non-cavitated proximal lesions extending up to the outer third of dentine has been reduced by the infiltrant application (Martignon *et al.* 2012).

The present commercially available infiltrant resin (ICON®) is composed of 80wt% Triethylene Glycol Dimethacrylate (TEGDMA), 20wt% Bis-Glycidyl Dimethacrylate (BISGMA), 0.5wt% camphorquinone as a photo- initiator and 2wt% Dimethyl Amino Ethyl Methacrylate (DMAM) as co-initiator (Paris *et al.* 2014). The infiltrant resin shows good penetration into the porous structure of the WSL due to its low viscosity (Paris *et al.* 2011) and a penetration coefficient (PC) larger than 50 cm/s (Paris *et al.* 2007). One study suggested that resin materials with a high concentration of triethylene glycol dimethacrylate (TEGDMA, Figure 4.1a) would inhibit the lesion progression better than those with high concentrations of bis-glycidyl dimethacrylate (Bis-GMA, Figure 4.1b) (Meyer-Lueckel and Paris 2008). Another experimental resin comprised of a mixture of TEDGMA and Bis-GMA provided the

similar outcome with a PC value of 185 cm/s (Feilzer and Dauvillier 2003). These studies show that the high penetration capability of TEGDMA-based resin is the key factor for its success in caries prevention (Paris *et al.* 2007).

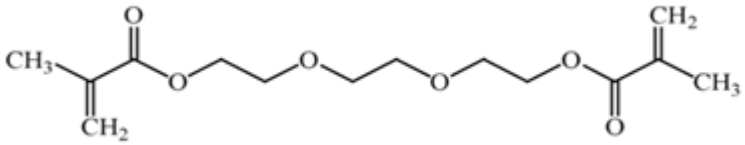

TEGDMA

a

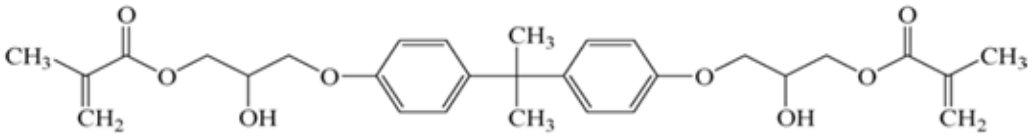

Bis-GMA

b

Figure 4.1 The chemical structure of (a) triethylene glycol dimethacrylate (TEG-DMA) and, (b) bis-glycidyl dimethacrylate (Bis-GMA) (www.data.epo.org, accessed on 26/10/2016).

4.2 ICON® resin application

4.2.1 Pre- treatment

Capillary forces play an important role in the infiltration of the resin into WSL. It is dependent on the pore volume and the radius of the pore. The penetration depth of resin is lower in natural carious lesions in comparison with artificial lesions. This is due to a difference between the lesion structures, in particular, the surface layer. The surface layer of natural caries is heterogeneous and has a higher mineral content compared to artificial lesions, because of the de- and remineralisation cycles in the oral cavity (Eggerath *et al.* 2011). For complete occlusion of the lesion bodies with the infiltrant, it is necessary for the surface layer of the WSLs to be made porous (Meyer-Lueckel *et al.* 2007).

A previous study recommended the use of 15% hydrochloric acid (HCl) gel for 120 seconds to perforate or remove the surface layer in order to increase resin infiltration into the lesion body (Meyer-Lueckel *et al.* 2007). Furthermore, researchers suggested that the acid treatment will improve remineralisation of initial subsurface lesions because of the increased access of the ions required for remineralisation (Al-Khateeb *et al.* 2000). This effect might be helpful in order to increase the accessibility of resin infiltrant into the WSL resulting in a better infiltration ability of the resin infiltrant into the WSL. However, HCl is a very strong acid and is able to destroy crystalline structure of the hydroxyapatite. It has been showed that two minutes of 15% HCl, (4.1M), application on enamel leads to a surface substance loss of 35.95µm (Arnold *et al.* 2015). Hence, it is important not to contact the areas of sound enamel adjacent to the lesion (Tong *et al.* 1993).

4.2.2 Ethanol

Ethanol is used to remove the remaining residual water at the bottom of the body lesion and decreases the infiltrant resin viscosity. The addition of 10% and 20% of ethanol increased the penetration coefficient (PC) and the penetration depth (Meyer-Lueckel and Paris 2010).

It was shown that a 99% of TEDGMA resin has a PC value of 204 cm/s, while a mixture of TEDGMA and ethanol increases the PC value to 391 cm/s (Paris *et al.* 2007). However, solvent gives rise to heterogeneity and uncured resin layer might occur. Therefore, it is a balance between the use of the ethanol to increase penetration abilities and its negative properties on the cured material. The authors concluded that low-viscosity resin infiltrants based mainly on TEGDMA have relatively high PC (> 200 cm/s) and are capable of almost completely inhibiting the progression of natural enamel caries lesions in a low-demineralising environment (Paris *et al.* 2007).

4.2.3 Repeated application

Paris and Meyer-Lueckel suggested a repeated application of the resin infiltrant to the surface lesion after surface pre-treatment to overcome the problem of polymerisation shrinkage. In addition, the repeated application of dental adhesives will provide a better acid resistant surface (Paris and Meyer-Lueckel 2010).

4.3 Disadvantages

Sufficient radiopacity of the dental material is desirable or essential to allow for a clear distinction between the material and the surrounding tooth structure. This will facilitate and enable the evaluation of the dental restoration quality (Carvalho-Junior *et al.* 2007). However, ICON® is a radiolucent material and its use must be precisely recorded in the clinical record. If the patient leaves the practice and attends another dental surgery, the radiolucent area might be considered as a carious lesion, unless there is a communication between the old and the new practices. Furthermore, it is extremely difficult to prove the radiolucent resin has been applied on the lesion clinically, which may be an issue in a legal dispute. Thus, these concerns lead the current examiner to a burning question: “How to develop a radiopaque infiltrant resin or make ICON® radiopaque?”.

Chapter 5- Radiopaque Agents

5.1 Introduction

Radiopacity is an essential property for dental materials and maybe defined as the inverse of the optical density of a radiographic image. The development of X-ray radiographs is very valuable in both medical and dental fields to facilitate appropriate diagnosis.

American Dental Association Council on Dental Materials, Instruments and Equipments (1981) stated that the relative radiopacity of the dental materials compared to the tooth structure is crucial for the following reasons. A dental material with a sufficient contrasting radiopacity in comparison with dental tissue (relative radiopacity) helps to locate and monitor the material precisely to evaluate the restoration contour, the contact with the adjacent teeth, overhangs, the interfacial gap, detect voids and any secondary caries as part of the long-term assessment of dental materials' stability (Tsuge 2009).

The radiopacity of a material should be equal to or greater than that of the same thickness of pure aluminium (Al) based on the International Standards Organization (ISO)- 4049 (Standard 2000). The incorporation of a contrast agent is helpful to make a material radiopaque. All elements absorb X-rays to some extent and this depends on the average atomic number, density and the thickness of the material. The higher the atomic number and/or the greater material thickness is, the more radiopaque the material generally is. Linear attenuation coefficient (LAC) is the standard measurement of radiopacity. It is the fraction of the incident x-rays that is absorbed or scattered per centimetre thickness of the medium. It defines the amount of energy loss within an absorber, by a photon beam per centimetre (Figure 5.1). The unit is cm^{-1} and it is denoted by the symbol μ (Bushberg and Boone 2011). It should be noted that the mass attenuation coefficient (MAC) is the volume of a material showing how easily the beam can penetrate into it and its unit is m^2/kg or cm^2/g (Hubbell and Seltzer 1995).

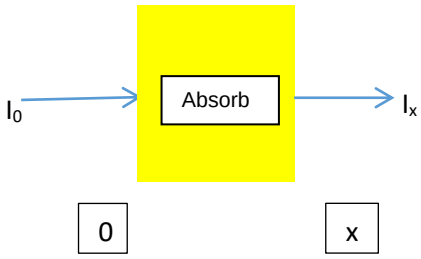

Figure 5.1 A schematic diagram showing the concept of linear attenuation coefficient (LAC), which is the energy loss (I_x-I_0) within an absorber.

It is possible to calculate LAC if MAC and density of the material is available (Equation 5.1).

LAC = MAC $\times \rho$ Equation 5.1

LAC: Linear attenuation coefficient (cm^{-1}),

MAC: Mass attenuation coefficient (cm^2/g),

ρ: Density (g/cm^3).

Since ICON® is an organic resin that has no high atomic number elements, it has a LAC as low as water. In order to modify this material to be radiopaque, a number of approaches can be tried, including:

- Incorporation of radiopaque fillers such as strontium hydroxyapatite (SrHA) or strontium bioactive glass (SrBG),
- Incorporation of radiopaque monomers such as Bromine or Tin in the form of bromine-methacrylate (BrM) and tin-methacrylate (SnM).

5.2 Radiopaque Filler

5.2.1 Hydroxyapatite (HA)

Hydroxyapatite ($Ca_{10}(PO_4)_6(OH)_2$), the most broadly used synthetic Calcium Phosphate, is an important biomaterial and a major component of the mineralised

structure of the teeth and bones (Ferraz *et al.* 2004). In the literature, researchers mentioned that parameters such as ion substitution, crystal size and surface feature of HA showed significant roles in its properties.

- ***Ion Substitution***

The calcium apatite present in teeth contains other ions in different amounts substituting for calcium and phosphate in the HA lattice. Synthetic hydroxyapatite has been used as a bone replacement material (Bigi *et al.* 2007). The natural apatite is non-stoichiometric due to the presence of cations (Mg^{2+}, Mn^{2+}, Zn^{2+}, Na^{+}, Sr^{2+}) or anions (HPO_4^{2-} or CO_3^{2-}). For instance, the ion substitutions lead to changes in HA surface structure and charge, which gives rise to changes in both solubility and bone formation and remodelling (Miao *et al.* 2005).

- ***Crystal Size***

The crystal size of HA has an important role in properties such as hardness, surface area activity, chemical reactivity and biological activity (Balasundaram *et al.* 2006; Cai *et al.* 2007). Particles that are 100nm or smaller are considered as nano-particles (Allaker 2010). Researchers suggested that the nano-technology in dentistry provides stimulating applications for nano-hydroxyapatite, which presents crystals ranging in size from 50 to 100nm. Higher surface energy, increased surface area, optimal biocompatibility and faster dissolution are some of the nano-HA's unique properties in comparison with conventional HA (Hannig and Hannig 2010). For example, nano-HA is more effective to fill porous enamel defects, in comparison with conventional HA due to its higher solubility. Furthermore, nano-HA is releasing inorganic ions such as calcium leading to an increase in bonding strength between the teeth and material (Lee *et al.* 2010). Huang *et al*.(2011) demonstrated that nano-HA has a better effects in remineralisation of initial enamel caries under dynamic pH-cycling or neutral conditions in comparison with conventional HA (Huang *et al.* 2011). Li and colleagues (2008) showed that nano-HA is able to both prevent and repair initial erosive lesions simultaneously in comparison with conventional HA (Li *et al.* 2008).

Nano-HA has been widely used in the following fields of dentistry (Kumar and Vijayalakshmi 2006):

- Preventative and operative dentistry

Nano-HA has been introduced as a filler component to improve the properties of widely used dental materials. For example, dental resin loaded with nano-HA filler in dentistry is considered as a potential restorative material for non-load bearing human tooth tissues (Chen *et al.* 2011). Lee and colleagues (2010) showed that incorporation of nano-HA into glass ionomer cements (GIC) increased the bonding strength to tooth structure and the tooth resistance to demineralisation, which could possibly lead to the prevention of demineralisation of enamel surfaces in-vivo (Lee *et al.* 2010).

Initial dental caries can be remineralised by using fluoride, administered via either mouthrinse or toothpaste (Schäfer 1989; Wefel *et al.* 1995). As there is a possibility of dental fluorosis, in particular in the pre-school children age group due to chronic ingestion of these products (Pendrys and Stamm 1990), nano-HA could be beneficial as an alternative caries remineralising and preventive agent. Jeong *et al*. (2006) and Najobfard*et al*.(2011) showed that incorporation of nano-HA in a toothpaste results in remineralisation of the incipient carious lesion (Jeong *et al.* 2006; Najibfard *et al.* 2011). This could be explained by the potential of nano-HA crystals precipitation on the lesion surface due to its strong surface bioactivity in combination with its similar chemical and physical properties to the natural enamel (Li *et al.* 2008).

Haghgoo and colleagues found a positive correlation between the amount of nano-HA in sodium fluoride (NaF) mouth rinse and its remineralisation ability of enamel in primary carious lesions (Haghgoo *et al.* 2014). This study also proposed that there is synergy between nano-HA when combined with a fluoridated mouth rinse. In another study carried out by Haghgoo *et al.* (2011), exposure to nano-HA solution enhanced the enamel micro-hardness on erosive lesions significantly (Haghgoo *et al.* 2011).

- Periodontology, oral and maxillofacial surgery

Nano-hydroxyapatite (nano-HA) is helpful in medical and dental applications including dental implants, orthopaedics, alveolar reconstruction and drug delivery system because of its biocompatibility, biological and chemical similarity to the bone structure. Hydroxyapatite has a key role in osteo-inductivity and osteo-integration resulting in bone remodeling. It can be in either granular powder or shaped blocks using in pre-prosthetic surgery to increase the thickness of the alveolar ridge or reconstruction of facial skeleton and bone replacement, respectively. Furthermore, nano-HA has been used in implantology due to its key role at the bone-implant interface (Pepla *et al.* 2014).

- ***Surface feature***

The surface properties of hydroxyapatite (HA) have a significant role in its applications because the surface is in direct contact with the environment such as body fluids. For instance, surface modified groups are considered as a useful technique to avoid agglomeration of nano-particles, an aid for a controlled particle growth as well as making the surface to be more appropriate to the host tissue (Lu *et al.* 2007). The HA surface could be modified by either organic molecules or polymers. There are two common methods to modify the HA surface by organic molecules:

- Surface adsorption: where polymers and proteins are adsorped onto the surface of HA (Hlady and Füredi-Milhofer 1979),
- Grafting: organic molecules, which are able to be grafted to the hydroxyl groups via covalent bonding. Hydroxyl groups are available on the crystal surface of HA. These surface grafted nano-particles including methyl methacrylate, vinyl phosphonic acid, poly(ethylene), and poly(urethane) have a great range of applications in the field of HA/polymer composites, column chromatography of protein, cell culture carrier and carriers of catalysts in chemical engineering (Puvvada *et al*. 2010). Anwar (2014) found that particles coated with methacrylic acid have a higher surface area in Brunauer–Emmett–Teller (BET) measurement, meaning a lower particle size

in comparison with the other surface modifying agents including polyvinyl alcohol, adipic acid, citric acid and vinyl phosphonic acid (Anwar 2014).

5.2.2 Bioactive glass (BG)

5.2.2.1 Glass

Glass is defined as an inert non-crystalline solid material, which is brittle and transparent. It is an amorphous material with random structures of atoms lacking order or periodicity with short-range order between atoms. Crystalline materials have well-defined structures with periodicity with long-range order between atoms. Scientists based on glass processing, physical and chemical properties have proposed different definitions for glass:

- The American society for Testing Materials stated that glasses are “inorganic products of fusion that have been cooled to a rigid condition without crystallising” (Winter 1957);
- According to McMillan, a glass is a transparent or translucent material, which is rigid, brittle and hard (McMillan 1964);
- Dremus (1973) proposed that glass is an amorphous solid with the lack of a periodic arrangement in its network and a time-dependent glass transformation feature. This definition outlines the two special characteristics of glass and covers glass and bioactive glass (Shelby 2005).

In summary, glass is an amorphous material with a transition temperature regardless of the synthesis route.

5.2.2.2 Bioactive Glass

Larry Hench developed bioactive glass (45S5) in late 1960’s as the purpose of bone regenerative properties. Bioactive glass is not an inert material. Bioglass, composed of 46.1mol% SiO_2, 26.9mol% CaO, 24.4mol% Na_2O, 2.6mol% P_2O_5, has a relatively high bioactivity and can bind to living tissues (Hench 2006).

Zachariasen proposed the continuous random network model, explaining the role of the different elements to make glass and their interaction with each other in glass’s structure. This model divides the role of all glass atoms into three different

categories including network formers, network modifiers, and intermediates. The network former is the backbone of a glass and involves connected silicone atoms by oxygen atoms known as bridging oxygen (BO) atoms and might co-ordinate with non-bridging oxygen (NBO) atoms. Network modifiers such as sodium oxide and calcium oxide break up Si-O-Si bonds and then introduce NBO atoms into the system. It should be mentioned that many changes in the structure of the glass network occur by various numbers of bridging oxygen atoms per silicone atom (Phillips 1983). Researchers introduced models to determine the average number of BO atoms per silicone atom in bioactive glass and then used this to understand the structure of new glass compositions. The rate of glass degradation and apatite formation in a biological medium is considered as important factors to predict the glass bioactivity (Fredholm *et al.* 2010).

Bioglass is able to form a layer of apatite on its surface leading to an integrated bond with a living bone when it is immersed in physiological solutions (Lockyer *et al.* 1995, Hench 2006). Previous studies showed that the bio-glass (45S5) could form hydroxyapatite (HA) after immersion in Tris buffer and stimulated body fluid (SBF) for 24 hours and 3 days, respectively. The BG contact with fluids results in dissolution of Ca^{2+}, PO_4^{3-} and Si^{4+} at the glass surface, leaching of Na^{+} and formation of a poly-condensated silica-rich layer on the glass bulk. This layer will be a template for the formation of a calcium phosphate (Ca/P) layer at the outer surface of BG (Hench and Wilson 1996) which crystallises into HA. This phenomenon explains the bioactivity feature of BG.

BGs were introduced to dentistry due to their bioactivity and good biocompatibility. For example, it might be possible to use BG as mineralising agents in caries prevention or desensitising agent for hypersensitive teeth (Orchardson *et al.* 1994). It has been introduced as a biocompatible material in early enamel caries treatment by assessing the viability and the morphological alternations of pulp cells (Bakry *et al.* 2011). Bioactive glass present in NovaMin (toothpaste) aid the remineralisation of teeth or it could be beneficial and useful as part of composite resins in order to remineralise the tooth (Höland *et al.* 2006). Furthermore, bioglass has been used in orthopaedics (e.g. NovaBone) and periodontal treatment (PerioGlas). In

implantology, a coating of BG on the fixture surface of implant assist osseo-integration by forming a HA bridge between the implant and mucosal or dermal soft tissues. Furthermore, BGs incorporation in root canal therapy materials assists to provide a biological seal in the root canal and at the apex (Hench 1998; Behbehani and Zaatar 1999).

5.2.3 Strontium (Sr)

Strontium (Sr) is a naturally trace element in the human body with 98% of it found in the skeleton which is only 0.02 mol% of the calcium (Li *et al.* 2007; Aaseth *et al.* 2012). Strontium at levels of 320-400mg is present in the mineral phase of bone and connective tissue. The ionic radius of calcium and strontium are 0.94 Å and 1.16Å, respectively. This small difference allows the substitution of strontium for calcium in many crystal lattices. Strontium content presents greater X-ray radiopacity in both glass and apatite due to the higher atomic number, which is 38 in comparison with the atomic number of Ca, which is 20 (O'Donnell *et al.* 2010).

There is an interest in strontium from the caries and caries-related research community due to its similar chemistry to calcium (Ca) (Lippert and Hara 2012), but, there is no clear indication of the relative importance of strontium in caries prevention. The relevant research results varied including no effect (Olson *et al*. 1978); an increased (Hunt and Navia 1975; Joseph *et al.* 1977), or a decreased effect (Meyerowitz *et al*. 1979; Curzon and Spector 1981) on caries incidence.

5.2.3.1 Strontium in dental applications

Dental materials with strontium have been widely used in following purposes:

- To treat dentine hypersensitivity

Polish investigator, Pawlowska, (1956) showed that 25% aqueous solution of strontium chloride is an effective product in treating dental hypersensitivity. The author explained this effect due to ability of strontium chloride to combine with enamel and dentine via adsorption (Pawlowska and Jego 1956). Strontium has been the active agent of toothpastes for treating dentine hypersensitivity for the last 50 years (Pearce *et al.* 1994). In addition, strontium chloride and strontium acetate

were used in Sensodyne toothpaste (GlaxoSmithKline, London, UK) as the dentine hypersensitivity prevention agents.

- A component of dental restorative material

Fuji IX® glass ionomer cement (Stamboulis *et al.* 2004) and Fuji IX®(Da Silva *et al.* 2007) have been introduced to repair decayed tooth and provide antibacterial effects in Atraumatic Restorative Treatment (ART), respectively.

- Bone regeneration products

In-vivo, strontium has key beneficial effects on bone growth in particular at the regions with high metabolic turn-over (González Cabrera *et al.* 2012). Due to this effect on bone cells, strontium bioglasses have been introduced by Gentleman (2010) as a bone regeneration material by substituting strontium for calcium in bioglass on a mol% basis (Gentleman *et al.* 2010). Additionally, strontium containing biomaterials have been developed for implant and tissue engineering applications such as StronBone® by RepRegen Ltd (London, UK) which have been approved in Europe for hard tissue repair and regeneration (Hill and Stevens 2007; Jallot *et al.* 2008).

Researchers set up experiments to investigate the effect of strontium on the structure and properties of apatite and bioactive glasses. For instance, O'Donnell *et al.* (2008) found that the substitution of slightly larger and heavier strontium to calcium result in an increase in the unit cell volume and density in apatite (O'Donnell *et al.* 2008). Furthermore, the Sr substitution in bioactive glass increases the glass density and molar volume without any change in the network structure (Xiang and Du 2011).

Since strontium has a higher atomic number (38) in comparison with calcium (20), it is assumed that the incorporation of strontium into hydroxyapatite and bioglass structures could be beneficial to make them radiopaque. The calculated mass attenuation coefficient (MAC) values for SrHA ($Sr_{10}(PO_4)_6(OH)_2$) and SrBG (SiO_2 – P_2O_5 –SrO –Na_2O) are 8.6 and 3.82 cm^2/g at 70Kv, respectively, (http://physics.nist.gov/PhysRefData/Xcom/html/xcom1.html). The Density of

SrHA and SrBG is 4.05 and 3.10g/cm^3, and the LAC values for SrHA and SrBG are 34.83 and 11.82 cm^{-1}, respectively.

5.3 Radiopaque Monomer

5.3.1 Bromine-methacrylate

2,3-dibromopropyl methacrylate ($C_7H_{10}Br_2O_2$), or bromine-methacrylate (BrM) has a molecular weight of 285.96 g/mol (Figure 5.2). The atomic number for bromine is 35, thus a high radiopacity would be gained with its presence. The calculated MAC value for 2,3-dibromopropyl methacrylate was 6.508cm^2/g at 70kV (http://physics.nist.gov/PhysRefData/Xcom/html/xcom1.html). The density is 1.24 g/cm^3 and its LAC is 8.07 cm^{-1}. BrM contains 55.9 wt% bromine thus, this polymer will hold the high radiopacity when it is diluted with Poly(methyl methacrylate) PMMA (Davy and Causton 1982).

Davy and Causton (1982) compared the mass attenuation coefficients of bromine (Br) and barium (Ba) and found their absorptions are similar. He found that bromine-methacrylate monomers could produce radiopaque materials on polymerisation. Under this technique, there is a covalent bond between the halogen (bromine) and the backbone polymer chain. Furthermore, these copolymers exist as a single-phase system in comparison with the two-phase system, which incorporate radiopaque materials as fillers**.** These authors found an excellent X-ray radiopacity and good mechanical properties for co-polymers containing 36-40 wt% (2,3dibromopropyl methacrylate) (Davy and Causton 1982).

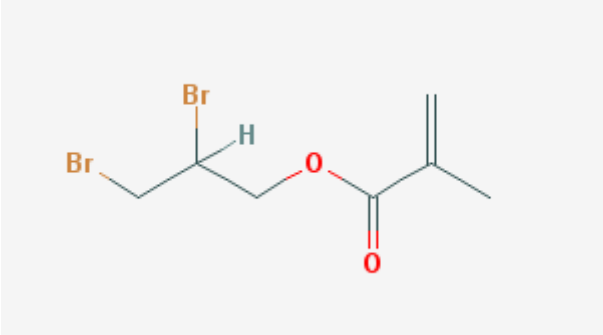

Figure 5.2 The chemical structure of 2,3 di-bromopropyl methacrylate (www.pubchem.ncbi.nlm.nih.gov,accessed on 02/02/2017).

5.3.2 Tin-methacrylate

Methacyloxytri-n-butyltin($C_{13}H_{30}OSn$) or tin-methacrylate (SnM) has a molecular weight of 375.12g/mol. The chemical structure of SnM (Figure 5.3) has one methacrylate group on one end, attached to the butlytin compound at the other end (GELEST Inc., Morrisville, PA, USA. Lot no. 5D-6588).

Figure 5.3 This is the chemical structure of methacyloxytri-n- butyltin (http://www.chemspider.com/Chemical-Structure.21171291.html, accessed on 02/02/2017).

The atomic number for tin is 50, which makes it capable of providing a high radiopacity feature. This value is even higher in comparison with Br, which is 37. The calculated MAC value for methacyloxytri-n-butyltin is 1.057E+01cm^2/g at (http://physics.nist.gov/PhysRefData/Xcom/html/xcom1.html). The density is 0.89 g/cm^3 and its LAC is 9.41cm^{-1}.

Anderson *et al*. (2006) introduced tin-methacrylate as a radiopaque resin-based fissure sealant monomer. This gives a new insight on the potential of using this compound in development of new dental materials with a high radiopacity (Anderson *et al*. 2006).

5.4 Ideal radiopaque infiltrant resin

The main aim of this study was to make the ICON® resin infiltrant radiopaque and overcome the most important drawback of ICON® resin as a material to seal the early enamel carious lesion. In order to fulfil the aim, the following three main questions would be raised:

- **Question 1:** what is the structure of WSLs?

WSL is defined as a porosity in enamel structure without cavitation whereas there is no clear definition for porosity in the literature. Furthermore, the previous studies on WSLs improved our knowledge on development of WSL and its structure without any information about the pore size and pore structure in the lesion. The latter information is crucial in order to develop infiltrant resins incorporating fillers for treating early enamel caries lesions, because if the size of a filler particle is larger than the pore size (in any dimension) it will not be feasible for the radiopaque resin to infiltrate (Figure 5.4). Furthermore, the interconnectivity of the pores will also have an effect on the penetration depth and infiltration ability of the resin (Figure 5.5).

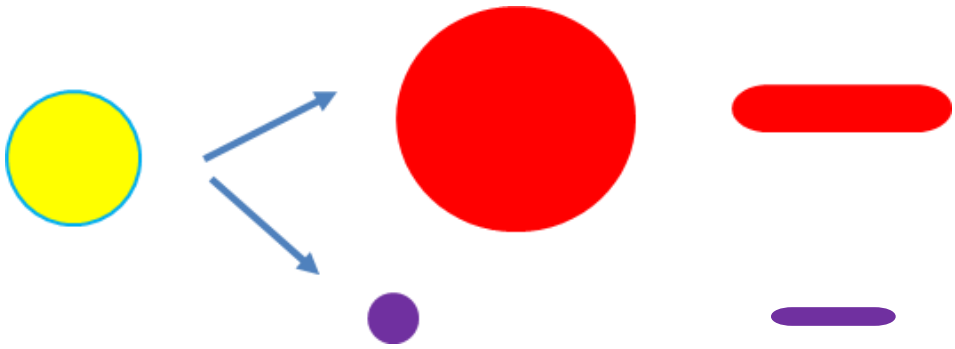

Figure 5.4 Schematic diagram showing the importance of the pore size in infiltration of particulate resins. If the particles, in any dimensions, are larger (red shapes) than the pores (yellow circle), they cannot (maybe a small amount if the direction is favourable) infiltrate to fill the pores. Only if the particle size is smaller (purple shapes) than the pore size then infiltration can occur completely.

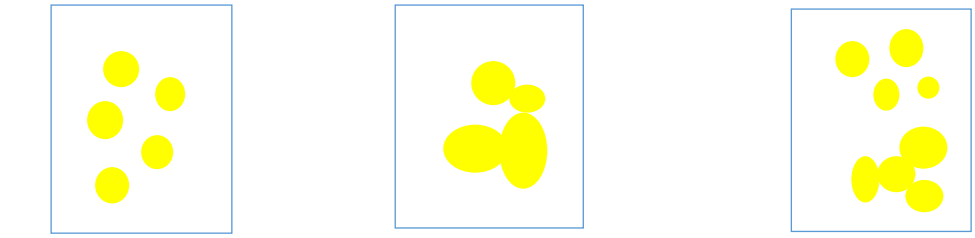

Figure 5.5 Schematic representation of the possible structures of the pores (yellow areas) in white spot lesion (in blue rectangle): (a) there is no connection among pores, (b) all pores interconnected and, (c) there is a combination of (a) and (b) in different areas of the same white spot lesion.

- ***Definition of pores and porosity***

In the Oxford Dictionary (https://en.oxforddictionaries.com/definition/pore, accessed on 22/01/2017), the pore is a term defined as a tiny opening in skin or organism structures, while Collins Dictionary (https://www.collinsdictionary.com/dictionary/english/pore, accessed on 22/01/2017) defines "Pore" in the following ways:

- Anatomy: any small opening in the skin or outer surface of an animal,
- Botany: any small aperture where the water, vapour and gases pass,
- Any other small holes such as a space in a rock, soil etc.

International Union of Pure and Applied Chemistry (IUPAC) described a porous solid as any solid material with cavities, channels or cracks; however, this definition might modify in each context (Author 1964).

Porosity is a Greek word from "poros" meaning passage. Therefore, porosity means to let things pass through. In other words, it defines a state of interconnecting tiny holes and a measurement of the open spaces in a material. Wikipedia defines porosity as void fraction, which is a fraction of the volume of voids over the total volume of the material. The number is in a range of 0 to 1 (0-100%). IUPAC defines porosity (Ɛ) as a ratio of the total pore volume (V_p) to the apparent volume (V) of the material, excluding any voids among particles (Author 1964).

- ***Pore classification***

Pores in porous materials are characterised by two main parameters, the pore size and pore structure. The former feature is the main important factor in characterising porous materials. The individual pores may vary greatly both in size and in shape within a given solid, and from one solid to another.

IUPAC defined the pore size as the distance between two opposite walls of the pore (Author 1964). The definition of the pore size is precise in pores with well- defined geometrical shape. For example, the diameter of a cylindrical pore, the distance between the sides of a slit-shaped pore, or the smallest dimension in fissure pore. Dubinin (Dubinin 1960) proposed pore size classification based on adsorption mechanisms and corresponding linear pore size ranges. This is now officially adopted by IUPAC (Harris *et al.* 2002). The IUPAC classifies pores with respect to the different mechanisms occurring within them during N_2 isothermal adsorption at 77 K and 1 atmospheric pressure. These are divided into three groups: macro-, meso-, and micropores, which are 50 ≤, 2≤ to <50 and <2 nm in size, respectively (Author 1964).

Kaneko (1994) classified pores as either open or closed. Open pores communicate with external surfaces and there are accessible pathways for ions and molecules, etc. Open pores could be sub-classified into blind or through pass. Blind pores, known as dead end, are closed at one end, while through pass pores are open at two ends (Figure 5.6). Closed pores are defined as those pores that with helium at 303 K cannot be penetrated (Setoyama *et al.* 1993), or open pores with the width smaller than the probe's molecular size (Kaneko 1994). Alternatively, pores structures can be defined based on the pores geometry including the cylinder, slit-shape, cone-shape (funnel shape) and ink-bottle shape (Figure 5.7) (Harris *et al.* 2002).

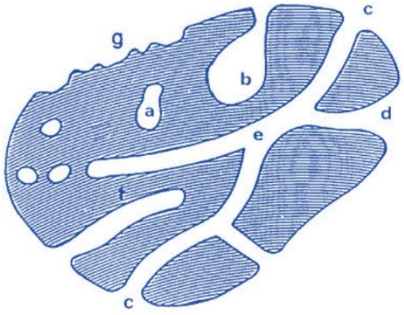

Figure 5.6 Schematic drawings on pores classification, according to their availability to environment. a - closed pores, b, f - pores open only at one end, c, d, g – open pores, e - open at two ends (through) pores (Harrisr *et al*. 2002).

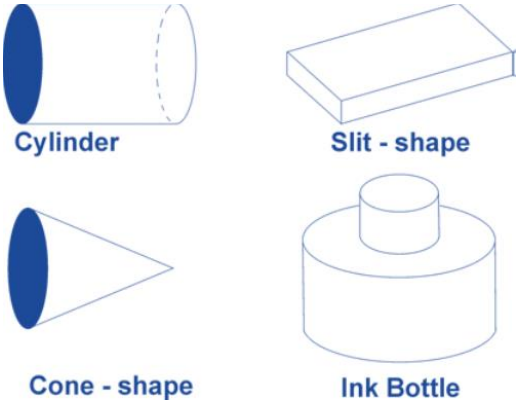

Figure 5.7 A schematic diagram of pores classification according to the pores geometry (modified from Kaneko 1994).

In this study, Brunauer–Emmett–Teller (BET) and Focussed Ion Beam Scanning Electron Microscope (FIB-SEM) were used to investigate the pore size and pore structure in WSLs.

- **Question2:** How to make the infiltrant resin radiopaque?

In this study, incorporation of radiopaque fillers such as nano-SrHA, SrBG and incorporation of radiopaque monomers such as BrM, SnM considered to make the infiltrant resin radiopaque.

Nano-SrHA/ SrBG selected as radiopaque fillers due to the presence of the strontium. Furthermore, Sr has an antibacterial effect and HA/BG are able to

promote the remineralisation inside the pores structure and these feature might be additional benefit to treat white spot lesions. However, since it is assumed that the porosity would be filled with resin infiltrant fully, there is no space available for mineral crystal growth. Moreover, HA/BG might not show any remineralisation ability when the infiltrant resin is cured fully. Thus, the latter features of Sr, HA and BG might be beneficial when the resin infiltrant does not penetrate fully to the WSL or there are voids between the enamel and the cured material and the infiltrant resin is not cured fully within the lesion.

In this study, BrM and SnM were used as radiopaque monomers. They are in liquid forms and it assumed that the developed radiopaque resins including BrM or SnM might have a higher penetration ability in comparison with resin infiltration including the radiopaque fillers as there is no particles incorporated in the former materials.

- **Question3:** What is the criteria for an ideal radiopaque infiltrant resin?

In an attempt to make an ideal radiopaque resin infiltrant, the following points were considered:

- Curing ability: the experimental radiopaque resin should be able to cure into solid phase in 40s by light curing (Standard 2000);
- Radiopacity: the experimental radiopaque resin needs to have a radiopacity equal to or greater than that of the same thickness of pure aluminium (Al) (Standard 2000);
- Consistency: the experimental radiopaque resin should have a smooth (unagglomerated) consistency because agglomeration will prevent infiltration of the material into the white spot lesion (Neffgen *et al*. 2012);
- Viscosity: the dynamic viscosity of the developed radiopaque resin should be less than 32mPa.s, which equals to a penetration coefficient >50cm/s (Paris *et al*. 2007);
- Wettability: the experimental radiopaque infiltrant resin should be hydrophilic, *i.e.* the contact angle should be less than 90° (Craig *et al.* 2000);

- Infiltration ability: the experimental radiopaque infiltrant resin should be able to infiltrate into the depth of a deep lesion (Paris *et al.* 2007);
- Biocompatibility: the developed material should have a cell viability reduction less than 30% (ISO 1999).

Experiments, Results and Discussion

Chapter 6- Characterisation of Porosity in White Spot Lesion

6.1 Introduction

The basis of the infiltration concept is to penetrate and fill the pores of white spot lesion (WSL) with resin through capillary action. Since one of the aims of this study was to investigate the incorporation of nano-particles in the resin to increase its radiopacity, it is crucial to investigate the structure and size of the pores (Section 5.4, Question 1). In this study, Brunauer-Emmett-Teller (BET) and focused ion beam scanning electron microscope (FIB-SEM) techniques were used to characterise the porous structure in early enamel carious lesion for the first time. BET data could be helpful to investigate the pore size and structure in early enamel carious lesion while FIB-SEM is able to image and visualise the porous structure in WSL in three dimensions.

6.1.1 Brunauer-Emmett-Teller (BET)

Brunauer, Emmet and Teller developed a method to calculate the specific surface areas of porous solids. It is a cheap, fast and reliable method. This method is based on the gas adsorption concentration at an interface with a solid, without actual penetration of the gas into the solid. In other words, adsorption can be defined as the adhesion between a surface and atoms, ions, or molecules from a gas, liquid, or dissolved solid leading to creation of a film of the adsorbate on the surface of the adsorbent (Figure 6.1). When a gas is exposed to a solid, the gas molecules intrude upon the solid and might reside upon the surface for a limited time. The adsorbed amount depends on the nature of both the solid (adsorbent) and the gas (adsorbate), and on the pressure at which adsorption takes (Atkinson 1986). The volumetric method is used to calculate the amount of gas adsorbed, which states the amount of gas removed from the gas phase due to adsorption on the solid surface. The adsorption process provides valuable information about the surface area and pore structure of the solid. Surface area is the number of molecules in a completed monolayer multiplied by the effective cross-sectional area of an adsorbate molecule. The BET method is based on the monolayer capacity of the solid calculation, which in turn can be used to calculate the specific surface of the solid. The monolayer capacity is the amount of adsorbate, which is accommodated in a monolayer on the surface of the unit mass of the solid. The rate of product

formation depends on the available surface area. The greater the amount of surface area accessible to the reactants, the smaller pore size is (Lowell, Shields et al. 2012).

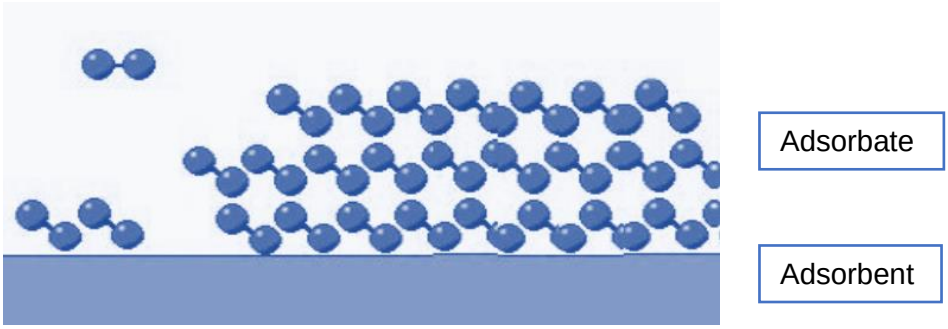

Figure 6.1 The adsorption of a gas at an interface with a solid, without actual penetration (Atkinson 1986).

Adsorption processes can be divided into two categories, chemical or physical with respect to their strength of interaction. Chemical adsorption (chemisorption) is a single layer of chemically bound adsorbate at the surface, which involves chemical bonding of the gas or vapour with the surface. Chemisorption leads to localised adsorbed molecules on the surface, which enables to determine the number of active sites on the catalyst by merely measuring the quantity of chemisorbed gas.

Physical adsorption, which is reversible and based on the Van der Waals force, is suitable to determine the surface area. Low heats of adsorption inhibit disruptive structural changes of the surface during the adsorption measurement. Physical adsorption is able to cover the surface by more than one layer of adsorbate, meaning that pores can be filled by the adsorbate for pore volume measurements. The adsorption and desorption processes can be reported because physical adsorption is fully reversible. Physically adsorbed molecules are free to cover the entire surface and are not engaged to specific sites; therefore, the surface areas would be calculated rather than number of sites.

Lowell stated that the amount of adsorbed on a solid surface will depend upon the function (F), temperature (T), the pressure (P), and the interaction potential (E) between the gas (adsorbate) and the surface (adsorbent) (Lowell *et al.* 2012). Therefore, at equilibrium pressure and temperature the weight (W) of gas adsorbed on a unit weight of adsorbent is given by:

$$W = F(P, T, E) \qquad \text{Equation } 6.1$$

Usually, the quantity adsorbed is calculated at constant temperature and equation reduces to:

$$W = F(P, E) \qquad \text{Equation } 6.2$$

The measurement cycle aims to reach equilibrium between pressure and amount of gas adsorbed. There are different gases, which could be useful in BET, such as Nitrogen, Krypton, and Helium.

There are six different isotherm graphs showing the amount of adsorbed gas as a function of the relative pressure under a fixed temperature (Figure 6.2).

Isotherm I is encountered with the micro-porous materials. All pores will be filled with the gas in lower pressures and adsorption is related to a few molecular layers.

Isotherm II is relevant to non-porous or macro-porous adsorbate. The knee of the isotherm shows the completion of the first adsorbed monolayer. With an increase in pressure, higher layers are completed.

Isotherm III shows that the adsorbate interaction with the adsorbent layer and is less than that of with an adsorbed layer.

Isotherm IV involves the monolayer, multilayer adsorption, and capillary condensation. A characteristic of this isotherm is the hysteric loop. The lower and the top branches of the loop show the progressive addition and withdrawal of the gas.

Isotherm V shows the weak interaction and capillary condensations and it is similar to the isotherm III.

Isotherm VI is relevant to the stepwise multilayer adsorption on a non-porous non-uniform surface (Lowell *et al.* 2012).

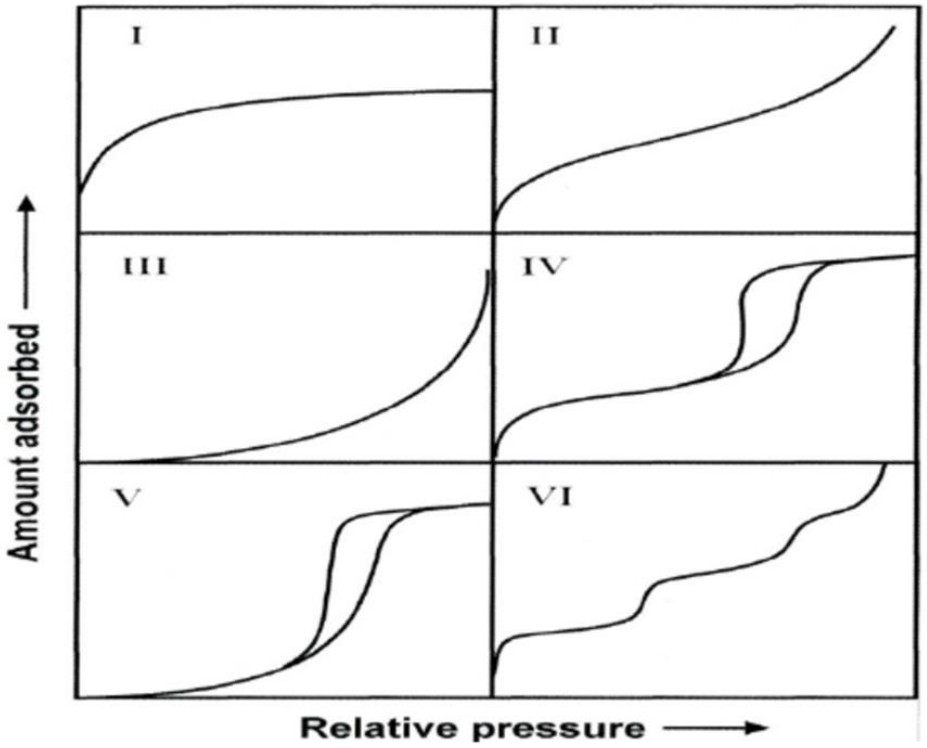

Figure 6.2 Six different types of isotherms by BET measurements showing the amount of adsorbed gas as a function of relative pressure at a fixed temperature (Lowell *et al.* 2012).

6.1.2 Focused Ion Beam- Scanning Electron Microscopy (FIB-SEM)

Focused ion beam scanning electron microscope (FIB-SEM) was introduced in research laboratories in 1990s. It provides both high-resolution imaging and flexible micromachining in a single platform. It has a well-known use in fundamental materials studies and technological applications over the past several years.

Three dimensional (3D) imaging can be carried out at cellular and sub-cellular levels. FIB-SEM is volume electron microscopy technique, which covers these two features together, leading to broad-spectrum resolution in a larger tissue volume. It plays a key role in a wide spectrum, including life sciences such as developmental biology, pathology and microstructure anatomy or in order to assess the integration of new implants. This technique is important for materials science applications, including circuit editing and transmission electron microscopy (TEM) sample preparation to microstructural analysis and prototype nano-machining. Also, the most modern FIB

instruments (Figure 6.3) have an additional scanning electron microscope (SEM) column so that the instrument becomes a multipurpose “dual-beam” stage FIB–SEM for imaging, material removal, and deposition at length scales of a few nanometers to hundreds of microns. The FIB instrument becomes a powerful tool for nano-manipulation and fabrication through the augmentation of FIB instrument with micromanipulators and gas injection for local chemical vapour deposition (CVD).

The FIB instrument and SEM are very similar. The difference between these two methods is the beam, which is an ion beam for FIB and an electron beam for SEM. Gallium ions are being used in the most FIB machines where their sputtering action enables accurate machining of samples. The gas injection on these systems helps the deposition and increases etching. This technique can display complex microanatomy with high resolution and provides structural information in 3D with micron resolution. The machine is able to mill the sample with thickness down to <10nm.

FIB-SEM could be applied to biological tissues. A focused gallium ion beam mills away the sample surface sequentially and a backscattered electron (BSE) images the milled surfaces. This generates a series of images that can be combined into a 3D image of embedded biological tissue (Volkert and Minor 2007; Bushby *et al.* 2011). For sub-surface imaging of enamel, the operator can manually halt the milling process to take a high quality SEM image of the sub-surface. Alternatively, using the “slice and view” option, this process can be automated to take multiple sequential images. It has been suggested that platinum deposition over the area of interest could improve the image contrast.

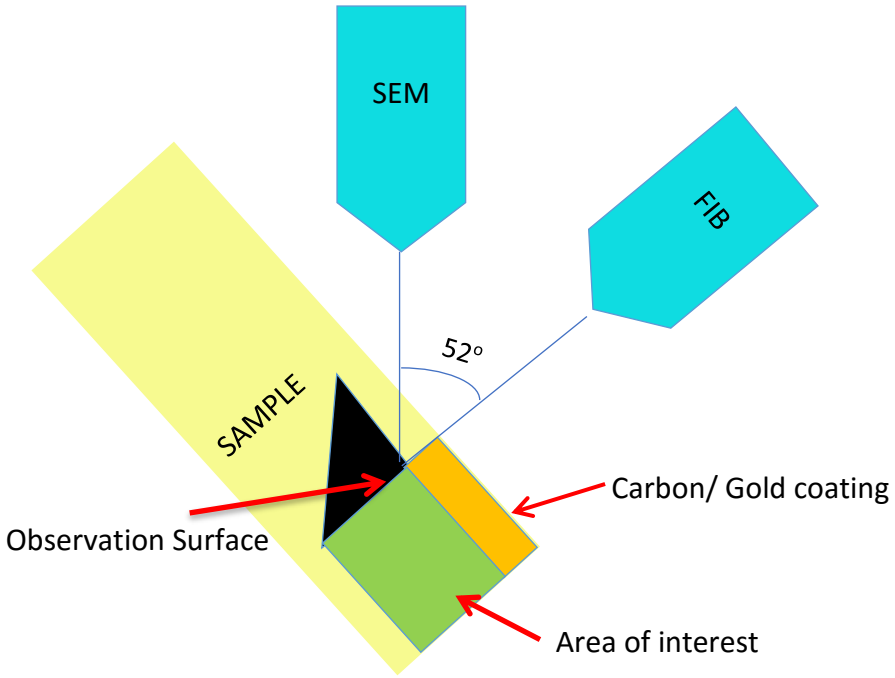

Figure 6.3 A schematic representation of a dual-beam focused ion beam-scanning electron microscopy (FIB–SEM) instrument.

6.2 Aims and objectives

In this chapter, the aims of the experiments were to explore the use of BET and FIB-SEM techniques to characterise:

- the pore structure and,
- the pore size in early enamel carious lesion.

6.3 Materials and Methods

6.3.1 Brunauer–Emmett–Teller (BET)

The BET pilot study was carried out on one healthy tooth and one tooth with white spot lesion by Quantachrome® (Hartley Wintney, Hook, UK), in order to compare and evaluate the surface area, the degree of the porosity and pores structure between the two.

6.3.1.1 Sample preparation- 1

Teeth from tooth bank (approval from Queen Mary Research Ethics Committee QMREC 2011/99) stored in 70% ethanol (Sigma-Aldrich, Gillingham, UK) were examined visually. The examination was carried out by cleaning the tooth by bristle brush (Henry Schein, London, UK) and slow handpiece (NSK Ltd, Stevenage, UK), drying the tooth with compressed air, and using a good light (A-dec 6300 Light Bulb 17V, 95W, Mercia Dental, UK). Two first permanent premolars, one with a white spot lesion on the proximal surface and the other one with an intact crown, were selected. A trephine drill 2.0mm x 22mm (Salvin Dental Specialties, Charlotte, USA) was used to remove the white spot lesion from the tooth. The same procedure carried out to provide a sample of normal enamel (Figure 6.4). These two samples were sent to Quantachrome® (Hartley Wintney, Hook, UK) for BET test; however, the sample size was too small and the experiment could not been carried out.

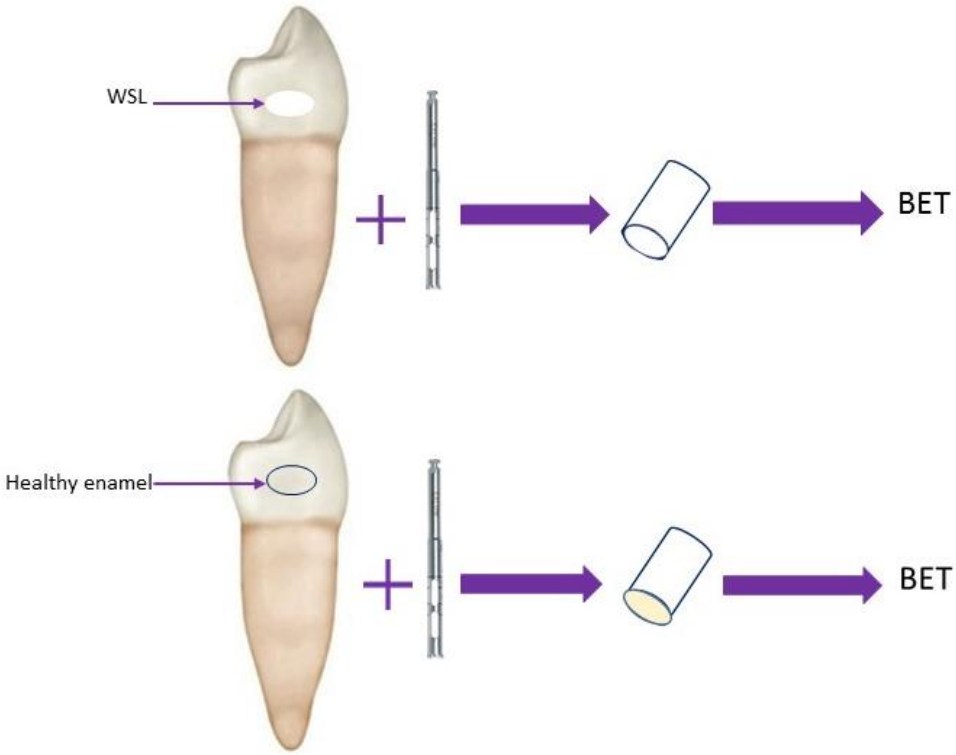

Figure 6.4 Schematic representation of sample preparation for BET using a trephine drill.

6.3.1.2 Sample preparation- 2

Two first permanent premolars, one with white spot lesion and one with intact crown, were selected as described earlier in section 6.4.1.1. Both teeth were cut at the tooth cervical region using an annular diamond blade (Microslice 2, Malvern Instruments, Malvern, UK) to exclude the roots for BET measurements. Two layers of nail varnish (Number 7 'Colour Lock', Quick dry nail polish Boots, Nottingham, UK) were applied at the cervical area of the teeth to inhibit gas penetration from the cervical area into dentine and pulp. Therefore, only the enamel surface of the teeth was exposed to the adsorbate. The samples were sent to Quantachrome® (Hartley Wintney, Hook, UK) to carry out the BET experiment (Figure 6.5). The samples were weighed on scaler before and after degassing for 16 hours at 25°C±1℃. Nitrogen adsorption/desorption was applied to estimate the surface area of the healthy tooth. However, initial results found that the surface area of the tooth with WSL was too small to be assessed with Nitrogen. Therefore, Krypton adsorption was used to evaluate the surface area, instead. The parameters were summarised in Table 6.1.

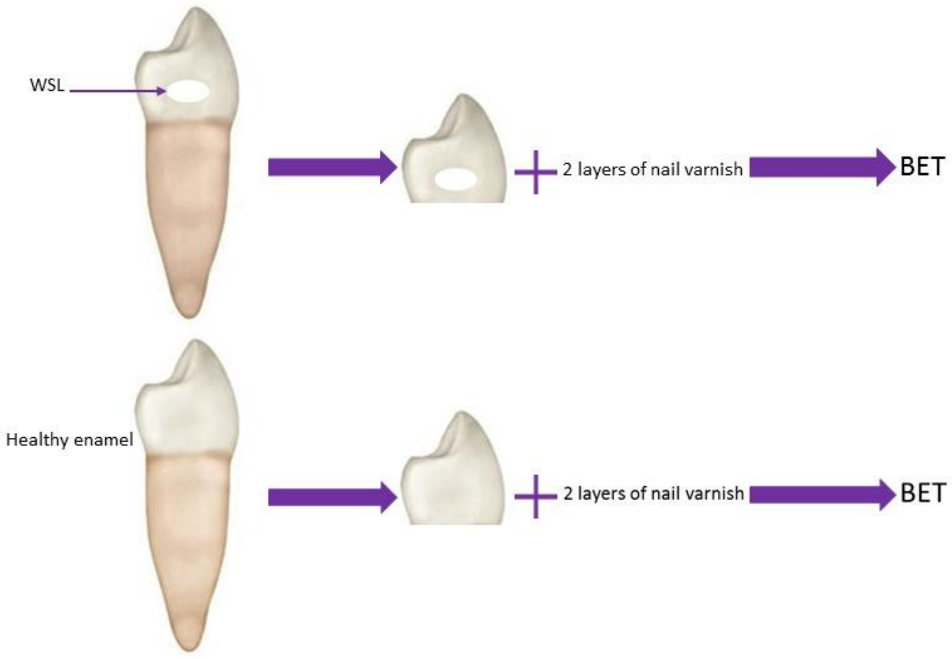

Figure 6.5 Schematic representation of sample preparation for BET by cutting the crown and using two layers of nail varnish at cervical area.

Table 6.1- Summary of the parameters used for the BET test by Quantachrome®.

	Tooth with an intact crown	Tooth crown with WSL
Sample weight (g)	0.56	0.36
Outgas time (h)	16	16
Outgas Temperature (°C)	25	25
Analysis Gas	Nitrogen	Krypton
Adsorbate molecular weight (g/mol)	28.01	83.80
Adsorbate Cross section (Å)	16.20	20.50
Adsorbate specific surface area (Å)	3.54	3.54
Bath Temperature (Kelvin)	77.35	77.35

6.3.2 Focused Ion Beam- Scanning Electron Microscopy (FIB-SEM)

A lower first permanent molar with white spot lesion on the mesial surface was selected as described earlier in section 6.4.1.1. Then, it was cut into half along the tooth long axis in the middle of the lesion using an annular diamond blade (Microslice 2, Malvern Instruments, Malvern, UK). Then, the tooth was embedded in poly(methylmethacrylate) (PMMA) (Sigma-Aldrich, Gillingham, UK) at 37℃ ± 1℃. for 30 days. Then, the surface of the specimen was polished with 4000 grid paper (Sigma-Aldrich, Gillingham, UK). The embedded sample was inserted in the FIB-SEM imaging machine (FEI Quanta™ 3D FEG, Thermo Fisher Scientific, USA). Firstly, the area of interest was detected by the use of backscattered electron imaging with a current and voltage of 1.1nA and 30kV, respectively. Afterwards, one micron layer of platinum was deposited over 25µm x25µm of the enamel region of interest with 0.5nA and 30kV. A rough cut (25µm x 25µm x 15µm, WxLxD) with 30kV, 3nA and drift suppression (DS), using a standard “cross-sectional” cutting pattern, was taken on the enamel, which ended at the front of the deposited platinum layer.

Additionally, two more areas (7µm x 25µm x 15µm) on both sides of the platinum layer were milled under the same condition. Subsequently, cleaning cross-sections were applied to polish the sub-surface edge of interest running perpendicular to the surface, beneath the deposited platinum. The lower milling current of 1nA was used in order to clean the surface of the area of interest. Then, the slice and view were carried out overnight to mill 700-1000 slices, 0.02 µm thickness each, with 2kV and 4nA. BSE images were taken for each slice (Figure 6.6). The slice and view were carried out at the subsurface, middle and advancing front of the WSLs and normal enamel. Two regions were selected in each group (Figure 6.7).

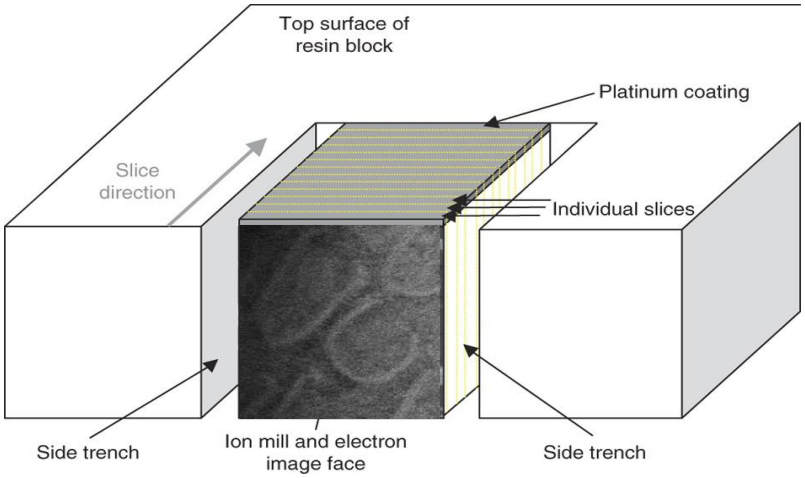

Figure 6.6 Schematic drawings of platinum deposited area, side trenches, image face and individual slices (modified from Bushby *et al*. 2011).

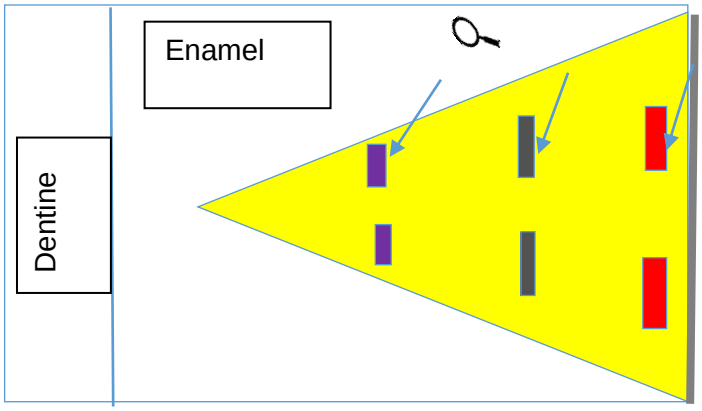

Figure 6.7 Schematic drawing of the two trenches each in surface (red rectangular), middle (grey rectangular) and advancing (purple rectangular) regions of the WSL (yellow triangular). The arrows indicate the viewing direction of the cut slices.

6.3.3 Data Analysis

The images obtained from FIB-SEM were exported to Image J™ (Image Processing and Analysis in Java, National Institute of Health, Bethesda, Maryland, USA). The stack of slices that did not show artefacts or movements were used to render 3D images.

6.4 Results

6.4.1 BET

The specific surface area was higher in the healthy tooth than in the WSL tooth (0.662 and 0.201 m^2g^{-1} respectively, Table 6.2). There was not enough data to complete isotherm of adsorption/desorption calculation because of the very little surface in the sample cell (e.g. 0.662 m^2/g x 0.56 g = 0.37 m^2 total area). It is recommended that at least 10 m^2 is needed for full isotherm calculation. Since the samples were a lack of micro/mesopores, and there was no plateau at higher P/P_0, the total pore distribution could not be calculated.

Table 6.2 Specific surface area for normal enamel and WSL from BET measurement.

Tooth	Specific surface Area (m^2/g)
Healthy tooth	0.66 using N_2
Tooth with WSL	0.20 using Kr

6.4.2 FIB-SEM

Figures 6.8 is the cross section BSE views of a WSL prior to FIB-SEM showing derangement of enamel prisms. Pores of various size (dark areas) can be seen among the mineralised prismatic structures (white areas). The milling FIB-SEM window and a slice view are shown in Figure 6.9. The representative FIB-BSE stack slices for each sampling regions are shown in Figures 6.10-6.13. In the advanced regions, clearer enamel prismatic structures can be seen with a diameter of 3-4µm. This indicates that there was much dissolution of enamel in the body of the lesions, leaving large areas of empty space. In the advancing region, the enamel appeared

as they have been etched by acid, with the dissolution of crystals within the enamel prisms and between the enamel prisms. In the normal enamel, surface and middle regions of the WSL, the enamel prismatic structures were hardly noticeable. When the slices (0.02µm thickness each) were stacked and 3D image rendered (Figures 6.14-6.17), the dissolution appeared to be mainly in the intra-prismatic regions, with demineralising channel throughout the core in the advancing front area. In the surface region, most of the enamel prismatic structures, including the boundary, were absent. In the middle regions, whole enamel cores appeared to have dissolved. Crystallites within the enamel cores could hardly be detected. In the normal enamel, no features can be detected apart from the enamel prism boundary.

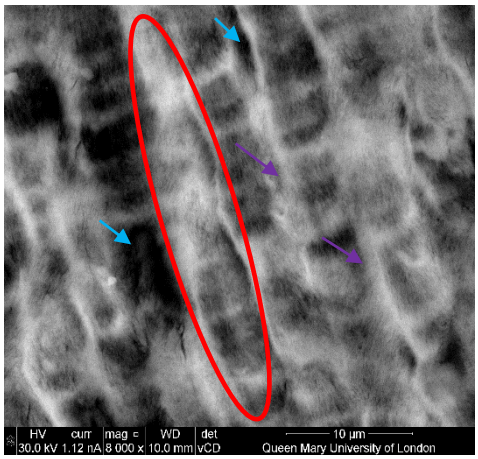

Figure 6.8 BSE image of WSL on the surface showing intact enamel prism (red oval) with mineralised boundaries (purple arrows). Dispersed pores (blue arrows) can be seen within this region.

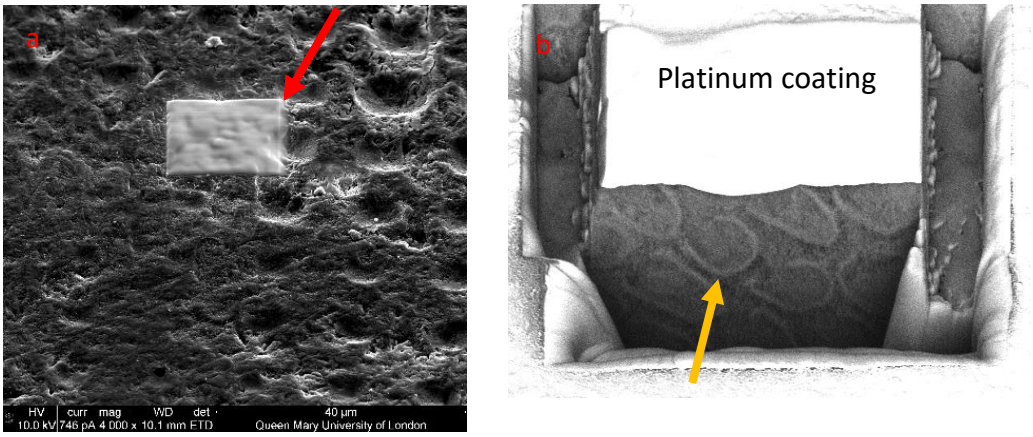

Figure 6.9 FIB-SEM window on the WSL. (a) Platinum coating on surface (red arrow); (b) BSE image in milling window (yellow arrow).

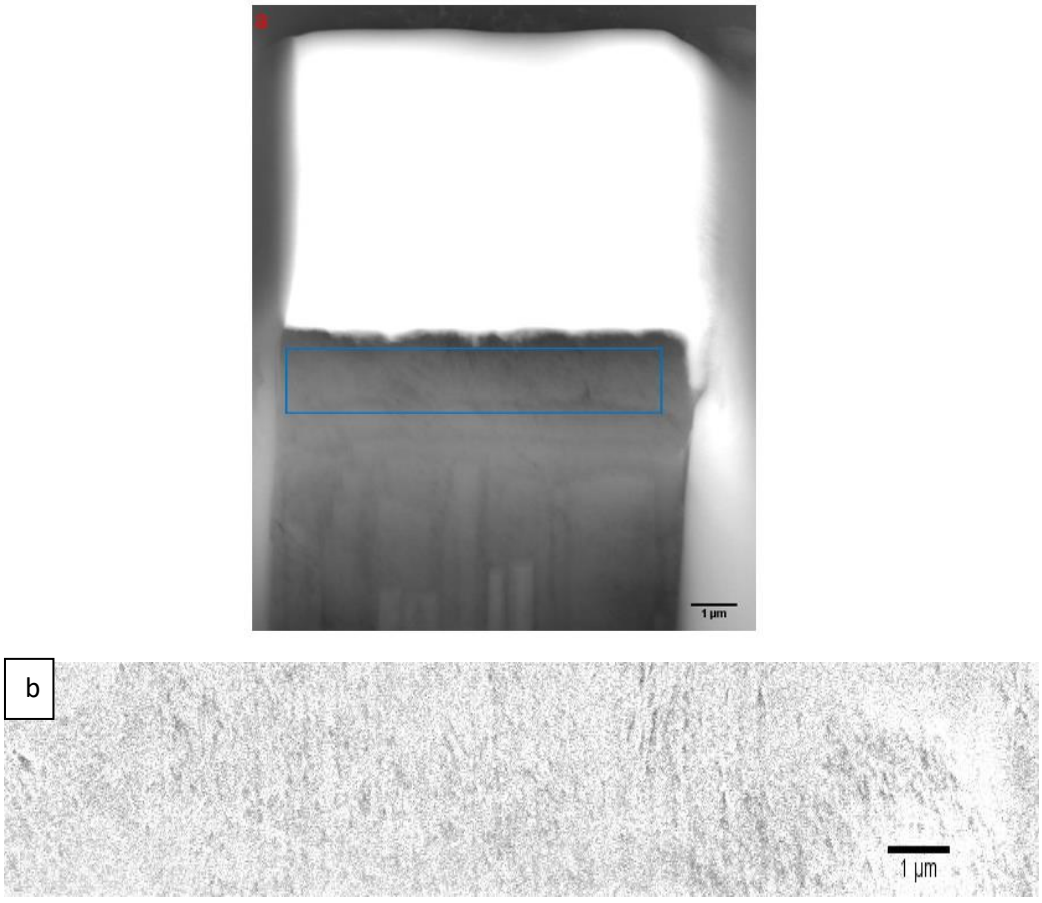

Figure 6.10 (a) FIB-SEM image of WSL at the surface region. The blue box indicates the selected cropped region for analysis. (b) Representative images of stacked slices from the two sampling regions, showing much of the enamel structures were dissolved. The scale bar is 1µm.

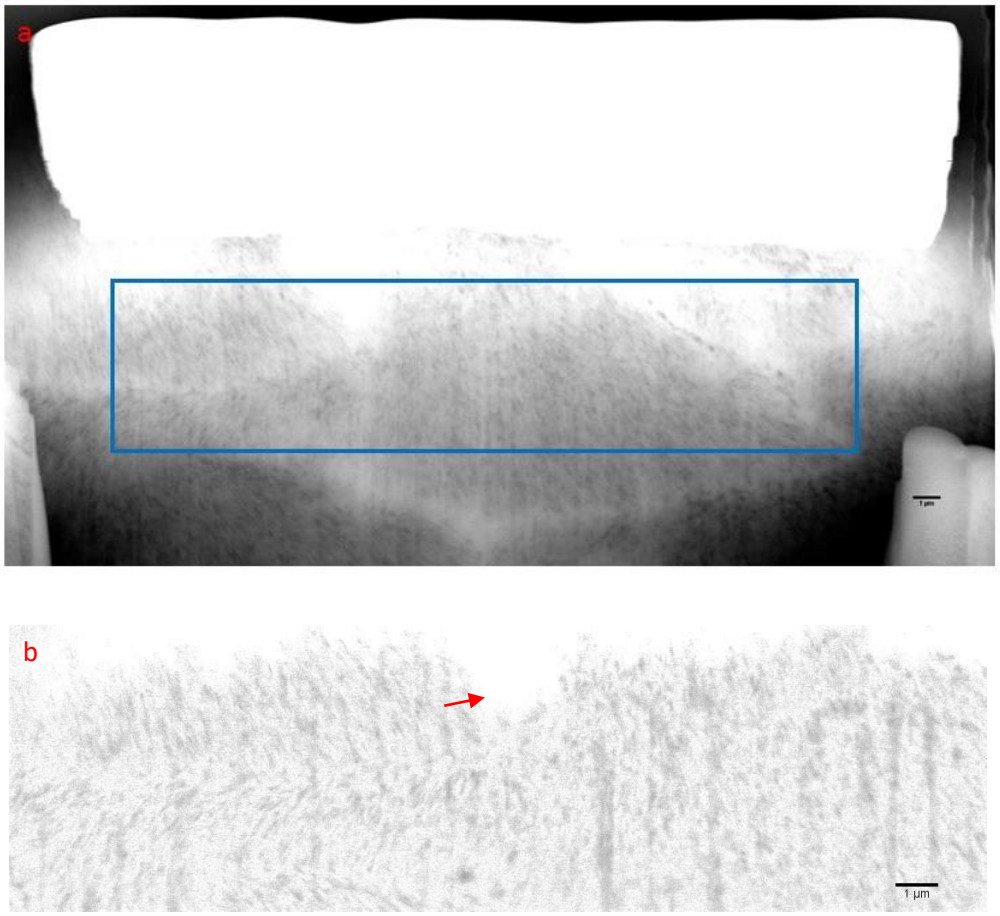

Figure 6.11 (a) FIB-SEM image of WSL at the middle region. The blue box indicates the selected cropped region for analysis. (b) Representative images of stacked slices from the two sampling regions, showing much of the enamel structures were dissolved. The bright white area (red arrow) is part of the platinum coating. The scale bar is 1µm.

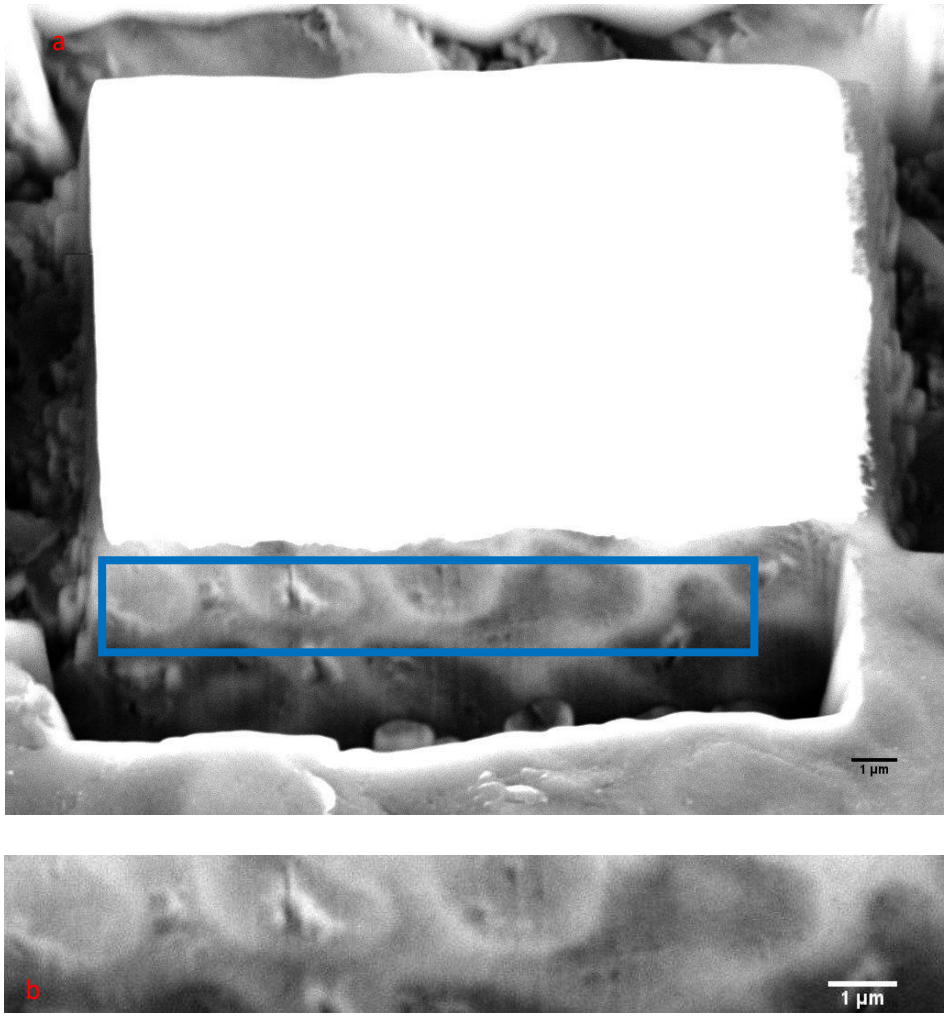

Figure 6.12 (a) FIB-SEM image of the WSL at the advanced region. The blue box indicates the selected cropped region for analysis. (b) Representative images of stacked slices from the two sampling regions, showing 'etched' pattern. The scale bar is 1µm.

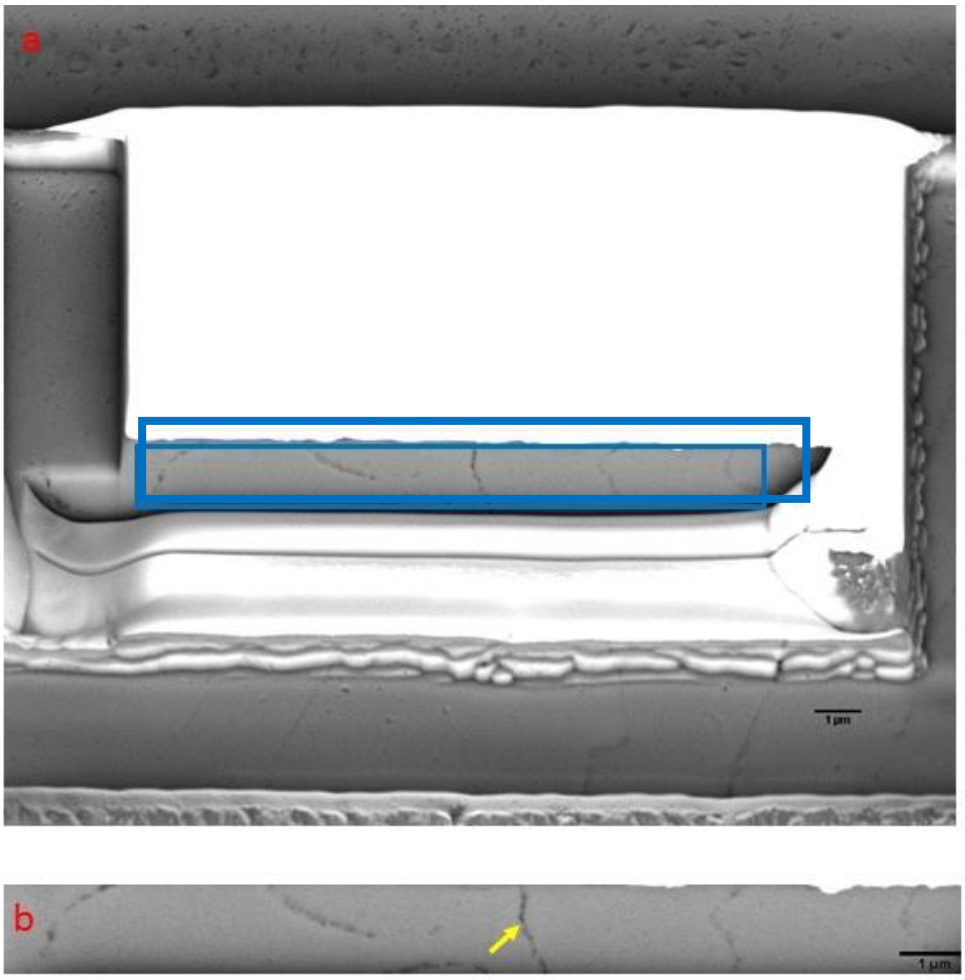

Figure 6.13 (a) FIB-SEM image of normal enamel. The blue box indicates the selected cropped region for analysis. (b) Representative images of stacked slices showing the enamel prism boundary (yellow arrow) and no features are seen. The scale bar is 1µm.

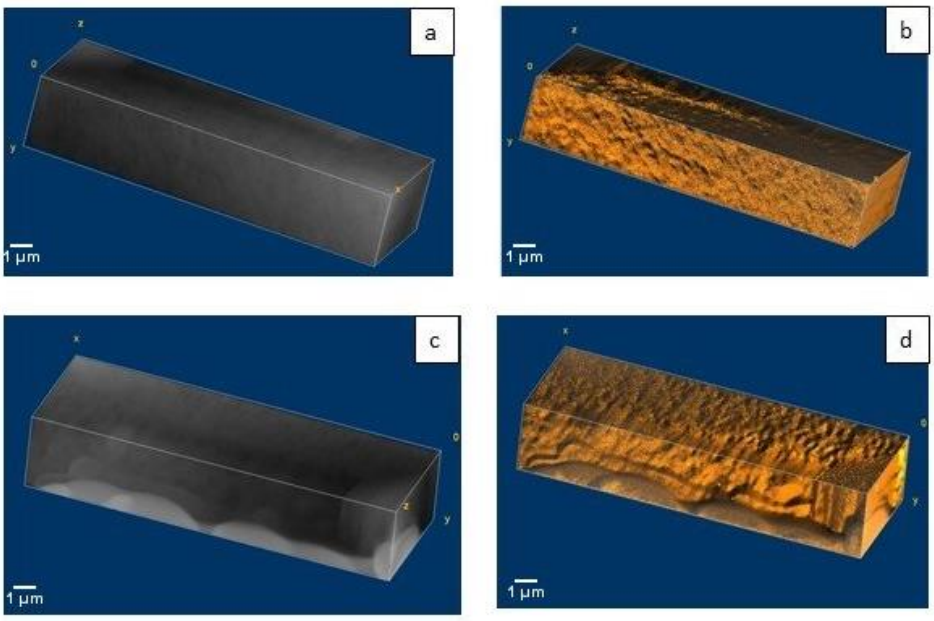

Figure 6.14 Three dimension rendering of a stack of FIB-SEM imaging at the surface region of the WSL (2.4µm thickness). No obvious enamel structure can be observed. (a) front view; (b) front view with light shadow; (c) back view; (d) back view with light shadow. The scale bar is 1µm.

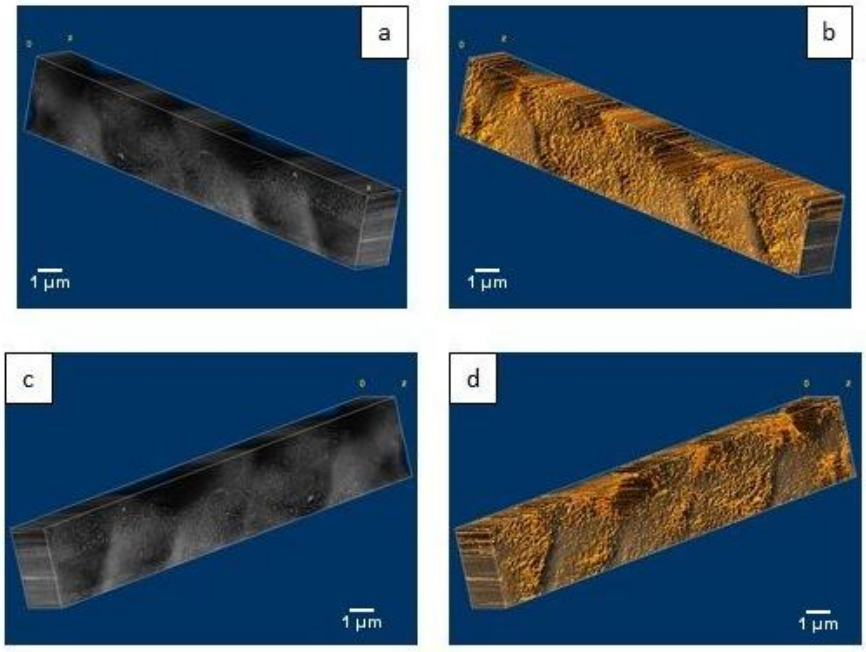

Figure 6.15 Three dimension rendering of a stack of FIB-SEM imaging at the mid region of the WSL (2µm thickness). Enamel prism cores appear to be dissolved. (a) front view; (b) front view with light shadow; (c) back view; (d) back view with light shadow. The scale bar is 1µm.

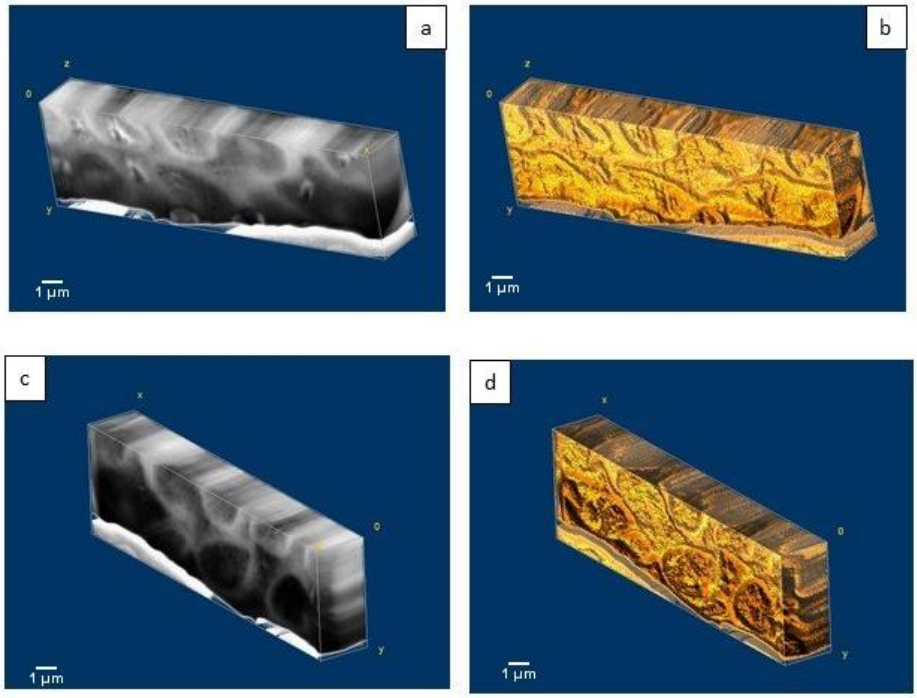

Figure 6.16 Three dimension rendering of a stack of FIB-SEM imaging at the advancing region of the WSL (2µm thickness). Some enamel prism structure still remained. (a) front view; (b) front view with light shadow; (c) back view; (d) back view with light shadow. The scale bar is 1µm.

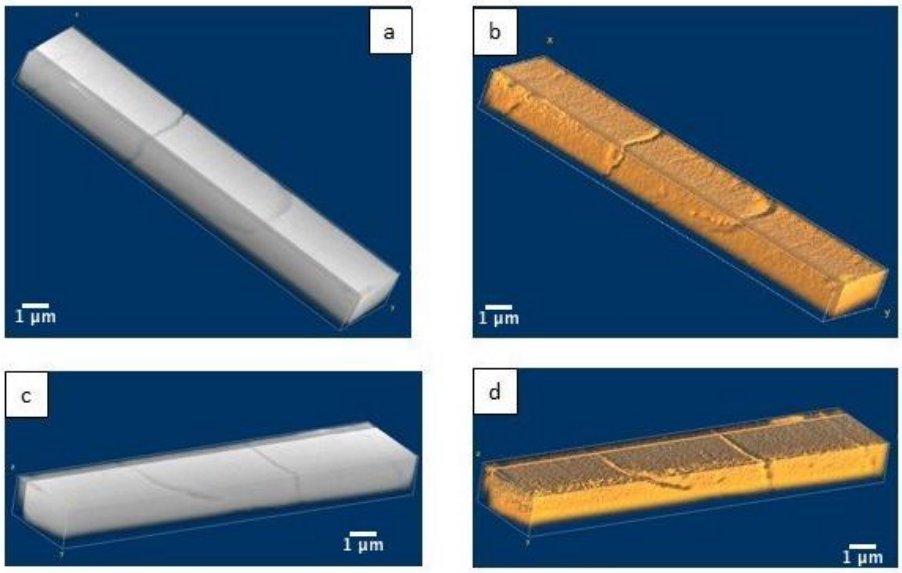

Figure 6.17 Three dimension rendering of a stack of FIB-SEM imaging at the normal enamel (2µm thickness). The enamel prism boundary with no other features are seen. (a) front view; (b) front view with light shadow; (c) back view; (d) back view with light shadow. The scale bar is 1µm.

6.5 Discussion

In this study, two techniques were used in an attempt to characterise the pore size and structure in WSLs.

- ***BET***

In BET method, firstly, a trephine drill was used to remove the white spot lesion in order to limit the BET measurements to the lesion only. However, the sample size was too small for the measurement and BET experiment could have not been carried out. Therefore, an alternative method was used to prepare teeth samples by cutting the crown and prevent the gas penetration from the cervical area of the crown by using nail varnish. However, it was found that the surface area was still insufficient for proper data analysis. For the BET calculation, the data are required to fulfil the following criteria:

  - The intruded volume should be at least 10% of the stem volume. This means an intruded volume of at least 0.05cc is needed for the present experiment;
  - At least 10mm^2 of a total area in the cell is required to have a full isotherm.

Unfortunately, the present data show that only ~0.03cc/g intruded volume was achieved and the total cell area was much lower than the recommended value. Thus, the BET data was invalid.

It should be mentioned that the white spot lesion does not have a defined size or shape. Thus, there is almost impossible to have white spot lesion sample only and BET experiment cannot provide accurate data to characterise the pore size and structure in WSLs even if there are more samples with WSLs allocated to BET experiment.

Based on the IUPAC standard, nitrogen adsorption/desorption technique was used to estimate the surface area of the healthy enamel. However, it was found that the surface area was too small in the selected sample tooth with white spot lesion. Thus, Krypton gas was used instead. Previous researchers (Moreno and Zahradnik 1973) have used Krypton with small size of 0.38nm to investigate enamel pores ranging 1-

30nm. Nevertheless, the authors commented on the difficulties of using BET techniques that:

- The pores in enamel can be so small that they are accessible to the gases;
- Enamel crystals may have ionic charges that form a polar surface but the N_2/Kr adsorption is based on as non-polar elements;
- The adsorbate temperature might change the enamel structure and can affect calculations.

Furthermore, it has been suggested that water vapour adsorption may be more appropriate to estimate the pore size (Dibdin and Poole 1982). However, this technique was not available for the present investigation.

Due to above reasons, BET experiment was excluded in order to further investigations on pore size and structure in WSLs.

- ***FIB-SEM***

Scanning electron microscopy (SEM) is regarded as a gold standard for surface topography and backscatter electron (BSE) imaging is recommended for tissues with mineral content such as enamel (Shellis and Hallsworth 1987). FIB-SEM, with its ability to automate surface milling and take BSE images, is an ideal method to view the microstructure of enamel in 3D. We believe that this is the first time that this technique was used for enamel investigation. However, for the resolution needed in this study, only a small region can be milled because of time constraints. Hence, only two representative regions on each depth level of WSL were taken.

With the use of low voltage and high current (Bushby *et al.* 2011), curtaining artefacts (appeared as vertical lines in the image) were reduced, and images were further improved with the platinum coating. Furthermore, in order to avoid topographic artefacts, the samples were prepared by vacuum drying and embedded in poly(methylmethacrylate) (PMMA) as suggested by Boyde (Boyde 1989). However, the embedded resin could melt due to the high temperatures reached during the ion beam milling. This will cause movement in subsequent slice especially when the “Drift Suppression” (DS) mode could not be applied while “Slice and View”

mode was used in the machine. Hence, it was not possible to create a large 3D image using all the ~1000 slices, because some of the slices had too many artefacts.

The FIB-SEM images show that the inter- and intra-prism structures within the WSLs are more noticeable in the advancing region near the enamel-dentine junction (EDJ). This is in agreement with the results of Pearce and Nelson (1989), indicating that most minerals are lost in the body of lesion. In the advancing regions, the bright prism boundary indicates that this structure is more resistant to acid dissolution. This feature is similar to the pattern of artificial etching with phosphoric acid (Pearce and Nelson 1989). At ultra-high resolution, it was shown that the intra-prismatic crystallite is the first structure to be dissolved, starting as a tiny hole in the basal plane, and channelling through along the c-axis, the lattice vector, showing the directions of the z-axis for a crystal (Takuma *et al.* 1987). Hence, if pores are defined as space within the enamel, their size could be as small as an enamel crystallite, 28x48nm (Yanagisawa and Miake 2003). However, these pores would not be detected or classified as a WSL. For the light to be scattered rather than reflected back, the pore spaces should match the wavelength of the visible light (400-700 nm), a phenomenon known as Mie scattering (https://en.wikipedia.org/wiki/Mie_scattering, accessed 25/3/2017). As the diameter of enamel prism is about 3-4µm, when the intra-prismatic crystallites dissolve, it is likely to leave pore spaces with dimensions close to the wavelength of visible light to give the opaque white effect.

In the present study, although the aim was to determine the pore size with FIB-SEM, many difficulties were encountered. Firstly, the specimen shift due to melting of the embedding resin prevented stacking of large number of slices. The trench was not wide enough, and blocked the electron beam. Thus, shadows were cast on the SEM images and only part of the area of the interest was imaged clearly. Furthermore, the shadow prevented automated image analysis because a threshold to identify the pores could not be set for the whole image. Hence, further modification for the FIB-SEM is needed in future to overcome these challenges.

6.6 Conclusion

BET and FIB-SEM were explored as new techniques to characterise the pores in WSLs. Although theoretically, they are the appropriate methods, a number of technical issues were encountered and the aim could not be fulfilled. However, qualitative comparison could be made between the structure in the advancing and the middle regions of the lesion, showing etched pattern and dissolved enamel structure, respectively.

Chapter 7- Preparation and Characterisation of the Radiopaque Fillers

7.1 Introduction

Strontium (Sr^{+2}) plays a key role in dental materials for its beneficial role in X-ray radiopacity. It is often added to dental composite resin restoratives and glass ionomers to make them radiopaque. Patents were filed for the use of strontium and strontium fluoride as a radiopacifying glass component and a radiopacifying cement additive, respectively (Forsten1994; Billington *et al.* 2001).

Since strontium is the most similar element to calcium, it can replace calcium in both hydroxyapatite (HA) and bioactive glasses (BG) without significant changes in structure. The higher atomic number of Sr relative to Ca is useful for conferring radiopacity (Section 5.2.3).

7.1.1 Synthesis of radiopaque fillers

7.1.1.1 Synthesis of nano-SrHA and surface modified nano-SrHA

There are different techniques to synthesise HA including:

- Solid state synthesis, which is the high-temperature synthesis of hydroxyapatite using solid precursors of calcium and phosphate (Güler *et al*. 2011);
- Co-precipitation methods, which involve a mixture of soluble calcium and phosphorus sources and the addition of base leading to precipitation of crystalline HA (Saeri *et al*. 2003);
- Sol- gel technique, which has three distinct steps including:
    - the formation of sol (a stable solution of alkaloid or metal precursor),
    - gelation (formation of oxide or alcohol- bridged network), which increases the viscosity of the solution and,
    - transformation of the gel to solid mass giving rise to drying and dehydration (Cushing *et al*. 2004);
- Emulsion synthesis, which requires a large amount of surfactants with organic solvent (oil) followed by heat treatment to achieve crystalline HA products (Koumoulidis *et al.* 2003);

- Batch hydrothermal synthesis, which is mixing and pouring Ca^{+2} and PO_4^{-3} into a sealed container. It produces well-defined and pure phase HA in a single step (Guo and Xiao 2006);
- Continuous hydrothermal flow synthesis (CHFS), the starting materials are formed in aqueous solution and then reactants are combined at a mixing point with high temperature and pressure (Chaudhry *et al*. 2011).

In this study, Continuous Plastic Flow Synthesis (CPFS) was used to synthesise strontium-substituted hydroxyapatite (SrHA) and coated nano-SrHA at University College London by the current investigator. This method is a simple, single step method for the synthesis of HA under near ambient conditions with affordable and readily available reagents. The CPFS system allows access to the range of reaction conditions required for rapid and continuous synthesis of ion substitute of calcium phosphates. Anwar (2014) showed that the best conditions to produce nano-HA, nano-SrHA, and surface modified nano-SrHA involves a pH about 10 for precursors and oil bath temperature between 90˚C and 95˚C (Anwar 2014).

7.1.1.2 Synthesis of bioactive glasses (SrBG)

Traditionally, bioactive glasses (BG) are manufactured with SiO_2, Na_2O, CaO, and P_2O_5 as base components at high temperature, followed by melting, casting and sintering (Chen *et al.* 2002). In this study, the melt-quench method was used to make the SrBG at Dental Physical Science, Queen Mary University of London by the current investigator. This melt-quench technique involves a conventional high-temperature melting of oxides mixed together at higher than 1300 ℃, followed by a quenching step (Hench 2006). In this method, fast cooling prevents crystallisation due to limited time for atomic rearrangement and the long-range order development associated with the crystal. There is a decrease in glass volume and an increase in viscosity during the rapid cooling. Fast degradation and rapid apatite formation show a high bioactivity (Turnbull 1969). Strontium completely replaced calcium on a molar basis in order to gain the ultimate advantages of Sr^{+2} including radiopacity. It should be mentioned that in flame spray method, metal-organic precursors are mixed and provided for a flame reactor. Then, the nano-particles are collected on a filter above the flame. This technique results in the formation of 20–

80nm amorphous bioglass particles (Pirayesh and Nychka 2013); however, the relevant facilities were not available in our centre.

7.1.2 Characterisation of radiopaque fillers

7.1.2.1 Fourier Transform Infrared (FTIR) Spectroscopy

FTIR spectroscopy (Figure 7.1) is a quantitative and qualitative analytical technique that is used to measure the active groups' vibration in the molecular structure of the material, which is responsible for the chemical reaction. The FTIR spectroscopy principle is the radiation interference between two beams to produce an interferogram. The infrared spectrum should be in the range between 400 and 4000cm^{-1} as the infrared light frequencies are corresponding to the molecular vibrational modes of the substance in this spectrum. In other words, infrared radiation leads to a degree of vibration and rotation of molecules in the material when it absorbs the radiation. Each energy peak in an absorption spectrum corresponds to the frequency of a particular molecule. Therefore, each material will produce a unique identification infrared spectrum because each of the materials has a different combination of atoms (Doyle 1992).

There are different kinds of FTIR spectrometers based on the different interferometers, but the most commonly used one is the Michelson interferometer. In this instrument, the infrared radiation is emitted from the light source and projects toward a beam splitter. The beam splitter is able to reflect 50% of the radiation to the stationary mirror, and transmit the other half to the constant speed-moving mirror; then these two beams combine again at the beam splitter and split into two other beams, one of them would direct towards the source and the other toward the detector. Beams interface with each other either constructively or destructively depending on the distance between the two arms of the interferometer. As a result, the detector would discover two beams with a fixed path difference. Fourier Transformation transforms the result into the spectrum and this final signal converts to spectra or a graph after being amplified. Each molecule's vibration is identical for specific molecules at a specific wavenumber leading to a unique molecular fingerprint (Schmitt and Flemming 1998).

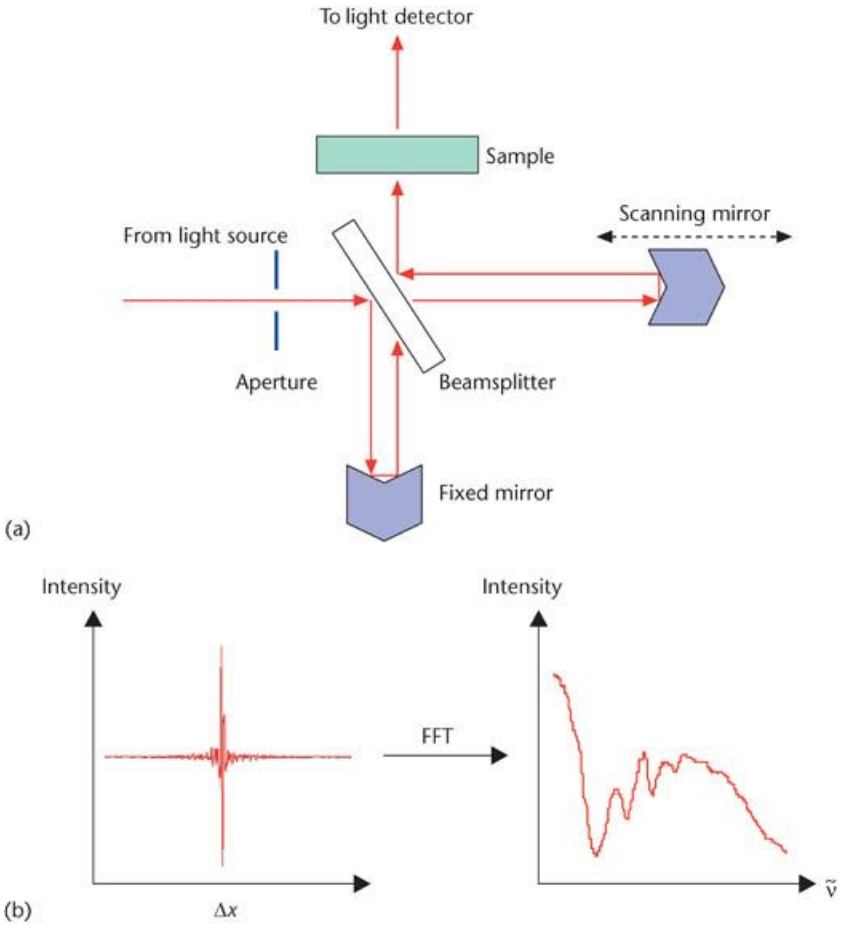

Figure 7.1 A schematic picture illustrating (a) different parts and principle of the FTIR machine and, (b) the conversion of final signal to a spectrum or a graph (www.researchgate.net, accessed on 31/08/2016).

7.1.2.2 Particle size measurement

Particle size of a powder is considered as one of the most significant physical properties with a critical role in determining different properties of the material as follows:

- Rate of reactions

The size of particles in a material plays a key role to determine the rate of chemical reaction of the material. There is an inverse proportion between the particle size

and the rate of chemical reaction. In other words, the finer particle is, the higher reaction is.

- Potential to dissolve

This feature is similar to the chemical reaction. When the particles get finer, they dissolve quicker. This property is important in the pharmaceutical industry because the speed of dissolution of any given drug has direct effects on bioavailability and its effectiveness.

- Packing density

Finer particles are able to pack more efficiently compared to the larger particles. Furthermore, the unoccupied volume is reduced when the particles are finer.

- Sedimentation

Sedimentation occur when the particles in suspension tend to settle out of the fluid. Suspension “stability” would be achieved by the avoidance of the sedimentation.

- Product appearance

Particles will scatter light in different ways depending on their size. This could be important in paint manufacturers as the light scattering plays a key role to define parameters such as hue, tint, transparency, etc. (Allen 2013).

Since radiopaque fillers including SrHA and SrBG produced in order to incorporate into ICON® resin, the particle size of SrHA and SrBG plays a key role regarding to their rate of reactions, potential to dissolve, sedimentation and product appearance. It assumes that the finer the particle is the higher its potential is to react with and dissolve in ICON® resin. Furthermore, the particle size of filler incorporating the resin might affect the light scattering and the refractive index leading a change in appearance of the masked white spot lesion with the experimental radiopaque resin.

There are several methods to measure the particle size and in most techniques used to measure the particle size, it is supposed that particulates have regular geometry with equivalent spherical diameter. Some of these techniques are (Syvitski 2007):

- Microscopy including optical and electron microscopes, is able to measure the shape and absolute size of particles individually.
- Sieving is another technique to provide the particles size in a powder but it does not provide any information on particle shape.
- Sedimentation method, which is based on the concept that an increase in size of a particle rises the velocity of a particle in fluid.
- Electrical sensing zone method, coulter counter, is an instrument in order to determine particle size. It assumes that the particles are as equivalent spheres.
- Optical devices based upon particle attenuation of a light beam or measurement of scattering angles. The scattering pattern is unique for each size of particle, like a fingerprint.
- Permeametry method to measure the average size of fine particles in a fluid. In this technique, the mixture is passing through a powder bed with known dimensions and then the pressure drop and flow rate through the bed would be recorded (Syvitski 2007).

In this study, laser diffraction was used to measure the particle size distributions, which measures the angular variation in intensity of light scattered when a laser beam passes through a dispersed particulate sample. In other words, small particles scatter light at large angles while large particles scatter light at small angles. The size of the particles was calculated by the angular scattering intensity data using the Mie theory of light scattering assuming a volume equivalent sphere model.

Laser diffraction technique was used as it is a common technique to measure the particle size ranging from hundreds of nm to mm in size. Furthermore, this method is simple, easy and reliable with several benefits such as fast measurement, repeatability, high sample throughput and being well established ISO-13320 (2009).

7.1.2.3 Transmission Electron Microscopy (TEM)

The transmission electron microscope (TEM, Figure 7.2) is an analytical method used to visualise and analyse of specimens including SrBG and nano-SrHA (coated and non-coated) ranging from micro- to nano-particles. The principle of light microscope and TEM are the same. The only difference is TEM uses electrons instead of light. The electrons with the lower wavelength provide a higher resolution. A source at the top of the microscope emits the electrons travelling through the column under vacuum environment. The electromagnetic lenses will focus the electrons into a very thin beam, which then travels through the sample. Based on the material density, some of the electrons will be scattered and disappear. The unscattered electrons hit a fluorescent screen and make a shadow image in a dark background. It is possible to study this image on the screen directly or photographed with a camera (Williams and Carter 1996).

In this study, TEM was used to image the crystal shape of the radiopaque fillers and measure their crystal size and possibly particle size. Furthermore, this technique used to confirm the crystal structure in nano-HA and its modifications.

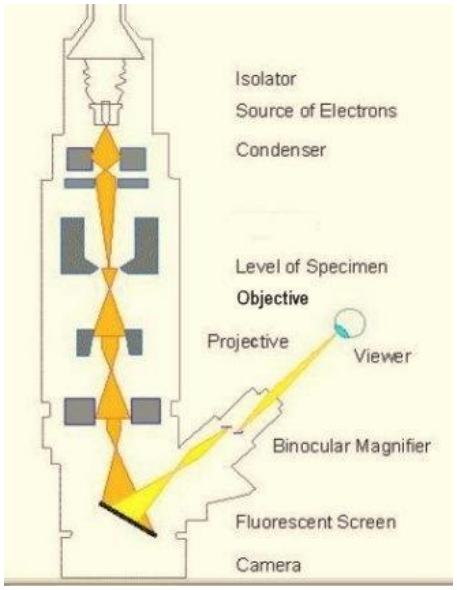

Figure 7.2 A schematic picture showing the principle of transmission electron microscope (TEM) (https://universe-review.ca, accessed on 31/08/2016).

7.1.2.4 X-ray Diffraction (XRD)

X-ray Diffraction (XRD) relies on the interaction of X-ray and the crystal lattice structure of a material at an atomic level to provide detailed information of a material. XRD is used to measure the space between the atomic planes; it is a valuable technique to determine the crystalline phase and the crystals orientation of solid materials (Fultz and Howe 2012).

The XRD principle is based on the interaction between an electromagnetic radiation of short wavelength about 0.5-2.5°A and the atoms of the crystalline materials. This interaction depends on the scattered waves to one another and it could be either constructive or destructive (Fultz and Howe 2012).

A crystalline structure is made of the smallest volume element, called a unit cell, that repeats in three dimensions and the atoms are in a regular pattern. If a crystalline material is exposed to x-rays, the scattered waves move towards each other in the phase, this is called the constructive interferences. This leads to a diffraction pattern, which is the substance fingerprint and may be also used to determine the degree of crystallinity of materials (Jenkins 2000). On the other hand, atoms in an amorphous structure are in a random arrangement and thus, waves will not superimpose (Warren 1969).

In 1931, Bragg explained the intense peaks of scattered radiation from a diffraction pattern based on the crystals atoms, which are in parallel planes by a distance (d) (Figure 7.3).

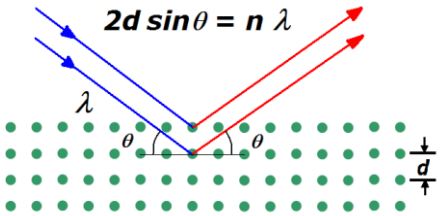

Figure 7.3 A schematic picture presenting the Bragg's law. The reflected rays from the atomic planes with the distance (d) interface constructively (Wikimedia, accessed on 31/08/2016).

The reflected rays from the atomic planes should interface constructively so the wavelength integer is equal to the path difference. Then, Bragg's law of diffraction states (Equation 7.1):

Bragg's Law: $2dSin\Theta = n\lambda$ Equation 7.1

d: the spaces between the planes in the atomic lattice (metre),

Θ: the angle between the incident beam and the scattering beam (radians),

n: the diffraction integer and,

λ: the wavelength of the incident beam (angstrom).

It should be noted that X-ray line broadening is considered as the one of the most accurate indirect measurement methods to calculate crystallite sizes smaller than 1000Å in diameter. Scherrer (1918) showed that small crystallites could lead to line broadening and he introduced an equation for relating the crystallite size to the known broadening line (Holzwarth and Gibson 2011).

Scherrer Line Broadening $D = K\lambda / B\cos\Theta$ Equation 7.2

D: diameter of the particle (angstrom),

K: constant,

B: the broadening of the line (radians),

λ : the wavelength of the radiation (angstrom) and,

Θ: the Bragg angle (degree).

There are several methods to determine B. For example, Scherrer measured the width of the diffraction line in radians where the intensity was the half of the maximum value, while Von Laue measured the area under the diffraction line and then divided by the maximum intensity, known as the integral width method (Holzwarth and Gibson 2011).

7.2 Aims and objectives

The aim of experiments in this chapter were:

- To prepare the radiopaque fillers including nano-SrHA, modified surface nano-SrHA and SrBG;
- To characterise the prepared radiopaque fillers as follows:
    - FTIR to prove the nature of the produced nano-SrHA (coated and non-coated),
    - Particle size measurement to determine the particle size and distribution,
    - TEM to measure the crystal size, investigate the shape of crystals and to confirm the crystalline nature of the particles,
    - XRD to confirm the nature of the material and measure the crystal size.

It should be noted that FTIR was carried out for the nano-SrHA (non-coated and coated) materials only, to prove the nature of the produced materials.

7.3 Materials and Methods

7.3.1 Synthesis of Strontium-Substituted Hydroxyapatite

Continuous Plastic Flow System (CPFS) (Figure 7. 4) at University College London was used by the present investigator to synthesise strontium-substituted nano-hydroxyapatite (nano-SrHA) and coated nano-SrHA. All reactions were carried out at 95°C$\pm$1℃ and atmospheric pressure (1atm). In this process, 0.3M diammonium hydrogen phosphate solution ($(NH_4)_2HPO_4$) (Sigma-Aldrich, Gillingham, UK) and 0.5M strontium nitrate solutions ($Sr(NO_3)_2.4H_2O$) (Sigma-Aldrich, Gillingham, UK) were used (Sr: P molar ratio: 1.67). 5 ml and 35ml of ammonium hydroxide (Sigma-Aldrich, Gillingham, UK) were added to diammonium hydrogen phosphate (500ml) and strontium nitrate (500ml) solutions, respectively to keep the pH of both solutions above 10 prior to the reaction. The pH was checked with the use of pH test strip (Sigma-Aldrich, Gillingham, UK). Both reagent solutions were pumped at 20ml/min to meet at a T-piece. This initial mixture was connected to an 8m long

Poly(tetrafluoroethylene) (PTFE) tubing, which was coiled inside an oil bath. A pump rate of 20ml/min was used for both strontium nitrate and diammonium hydrogen phosphate solutions. The flow rates used for pump 1 and pump 2 were adjusted to give a total residence time of 5 minutes. In this method, the precipitation of nano-SrHA can be described by the following equation (Equation 7.3):

Equation 7.3

$$\mathbf{10\ [Sr(NO_3)_2.4H_2O] + 6\ [(NH_4)_2HPO_4] \rightarrow 8\ NH_4OH\ [Sr_{10}(PO_4)_6(OH)_2] + 20NH_4NO_3 + 6H_2O}$$

The slurries were collected from the end of tube in Falcon™ 50ml conical centrifuge tubes (Fisher Scientific, Hampton, USA). Each slurry product was centrifuged at 4500 revolutions per minute (rpm) for five minutes (per 50ml suspension). Supernatant was decanted and then deionised water was added followed by vigorous shaking using a vortex mixer (Cole-Parmer Vortex Mixer, 0 to 2850 rpm, 230 VAC, London, UK) and repeated centrifuging. Between each centrifuge cycle, the conductivity of supernatant was measured using a conductivity tester (OMEGA™, Manchester, UK). The re-dispersal and centrifuging were continued until the conductivity was lower than 50uS/cm. Then, the supernatant was decanted and the slurry was frozen in liquid N_2 and then freeze-dried using a VirTis Genesis (35XL, Pilot Lyophilizer, SP scientific, USA) at 0.3Pa for 24h. Between consecutive collections, the CPFS system was cleaned with deionised water and acetic acid solution (Sigma-Aldrich, Gillingham, UK) for 20 minutes.

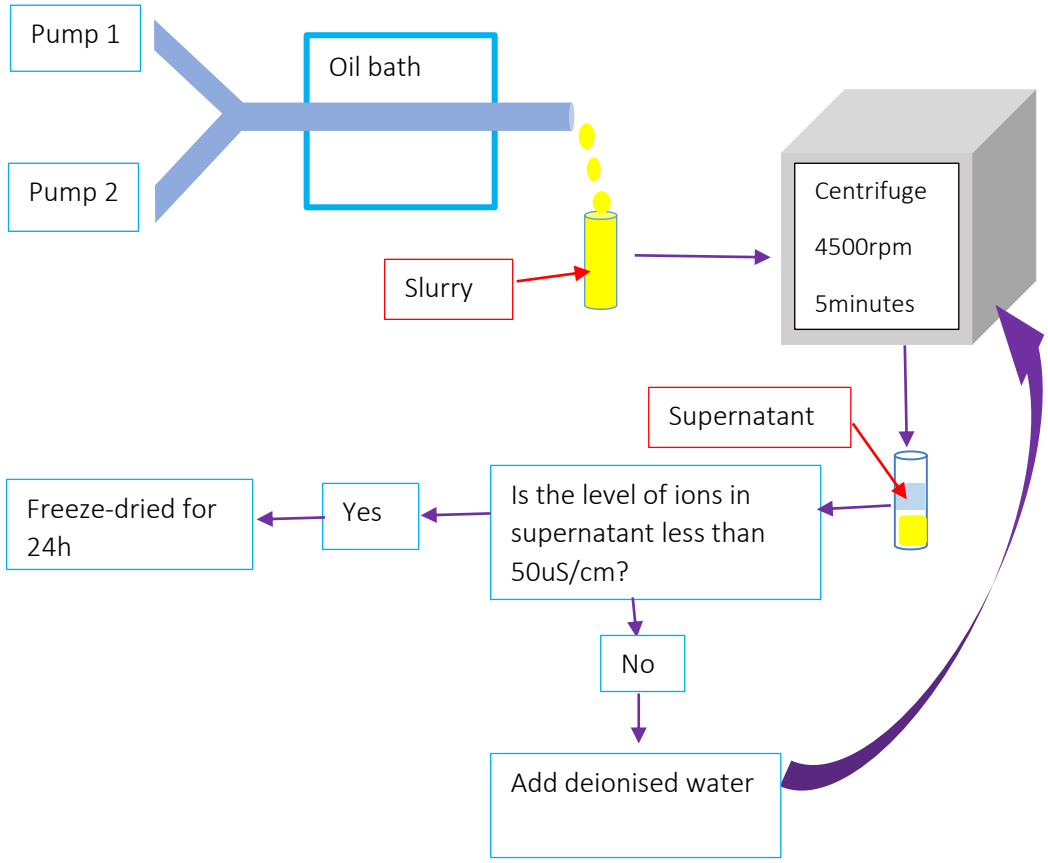

Figure 7.4 A schematic picture presenting the synthesis of nano-SrHA with continuous plastic flow system (CPFS).

7.3.1.1 Synthesis of surface-modified strontium hydroxyapatite

The surface-modified strontium (containing no calcium) hydroxyapatite was prepared at 95 °C±1℃ using the continuous (plastic) flow synthesis system (CPFS) method, details of which are described in the previous section 7.3.1. In the synthesis process, 0.5M basic solutions of strontium nitrate with methacrylic acid (Sr+RCO2 - R) / P = 1.67) and 0.3M diammonium hydrogen phosphate, respectively, were pumped to meet at a T-piece, details of which are described in the previous section (Section 7.3.1).

7.3.2 Bioactive glass synthesis

Strontium bioactive glass (SrBG) was made using a melt-quench route (Figure 7.5). 100 per cent of the calcium was substituted by strontium on a molar basis (Table 7.1) in order to preserve the silicate glass structure (SiO_2 –P_2O_5 –SrO –Na_2O). The

weight percentage was calculated for the glass based on the mol%. All the components, silica, sodium carbonate, strontium carbonate and phosphate (Sigma-Aldrich, Gillingham, UK) were weighed using a balance and mixed together in a glass container (total= 200g). Phosphate was added last due to its hygroscopic nature followed by vigorously mixing all the powders in the batch together. Then, the powder was transferred to a platinum crucible (Sigma-Aldrich, Gillingham, UK) and placed in an electric furnace (Lenton, Hope Valley, UK) and heated to 1420°C for 1 hour. The melt was then rapidly quenched into deionised water to prevent crystallisation and phase separation. Then, the glass frit was collected with a sieve (Sigma-Aldrich, Gillingham, UK) and placed in a drying cabinet at 37°C$\pm$1℃ overnight to dry. 100g of dried glass frit was ground using a vibratory mill (Gyro Mill, Glen Creston, London, UK) for 14 minutes. The glass powder was sieved with a 38-micron sieve for 30 minutes. Finally, the fine powders of less than 38μm were collected for experimental analysis. After each experiment, the platinum crucible (Sigma-Aldrich, Gillingham, UK) had been soaked in nitric acid overnight and washed with deionised water to remove the residual glass remaining in crucible.

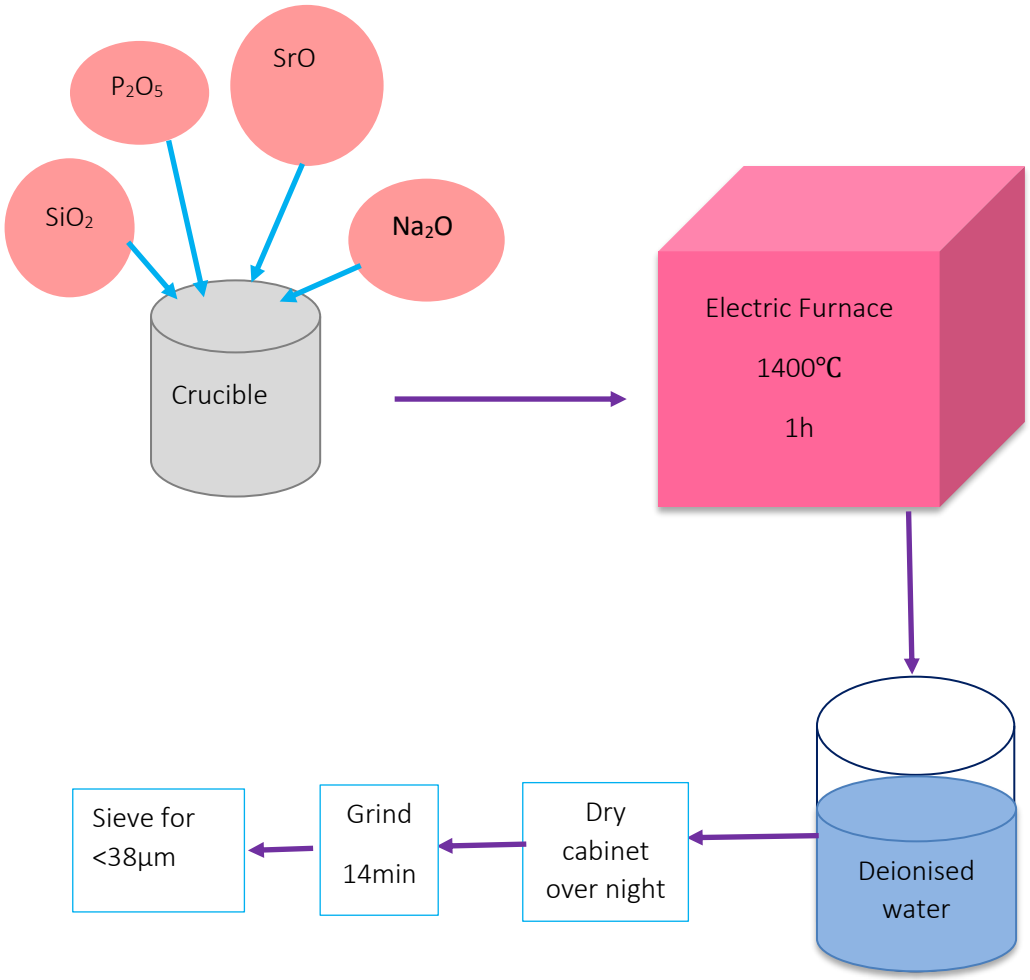

Figure 7.5 A schematic picture presenting synthesis of SrBG with melt-quench pathway.

Table 7.1 The bioglass composition (mol%) for a glass without strontium (Sr-0) and a glass with 100% replacement of calcium with strontium (Sr-100).

Glass	Sr for Ca substitution	SiO_2	P_2O_5	CaO	Na_2O	SrO
Sr-0	0	49.47	1.07	23.08	26.38	0
Sr-100	100	49.47	1.07	0	26.38	23.08

7.3.3 Characterisation of radiopaque fillers

7.3.3.1 Fourier Transform Infrared Spectroscopy (FTIR)

The chemical and structural properties of SrHA and SrBG were analysed using Fourier Transform Infrared spectroscopy (FTIR) (Perkin-Elmer Spectrum GX IR spectrometer, Shimadzu, Milton Keynes, UK). The sample stage was cleaned with ethanol (Sigma- Aldrich, Gillingham, UK) and then a background scan was carried out in order to remove the unwanted background noise. A small amount of sample was placed on the stage covering the IR window. Then, the sample was covered and compressed under compression head anvil. The spectra were collected in the range of 500-1800cm^{-1} at a resolution of 4cm^{-1}. 10 scans for each sample were taken.

7.3.3.2 Particle size measurement

In this study, a particle size analyser (Malvern Mastersizer 2000, Malvern, UK) was used to determine the particle size and particle size distribution. Firstly, a representative amount of sample was dispersed and mixed in deionised water by spatula (Sigma- Aldrich, Gillingham, UK). Based on the manufacturer's instructions, this prevents the movement of the larger particles to the bottom of the container and smaller particles to the top of the container. A background measurement was performed automatically. Then, the sample was added into the chamber while observing the obscuration value on the screen reached 10%. This value should be between 2 to 40% based on the manufacturer's recommendation (Table 7.2).

Table 7.2 A table presenting the obstruction value (%) based on particle size.

Sample	Obscuration value (%)
≤ 4µm	10
=50µm	15
Coarse or broad	20

When the obscuration was at 10%, the measurement was started. The measurements were displayed on the screen automatically. The experiment was

repeated three times for each sample. Between experiments, the dispersion tube was filled with clean dispersant (deionised water), the revolution speed was increased to 3000rpm, then returned to 0. The cleaning procedure was repeated three times.

7.3.3.3 Transmission Electron Microscope (TEM)

Transmission electron microscope (TEM) images were collected using a JEM- 2010 Microscope (JEOL Ltd, Japan). Digital images were taken with a side mounted AMT 2K high sensitivity digital camera (Debens, East Grinstead, UK). A small amount of sample (~10mg) was dispersed in 10ml neat ethanol (Sigma-Aldrich, Gillingham, UK) and ultra-sonicated for 5 minutes to yield a dilute suspension by a QS25 Ultrasonic Bath (Medisave, Dorset, UK). A few drops of the resulting suspension were then deposited on a carbon-coated copper grid (Agar Scientific, Stansted, UK), which was used as the TEM specimen. The grid was dried in air at room temperature ($25 \pm 1^{o}C$). TEM images were taken, which could be studied directly on the screen or photographed with a camera.

7.3.3.4 X-ray Diffraction (XRD)

A XRD diffractometer (X'Pert Pro X-ray diffractometer, Panalytical, Netherland) was used. The dried powders were collected into 1.5ml Eppendorf tubes (Cole-Palmer, London, UK). The data were collected in the 2θ range from 5° to 70° with a scanning step size of 0.0334 ° and a count time of 200.03 seconds. Ni-filtered Cu-Kα radiation (λ1 = 0.1540598 nm and λ2 = 0.15444260 nm) at 40kV/ 40mA was used.

7.3.4 Data Analysis

- ***FTIR***

FTIR data were collected and transferred to an excel sheet. Then, a graph was plotted showing the wavelength against the absorbance for each tested material. The graphs were analysed by matching with standard FTIR graphs to prove the chemical property of the materials.

- ***Particle Size***
    - Particle size data for different materials were plotted. Comparisons were carried out among the particle size of the different materials.

- ***TEM***
  - TEM images on the screen were used to investigate the presence of crystal structure and their morphology.
  - TEM images were imported to Image J™ (Image Processing and Analysis in Java, National Institute of Health, Bethesda, Maryland, USA). The mean of the length and width of 100 crystals were measured.
- ***XRD***
  - XRD data was collected, transferred to an excel sheet and plotted showing the intensity against 2Θ for the tested materials. The graphs were used to investigate the presence of Sr and crystal structure.
  - The crystal size of nano-SrHA and surface modified nano-SrHA were calculated by "Scherrer Equation" (Equation 7.4):

Equation 7.4

$$L = 0.9\,\lambda / \beta \cos\theta$$

Where:

L: crystallite size (angstrom),

β: full-width half maximum (FWHM) (radians),

λ: wavelength of X-rays (angstrom) and,

θ: the angle corresponding to the peak (degrees).

7.4 Results

7.4.1 Fourier Transform Infrared spectroscopy (FTIR)

FTIR data for nano-HA, nano-SrHA and 10 and 20wt% coated nano-SrHA (Figure 7.6) showed characteristic peaks for pure nano-HA. In pure nano-HA, the peak at 601 cm^{-1} corresponded to the vibration mode of the hydroxyl group. Furthermore, peaks at 1053 and 1091 cm^{-1} corresponded to the P–O asymmetric stretching mode of phosphate, whilst the peak at 962 cm^{-1} corresponded to the symmetric stretching

of the same bond. Peak at 878cm^{-1} in SrHA corresponded to carbonate. The most obvious change in the spectrum of SrHA and coated SrHA was the shift of the graph to the right side.

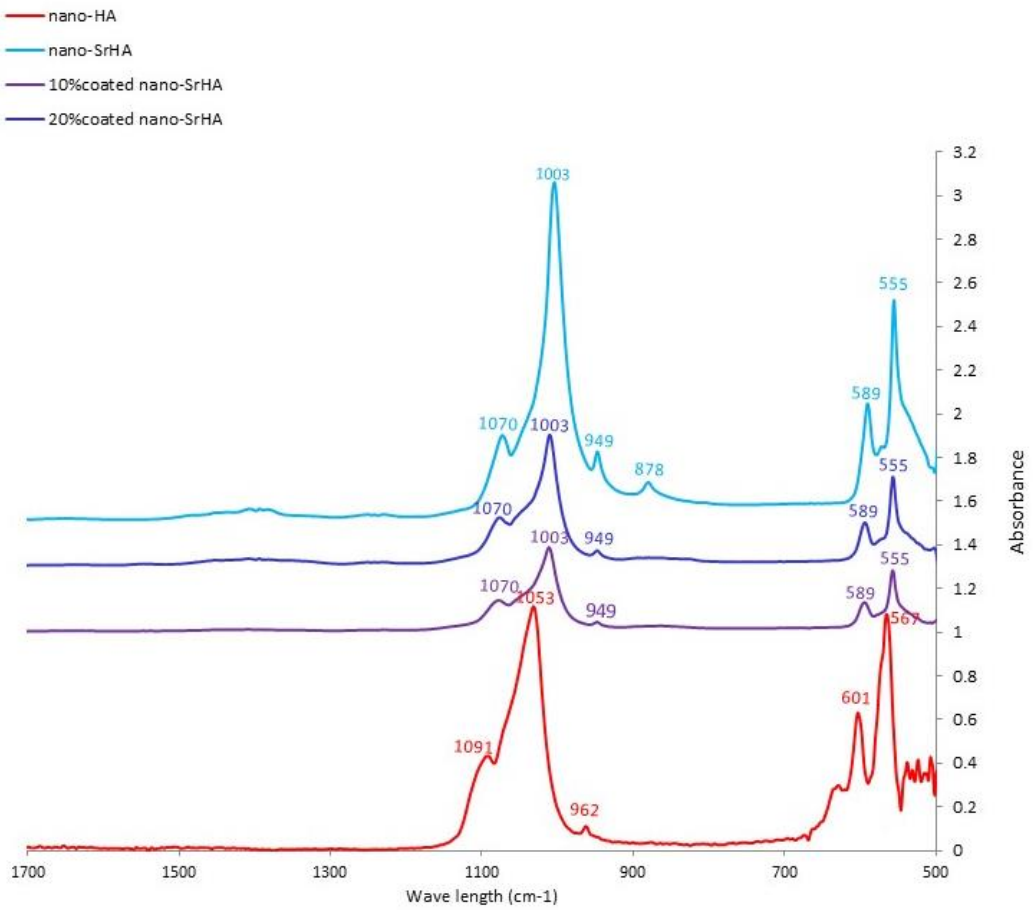

Figure 7.6 FTIR data for nano-HA, nano-SrHA (non-coated and coated in10 wt% and 20 wt%). There is a shift in the graph to the right side in the presence of Sr in the structure.

7.4.2 Particle size measurement

The results (Figure 7.7) showed that nano-HA had a smaller particle size in comparison with the nano-SrHA (either coated or non-coated) and SrBG. Three quarters of the particles in nano- HA were less than 11.48µm and this number increased to 42.76µm and 120.22µm for nano-SrHA and coated nano-SrHA, respectively. The coated nano-SrHA showed a larger particle size in comparison to non-coated ones. The data presented that three quarters of SrBG particles were less

than 60.25µm in size, which was larger than nano-SrHA (42.76 µm) and smaller than coated nano-SrHA (120.22 µm).

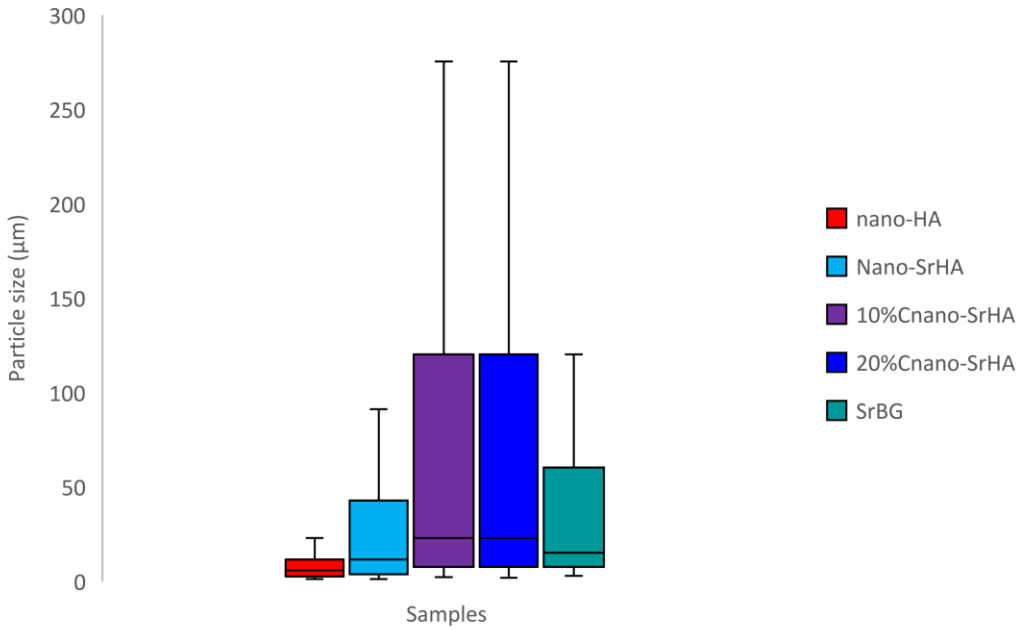

Figure 7.7 Particle size for nano-HA, nano-SrHA (non-coated and coated (C)) and SrBG. The upper bars showed the maximum and the lower bars showed the minimum particle size for each sample. The line in the box presents the median. The bottom and top borders of each box presents 25% and 75% particle size in each sample, respectively.

Nano-HA gave one peak, monomodal, for particle size distribution while the other groups of materials showed 2 or 3 peaks, bimodal and trimodal, respectively. The bimodal and trimodal represents the possible agglomeration of particles (Figure 7.8).

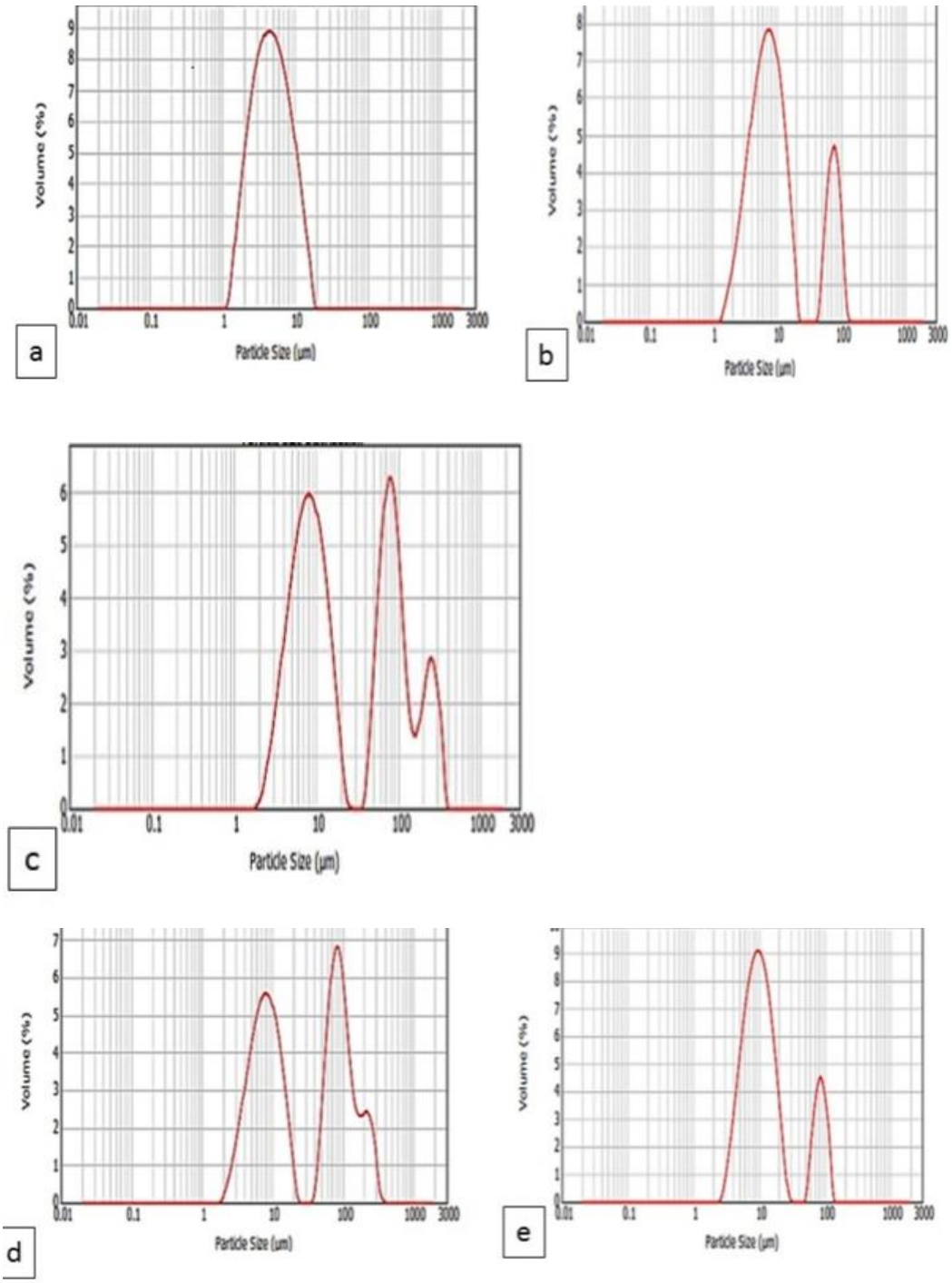

Figure 7.8 Particle size distribution graphs for (a) nano-HA (monomodal), (b)nano-SrHA, (c) 10wt% coated nano-SrHA , (d) 20wt% coated nano-SrHA and (e) SrBG.

7.4.3 Transmission Electron Microscope (TEM)

TEM images of pure nano-HA revealed its crystal structure (Figure 7.9a) of distinct nano-prisms/spherical of size ~ 58.2nm, along the longest axis and ~12.9nm, along the smaller axis (Figure 7.9b).

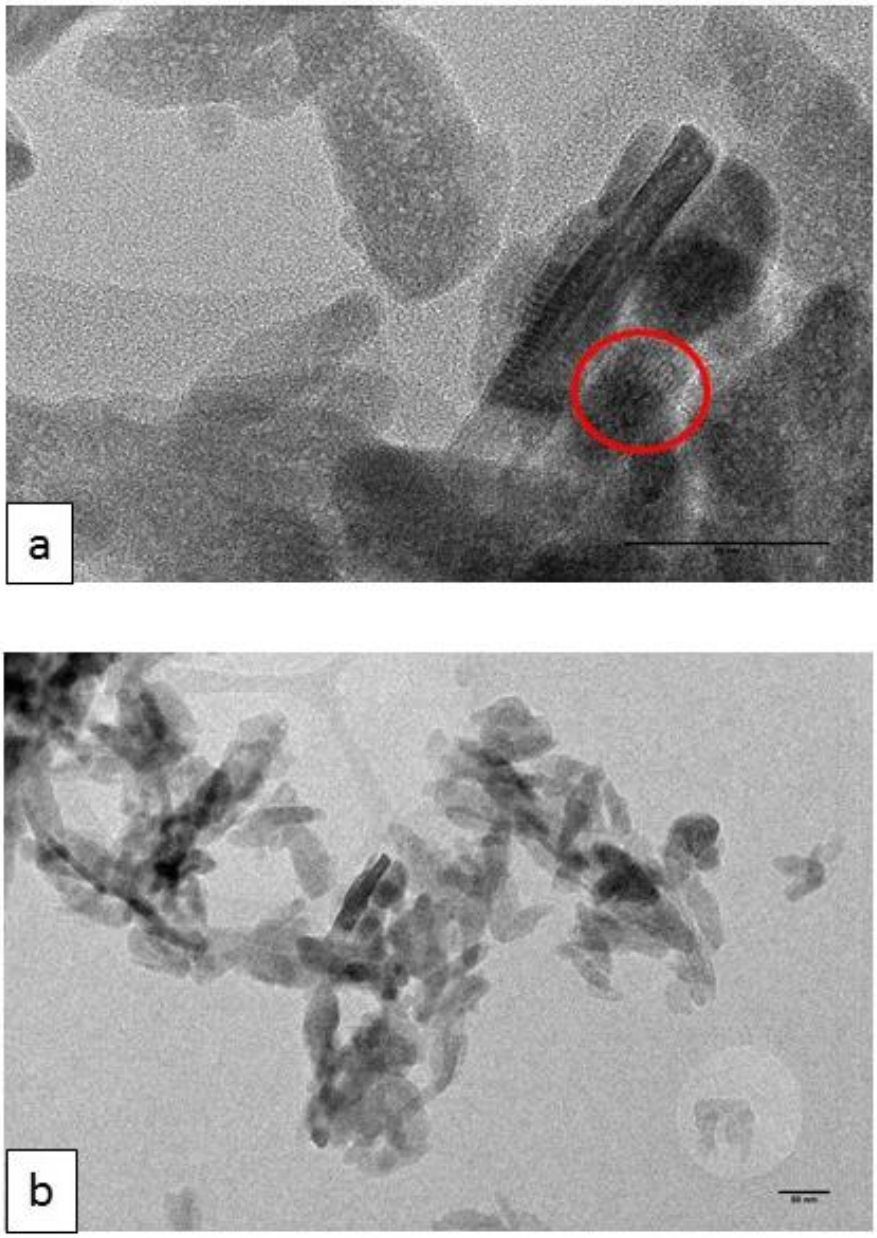

Figure 7.9 Nano-HA sample showing (a) the crystal structure (red circle) and, (b) prism/spherical shape of the particles. The scale for both images is 50nm.

TEM image of nano-SrHA proved its crystal structure and presented with average particle size of ~73.07nm and ~23.01nm in the longest and smallest axis, respectively (Figure 7.10).

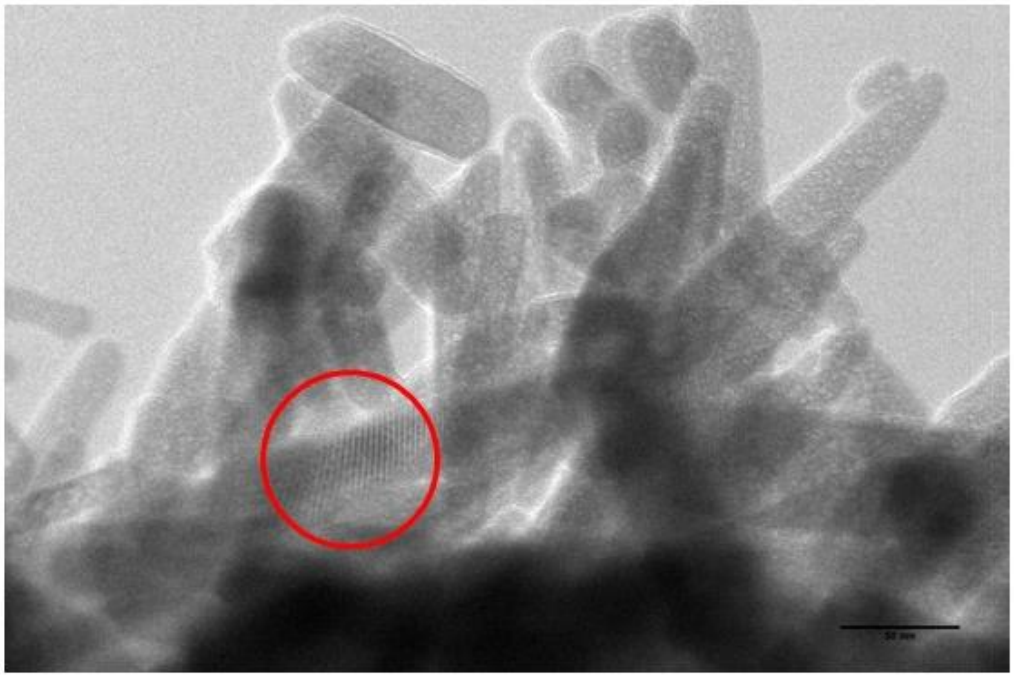

Figure 7.10 Nano-SrHA showing the crystal structure (red circle) and oval shape of particles. The scale for the images is 50nm.

TEM images collected for 10wt% surface modified strontium substituted HA showed its crystal structure (Figure 7.11a). Additionally, images revealed less aggregation compared to nano-SrHA and more pronounced nano-rods with the size of ~105.3 nm, along the longest axis and the size of ~10.8nm in the smallest axis (Figure 7.11b).

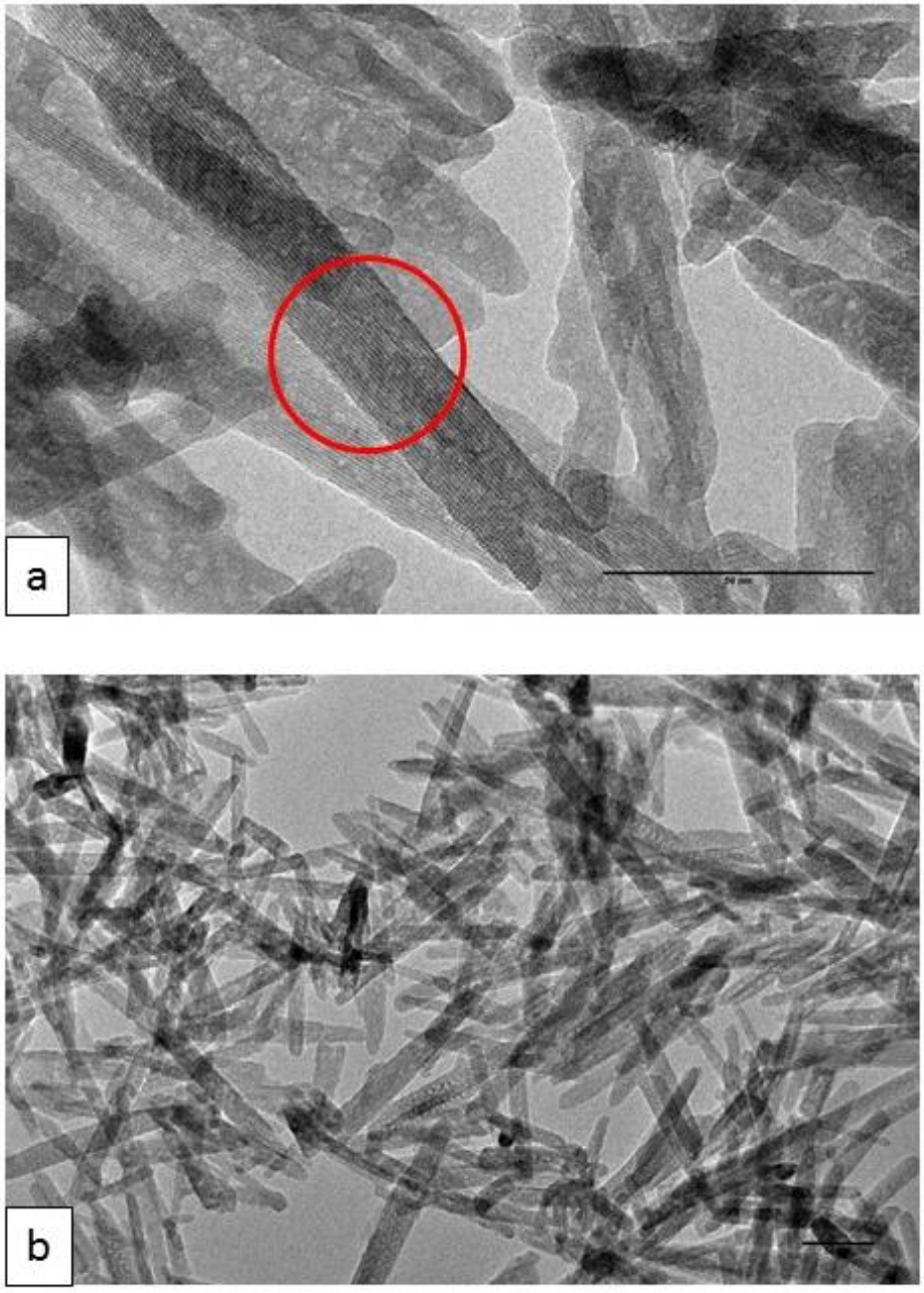

Figure 7.11 10wt% coated nano-SrHA showing (a) the crystal structure (red circule) and, (b) rod shape of particles with less agglomeration compared to nano-SrHA. The scale bar for both images is 50nm.

TEM images collected for 20wt% surface modified strontium substituted HA showed its crystal structure (Figure 7.12a). Additionally, images revealed pronounced nano-rods with the size of ~ 155.8 nm, along the longest axis and the size of 12.7nm in the smallest axis (Figure 7.12b).

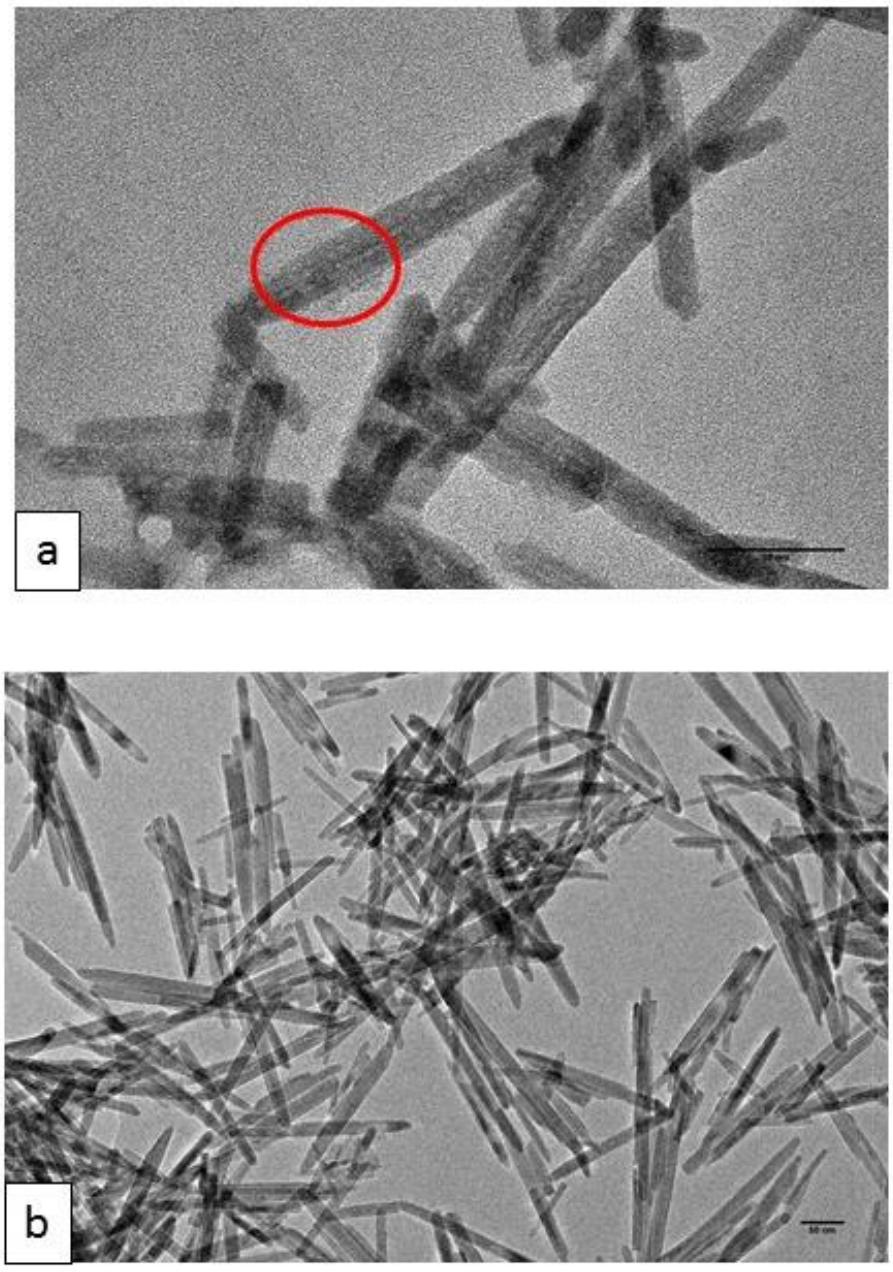

Figure 7.12 20wt% coated nano-SrHA showing (a) the crystal structure (red circle) and, (b) the elongated rod with a reduced agglomeration compared to other groups of nano-SrHA. The scale for both images is 50nm.

SrBG revealed micron-sized particles and in some areas possible SrHA crystals were seen. The particle size could not be measured precisely as the particles were agglomerated promptly (Figure 7.13).

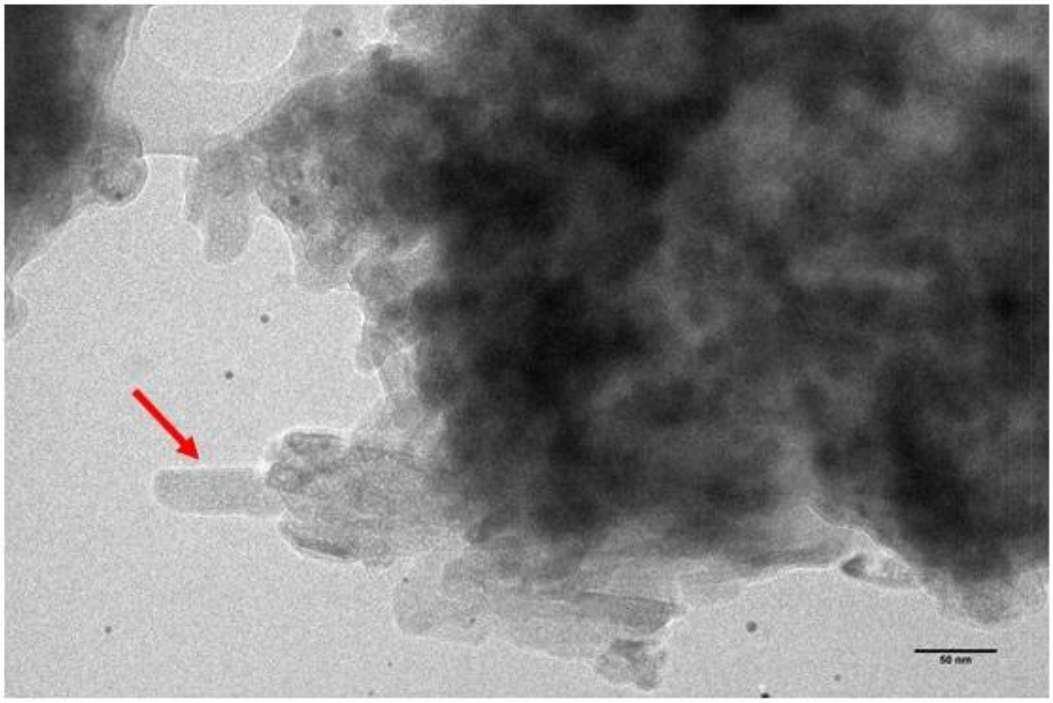

Figure 7.13 TEM image showing the heavy agglomeration of SrBG and presence of possible SrHA and its crystal structure (red arrow) on the surface. The scale for the images is 50nm.

7.4.4 X-ray Diffraction (XRD)

The powder X-ray diffraction data (XRD) of pure hydroxyapatites displayed broad peaks due to the apatite structure as shown in Figure 7.14.

The XRD data indicated the strontium hydroxyapatite as a unique crystalline phase and presented a shift to a lower 2Θ on the graph in agreement with a large size of Sr^{+2} in comparison with Ca^{+2}.

The XRD analysis of synthesised 10 and 20wt% coated nano-SrHA product indicated that this product was exclusively strontium hydroxyapatite particles. The XRD patterns shown in Figure 7.14 showed a good match to the pure strontium hydroxyapatite [$Sr_5(PO_4)_3(OH)$].

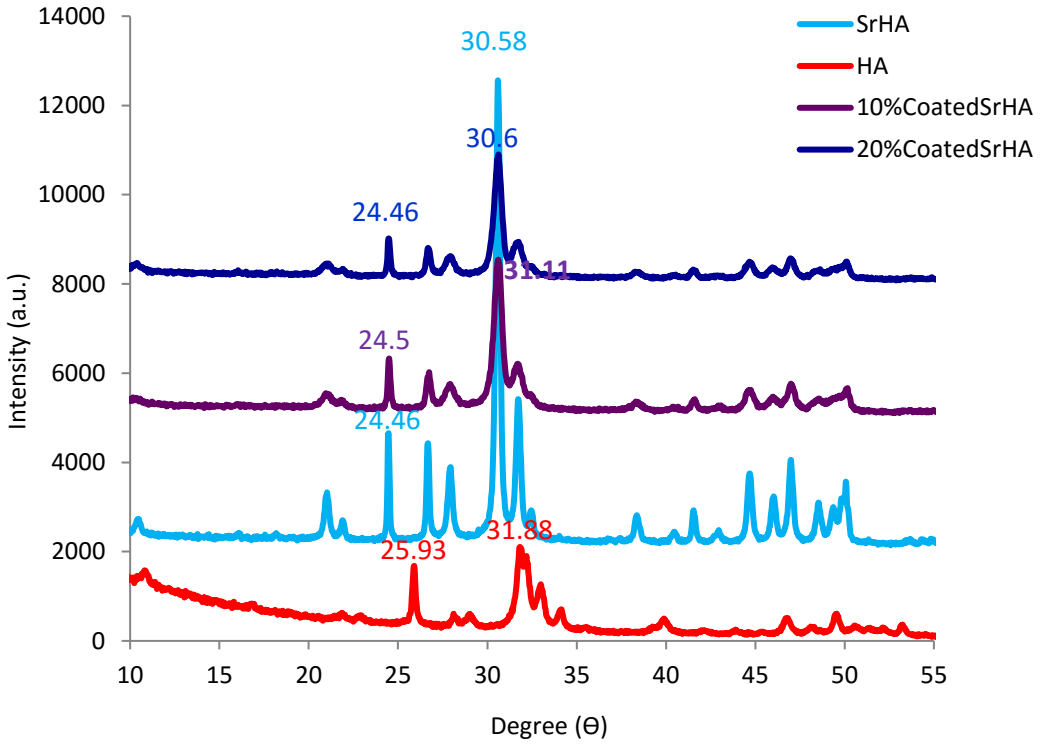

Figure 7.14 XRD data, the intensity against 2Θ, for nano-HA, nano-SrHA (non-coated and coated (C)). There was a shift to the lower 2Θ for all nano-SrHA groups in comparison with nano-HA.

The crystal size of nano-HA, nano-SrHA and surface modified nano-SrHA were estimated by using the Scherrer Line Broadening (Table 7.3).

Table 7.3 Crystal size of nano-HA, nano-SrHA and coated nano-SrHA reflected by XRD pattern and using the Scherer Line Broadening equation (FWHM= full-width half maximum). *This value is not valid because of peak overlap.

Material	FWHM (Radian)	Crystal size 211 direction (nm)	Crystal size 002 direction (nm)
Nano-HA	0.00666	14.5*	24.6
Nano-SrHA	0.00306	31.0	67.5
10%coated SrHA	0.00432	80.7	137.8
20%coated SrHA	0.00486	24.1	41.1

XRD data collected for SrBG displayed a broad peak due to the variation of bond angles and distances in the glass as the SrBG is an amorphous material (Figure 7.15).

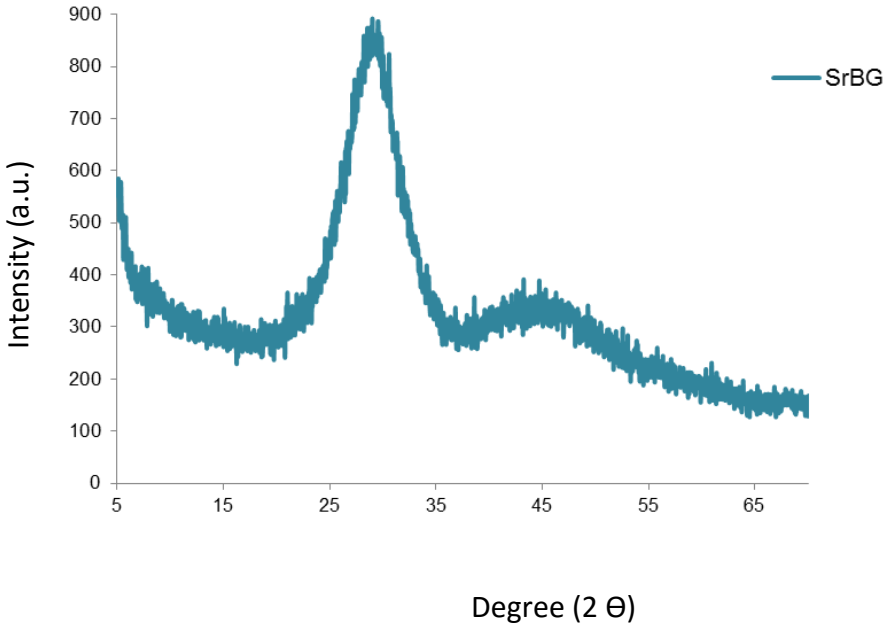

Figure 7.15 XRD data, the intensity against 2Θ, for amorphous structure of SrBG.

7.4.5 Crystal size measurements

The crystal size in different samples were all less than 200nm using the different methods (Table 7.4). The crystallite width from TEM matches more closely with the 211 measurement whilst the length matches the 002 measurement. However, the 20% coated nano-SrHA had a much smaller crystallite size in the 002 direction by XRD (41.1nm) compared to the crystal length from TEM (155.8±3nm).

Table 7.4 Crystal size of nano-HA, nano-SrHA and coated nano-SrHA measured by the different techniques.

		TEM		XRD	
		Length(nm)	Width(nm)	211 direction	002 direction
Material	Nano-HA	58.2±5	12.9±3	14.5	24.6
	Nano-SrHA	73.1±4	23.0±4	31.0	67.5
	10wt% coated nano-HA	105.3±3	10.8±5	80.7	137.8
	20wt% coated nano-HA	155.8±3	12.7±7	24.1	41.1

7.5 Discussion

- ***SrHA***

Synthetic hydroxyapatite (HA), $[Ca_{10}(PO_4)_6(OH)_2]$, is chemically similar to the mineral component of hard tissues (biological apatite) and is widely used in hard tissue augmentation and replacement, with slow resorption (Elliott 1997). Strontium is able to substitute the calcium in the HA structure leading to the use of strontium for increasing the radiopacity.

The FTIR pattern of nano-SrHA and coated nano-SrHA were similar to nano-HA; however, peaks at lower wavelengths for nano-SrHA (non-coated and coated) were obtained in comparison with nano-HA. This is due to the higher atomic mass of strontium (87) compared to calcium (40) in the structure leading to a lower frequency vibration in the FTIR.

Nanoparticles present a high surface area to volume ratio. Since everything in nature tends to be in the lowest energy state, the nanoparticles tend to agglomerate in order to minimise their excess surface energy. Nanoparticles agglomeration could be prevented, if particles stay apart by conventional methods such as using surfactants, oil and emulsification (Dave *et al.* 2006). In the current study, TEM images proved that surface modification aided in decreasing the level of agglomeration of nano-SrHA particles. Our findings are in agreement with Anwar's data (2014) who performed zeta potential on pure HA, surface modified HA and nano-SrHA to investigate the colloidal stability related to their surface charge. She showed a zeta potential of 28, 33 and 35mV for nano-HA, 10 and 20% nano-SrHA, respectively. In her study, this number increased to -43.8mV for coated nano-HA with methacrylic acid. It should be mentioned that zeta potential is the principle of surface charge measurement methods and the crucial factor in colloidal stability. Zeta potential is a scientific term for electrokinetic potential of colloidal dispersions. It measures the electrostatic potential of particles, which is directly related to their dispersion stability by the electrostatic repulsion. The smaller the electrostatic repulsion, the lower the zeta potential values and thus the colloidal stability of the suspension will decrease (Anwar 2014).

TEM images revealed that the size and the shape of particles had changed from more spherical (nano-HA) to more needle shape (surface modified nano-SrHA). Present results were similar to previous studies by Bigi (2012) and Anwar (2014) who showed that the coating of nano-SrHA particles leads to less agglomeration of the particles and cluster formation due to a charge on the surface of coated nano-SrHA (Bigi *et al.* 2007; Anwar 2014). However, it increases the particle size and the shape of the particles are changing from the short nano-prism to elongated prism shape particles. Since the shape of the coated nano-SrHA is an elongated prism/

needle shape, there is an increase in the agglomeration of the particles in the resin infiltrant. Thus, it is crucial that all coated nano-SrHA in infiltrant resin to be parallel and facing towards the opening of pores in the white spot lesion from the smaller axis in order to penetrate the porosity in initial enamel carious lesions fully and successfully (Figure7.16).

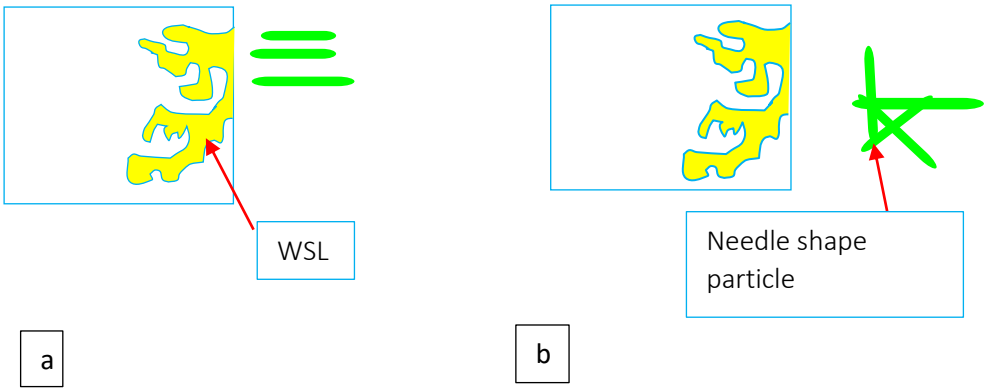

Figure 7.16 A schematic presenting the importance of the direction of the needle shape particles in penetration ability (a) possible penetration and, (b) almost impossible to penetrate into WSL.

The XRD pattern of nano-SrHA (coated and non-coated) was similar to that of nano-HA; however, lower 2Θ values and higher estimated crystal sizes for nano-SrHA were measured. This could be due to bigger atomic radius of the strontium ion (1.16˚A) compared to calcium ion (0.94˚A) in the structure. XRD results for coated nano-SrHA did not detect the methacrylic acid peak. This could be possibly due to not having enough coated particles in the tested sample for XRD or most of the particles were nano-SrHA, rather than coated nano-SrAH in tested samples. These findings were similar to data form the previous studies (O'Donnell *et al.* 2008; Anwar 2014; D'Onofrio *et al.* 2016).

It is crucial to understand that the particles are not individual crystals but are comprised of many crystals. The different techniques used to measure the crystal size, all give different values. This is because they determine crystallite size by

making different assumptions. For example, XRD determines crystallite size with regard to the diffraction planes in the crystal. The crystals do not approximate to spheres but they are observed to be needle-like in the TEM. In general, apatite crystals grow in the 002 direction so we would expect the length to correspond more closely with the crystallite size in the 002 direction, whilst the width would correspond more closely with the 211 crystallite size measurements. However, the 20% coated nano-SrHA had a much smaller crystallite size in the 002 direction by XRD (41.1nm) compared to the crystal length from TEM (155.8±3nm). This may be due to overlapping crystals and the assumption that what is observed is a single crystal.

To develop the nano radiopaque fillers, there is a need to make nano-particle filler rather nano-crystals one. In the current study, the crystal size in different samples were all less than 200nm using the different methods. However, the particle size was not in nano-scale for any of these materials.

- ***SrBG***

Sieving of the produced SrBG suggested that the particle size was expected to be less than 38µm and particle size measurement showed that 75% of the particles were less than 60µm in size. The presence of particles >38µm could be associated with particle agglomeration.

TEM images and XRD data of SrBG proved the amorphous structure of SrBG which was similar to the previous study by Anwar (Anwar 2014). Furthermore, TEM images showed the hydroxyapatite formation in some areas similar to Lynch and colleagues findings on BG study. They believe that HA formation could be possibly due to the reaction between BG and water from the environment (Hench and Andersson 1993).

7.6 Conclusion

Strontium can readily substitute the calcium in HA and BG structures. SrHA and surface-modified (coated) SrHA were successfully produced as nano-crystals but it is important to emphasise they are not nano-particles. All these materials tend to

agglomerate and form clusters leading, which possibly makes them unsuitable as a radiopacifying agent in infiltrant resin.

Chapter 8- Experimental Radiopaque Infiltrant Resin (Curing, Radiopacity and Consistency)

8.1 Introduction

The resin infiltrant ICON® is a very low viscosity resin proposed as a minimally invasive treatment for early enamel carious lesions. It occludes the pores in the lesion and inhibits caries progression. The application of this material does not require any cavity preparation and the healthy tooth structure is preserved; however, this material is radiolucent and cannot be assessed or monitored by taking X-rays in dental surgeries (Meyer-Lueckel and Paris 2010).

Radiopacity (radiodensity) in dentistry is defined as the relative failure of X-rays to pass through a particular material leading to a relatively opaque white appearance of dense materials or substances on radiographic images (Novelline and Squire 2004). It should be kept in mind that the desirable amount of radiopacity of resin composites is debatable. On one hand, some researchers suggest a material should have higher radiopacity than the enamel in order to distinguish the interface between the restoration and tooth (Murchison *et al.* 1999; Imperiano *et al.* 2007). On the other hand, other researchers stated that highly radiopaque composite resins show a negative effect on the visual acuity and the details' description (Espelid *et al.* 1991; Watts and McCabe 1999). It seems that the semi-radiopaque restorative material is the most favourable option due to two following main reasons:

- Match band effect: A dark borderline appears darker due to an increase in the contrast between a light and a dark area due to an illusion effect. Then, there is a possibility to misinterpret a healthy area in tooth structure as part of dental caries (Berry 1983);
- The tooth structure and the restorative materials show a different grade of radiopacity because they have different absorption of the radiation. This difference in absorption of radiation is associated with two factors including the composition and the thickness of material in the x-ray beam direction (Shey and Oppenheim 1979).

This concept raises an important question: how radiopaque a restorative material should be for desirable diagnostic purposes. Radiopacity is usually a measurement

in comparison with enamel, dentine or aluminium (van Dijken *et al.* 1989; Chan *et al.* 1999). Van Dijken and colleagues (1989) stated that the radiopacity of dentine was almost equivalent to that of aluminium (Al) of the same thickness. Moreover, the radiopacity value for enamel was about twice the radiopacity of Al with the same thickness (van Dijken *et al.* 1989). Most studies recommended that a dental material with radiopacity slightly greater than, or equal to, enamel is optimum (Espelid *et al.* 1991; Chan *et al.* 1999), whereas the International Standardisation Organisation (ISO-4049) suggests that the minimum standard for dental material radiopacity should be equal to or greater than that of the same thickness of pure aluminium (Al) (ISO:DP-4049,1985)(Salzedas *et al.* 2006). Furthermore, the American Dental Association (ADA) recommends that a radiopaque material should present radiopacity equivalent to 1mm of Al, almost equal to that of human tooth dentine (Council on Dental Materials and Equipment 1981).The ISO-4049 was used in this study in order to develop a radiopaque infiltrant resin.

Since the application of developed radiopaque infiltrant resin would be in non-cavitated early enamel carious lesions, we believe that the consistency of the developed material is important. This is because the radiopaque agent in the developed material should be able to penetrate to the enamel porosities and not agglomerate on the surface. Furthermore, it is essential for the developed resin infiltrant to change from a liquid phase to solid phase under light curing. We believe that this helps to provide a higher retention of the material in porosities and possibly reduce the water uptake and wear of the material on the surface of the carious lesion.

In this chapter, three features including curing ability, consistency and radiopacity of the developed radiopaque infiltrant resins were measured.

8.2 Aims and objectives

The aims of this part of the study were to investigate the following properties of the experimental radiopaque resins:

- Curing ability: to investigate whether 2mm thickness of various experimental radiopaque resins set and changes from liquid form to solid upon 40s of light curing qualitatively (Standard 2000);
- Radiopacity: to investigate whether the experimental radiopaque resins meet the IS0-4049 standard, which states the radiopacity should be equal to or greater than that of the same thickness of pure aluminium (Al) (Standard 2000);
- Consistency: to investigate whether the radiopaque agents either dissolve or can be dispersed in the resin and make a smooth (unagglomerated) mixture or they agglomerate (Neffgen *et al.* 2012).

8.3 Materials and Methods

8.3.1 Preparation of experimental radiopaque infiltrate resins

The prepared radiopaque fillers including SrBG, nano-SrHA, and surface modified nano-SrHA agents (section 7.3) were added to ICON® resin (DMG, Hamburg, Germany) at loadings of 0.5 and 1.0g to make up a solution with a total weight of 5g in brown glass vials (light sensitive) (Sigma-Aldrich, Gillingham, UK). Thus, resins with 10 and 20wt% radiopaque fillers were produced.

Bromine-methacrylate (ABCR, GmbH, Karlsruhe, Germany) and tin-methacrylate (ABCR, GmbH, Karlsruhe, Germany) were added to ICON® resin (DMG, Hamburg, Germany) at loadings of 0.5, 1.0, 1.5 and 2.0g to make up a solution with a total weight of 5g in brown glass vials (light sensitive) (Sigma-Aldrich, Gillingham, UK). Thus, resins with 10, 20, 30 and 40wt% radiopaque monomers were produced.

The vials were labelled and stirred at room temperature (25°C$\pm$1℃) and setting 3 on the stirrer (Cole-Palmer, London, UK) for 24 hours. The experimental resins were stored in the fridge at 4°C between the experiments.

8.3.2 Curing

The experimental infiltrant resins were dispensed into stainless steel moulds (7mm×4mm×2mm), and cured by a blue LED activation light at 400 mW/cm^2 for 40s

(Demetron LC, Ser no 66004022, KERR corporation, Danbury). The light cure was in direct contact with samples. Then, a dental explorer (Henry Schein, New York, USA) was used to investigate whether the specimen was cured and changed from the liquid form to solid (Paris, Meyer-Lueckel et al. 2007).

8.3.3 Radiopacity measurement experiment

ICON® resin and experimental resins were carefully transferred into a disk-shaped mould, 6.0mm in diameter and 1.0mm in thickness, in accordance with ISO-4049. Then, samples were light-cured using a blue LED activation light at 400mW/cm^2 for 40s (Demetron LC, Ser no 66004022, KERR corporation, Danbury). A 1mm-thick slice of a first upper permanent molar's crown (approval from Queen Mary Research Ethics Committee QMREC 2011/99) was cut using an annular diamond blade (Microslice 2, Malvern Instruments, UK) as the standard for enamel and dentine radiopacities. All specimens were ground on 400-grit sandpaper (Sigma-Aldrich, Gillingham, UK) to create a flat surface and measured by a micrometre to confirm the 1mm thickness.

The prepared disc of each specimen was placed along with an aluminium (Al) step wedge (purity>98% aluminium, with less than 0.1% copper fraction and less than 1% iron fraction) on a digital radiographic sensor. The sensor was stabilised on the bench surface with Blu-Tack. The Al step wedge was used as a standard for measuring the equivalent radiopacity based on the thickness of the aluminium step wedge. This provided an internal standard for each digital X-ray image and allowed calculation of the radiopacity of each material in terms of aluminium thickness. A digital X- ray machine (CEI, Bologna, Italy) with an exposure for 0.5ms at 70kV and 8mA was used to take the radiograph. The distance between the surface of the film to the tube was 45cm (ISO-4049).

8.3.4 Data Analysis

- ***Curing***

Tested materials were divided into two groups of "soft" and "hard". Hard means that the disc is not easily broken or bent, while soft is used as a term for all other qualities. A dental explorer was used to investigate whether the tested material was

cured. If the material changed from liquid form to solid, it was considered as hard and cured.

- ***Radiopacity***

Image J™ (Image Processing and Analysis in Java, National Institute of Health, Bethesda, Maryland, USA) was used to measure the grey value of each radiographic image. The grey value is a numerical value of each pixel varying from 0 (black) to 255 (white) (Nummikoski *et al.* 1992).

The radiographic images were imported into Image J™ (Image Processing and Analysis in Java, National Institute of Health, Bethesda, Maryland, USA). On each image, a rectangular area was drawn inside of each step of Al wedge and the relevant grey value was then measured. A calibration curve was plotted for each image showing the Al wedge thickness versus the relevant grey value and a linear regression equation was calculated. Then, a circular area was drawn on the radiographic image of the disc followed by the relevant grey value measurement. The equivalent Al thickness (mm) for each sample was calculated from the linear regression equation. These values were then plotted against the samples while the grey values of 1mm ICON® resin disk and 1mm-thick enamel were used as references in this study.

- ***Consistency***

The consistency of the experimental resins in vials and digital X-ray images was examined by the naked eye. Then, it was categorised into either “Homogenous” or “Agglomerated” (Figure 8.1).

Figure 8.1 Showing the homogenous (bottle with the blue dot) and agglomerated (bottle with the red dot) consistency of samples.

8.4 Results

8.4.1 Curing

All experimental resins (except 40wt% BrM in ICON® resin) were changed from liquid to solid form and were classified as hard and cured after 40s light curing (Table 8.1).

Table 8.1 A table showing the light curing results of different experimental resins and ICON® resin using a blue LED activation light at 400 mW/cm^2 for 40s (SrBG= Strontium Bioglass, SrHA= strontium hydroxyapatite, C= coating, BrM= Bromine methacrylate, SnM=Tin methacrylate).

Name	Hardening
ICON® resin	Hard
10wt%SrBG in ICON® resin	Hard
20wt%SrBG in ICON® resin	Hard
10wt% nano-SrHA in ICON® resin	Hard
20wt% nano-SrHA in ICON® resin	Hard
10wt%C (10%) nano-SrHA in ICON® resin	Hard
20wt%C(10%) nano-SrHA in ICON® resin	Hard
10wt%C(20%) nano-SrHA in ICON® resin	Hard
20wt%C(20%) nano-SrHA in ICON® resin	Hard
10wt%BrM in ICON® resin	Hard
20wt%BrM in ICON® resin	Hard
30wt%BrM in ICON® resin	Hard
40wt%BrM in ICON® resin	Soft
10wt%SnM in ICON® resin	Hard
20wt%SnM in ICON® resin	Hard
30wt%SnM in ICON® resin	Hard
40wt%SnM in ICON® resin	Hard

8.4.2 Consistency

The experimental resins incorporating nano-SrHA and SrBG "agglomerated" while ICON® alone and other experimental resins containing radiopaque methacrylates appeared to be "Homogenous" (Table 8.2).

Table 8.2 A table showing the consistency of the different experimental resins (A=agglomerated and H=Homogenous) in a glass vial and radiographic images of the discs. (SrBG= Strontium Bioglass, SrHA= strontium hydroxyapatite, C= coating, BrM= Bromine methacrylate, SnM=Tin methacrylate).

Specimen	Mixture	Radiographic Image
ICON®	H	H
10wt%SrBG in ICON® resin	A	A
20wt%SrBG in ICON® resin	A	A
10wt% nano-SrHA in ICON® resin	A	A
20wt% nano-SrHA in ICON® resin	A	A
10wt%C (10%) nano- SrHA in ICON® resin	A	A
20wt%C (10%) nano- SrHA in ICON® resin	A	A
10wt% C(20%) nano- SrHA in ICON® resin	A	A
20wt% C(20%) nano- SrHA in ICON® resin	A	A
10wt%BrM in ICON® resin	H	H
20wt%BrM in ICON® resin	H	H
30wt%BrM in ICON® resin	H	H
40wt%BrM in ICON® resin	H	H
10wt%SnM in ICON® resin	H	H
20wt%SnM in ICON® resin	H	H
30wt%SnM in ICON® resin	H	H
40wt%SnM in ICON® resin	H	H

8.4.3 Radiopacity

8.4.3.1 Calibration Curve

For each image, the grey level of the steps on the Al wedge were measured. Then, a specific calibration curve was drawn showing the pixel grey value versus the aluminium thickness (mm). A calibration equation was calculated using the best-fit regression analysis for the selected data (Figure 8.2).

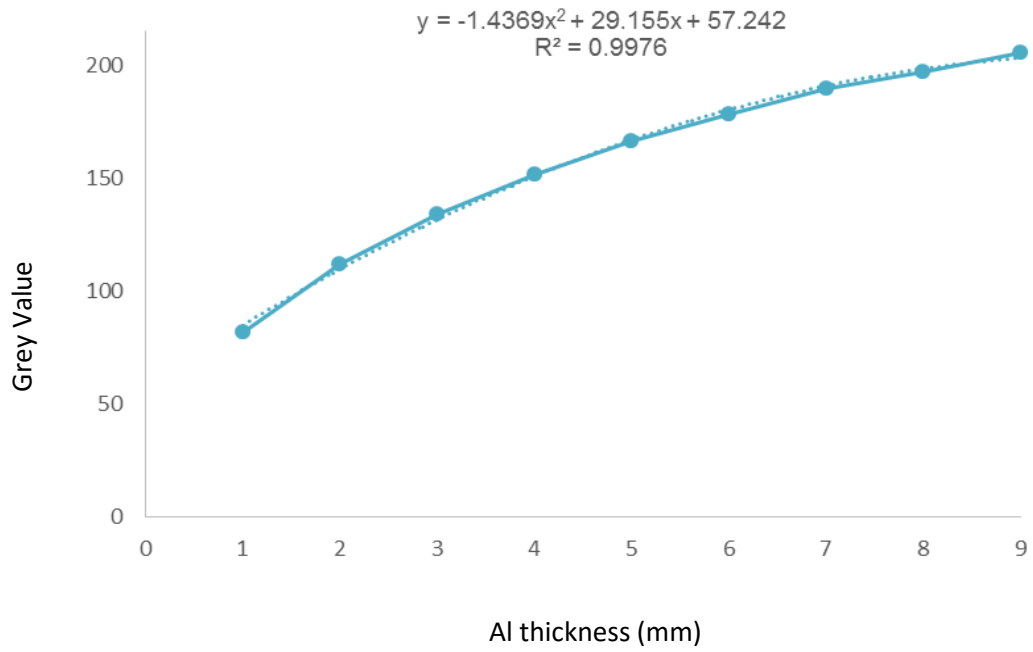

Figure 8.2 Calibration curve showing Al thickness (mm) against grey value and the relevant regression equation for the step wedge.

8.4.3.2 Radiopacity measurement

Figure 8.3 depicts the radiographic images of ICON® resin disc and 1mm thickness of the tooth, which is a cross section from the crown. The equivalent Al thickness for ICON® resin, dentine, and 1mm enamel were 0.27, 1.3 and 2.1 mm, respectively.

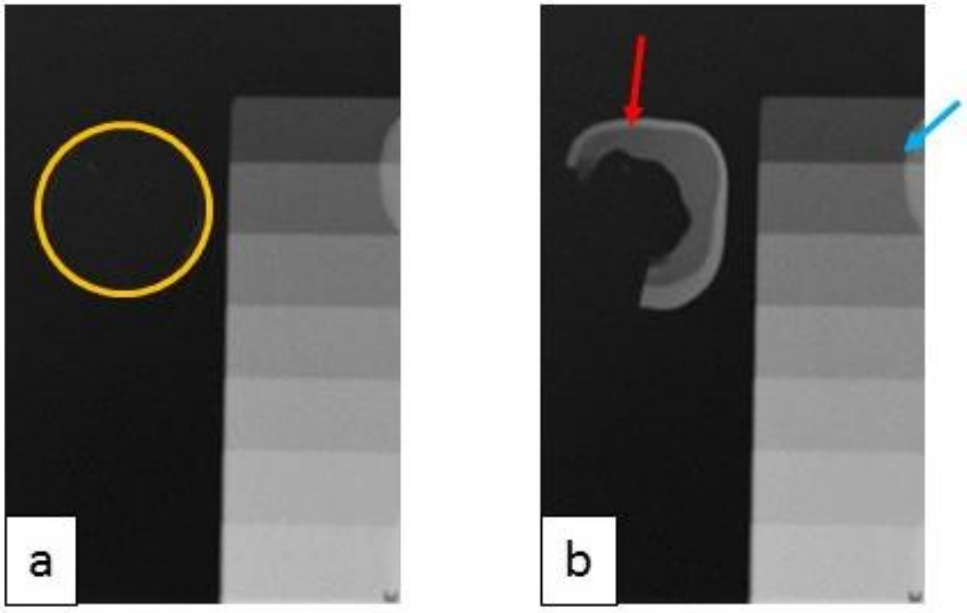

Figure 8.3 Radiographic images of 1mm thickness of (a) ICON® resin disc (yellow circle)and (b) 1mm-thick slice of tooth crown (red arrow) along with the Al step wedge (blue arrow).

8.4.3.3 Incorporation of radiopaque filler in ICON® resin

Figure 8.4 shows the radiographic images of the experimental resins incorporating the radiopaque fillers. All images showed agglomeration with a positive correlation with the amount of radiopaque fillers. The highest level of agglomeration was associated with 20wt% nano-SrHA filler incorporation. The coated nano-SrHA incorporation in ICON® resin mixture showed less agglomeration in comparison with the non-coated nano-SrHA incorporation in ICON® resin.

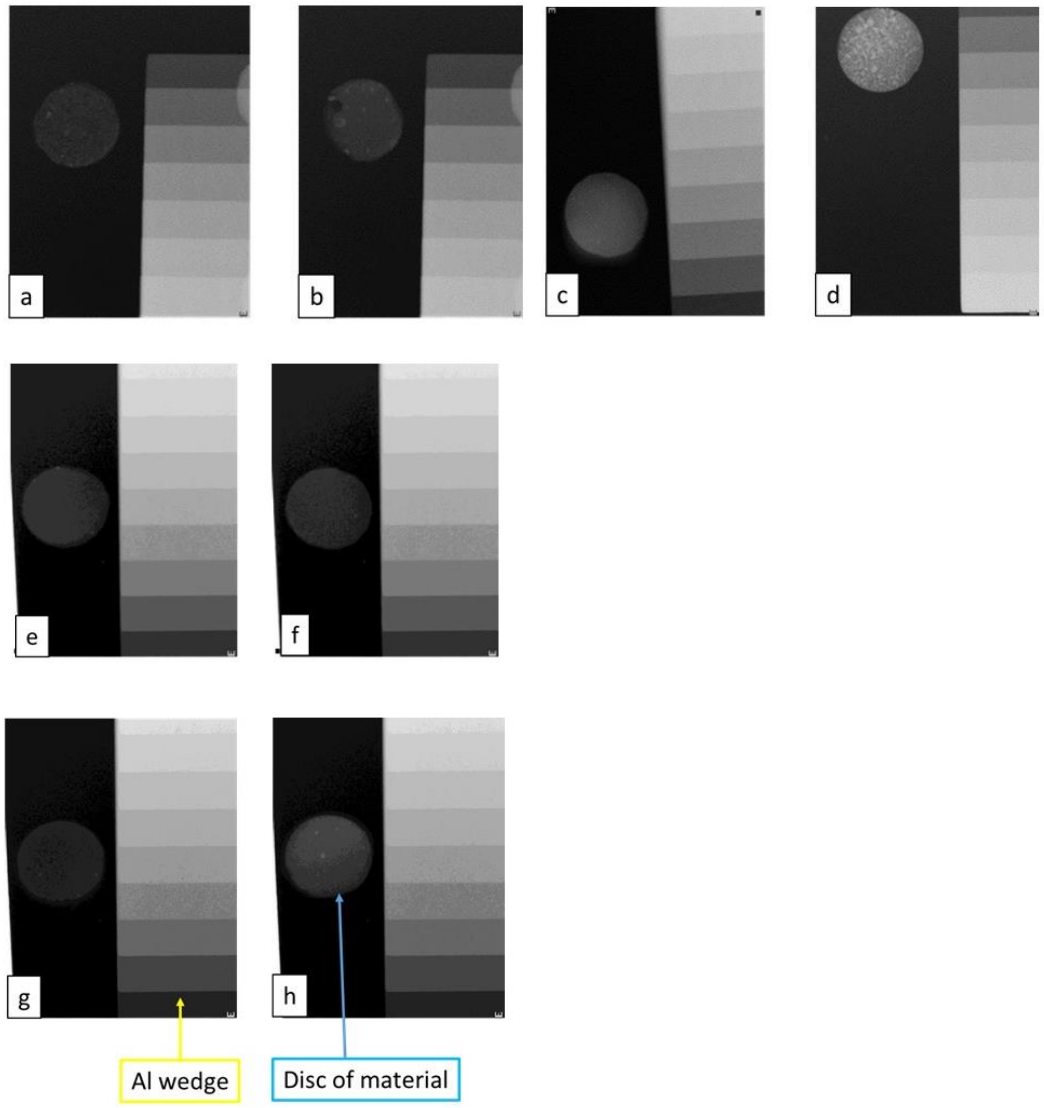

Figure 8.4 Radiographic images of: SrBG in ICON® resin with (a)=10wt%, (b)=20wt%; nano-SrHA in resin with (c)=10wt%, (d)=20wt%; 10wt% coated nano-SrHA in resin with (e) = 10wt%, (f) = 20wt%; and 20wt% coated nano-SrHA in resin (g) = 10wt% and (h) = 20wt%.

The radiopacity of SrBG in resin did not reach the ISO-4049 standard criteria while nano-SrHA incorporation and 20wt% incorporation of coated nano-SrHA showed a grey value equivalent to more than 1mm Al thickness. The radiopacity measurements for coated nano-SrHA incorporation in ICON® resin was lower than non-coated nano-SrHA incorporation in ICON® resin (Figure 8.5).

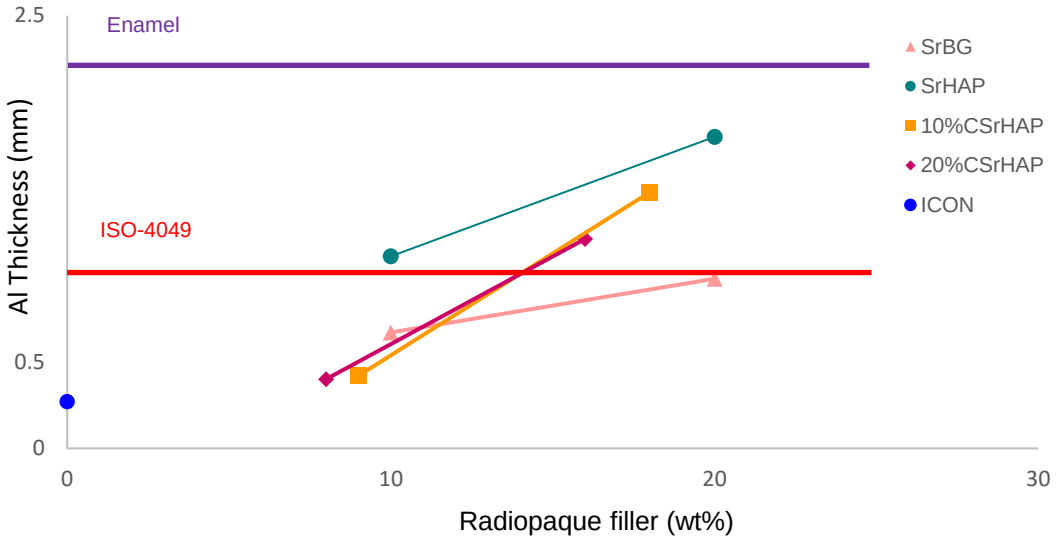

Figure 8.5 Radiopacity of the prepared discs in different percentages of the radiopaque fillers incorporation in ICON® resin against the equivalent Al thickness (mm).

8.4.3.4 Incorporation of radiopaque elements in ICON® resin

Figure 8.6 shows the radiographic images of the discs with different percentage of radiopaque monomers in ICON® resin. They showed no agglomeration and an increase in radiopacity in positive correlation with the radiopaque monomer weight percentage. Phase separation or de-mixing was observed on the disc with 30wt% bromine-methacrylate in ICON® resin (Figure 8.6 c).

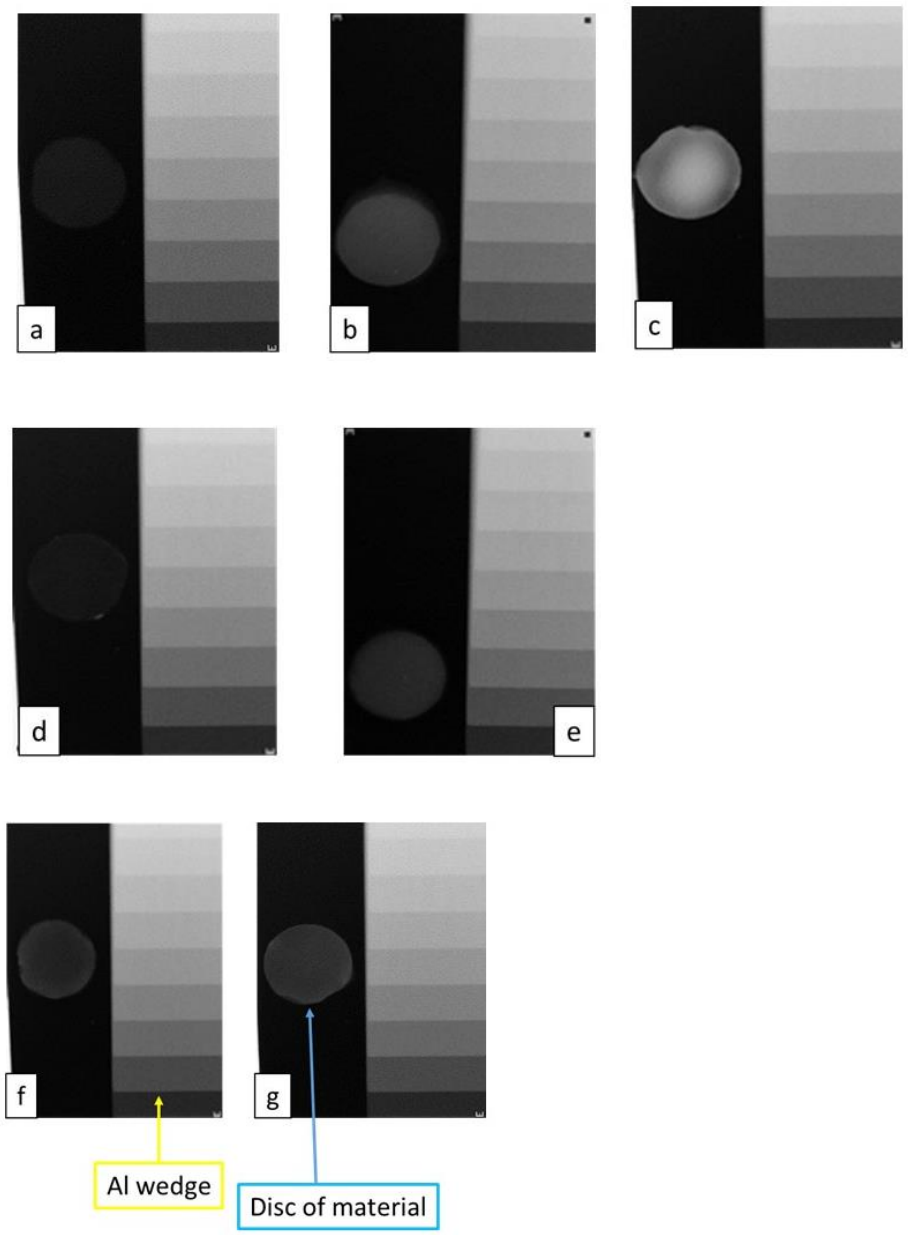

Figure 8.6 Radiographic images of: ICON® resin containing bromine-methacrylate(a)=10wt%, (b)=20wt% and (c)= 30wt% and ICON® resin containing tin-methacrylate (d)=10wt%, (e)=20wt%, (f) = 30wt%, (g) = 40wt%.

The equivalent Al thickness for 40% tin-methacrylate, 20 and 30wt% bromine-methacrylate resin were 1.06, 1.07 and 1.65 mm, respectively (Figure 8.7). The resins with lower wt% of radiopaque monomer did not reach the ISO-4049 standard.

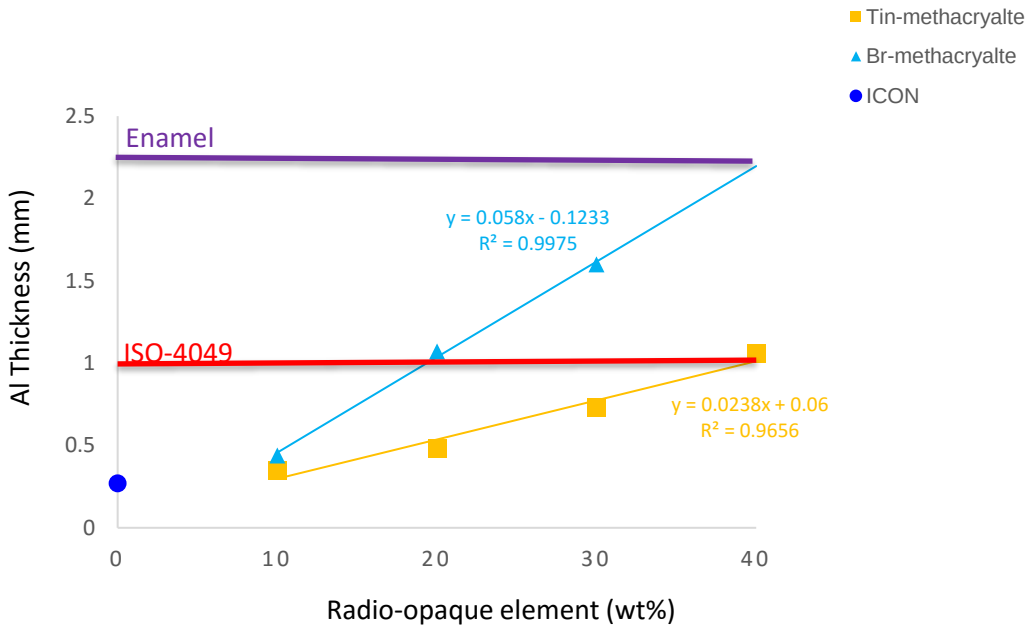

Figure 8.7 Radiopacity of resin discs with various percentages of the radiopaque elements incorporation in ICON® resin against the equivalent Al thickness (mm).

8.5 Discussion

Although both fissure sealants and resin infiltrants play a key role in preventing/managing dental caries, they are both difficult to identify radiographically. In the present study, incorporation of the radiopaque fillers such as SrBG, nano-SrHA (coated and non-coated) and incorporation of heavy elements were used to make ICON® resin radiopaque.

Researchers carried out studies to make the fissure sealant radiopaque via two different pathways including blending radiopaque fillers into the polymeric matrix or chemical incorporation of radiopaque agents in monomer units (Foster and Ahir 1976). The former work shows a tendency for these materials to leak into the body fluids over time, therefore, the radiopacity could be a temporary phenomenon, and could produce possible systemic toxicity, since the radiopaque agent is not chemically bonded to the base material (Thanoo *et al.* 1991).

- ***Curing ability***

All tested materials except 40wt% bromine-methacrylate in ICON® resin were shown to have changed from the liquid to solid form when cured using an emitting blue-light unit of 400 mW/cm^2 for 40s. This result was similar to the recommendation of ISO-4049 and a review article on light curing of the resin-based materials (Standard 2000; Malhotra and Mala 2010). Paris and his colleagues (Paris *et al.* 2007) developed a range of different radiolucent infiltrant resins and most of the tested materials were cured completely by 60s light curing. In the present study, a dental explorer was used to investigate whether the experimental resin changed from liquid form to a solid form to examine their curing. Although this method might be considered as a subjective and descriptive method, it has been used by Paris and his colleagues (2007) in their study (Paris *et al.* 2007) and the present data would be comparable with theirs.

Degree of conversion (DC) of a resin based dental material defines as the number of aliphatic carbon-carbon double bond links present in the monomer being converted into single covalent carbon-carbon bonds during the polymerisation process to form the polymer (Ferracane 1985). In ideal condition, all the resin monomers should converted to the polymer but this never occurs as the propagation of the polymerisation process is hindered by the limitation on the mobility of the free radicals imposed by the rapid formation of the cross-linked polymeric network after initiation of polymerisation by the light curing unit (Marghalani 2016). Fourier Transform Infrared (FTIR) spectroscopy is a highly reliable method to determine DC by measuring the reduced intensity of the carbon-carbon double bond stretch absorption band at 1,6838cm^{-1} when the methacrylate monomer is converted to polymer (DeWald and Ferracane 1987). In the present study, DC of the developed radiopaque infiltrant resins measured; however, the data was lost due to broken FTIR machine. Due to time scale, the FTIR investigation was not repeated. Hence, tactile sensation was used as a qualitative measure. 'Hard' indicated that the material was cured and polymerisation has reached an acceptable standard. 'Soft' meant that the resin was not polymerised properly.

It should be noted that a white spot lesion is defined as having porosity in enamel and thus the lesion is still surrounded by intact tooth structure with no clinically open cavity in the oral environment (Figure 8.8). If the white spot lesion extends to the enamel-dentine junction (EDJ), the lesion depth is approximately 2.5mm in permanent dentition. Although the depth of curing for resin-based materials was shown to be 2mm using standarised mould (Malhotra and Mala 2010), there is no evidence whether the tooth structure surrounding the resin infiltrant has an effect on the curing of the infiltrated material in the white spot lesion.

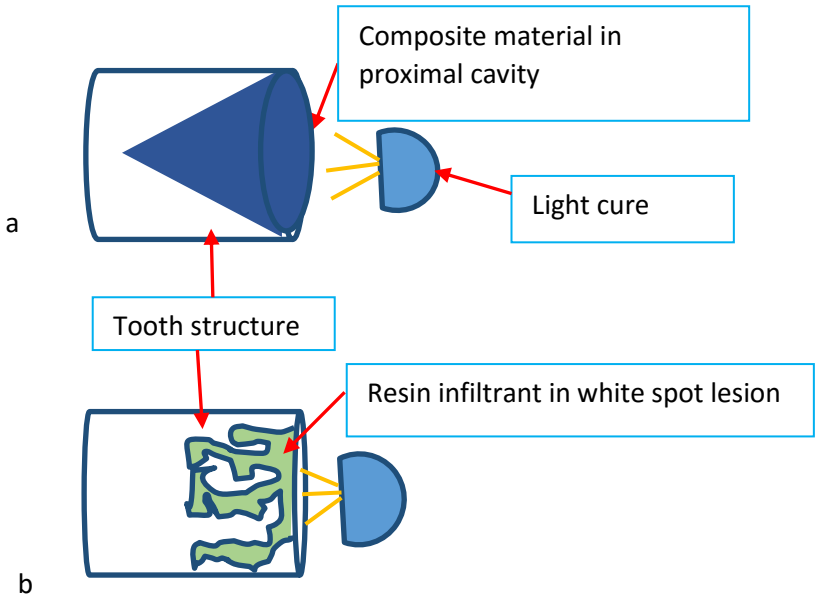

Figure 8.8 Schematic picture presenting the accessibility of the light emitted from light cure unit to (a) composite in the dental cavity and, (b) resin infiltration in white spot lesion.

- ***Radiopacity***

In the present study, the radiopacity values of enamel and dentine were 2.1 and 1.3 mm of Al respectively. These values were within the range reported in previous research (Murchison *et al.* 1999).

Strontium has a higher radiopacity value compared to calcium due to its higher atomic number (Romieu *et al.* 2010). However, SrBG group did not reach the ISO-

4049 standard in terms of radiopacity requirements whereas nano-SrHA group, coated and non-coated, met the ISO-4049 criteria. The radiopacity values were positively correlated with strontium content. D'Onofrio *et al.* (2016) and Anwar (2014) showed similar findings on the radiopacity of SrBG incorporated in calcium phosphate cement and radiopacity of nano-SrHA incorporation in dental composites (Anwar 2014; D'Onofrio *et al.* 2016).

The other method to make the ICON® resin radiopaque was the addition of radiopaque elements such as tin (Sn) and bromine (Br), both with high atomic number, in the form of the addition of SnM or BrM to the ICON® resin. Tin-methacrylate (SnM) and bromine-methacrylate (BrM) can be blended with the resin, which mainly consisted of triethylene glycol dimethacrylate (TEGDMA). In this study, tin-methacrylate and bromine-methacrylate were added to the resin up to 40wt%. The consistency of 40wt% of bromine-methacrylate in ICON® resin was soft with 40s of light curing; therefore, this sample was excluded from the measurement of radiopacity. 20 and 30wt% BrM and 40wt% SnM in ICON® resin were light cured in 40s completely, showed homogenous mixtures and met the ISO-4049 in terms of radiopacity. Our findings on the incorporation of tin-methacrylate were similar to the data from a MClinDent dissertation by Patel (2013) in our unit. She added 50wt% SnM into the ICON® resin and therefore, reported higher radiopacity values compared to our value. Furthermore, previous researchers used a maximum of 50%SnM to make a fissure sealant radiopaque. Other researchers used BrM to make polymers radiopaque and it showed a similar amount of radiopacity to our findings (Delaviz *et al.* 1989; Rawls *et al.* 1990; Smid *et al.* 1991).

- ***Consistency***

The consistency of experimental radiopaque resins is a crucial property to infiltrate the material into porous structure of white spot lesion. Although there was a lower agglomeration in coated nano-SrHA with methacrylic acid in comparison with the non-coated nano-SrAH, which was similar to the data from the previous study (Anwar 2014), the mixture of non-coated nano-SrHA in ICON® resin was not completely homogenous as they still formed clusters in ICON® resin. Hence, it is

envisaged that these fillers particles cannot infiltrate in the pores due to agglomeration.

8.6 Conclusion

The incorporation of BrM (20 and 30wt%) and SnM (40wt%) in ICON® resin was shown to be homogenous and had a radiopacity value above the ISO-4049 standard while they formed a solid phase after light curing. Therefore these three radiopaque resins were chosen to be used in the following experiments.

Chapter 9- Experimental Radiopaque Infiltrant Resin (Viscosity and Wettability)

9.1 Introduction

The infiltrant resin penetrates into the porous structure of early enamel caries mainly by capillary forces (provided that the pores are filled with air). Capillary action is defined as the movement of liquid through or along a narrow space, overcoming other forces such as gravity. This feature of the liquid depends on two characteristics of the liquid: cohesion and adhesion. The former and the latter are defined as an attraction between the same particles and attraction between two different particles, respectively. Capillary phenomenon in liquids such as water occurs when the adhesion is greater than the cohesion. It should be noted that in some liquids such as mercury, the cohesion is more than the adhesion leading to the absence of the capillary action feature (Figure 9.1) (Hocking and Rivers 1982).

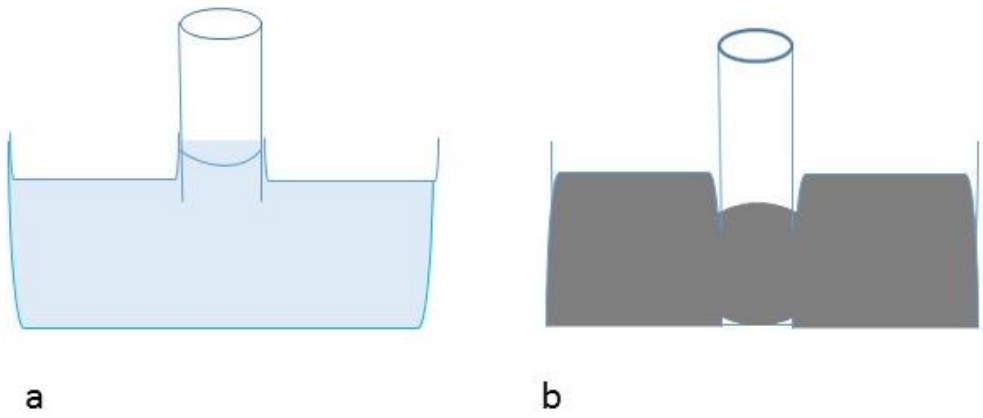

Figure 9.1 A schematic of liquids (a) with the capillary action feature such as water and (b) without the capillary action such as mercury.

In the previous study, the "Washburn equation" (Equation 9.1) was used to measure resin penetration into enamel porosity due to capillary forces (Paris *et al.* 2007). This equation assumes that the porous solid is made of a bundle of parallel capillaries with a uniform radius.

$$d^2 = (\gamma \cos\theta / 2\mu)\, rt$$

Equation 9.1

d: The distance moved by the liquid resin (m),

θ: The contact angle of the liquid resin (on enamel) (degree),

γ: The surface tension of the liquid resin (to air) (mN/m),

μ: The dynamic viscosity of the liquid resin (Pa.s),

t: The penetration time (s) and,

r: The capillary (pore) radius (m).

The bracketed part of equation 9.1 defines the penetration coefficient (PC), which has a linear correlation with the material's ability to penetrate the porous solid. Early enamel caries has porosities in the enamel where air or water can be trapped inside the porosity. Water is a polar material. The highly electronegative oxygen in the water molecules results in oxygen and hydrogen to be partially negative and positive, respectively and capable of hydrogen bonding infiltrant resin in order to increase the infiltration ability (Faghihnejad and Zeng 2013). It should be mentioned that a lower contact angle (being hydrophilic) leads to a higher penetration coefficient (PC), while the contact angle impact on PC is very limited as its cosine would be accounted in Washburn equation (Equation 9.1) (Paris *et al.* 2007). Furthermore, Paris and his colleagues pointed that viscosity of the liquid resin play a key role in predicting the infiltration ability of the experimental resins (Equation 9.1). As the dynamic viscosity decreases, the penetration coefficient increases. In other words, an experimental resin with lower viscosity has a higher penetration ability into the porosity of white spot lesions (WSLs) (Paris *et al.* 2007) .

9.1.1 Viscosity

Viscosity is defined as the internal liquids resistance to flow. A fluid with a high viscosity is resistant to flow whereas a liquid with a low viscosity tends to flow easily (Figure 9.2). The fluid's viscosity is related to the force causing the fluid to shear. This involves frictional forces within the fluid itself and friction between the fluid and its surroundings. Inside a tube, the adjacent layer of liquid to the walls of the tube, are almost static and layers of fluid closer to the centre move faster. In a viscous liquid, the layers of liquid are more resistant to shearing due to inter-layer frictional forces (Andrade 1952).

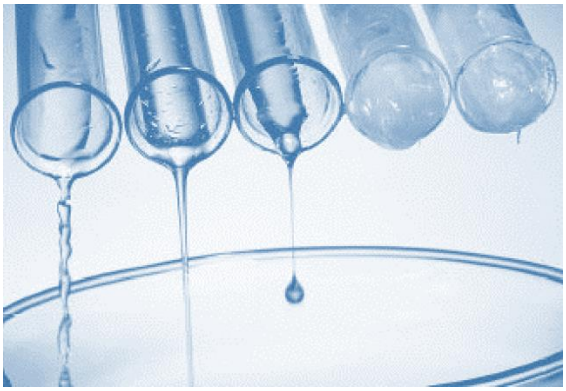

Figure 9.2 Viscosity is the resistance of the liquid to the deformation. This image is (left to right) showing an increase in viscosity of the liquids (http://www.synlube.com/viscosity.html, accessed on 21/02/2017).

There are two types of viscosity: 1) dynamic viscosity and, 2) kinematic viscosity. Dynamic viscosity, known as absolute viscosity, is defined as the quantitative manifestation of a fluids' resistance to flow. Newton's law of viscosity states that the shear stress on the fluid layer is directly proportional of the shear strain (Equation 9.2) (Bourne 2002).

$$\tau = \dot{\gamma} \times \eta$$

Equation 9.2

τ: Shear Stress (Pa),

$\dot{\gamma}$: Shear Rate (1/s),

η: Dynamic viscosity (Pa.s).

Shear stress is the stress that is parallel to the fluid's surface when one layer moves along on top of the other layer in the fluid (Figure 9.3).

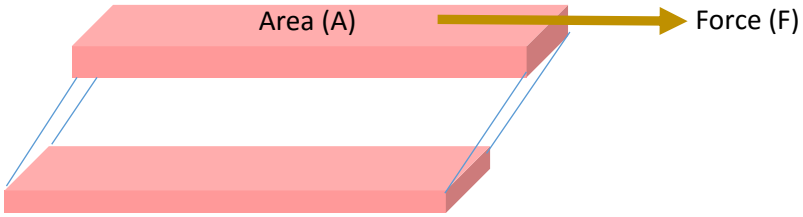

Figure 9.3 A schematic of shear stress between two adjacent layers in the fluid.

The shear stress (ζ) is measured as the force (F) applied to the upper layer divided by this layer's area (A) (Equation 9.3). It should be mentioned that the unit N/m^2 is called a Pascal (Pa)(Bourne 2002)

$$\zeta = \frac{F}{A}$$ Equation 9.3

ζ: Shear Stress (N/m^2 or Pa),

F: Force (N),

A: Plate's area (m^2).

Shear rate (Ɣ) is defined as the velocity (v) of the upper layer divided by the distance (h) between the two layers (Figure 9.4). The equation to measure the shear rate is (Bourne 2002):

$$\gamma = \frac{v}{h}$$ Equation 9.4

Ɣ: Shear rate (1/s),

V: Velocity (m/s),

h: The distance between the two layers (m).

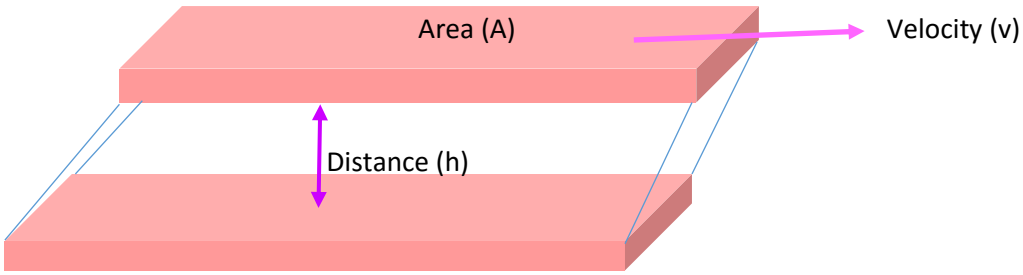

Figure 9.4 A schematic of shear rate between two adjacent layers in the fluid.

The reformulating Newton's law (Equation 9.5) would be used to measure the dynamic viscosity (Bourne 2002).

$$\eta = \frac{\tau}{\dot{\gamma}}$$ Equation 9.5

τ: Shear Stress (Pa),

γ̇: Shear Rate (1/s),

η: Dynamic viscosity (Pa.s).

Kinematic viscosity, known as diffusivity of momentum, defines the flow of the liquid under gravitational forces. Kinematic viscosity can be measured by recording the time taken for the experimental fluid to travel through an orifice in a capillary under the force of gravity. Kinematic viscosity (v) can be calculated by the following formula (Equation 9.6) (Bourne 2002).

$$\mathbf{v} = \frac{\eta}{\rho}$$ Equation 9.6

v: Kinematic viscosity (m^2/s),

η: Dynamic viscosity (Pa.s),

ρ: Fluid Density (Kg/m^3).

There are three main factors, which affect the viscosity of a fluid:

- The inter-molecular structure. The liquid resists flow more when there are stronger inter-molecular forces,
- The external forces such as gravity lead to liquid to flow. The intensity and the duration of the external forces are important,
- The ambient conditions such as temperature and the pressure (Andrade 1952).

9.1.2 Wettability

Wettability is defined as the interaction between fluid and solid phases due to intermolecular interactions between these two phases. In other words, it defines the affinity of a liquid for a solid and it shows how a drop of liquid spreads on the solid. The shape of the ultimate drop (Figure 9.5) presents the wettability which is identified by the contact angle (Θ) (O'Brien and Ryge 1965).

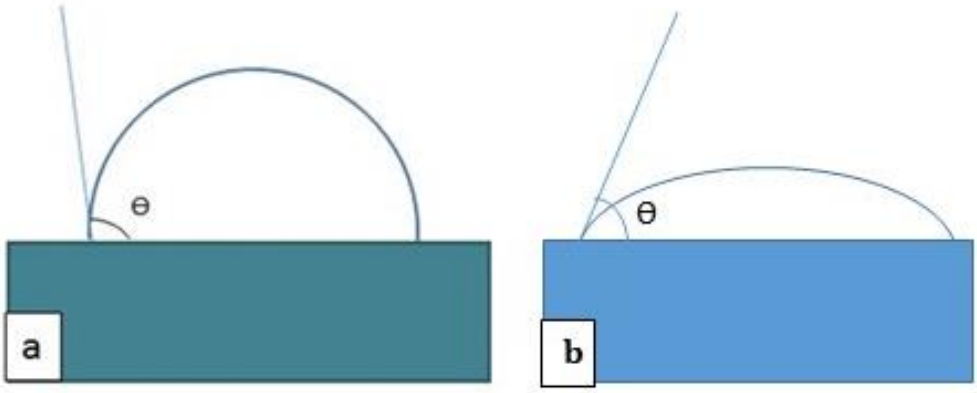

Figure 9.5 (a) Poor wettability and (b) good wettability by a drop of liquid on a solid forming (a) a high contact angle and, (b) a low contact angle modified from (O'Brien and Ryge 1965).

The contact angle (CA) is the angle between the liquid-solid interface and liquid-vapour interface when a liquid drop is placed on an even, horizontal solid surface. In a pure liquid, the internal equal forces between molecules in all directions, while the surface molecules are pulled inwards, as there are no compensating forces from different directions (Figure 9.6). This leads to an internal pressure which contracts

the liquid surface and it is defined as “surface tension”. Surface tension plays a key role in the shape of the liquid drop (Craig *et al.* 2000).

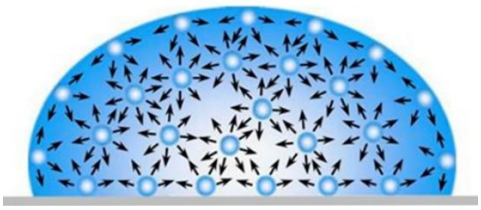

Figure 9.6 The balanced (between the internal molecules) and unbalanced forces (between the superficial molecules) of the liquid give rise to the surface tension (www.slideshare.net/bdougherty/hydrogen-bonds, accessed on 03/02/2017).

Thomas Young (1805) described the contact angle of a liquid by the following Equation (9.7), which involves the action of three interfacial tensions:

$$\gamma_{lv}\cos\theta_Y = \gamma_{sv} - \gamma_{sl}$$

Equation 9.7

γ_{lv}: Liquid- vapor interfacial tensions (mN/m),

γ_{sv}: Solid- vapor interfacial tensions(mN/m),

γ_{sl}: Solid-liquid interfacial tensions (mN/m),

θ_Y: Young’s contact angle (degree).

When a drop of water is placed on a surface dipped in oil, a contact angle is formed that ranges from 0° to 180°.

Contact angle is an inverse measure of wettability. When the contact angle is small (<90°) the liquid spreads on the solid surface and when the contact angle is large (>90°) the liquid beads on the solid surface. In other words, liquids with contact angles <90° are hydrophilic (water-wet) and show high wettability, whereas liquids with contact angles >90° are hydrophobic (oil-wet) with low wettability. It should be noted that at 0° complete wetting and at >150° non wetting or a lotus effect (super-hydrophobic) would occur (Table 9.1) (Craig *et al.* 2000).

Table9.1 The correlation between contact angle and wettability, solid/liquid interaction and liquid/liquid interaction (Craig *et al.* 2000)**.**

Contact Angle (Θ)	Wetting ability	Solid/ liquid interaction	Liquid/ liquid interaction
Θ= 0°	+++	strong	weak
0°< Θ <90°	++	strong	weak
90°≤ Θ <180°	+	weak	strong
Θ= 180°	-	weak	strong

Contact angles are important in many areas, such as oil recovery, printing, lubrication. The techniques used to measure contact angle can be divided into two main groups: 1) direct optical methods and, 2) indirect force methods. The common techniques are the conventional telescope-goniometer, the Wilhelmy balance, and the drop-shape analysis method (Craig *et al.* 2000). The hardware design and computational technology have been improved dramatically to increase the quality of the drop shape analysis for surface science over the past thirty years. The axisymmetric drop shape analysis (ADSA) method is one of the most accurate techniques to measure the contact angle with a reproducibility of ±0.2. Therefore, this method was used in this study (Yuan and Lee 2013).

Wettability plays a crucial role in the bonding or adherence of two materials. Wettability counts as an important factor regarding the control of the location, flow, and distribution of fluids in a porous medium and therefore, it affects relative permeability.

The wettability plays a key role in different areas of dentistry such as: the wetting of denture base plastics by saliva, the wetting of enamel by fissure sealants, and importantly the wetting of the porosity in early enamel carious lesion by infiltrant resin (Craig *et al*. 2000).

9.2 Aims and Objectives

Based on the previous studies, an ideal infiltrant resin should have a dynamic viscosity of less than 32mPa.s, which is equivalent to a penetration coefficient >50cm/s (Paris *et al.* 2007). Furthermore, it should have a high wettability and thus, have a contact angle less than 90° in order to be hydrophilic (Craig *et al.* 2000).

The aims of this part of the study were for each experimental resin:

- To measure and compare their dynamic viscosities;
- To ascertain whether their dynamic viscosities were less than 32mPa.s;
- To investigate and compare their wettability by contact angle measurement;
- To ascertain whether their contact angles were less than 90°.

9.3 Null Hypothesis

- There is no significant statistical difference among the experimental radiopaque and ICON® resins' dynamic viscosities.
- There is no significant statistical difference among the experimental radiopaque and ICON® resins' contact angles.
- There is no significant statistical changes in experimental radiopaque or ICON® resins' contact angles with time.

9.4 Materials and Methods

9.4.1 Viscosity

Viscosity was determined by using a simple method. A Pasteur pipette (Sigma-Aldrich, Gillingham, UK) was marked at 5, 70 and 75mm and then, fixed in a retort stand (Figure 9.7). The pipette was filled with the test material up to 75mm. Then, the first examiner released the digit pressure from the top of the pipette and the second examiner using a stop watch recorded the flow time of test sample between 70 and 0mm points. The room temperature was 25 ℃ $\pm$ 1℃ . The measurement was carried out 5 times per sample, which included water, ICON® resin, 20wt%

bromine methacrylate (BrM) in ICON® resin, 30wt% bromine methacrylate (BrM) in ICON® resin and 40wt% tin methacrylate (SnM) in ICON® resin.

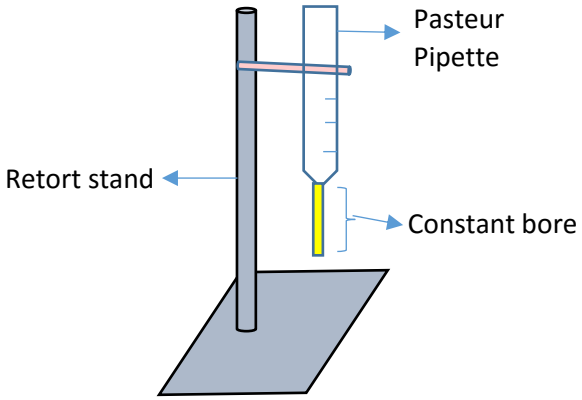

Figure 9.7 A schematic of Pasteur Pipette and retort stand to measure the viscosity.

9.4.2 Contact Angle (CA)

A drop shape analyser (DSA100, KRÜSS GmbH, UK) was used to measure the CA by capturing the profile of a liquid placed on a clean glass slab, using a mounted camera and software (DSA-1) to analyse the CA.

Firstly, the glass slab was cleaned by 70% ethanol (Sigma-Aldrich,Gillingham, UK) and dried with lint free tissue (Cole-Parmer, London,UK). Then, a droplet of material (approximately 1µl) was placed carefully on the clean glass slab placed on the DSA100 goniometer platform by means of a F1-ClipTip™ pipette (Thermofisher Scientific, MA, USA). Using the drop analysis software, the sample's droplet was focused on the screen, and the images were recorded at 10, 60, 120 and 180s with a charge-couple device (CCD) camera for each droplet. Each measurement was performed on a new glass slab in order to prevent any surface contamination. The room temperature was 25℃ ± 1℃. The measurement was repeated 5 times per sample, which included water, ICON® resin, 20wt% bromine methacrylate (BrM) in ICON® resin, 30wt% bromine methacrylate (BrM) in ICON® resin and 40wt% tin methacrylate (SnM) in ICON® resin.

9.4.3 Data Analysis

- ***Viscosity***

The readings from the viscosity measurement were transferred to an excel sheet and the dynamic viscosity of the materials was calculated using the Hagen-Poiseuilles equation (Equation 9.8):

$$\Delta p = 8\eta LQ / \pi r^4$$ Equation 9.8

Δp: The pressure reduction between two ends (Pa),

η: Dynamic viscosity (Pa.s),

L: The length of the Pasteur pipette, where the sample flows in (m),

Q: Volumetric flow rate (L/s),

r: The radius of the modified pipette (m),

π: The mathematical constant pi.

In the current study, the Pasteur pipette has a constant bore (Figure 9.7) and the Δp was considered to be as the same as atmospheric pressure (101kPa). The radius of the pipette was measured using a collimator and it was 0.001m and the length of the Pasteur pipette for this experiment was 70mm.

A bar graph showing the mean dynamic viscosity of the test materials against the name of the test materials was plotted. Student paired t-test was carried out to find out whether there was any significant difference in the dynamic viscosity between each of test materials and ICON® resin. *p* value <0.05 was considered to be statistically significant different.

The viscosity raw data and relevant calculations can be found in Appendix A.

- ***Contact angle***

The contact angel measurements were transferred to an Excel sheet. A bar graph showing the mean contact angle for the test materials at four time points (10s, 60s, 120s and180s) against the name of test materials was plotted. Student paired t-test

was used to investigate whether there was any statistically significant difference for the contact angle measurements between each specimen and the ICON® resin, and between the time for each specimens. *p* value <0.05 was considered to be statistically significant different.

The contact angle raw data and relevant calculations can be found in Appendix B.

9.5 Results

9.5.1 Viscosity

The dynamic viscosity for the experimental resins with incorporation of radiopaque fillers could not be measured as the materials did not flow through the pipette even after 5 minutes.

Figure 9.8 represents the dynamic viscosity of water, ICON® and 20%, 30%wt BrM and 40%wt SnM in ICON® resin by flowing the materials through the Pasteur pipette. In the current study, the viscosity of water was 0.8mPa.s. The 20wt% BrM and 40wt% SnM in ICON® resin had a viscosity lower than ICON® resin, whereas 30wt% BrM in ICON® resin had a higher viscosity compared to the ICON® resin. The viscosities of the resins were all less than 32mPa.s. The difference in viscosity between ICON® and experimental radiopaque resins was statistically significant (*p* value< 0.05).

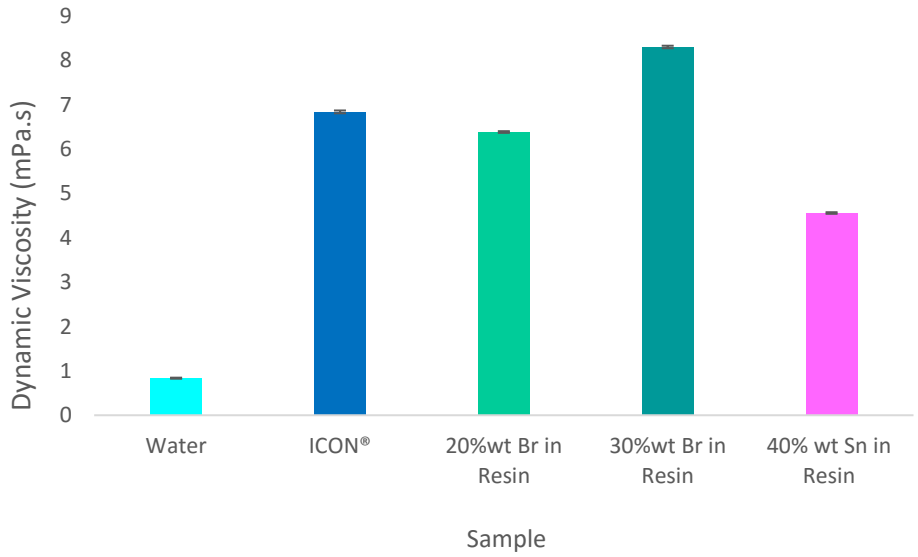

Figure 9.8 A bar graph presenting the mean dynamic viscosity with relevant standard error bar for water, ICON®, 20%, 30%wt BrM and 40%wt SnM in resin at 25 ℃ ± 1℃.

9.5.2 Contact Angle

All samples showed a contact angle less than 90° on the glass slab. Among all experimental samples, the mixtures including 30wt% bromine-methacrylate in ICON® resin and 40wt% tin-methacrylate in ICON® resin showed the lowest contact angles, which were even less than the water (Figure 9.9).

There was a statistically significant decrease in contact angle from 10s to 180s on all experimental radiopaque and ICON® resins. The reduction in contact angle was statistically significant between the different time points except for 30wt% bromine-methacrylate in ICON® resin between 60s and 120s. Furthermore, there was no significant reduction in contact angle measurements for water after 60s (Table 9.2). The contact angles of the experimental resins were significant lower than that for ICON® ($p<0.5$).

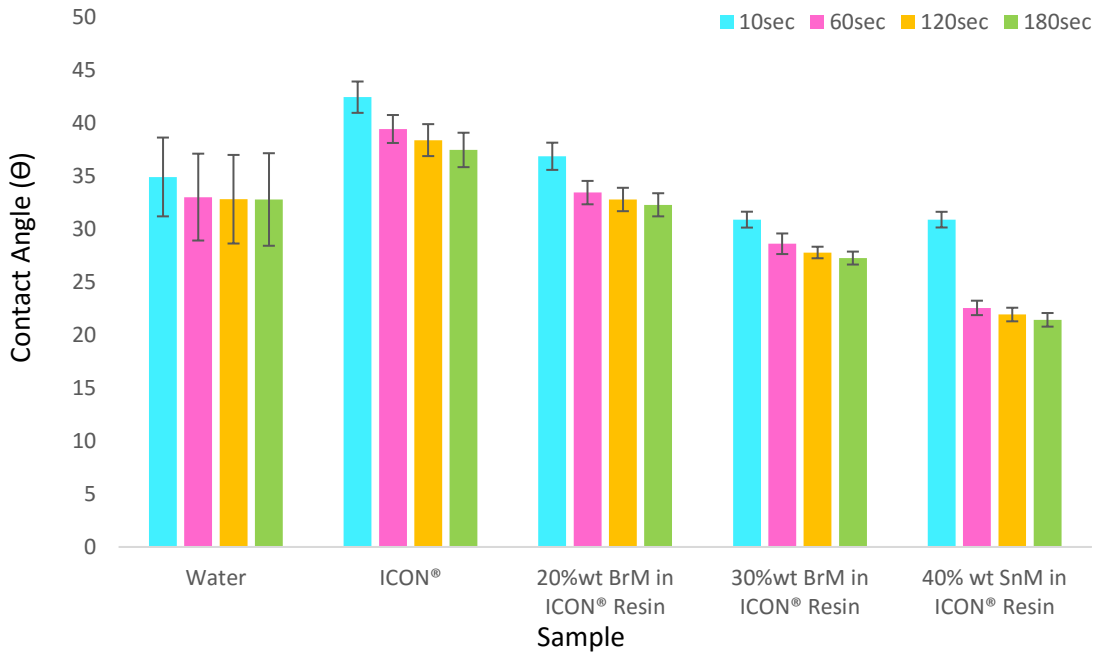

Figure 9.9 A bar graph presenting the mean of contact angles with the relevant standard error bars for water, ICON®, 20%, 30%wt BrM and 40%wt SnM in resin on the glass slab for 10, 60, 120 and 180s.

Table 9.2 Showing p-value (paired t-test) comparing the contact angle between different time points for the different samples. *p* value <0.05 was considered to be statistically significant different insignificant.

	Water	ICON®	20%wt BrM in ICON® Resin	30%wt BrM in ICON® Resin	40%wt SnM in ICON® Resin
10 to 60s	<0.05	<0.001	<0.001	<0.05	<0.001
10 to 120s	<0.05	<0.001	<0.001	<0.05	<0.001
10 to 180s	<0.05	<0.001	<0.001	<0.05	<0.001
60 to 120s	0.16	<0.05	<0.05	0.11	<0.05
60 to 180s	0.35	<0.05	<0.05	0.06	<0.001
120 to 180s	0.84	<0.05	<0.05	<0.05	<0.001

9.6 Discussion

The resins in this study had viscosities in the range of 4-8mPa.s. 20wt% BrM and 40wt% SnM incorporation in ICON® resin had a lower dynamic viscosity in comparison with ICON® resin. The viscosity increased with higher wt% of BrM. Previous research (Paris *et al*. 2007) showed that mixtures containing high amounts 2-hydroxyethyl methacrylate (HEMA), triethylene glycol dimethacrylate (TEGDMA), and ethanol, had higher penetration coefficients (PCs) compared to the five other commercially available adhesives and a fissure sealant in their study. They revealed that the viscosity range between 3.2mPa.s (80%HEMA and 20% ethanol) and 6637 mPa.s (100% bis-glycidyl dimethacrylate) for commercially available and experimental composites (Paris *et al.* 2007). Paris and colleagues (Paris *et al.* 2007) measured the penetration coefficient (PC) of different experimental resins and predicted their infiltration ability by using the Washburn equation. Since the cosine of contact angle is part of the calculation of PC, its role is negligible. In other words, for the same surface tension, a lower dynamic viscosity means a higher PC value. Furthermore, they stated that the greater penetration coefficient, the faster the liquid penetrates into the pores; therefore, we expect that radiopaque resins

including 20wt% BrM or 40wt% SnM with a lower dynamic viscosity compared to ICON® resin have a higher PC and a faster penetration into the pores in comparison with ICON® resin. Moreover, other studies on sealants showed that low viscosity sealants had deeper penetration ability, especially, when they were applied on etched enamel (O'Brien and Ryge 1965; Irinoda *et al.* 2000).

In the present study, the viscosity and contact angle of the experimental materials are considered as strong indicators of flow rate, wettability and predicting factors for resin infiltration in porous early enamel caries; however, the Washburn equation was not used in the current study for the following reasons: 1) it is crucial to know that the pores are assumed open-ended in Washburn equation, whereas the pores in early enamel caries are close-ended towards the sound tooth structure. This leads to trapped air, water and other organic materials such as proteins in the pore structure of the early enamel caries lesions, in particular at the bottom of the lesion; 2) the Washburn equation presents the strong link between the liquid penetration and interface factors. The solid surface contamination with organic agents can affect the interface parameters such as surface tension. Therefore, saliva components and food debris are considered as main contamination agents on natural enamel lesions (Silverstone 1973; Asmussen 1977).

- ***Dynamic Viscosity***

A basic method was used to measure the flow of the samples, by means of the Pasteur pipette. The dynamic viscosity of water was measured as its value can be used as a documented standard. Therefore, it is able to validate our findings and check the validity of the method in this study. The dynamic viscosity of water measured was 0.8mPa.s, while the value in literature was 0.89 mPa.s (Kestin *et al.* 1978). Moreover, the data from the experiment was reproducible. A viscometer was not used because there was a possibility that the test materials could polymerise and set inside the tube. Paris and his colleagues (2007) used a computed based device to measure the viscosity of experimental and commercially available resins and they claimed that this technique led to a low standard deviation (Paris *et al*.

2007). The standard deviation in their study was in the range of 0-9.7 whereas the value in the present measurements was in the range of 0.01-0.03.

- ***Contact Angle***

The contact angles of all the resins were less than 90° and can be considered as hydrophilic. There was a decrease in contact angle by incorporation of either BrM or SnM. Moreover, the contact angle of both BrM and SnM in ICON® resin was lower than ICON®. It assumes that this might be due to weaker inter-molecular forces in BrM and SnM in ICON® resin in comparison with ICON® resin only. In other words, a weaker inter-molecular force leads to an increase in the liquid flow and a decrease in the contact angle.

In this study, the contact angle for the experimental resins varied between 30.8° and 36.8° and between 21.4° and 32.2° at 10s and 180s, respectively, while the previous study showed a high variation in contact angles ranging between 3.2° and 54.2° for their commercially available and experimental resins (Paris *et al*. 2007). However, they did not mentioned the time point of measurement. In the current study, the contact angle for the experimental resins measured at different time points including 10s, 60s, 120s and 180s. 180s is the time to cure the resin with the blue light in clinical application based on manufacturer's instruction. The present findings showed a statistically significant difference in reduction of the contact angle over this period in all different types of resin. It is interesting that there was an insignificant reduction between 60s and 120s for 30wt% BrM in ICON® resin followed by a significant decrease between 60s and 180s and between 120s and 180s. This might be due to changes in intermolecular forces for 30wt% BrM in ICON® after 120s. The present data showed contact angles less than 90°, which means that all the materials are hydrophilic with a good wettability. All experimental radiopaque resins had a smaller contact angle compared to ICON® resin and among these materials, 40wt% tin-methacrylate in ICON® resin showed the lowest value.

This study showed that the contact angle decreased over the period of time for all the experimental resins. This may be due to the reorientation of molecules at the interface (Dettre and Johnson Jr 1964).

In the present study, a clean glass slab was used to measure the contact angle in order to obtain a reproducible data, whereas Paris and colleagues used disks of polished bovine incisor enamel to determine the contact angle (Paris *et al*. 2007). It is assumed that the data from the former study is less reproducible due to the possible differences among polished bovine incisor enamel samples. Although we cannot compare our findings with the results of the previous study by Paris, ICON® resin was used as a control in this study and the data from the other resin compositions would be comparable with ICON® resin. However, the results might differ for the human enamel. It is difficult to have a large and flat area of human enamel in order to measure the contact angle and it is not feasible to measure the contact angle inside the pores structure directly. It should be mentioned that a machinable glass-ceramic-Macor® might be considered as the standardised enamel analogue target substrate (Paolinelis *et al*. 2009). However, it might not stimulate the white spot lesion as it is non-wetting and exhibits zero porosity (Dabnun *et al.* 2005).

9.7 Conclusion

The following null hypotheses were rejected:

- There is no significant statistical difference among the experimental radiopaque and ICON® resins' dynamic viscosities.
- There is no significant statistical difference among the experimental radiopaque and ICON® resins' contact angles.
- There is no significant statistical changes in experimental radiopaque or ICON® resins' contact angles with time.

All experimental radiopaque resins in the current study, except 30wt% BrM in ICON® resin, had lower viscosities and they all showed a smaller contact angles (high wettability) compared to ICON®. Hence, it is expected that they infiltrate to WSLs like ICON® if not better. Furthermore, it would be advisable to wait for 180 seconds before light curing for better penetration as the contact angles decrease further with time.

Chapter 10- Experimental Radiopaque Resins (Infiltration Ability in Natural White Spot Lesions)

10.1 Introduction

As mentioned in previous chapters, it is desirable, and probably essential, to have a radiopaque infiltrant resin. The conclusion from the above work was to incorporate radiopaque monomer in the ICON® resins. Hence, this chapter's main aim was to investigate whether the novel radiopaque resins could infiltrate and increase the radiopacities of white spot lesions (WSLs). Apart from using clinical radiography, X-ray microtomography was used to quantify the change of radiopacities.

10.1.1 X-ray microtomography (XMT)

The X-ray attenuation coefficient is a measure of how easily an X-ray beam can penetrate through an object (Section 5.1). When an X-ray beam passes through an object, depending on the object's composition and density, it can be transmitted, absorbed or scattered. The ratio of transmitted photons to the incident number of photons forms the basis of the attenuation coefficient. If the X-ray is measured using a detector, the attenuation coefficients can be converted into a grey-scale image (Swain and Xue 2009). As the two dimensional (2D) image suffers from ambiguity from the superimposition of structures, Allan Cormack and Godfrey Hounsfield developed a three-dimension (3D) imaging system, named computed tomography (CT), in the early 1970s, to provide more precise diagnostic and treatment aids for internal structures. CT is based on using X-rays to image a sliced plane of a specimen at different angles and then reconstruct the slices using a mathematical algorithm. Hence, tomography is effectively a method of cutting a specimen into slices by X-ray, in order to display the internal structures of the specimen. When these slices are stacked together, a 3D reconstruction of the object can be visualised (Ahmed *et al.* 2012).

In the early 1980s, Elliot *et al* introduced X-ray microtomography (XMT) as a miniaturised form (in micron resolution) of CT. Like CT, XMT is a non-destructive method, which is able to review the internal structure and therefore, a number of repeated scans for the same sample (Elliott and Dover 1982).

There are three main components in XMT structure including an X-ray source, a detector and sample manipulators (Figure 10.1). The X-ray source and detector are

usually fixed while the specimen rotates during the exposure time (Mizutani and Suzuki 2012).

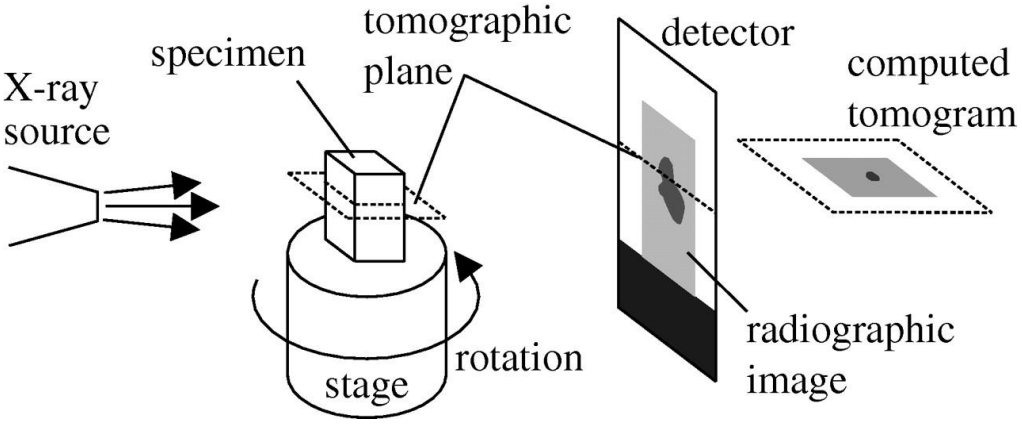

Figure 10.1 Schematic drawing of axial computed micro-tomography (Sutton 2008).

The image obtained from CT scanner can have artefacts. The two main issues are caused by polychromatic radiation (causing dishing artefacts) and uneven performance of the detector (causing ring artefacts). The MuCat XMT scanner at Queen Mary University of London was developed using time-delay integration readout in order to minimise the ring artefact, and polychromatic calibration using a number of samples (Davis *et al.* 2013). Hence a high signal to noise ratio (SNR) and a high contrast image can be achieved.

XMT is an interest for researchers in dentistry-related studies as follows:

- X-ray microtomography of bones and teeth (Davis and Wong 1996),
- Analysis of root canal morphology (Peters *et al.* 2000),
- Generation of 3D finite element models of restored human teeth using micro-CT techniques (Nly and Orm 2001),
- X-ray microtomographic study of mineral concentration distribution in deciduous enamel (Wong *et al.* 2004),

- Enamel thickness measurement (Smith *et al.* 2006),
- Mineral concentration of natural human teeth by a commercial micro-CT (Clementino-luedemann and Kunzelmann 2006),
- Dentinal carious lesion in three dimensions (Wong *et al.* 2006),
- An X-ray microtomography study on the mineral concentration of carious dentine removed during cavity preparation in deciduous molars (Willmott *et al.* 2007)
- Efficient 3D finite element analysis of dental restorative procedures using micro-CT data (Magne 2007),
- Construction of three-dimensional tooth model by micro-computed tomography and application for data sharing (Kato and Ohno 2009),
- X-ray microtomography study to validate the efficacies of caries removal in primary molars by hand excavation and chemo-mechanical technique (Ahmed *et al.* 2012).

Since XMT requires extremely high radiation doses and long scan times, its application is limited to in-vitro studies (Davis and Wong 1996). However, researchers have used XMT to study the morphology and even function of small animals in-vivo (Nesteruk and Wiśniewski). It should be mentioned that XMT have some advantages compared to the conventional techniques including:

- It is non-destructive, as there is no need to cut the sample and the original structure of the specimen can be maintained. This allows them to be scanned and investigated in further studies (Davis *et al.* 2013);
- The resolution of 3D images by XMT is either micron or even nano-metre resolution under same circumstances. Therefore, highly mineralised tissues such as teeth and bone can be examined and presented clearly;
- XMT is a promising technique in order to study soft tissues by infiltration of a contrasting agent to provide a higher density in area of interest in comparison with the adjacent structures (Momose *et al*. 1996).

In the current study, XMT was used to investigate the relative radiopacity and infiltration ability of experimental radiopaque reins in natural WSLs due to the mentioned benefits.

10.2 Aims and objectives

The aims of this part of the study were:

- To investigate whether the experimental radiopaque resins penetrate into natural WSLs;
- To measure the penetration depth of the radiopaque resins;
- To investigate and quantify the change of radiopacities of the WSL after application of the novel resin, both in 2- and 3-dimensions.

10.3 Null Hypothesis

- There is no statistical significant differences ($p \geq 0.05$) in the linear attenuation coefficients of the natural white spot lesions before and after infiltration with the experimental radiopaque infiltrants.

10.4 Materials and Methods

10.4.1 Sample selection

The criteria used to select the teeth with early enamel carious lesion, suitable for the use of infiltrant resins, was based on the indications set by the manufacture as follows:

- Any filled surfaces were excluded,
- The early enamel caries was on proximal surfaces of the permanent posterior teeth (premolar and molars),
- The clinical appearance of the lesion shows the demarcated white-creamy to yellow-brownish colour under a good light when the tooth is dried,
- The caries lesion is non-cavitated,

- The digital radiograph showed radiolucency of the lesion up to the outer third of the dentine.

Extracted premolar and molar teeth from the Royal London Hospital tooth bank (approval from Queen Mary Research Ethics Committee QMREC 2011/99) stored in 70% ethanol (Sigma-Aldrich, Gillingham, UK) were examined visually for white spot lesion in proximal surfaces by the current investigators. The examination was carried out by cleaning the tooth by bristle brush (Henry Schein, London, UK) and slow handpiece (NSK Ltd, Stevenage, UK), drying the tooth with compressed air, and using a good light (A-dec 6300 Light Bulb 17V, 95W, Mercia Dental, UK). Digital radiographs were taken from the buccal surface of each of the selected teeth. The tube distance was 45cm perpendicular to the long axis of the tooth, and the exposure time was 0.5ms at 70 kV and 8 mA. The radiographic lesion depth was evaluated with magnification in the dark room on the computer screen and teeth with scores E1, E2 and D1 (Table 10.1) were selected for the experiments. Out of 14 selected teeth by clinical examination, six teeth met the selection criteria by radiographic examination.

Table 10.1 Radiolucency scores based on radiographic lesion depth (modified from (Ricketts *et al*. 2002).

Radiolucency score	**Radiographic lesion depth**
R0	No radiolucency
E1	To the outer half of enamel
E2	To the inner half of enamel
D1	To the outer third of dentine
D2	Between the outer third and inner third of dentine
D3	To the inner third of dentine

The six teeth were divided into three groups randomly. The lesions in each group were infiltrated with three types of experimental resin randomly (Table 10.2). Clinical photos, digital X-rays and XMT scans were taken before and after the application of radiopaque resins. All samples were stored in 0.9% sodium hypochlorite (NaOCl) solution containing 0.01% thymol (to inhibit the bacterial growth and mould) between the experiments.

Table 10.2 Teeth allocation for experimental resin infiltration with the radiolucency scores in bracket.

Experimental Resin	Tooth Notation (Lesion score)
20wt% Bromine-methacrylate+ ICON®	Br20A(E1), Br20B(E2)
30wt% Bromine-methacrylate+ ICON®	Br30A(E2), Br30B(E2)
40wt% Tin-methacrylate+ ICON®	Sn40A(E1), Sn40B(E1)

10.4.2 Clinical photographs

Photos for each sample were taken before and after application of the experimental resins. All photos were taken by iPhone6 with no use of flash while other automatic settings of the camera were off. Each tooth was stabilised on the black cupboard with the Blu-Tack in a flat horizontal position, parallel to the flat surface of the bench with WSL facing upwards. The lens of camera to the background distance was 30cm perpendicular to the long axis of the tooth. Clinical photographs were taken from the sample before and after the application of the experimental resins.

10.4.3 Digital radiographs

Each tooth was stabilised on the digital sensor with the Blu-Tack in a flat horizontal position, parallel to the flat surface of the bench with buccal surface facing upwards. An X- ray machine (CEI, Bologna, Italy), set at 70kV and 8mA with an exposure time for 0.5ms was used. The tube to sensor distance was 45cm perpendicular to the

long axis of the tooth. Digital radiographs were taken from the sample before and after the application of the experimental resins.

10.4.4 X-ray microtomography (XMT)

Each tooth was inserted into a tube and stabilised with wax. Three quarters of the tube was filled with distilled water and 0.01% thymol. The scanning system was 4th generation MuCAT2 XMT with TDI CCD camera readout aiming at eliminating ring artefacts. The X-ray source was a laboratory system (Ultrafocus HMX 225, X-Tek system Ltd., YK, 5mm source, tungsten target, 225kV max.). Each sample was scanned using an accelerating potential of 75kV and the current of 0.215 mA (Davis *et al.* 2013). 1125 projections were taken in each complete scan, which took approximately 24 hours.

10.4.5 Application of the experimental resin

After the pre-treatment photos, digital radiographs and XMT scans were taken, the resins with different compositions were applied to the allocated teeth as follows:

- The surface of the tooth was cleaned by bristle brush (Henry Schein, London, UK) and slow handpiece (NSK Ltd, Stevenage, UK);
- ICON®-etch was applied for 2 minutes on the white spot lesion using an etch applicator;
- The etch was rinsed off with water for 30 seconds and dried with water-free and oil-free air for 15 seconds;
- ICON®-dry was applied for 30 seconds and then dried with oil-free air;
- The experimental resins was applied on the surface using a micro-brush (Dental Directory, UK) and waiting for 3 minutes and cured by a blue LED activation light at 400 mW/cm^2 for 40s (Demetron LC, Ser no 66004022, KERR corporation, Danbury) in direct contact of the lesion;
- The second layer of experimental resins was applied on the surface for 1minute and cured by a blue LED activation light at 400 mW/cm^2 for 40s (Demetron LC, Ser no 66004022, KERR corporation, Danbury) in direct contact of the lesion.

10.4.6 Data Analysis

- ***Photographs***

They were examined independently by eight examiners to assess visually whether there were visible changes before and after infiltrations.

- ***Digital radiographs***

They were:

  - examined on a computer screen in a dark room and assessed qualitatively by the same eight examiners for any change of radiopacity before and after infiltration;

  - analysed quantitively using Image J™ (Image Processing and Analysis in Java, National Institute of Health, Bethesda, Maryland, USA). After importing the digital radiograph files into Image J, a line profile was drawn through the middle of the lesion in the displayed image of the lesions before and after infiltrations in the same location. The grey level values along that line were extracted and compared before and after infiltrations.

- ***XMT***

The following softwares are useful to describe the XMT images:

  - Tomview software

The purpose of Tomview is to view images of samples scanned with MuCAT XMT facility at Queen Mary University of London. It provides 2D slices in different planes, XY, XZ and YZ. In other words, it generates images in bucco-lingual, mesio-distal and corono-apical profiles. Furthermore, the specific points with red dots allow finding these points easily when moving through slices.

  - Tomalign software

In the current study, the XMT data taken, before and after infiltrations, were aligned using a house software “Tomalign” as it was nearly impossible to relocate the tooth exactly after manipulation. The software allowed 7 degrees of freedom: x, y and z offsets, x, y, and z rotation and scale for the alignment. The processed data could

be viewed in three orthogonal views with different colours; green for pre-scans, red for post-scans, and yellow for overlapping each other. It is feasible to adjust the offsets, rotation and scale manually prior the automatically alignment. After alignment, the pre-infiltration data were subtracted from the post-infiltration data to create a third data set which was used for reconstruction to show the differences. The XMT data were used to assess the changes of LAC values after infiltrations and the depth of the resin infiltration.

Both pre- and post-infiltration XMT images were imported into Image J™ (Image Processing and Analysis in Java, National Institute of Health, Bethesda, Maryland, USA). Each 10th XMT slice was used from the beginning to the end of the lesions. For each XMT slices, 3 lines were drawn: one in the middle of the lesion, two adjacent lines at half the distance between the first central line and the margins of the lesions on either side. The linear attenuation coefficient (LAC) values for all the lines were used to calculate the means and compare the changes before and after infiltrations. Student's paired t-test was used and $p<0.05$ was regarded as statistically different.

The lesion depth (LD) was defined as the distance from the surface of enamel to the end of the radiolucency on pre-infiltration XMT images. The penetration depth (PD) was defined as the distance from the surface of enamel to where the infiltrated material ended in the subtracted XMT images. The measurements were taken along the lines that were drawn for the LAC measurements as described above. The penetration potential (PP) was expressed as a percentage of the PD to LD for each tooth.

An example of data can be found in Appendix C.

10.5 Results

10.5.1 Photographs

The photographs of the lesions before and after resin application are shown in Figures 10.2-10.7. All examiners agreed that the colour of the early enamel caries changed from a yellow-brownish colour to a less yellowish colour after application

of the radiopaque resins containing 20wt% and 30wt% BrM (Table 10.3 and 10.4). However, there was no agreement among examiners on colour changes for lesions that were infiltrated with the resin containing 40wt% of SnM (Table 10.5).

10.5.2 Digital radiographs

The radiographs of lesions are shown in Figures 10.2-10.7. The detection of changes on the radiographs by eight examiners is shown in Tables 10.3-10.5. There was no consistent agreement among the examiners whether they could detect the changes. However, more examiners reported that they could detect changes in lesions after application of resins containing BrM than SnM.

The mean grey values measured by Image J™, along the line profiles on digital radiographs for each tooth lesion before and after applications of resins containing different radiopaque agents are shown in Figure 10.8. Apart from Br20A, there was a consistent increase in grey value (representing radiopacity) after application of resins.

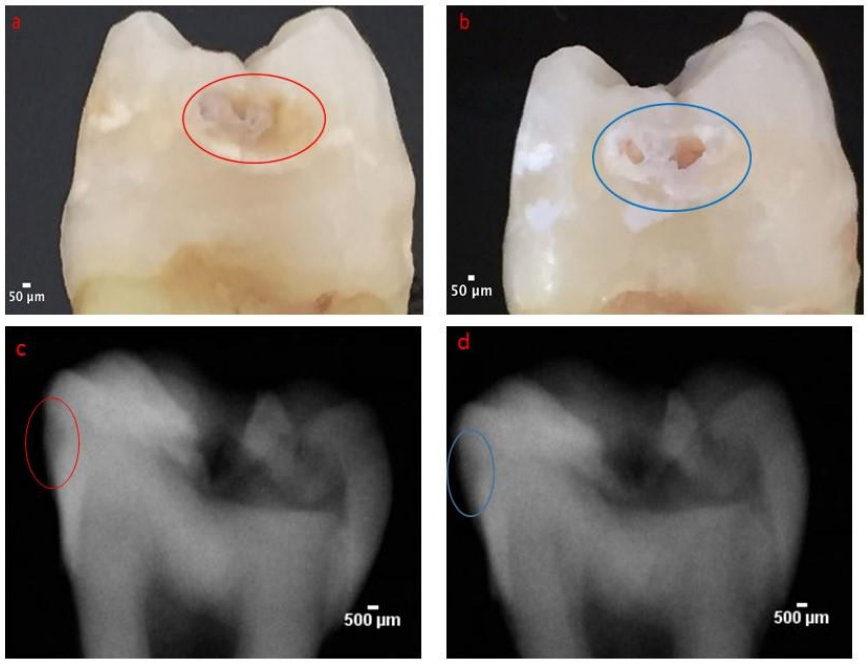

Figure 10.2 Photographs of white spot lesion for tooth Br20A before (a) and after (b) application of the resin containing 20w% BrM in ICON®. Corresponding radiographs are shown in (c) and (d), respectively. The circles show the lesion of interest.

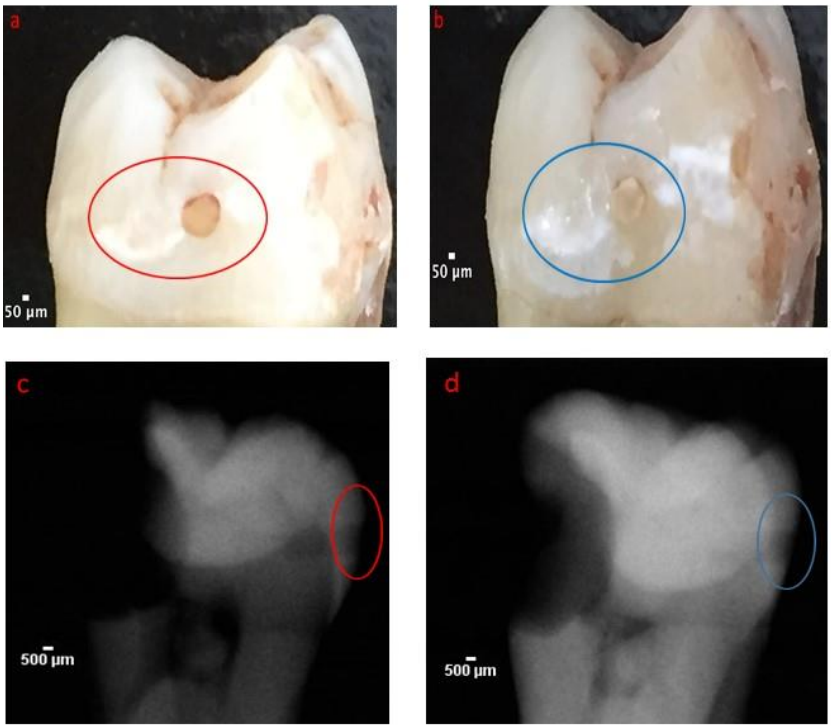

Figure 10.3 Photographs of white spot lesion for tooth Br20B before (a) and after (b) application of the resin containing 20w% BrM in ICON®. Corresponding radiographs are shown in (c) and (d), respectively. The circles show the lesion of interest.

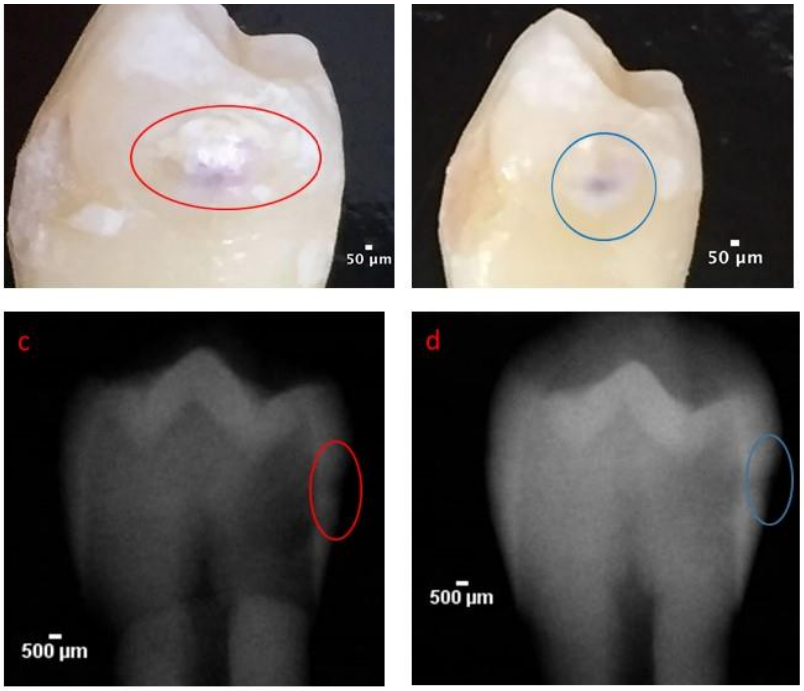

Figure 10.4 Photographs of white spot lesion for tooth Br30A before (a) and after (b) application of the resin containing 30w% BrM in ICON®. Corresponding radiographs are shown in (c) and (d), respectively. The circles show the lesion of interest.

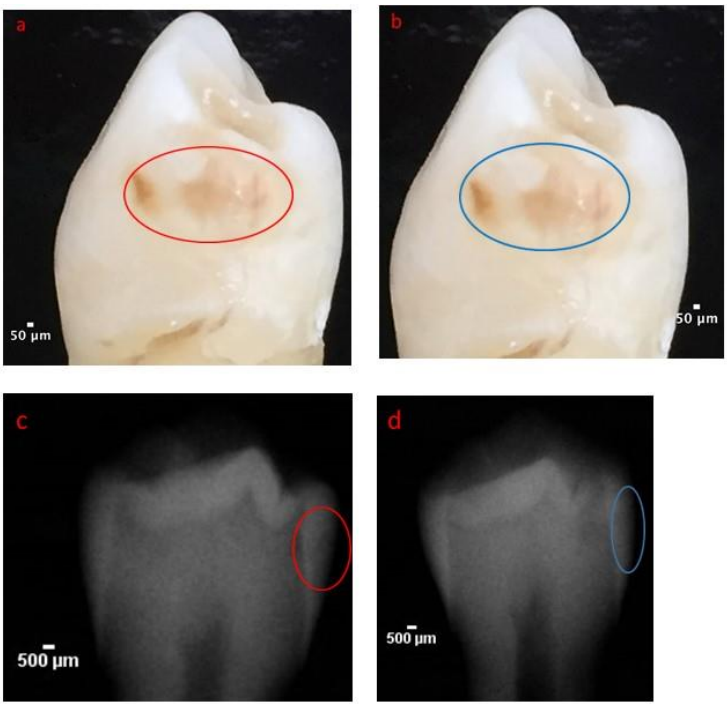

Figure 10.5 Photographs of white spot lesion for tooth Br30B before (a) and after (b) application of the resin containing 30w% BrM in ICON®. Corresponding radiographs are shown in (c) and (d), respectively. The circles show the lesion of interest.

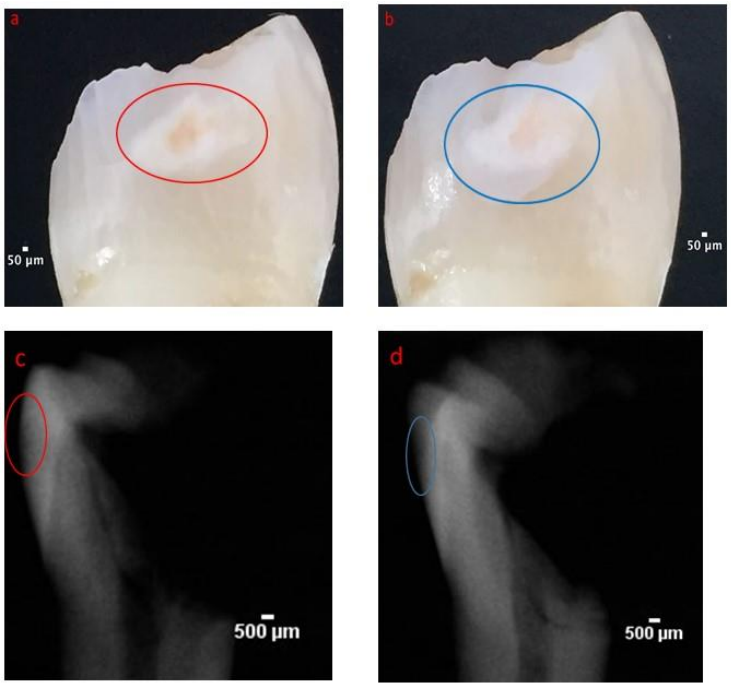

Figure 10.6 Photographs of white spot lesion for tooth Sn40A before (a) and after (b) application of the resin containing 40w% SnM in ICON®. Corresponding radiographs are shown in (c) and (d), respectively. The circles show the lesion of interest.

Figure 10.7 Photographs of white spot lesion for tooth Sn40B before (a) and after (b) application of the resin containing 40w% SnM in ICON®. Corresponding radiographs are shown in (c) and (d), respectively. The circles show the lesion of interest.

Table 10.3 Qualitative assessment of photographs and digital radiographs for samples Br20A and Br20B. (+) represents a less yellowish colour (photographs) or more radiopacity (radiographs). (-) represent an absence of a change in the lesions' colour (photographs) and radiolucency (radiographs).

	Sample- Br20A		**Sample- Br20B**	
	Clinical Photo	**Digital X-ray**	**Clinical Photo**	**Digital X-ray**
Examiner-1	+	+	+	+
Examiner-2	+	+	+	+
Examiner-3	+	-	+	+
Examiner-4	+	-	+	-
Examiner-5	+	-	+	-
Examiner-6	+	-	+	-
Examiner-7	+	+	+	+
Examiner-8	+	-	+	-

Table 10.4 Qualitative assessment of photographs and digital radiographs for samples Br30A and Br30B. (+) represents a less yellowish colour (photographs) or more radiopacity (radiographs). (-) represent an absence of a change in the lesions' colour (photographs) and radiolucency (radiographs).

	Sample- Br30A		**Sample- Br30B**	
	Clinical Photo	**Digital X-ray**	**Clinical Photo**	**Digital X-ray**
Examiner-1	+	+	+	+
Examiner-2	+	-	+	-
Examiner-3	+	+	+	-
Examiner-4	+	+	+	-
Examiner-5	+	-	+	-
Examiner-6	+	+	+	-
Examiner-7	+	-	+	+
Examiner-8	+	-	+	_

Table 10.5 Qualitative assessment of photographs and digital radiographs for samples Sn40A and Sn40B. (+) represents a less yellowish colour (photographs) or more radiopacity (radiographs). (-) represent an absence of a change in the lesions' colour (photographs) and radiolucency (radiographs).

	Sample- Sn40A		Sample- Sn40B	
	Clinical Photo	**Digital X-ray**	**Clinical Photo**	**Digital X-ray**
Examiner-1	+	+	+	-
Examiner-2	+	-	+	+
Examiner-3	_	-	-	-
Examiner-4	_	-	-	-
Examiner-5	+	-	-	-
Examiner-6	-	-	-	+
Examiner-7	-	+	+	-
Examiner-8	-	-	-	-

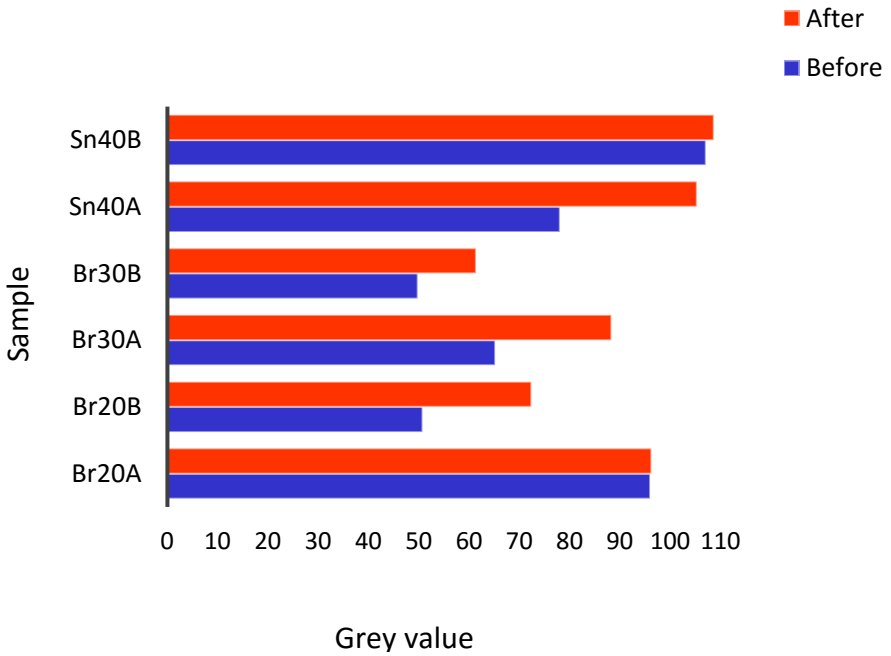

Figure 10.8 Bar charts showing the mean grey level along the line profile for each lesion before and after the application of resin.

10.5.3 X-ray microtomography (XMT)

The XMT images for the six teeth about the middle of the lesions are shown in Figures 10.9-10.14. Visually, it was difficult to detect differences before (e.g. Figure 10.9a) and after (e.g. Figure 10.9b) infiltration. However, in the subtracted images, when the contrast was adjusted (e.g. Figure 10.9c), materials with higher grey values could be detected in the lesions that were infiltrated with resin containing BrM or SnM.

The difference in LAC values along the three lines through the lesions are summarised in Figures 10.15-10.17. In all the measured regions, the LAC values were statistically higher after resin infiltration. The percentage of increase ranged from -0.07% to 7.04% (Table 10.6). There was no consistent pattern to support any type of experimental radiopaque resins with regard to the increase in radiopacities.

The penetrations of radiopaque resins are shown in Figures 10.18 to 10.20 and table 10.7. It ranged from 70.2 to 97% of depth of the lesion. Generally, the SnM had better penetration than BrM. However, there were variations of penetrations even within the same lesions. For example, the penetration along line 3 in Br30A was nearly half of that for line 2.

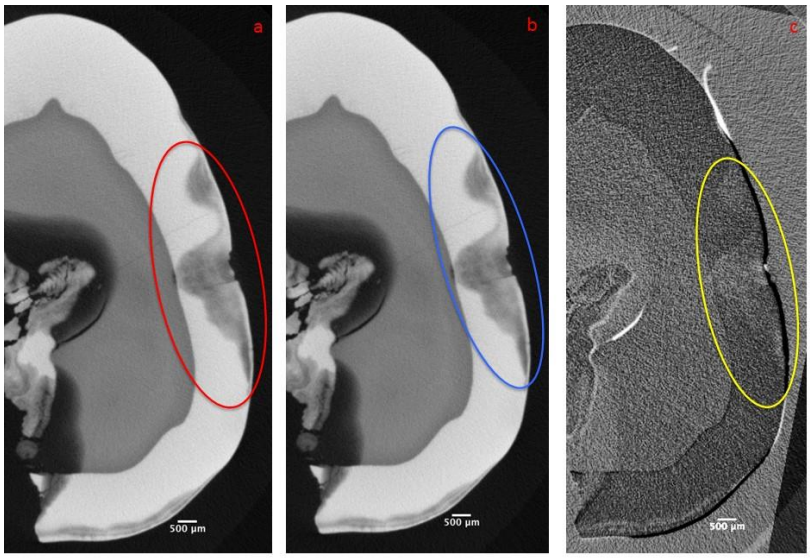

Figure 10.9 XMT images of Br20A: (a) before, (b) after infiltration. (c) Subtracted XMT image (contrast adjusted) showing the higher grey values (an indication of infiltrated radiopaque material in the lesion). The circles show the lesion.

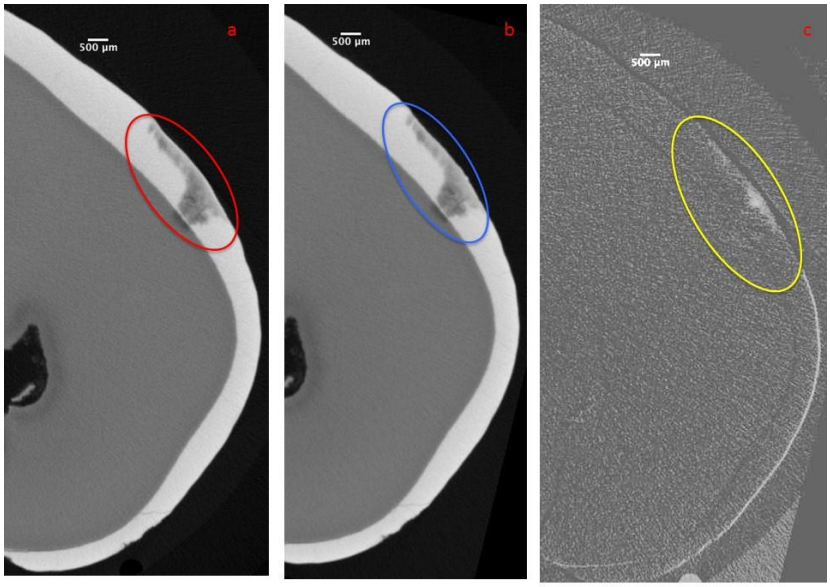

Figure 10.10 XMT images of Br20B: (a) before, (b) after infiltration. (c) Subtracted XMT image (contrast adjusted) showing the higher grey values (an indication of infiltrated radiopaque material in the lesion). The circles show the lesion.

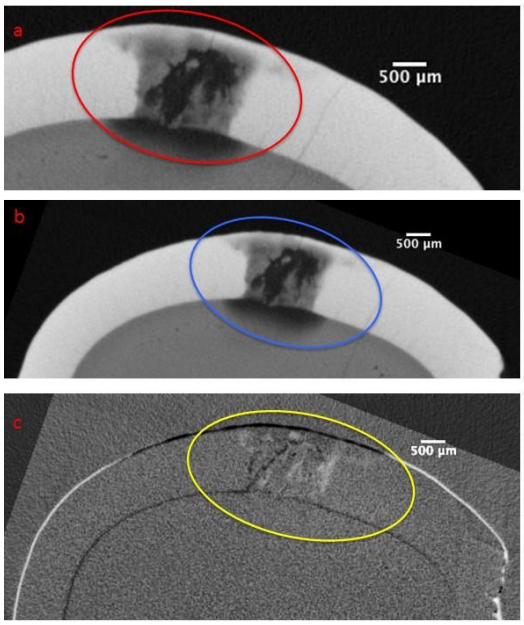

Figure 10.11 XMT images of Br30A: (a) before, (b) after infiltration. (c) Subtracted XMT image (contrast adjusted) showing the higher grey values (an indication of infiltrated radiopaque material in the lesion). The circles show the lesion.

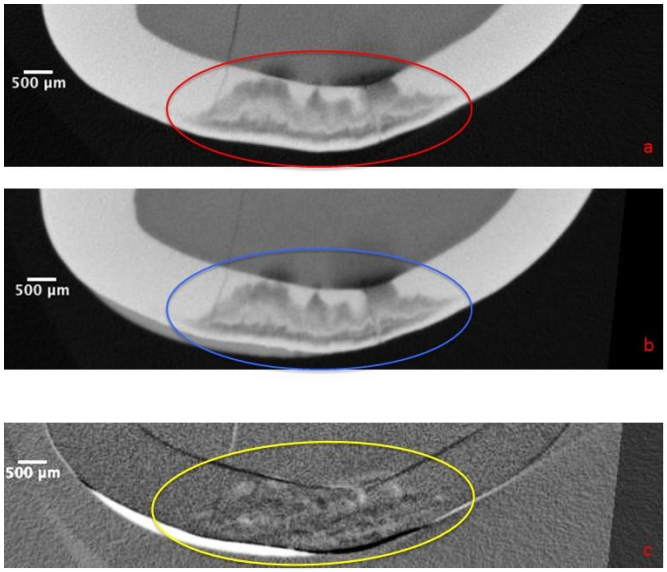

Figure 10.12 XMT images of Br30B: (a) before, (b) after infiltration. (c) Subtracted XMT image (contrast adjusted) showing the higher grey values (an indication of infiltrated radiopaque material in the lesion). The circles show the lesion.

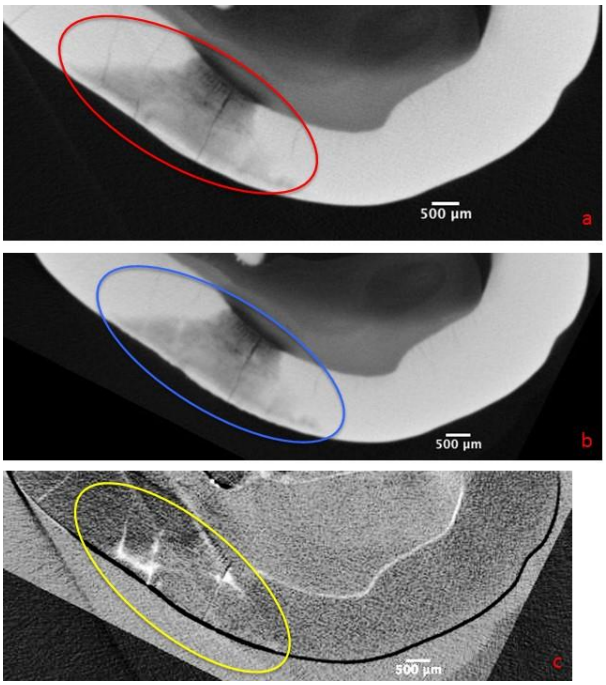

Figure 10.13 XMT images of Sn40A: (a) before, (b) after infiltration. (c) Subtracted XMT image (contrast adjusted) showing the higher grey values (an indication of infiltrated radiopaque material in the lesion). The circles show the lesion.

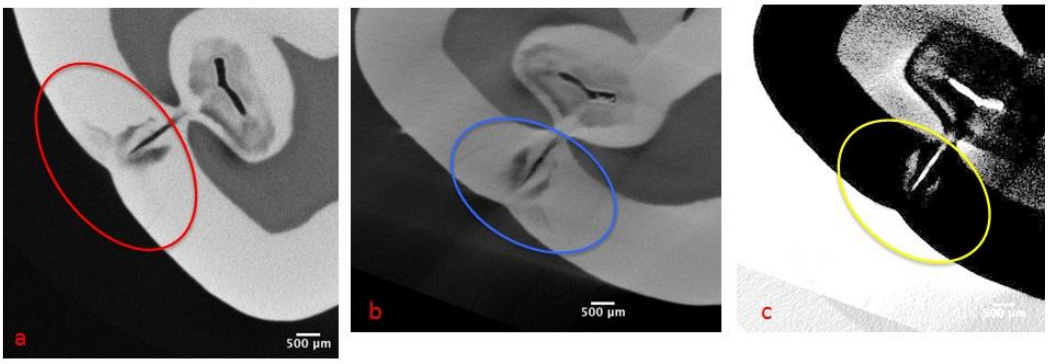

Figure 10.14 XMT images of Sn40B: (a) before, (b) after infiltration. (c) Subtracted XMT image (contrast adjusted) showing the higher grey values (an indication of infiltrated radiopaque material in the lesion). The circles show the lesion.

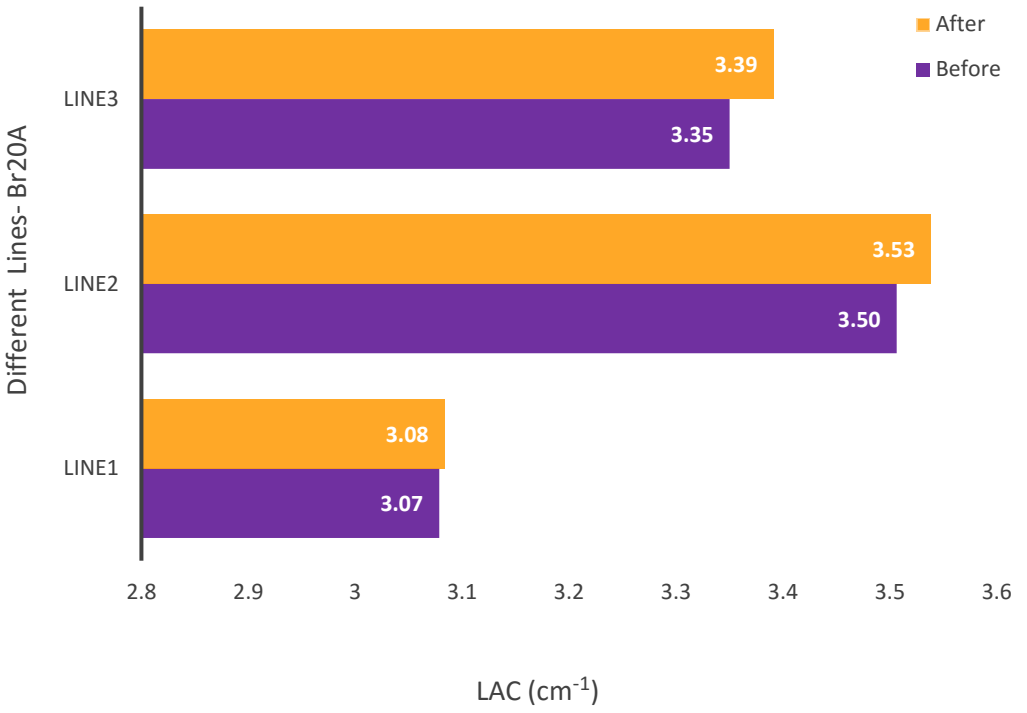

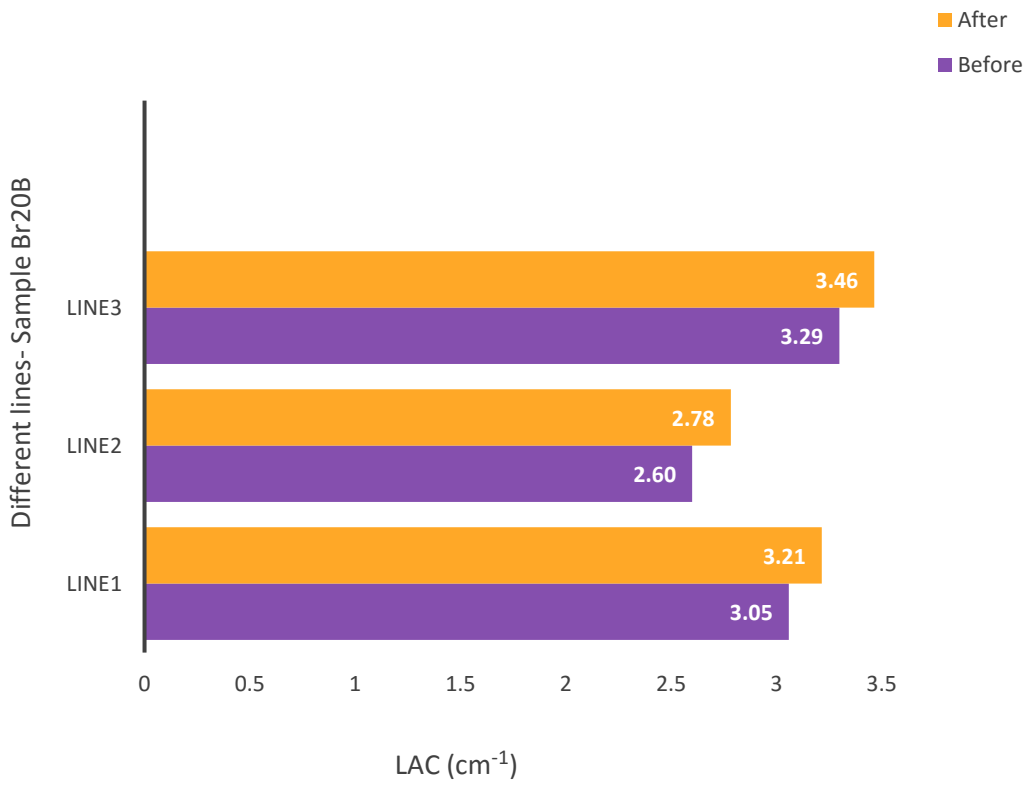

Figure 10.15 The graphs present the mean LAC values in three different areas of lesions on XMT images taken from sample Br20A and Br20B and compared the values pre- and post-application of the 20w% BrM in ICON® resin.

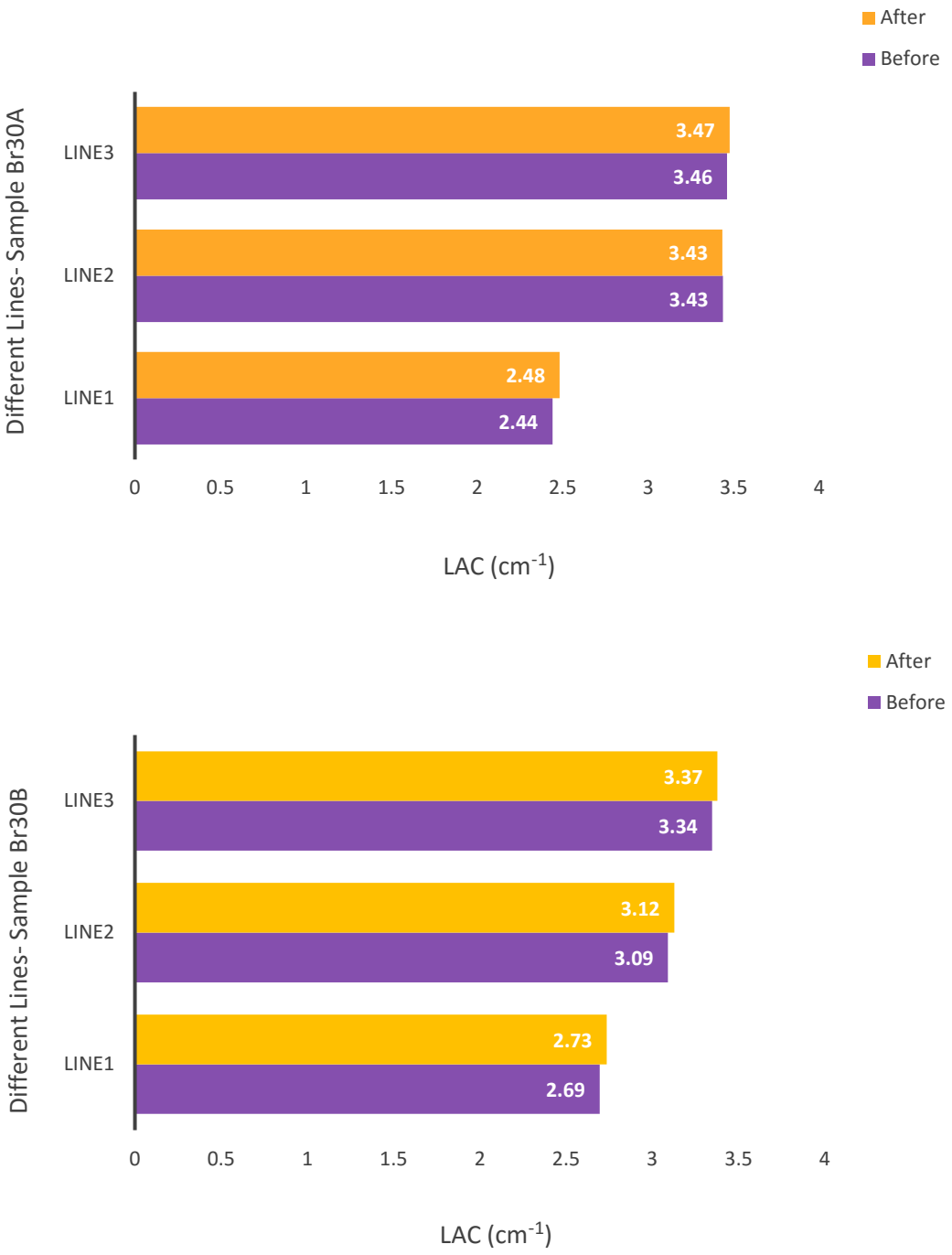

Figure 10.16 The graphs present the mean LAC values in three different areas of lesions on XMT images taken from sample Br30A and Br30B and compared the values pre- and post-application of the 30w% BrM in ICON® resin.

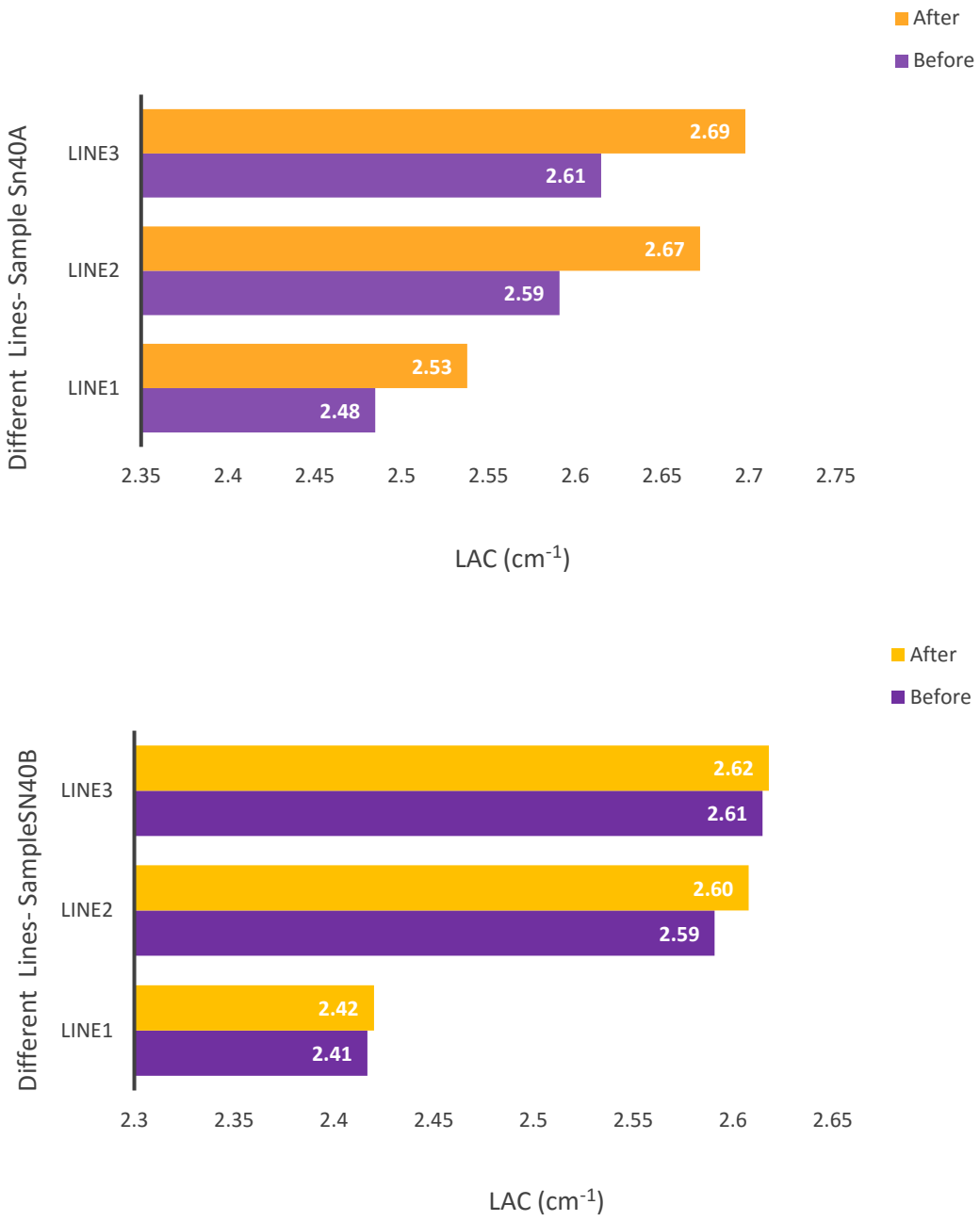

Figure 10.17 The graphs present the mean LAC values in three different areas of lesions on XMT images taken from sample Sn40A and Sn40B and compared the values pre- and post-application of the 40w%SnM in ICON® resin.

Table 10.6 The percentage changes and *p*-value (paired t-test) comparing the means of LACs along the three lines in the XMT images before and after infiltrations. * Indicate statistical difference.

	Line 1 (*p*)	**Line 2 (*p*)**	**Line 3 (*p*)**
Br20A	0.17 (0.63)	0.92 (<0.05)*	1.22 (<0.05)*
Br20B	5.13 (<0.001)*	7.04 (<0.001)*	5.04 (<0.001)*
Br30A	1.74 (<0.001)*	-0.07 (0.57)	0.43 (0.02)*
Br30B	1.52 (<0.001)*	1.20 (<0.01)*	0.92 (<0.02)*
Sn40A	2.13 (<0.001)*	3.13 (<0.001)*	3.18 (<0.001)*
Sn40B	0.13 (<0.05)*	0.66 (<0.001)*	0.12 (>0.05)

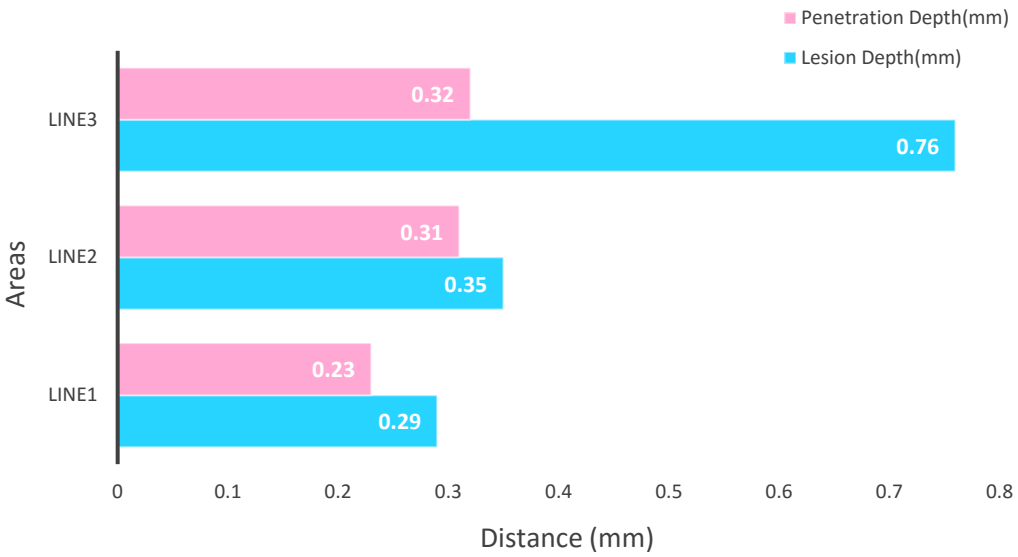

a

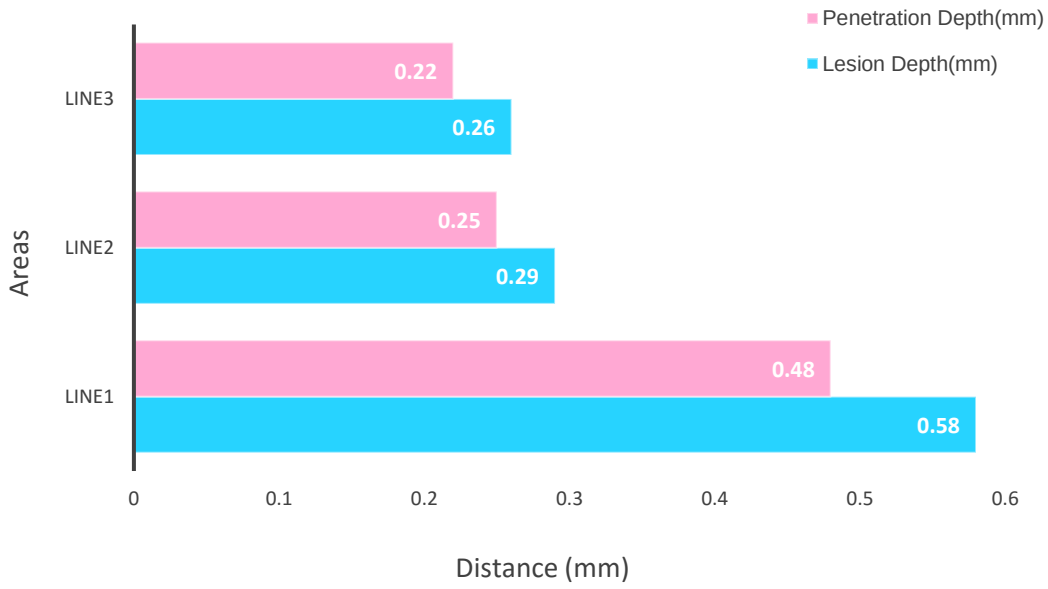

b

Figure 10.18 The graphs present the mean lesion depth and penetration depth along the three lines through the lesions on the XMT images for (a) Br20A and (b) Br20B.

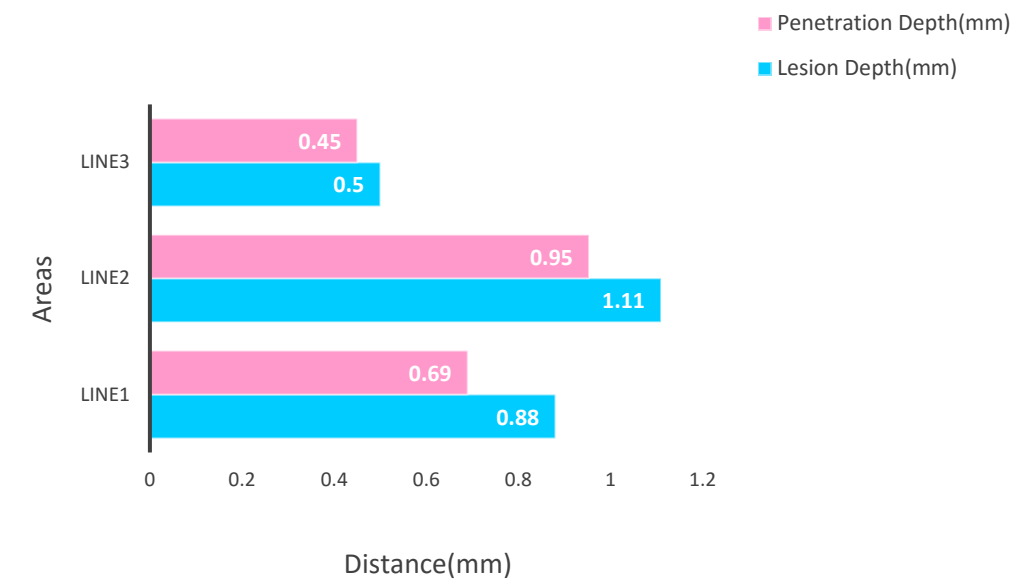

a

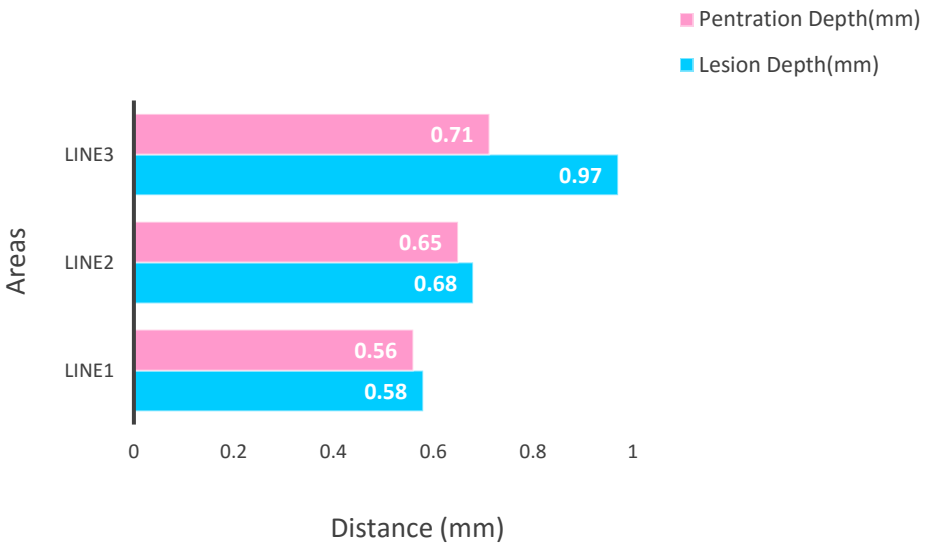

b

Figure 10.19 The graphs present the mean lesion depth and penetration depth along the three lines through the lesions on the XMT images for (a) Br30A and (b) Br30B.

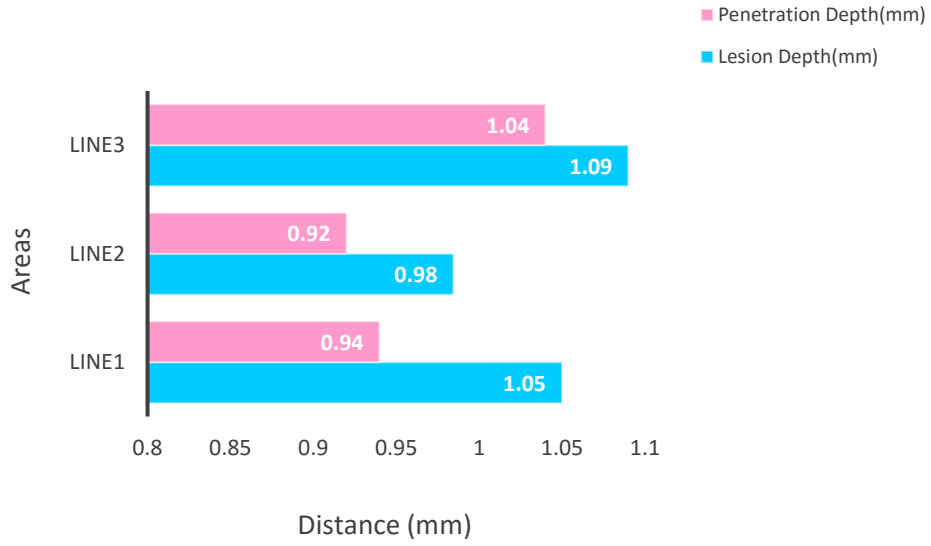

a

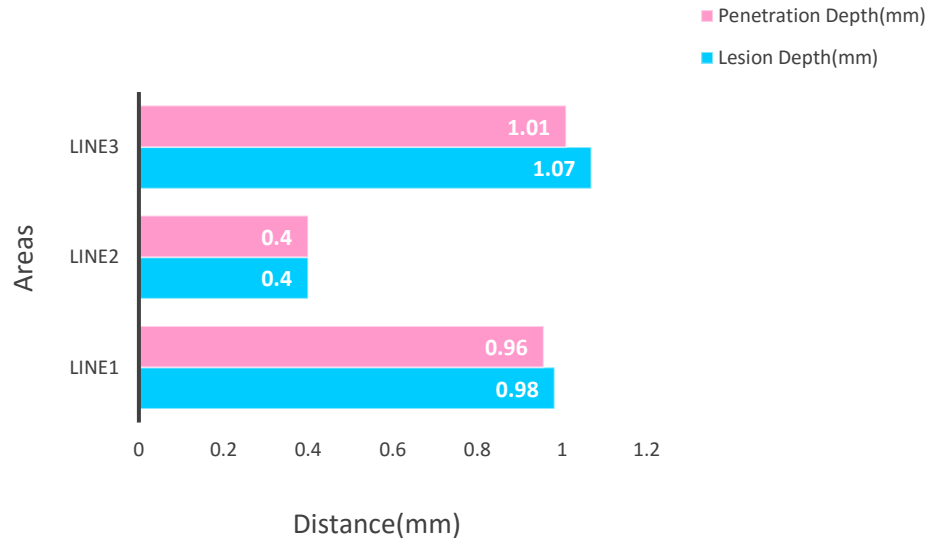

b

Figure 10.20 The graphs present the mean lesion depth and penetration depth along the three lines through the lesions on the XMT images for (a) Sn40A and (b) Sn40B.

Table 10.7 The percentage of penetration of radiopaque resin into the lesion.

	Line1	Line2	Line3	Mean
Br20A	80.3	87.4	42.8	70.2
Br20B	82.7	86.3	86.3	85.1
Br30A	78.4	85.9	90.1	84.8
Br30B	96.3	95.8	73.4	88.5
Sn40A	89.8	94.2	95.2	93.1
Sn40B	97.4	99.3	94.3	97.0

10.6 Discussion

The initial enamel carious lesion has a porous structure and infiltrant resin is proposed as a material which can penetrate into the early carious lesion structure. This material seals the porosity and inhibits the progression of caries (Paris *et al*, 2007). This feature is driven by the capillary forces inside the porous tissue provided that they are filled with air.

In the current study, the aim was to develop a radiopaque resin to infiltrate the initial enamel carious lesion. Two main features behind this aim are:

- Relative Radiopacity,
- Infiltration ability into the lesion depth in the depth and sealing the porosity.

In this chapter, photographs, digital radiographs and XMT images were used to investigate changes in early enamel carious lesion after the applications of the different types of the radiopaque resins in terms of colour changes, radiopacity and penetration depth compared to pre-application of the materials.

- ***Teeth selection***

Permanent human teeth were selected for this study from an anonymous tooth bank at Royal London Hospital. Although there were plenty teeth in the tooth bank, only six teeth met the selected criteria as it was difficult to find a tooth with natural WSL which can be used in the present study. No information on the patients' age, gender and the reason of tooth extraction was provided. Hence, it was not possible to ascertain whether the teeth were obtained from a person with active or inactive caries. From the colours, the lesions in teeth for Sn40A and Sn40B appeared to be more chalky white than the other teeth for BrM resin infiltrations. Hence, it is probable that the former lesions were more active and less mature. This may provide more connected demineralised pores/space for resin infiltration than the more mature lesions where the demineralised pores or connection between the pores might be blocked by remineralised substance, dead bacteria or salivary protein. This may explain that the percentage of penetration were higher in lesions infiltrated by SnM (Table 10.7).

Since it was difficult to collect teeth with white spot lesion despite a high number of extracted teeth in the tooth bank resource, only two teeth were allocated to each group of experiment. However, XMT is a 3D method and each white spot lesion involved at least 300 slices in the LAC difference and penetration depth calculations. Furthermore, the grey scale of each pixel was calculated for each XMT image. Thus, the data qualified for the paired t-test regarding statistical analysis.

It should be mentioned that it is more difficult to obtain extracted permanent teeth with early white spot lesions because they would be restored and are therefore not extracted. It is more likely that early WSL could be found on extracted deciduous teeth, especially if they are extracted for compensation or balanced reasons. Hence, future studies could be carried out using deciduous teeth. However, cautions should be taken as their prismatic structure is different from the permanent teeth.

Human teeth with natural lesions were used instead of using bovine teeth with artificial lesions. Although bovine teeth are a reasonable substitute, their enamel structure is very different from human. Furthermore, although the artificial lesions

showed the intact layer and body of the lesion, they are more uniformed (Spitzer and Ten Bosch 1975).

- ***Examiners***

There were eight participating examiners for assessing the lesions qualitatively. All examiners were dentists who were trained in post-graduate clinical dentistry. No training or calibration, amongst the examiners was carried out by the present investigator because the aim was to assess the spread of the ability to detect changes by dentists. However, it should be mentioned that this might affect the accuracy of the results.

- ***Photographs***

It is expected that the radiopaque resins, like the non-radiopaque ICON®, would change the refractive indices of the WSLs after infiltration. This was found consistently with BrM infiltrated lesions as assessed by the eight examiners (Table 10.3- 10.4). However, for the SnM infiltrated lesions, only 3 examiners reported a change in colour. This may be caused by:

- The colours of the WSLs in Sn40A and Sn40B were similar to the surrounding enamel because they were early lesions. Thus, the infiltrant did not make a distinguishable change;
- The refractive index of SnM resin might be less than that for BrM resin. Hence, the infiltration did not make a distinguishable change in colour.

In order to ascertain the real cause, future experiments are needed to infiltrate SnM resin into more mature lesions.

- ***Digital radiograph***

Using the line profile analysis, it was shown that there was an increase in radiopacities in the WSLs after infiltrations (Figures 10.8). However, these changes were not very apparent enough for examiners to detect. This indicates that radiopaque resins were not radiopaque to cause a distinguishable change in digital radiographs. Hence, if these resins are to be applied clinically, an objective digital

tool is needed in order to assess the efficacy of the infiltration rather than relying on visual examination only.

- ***XMT***

In this study, high resolution XMT technique was used as the gold standard to investigate the change in radiopacity and depth of infiltration. Previously, confocal microscopy was used to measure the penetration depth of the ICON® resins (Paris *et al.* 2007). The confocal technique requires the sample to be cut in half, and the maximum depth of investigation is up to 100µm. Furthermore, it does not allow assessment of radiopacities. With XMT, three data are available for analysis. The XMT system, MuCAT, used in the present study, is also able to measure small changes in LACs, thus it was an appropriate tool for this study. Although six teeth were examined in the present study (two samples per group), each XMT image from WSL region included 300-500 slices. Thus, a criterion was set to use each 10^{th} XMT slice from the beginning to the end of the lesions in order to calculate LACs and statistical analysis test.

The challenge to measure any changes quantitatively pre- and post-infiltration was the alignment of the 3D data because any movement will cause a systematic error on the measured points. The in-house software that allowed alignment with 7 degrees of freedom has solved this problem as observed in the subtracted images that there was no distinctive area or lines. The shape of the tooth could still be observed (after contrast adjustments) because of the noise in the images. Hence, the differences of LACs obtained in the line profiles on pre- and post-infiltration XMT images are real (if above the noise level) rather than due to realignment.

It is clear from the results that the infiltrants could increase the radiopacity by 7%. However, it was interesting to see that the increase was not uniform within the lesion, as shown by the large differences of increase in difference locations of the lines. This indicates that there were demineralised regions or pores, which may have radiolucent materials, which blocked the occupancy of the resins, or blocked the communicating channels of the pores to the surface of the lesion.

It should be mentioned that the novel radiopaque resin could have more that 95% penetration, which is comparable to that reported for ICON® (Paris *et al.* 2007). There were regional variations, like the radiopacity, probably caused by the same factors mentioned above. The SnM resin seemed to have better penetration. However, as noted previously, these lesion structures might be different from that for BrM infiltration. It was also noted that there was a small crack in Sn40B, which might have influenced the depth of resin infiltration. The tooth was not selected out as WSL was adjacent to the crack.

10.7 Conclusion

The null hypothesis, which was stating the insignificant increase of LACs after experimental radiopaque resins' infiltration into natural WSLs, were rejected as most lines showed statistical significant increase in LACs.

The novel radiopaque resins infiltrated into the WSLs with comparable penetration depth to ICON®. Although the increase in radiopacity was not easily detected visually, it can be detected by other measuring tools. Hence, these novel radiopaque resins have the potential to be used and detected clinically by X-ray subtraction technique or optical coherence tomography (OCT).

Chapter 11- Experimental Radiopaque Infiltrant Resin (Biocompatibility)

11.1 Introduction

The International Standards Organisation (ISO) has published a series of standards for medical devices (ISO 10993) in 1992, to underline the importance of a series of biocompatibility tests on any new medical device, prior to their use in-vivo. Among the various biocompatibility tests, the cytotoxicity test plays a key role as an indicator for the evaluation of biocompatibility of the medical devices. It is based on the assessment of the cell growth, replication and morphological changes in cells in-vitro (He and Shi 2011).

Biocompatibility is a term used to define a well-balanced interaction between the host and the implanted material (Wataha 2001). Horvath (1980) stated that a cytotoxic material can interfere with cellular attachment, cellular morphology, cellular growth rate, and potentially lead to cell death. Therefore, it is crucial to ensure the safe and effective application of new medical devices in the human population (Horvath 1980).

Regulations for cytotoxicity in-vitro (ISO 10993-5) are based on the biological evaluation of medical devices and includes two types of cytotoxicity tests:

- Direct contact assay: the most sensitive for testing the cytotoxicity of medical devices,
- Indirect contact assay: can be a useful method to evaluate toxicity of the biological medical devices that can leach toxic substances (Li *et al.* 2015).

The nature of the specimen, the potential site of use and the nature of use are key factors in selecting the most suitable type(s) of cytotoxicity tests. However, all the cytotoxicity tests are in-vitro and can be carried out at any time through the development of the new material. It is conducted at the cell level and is designed to measure any cytotoxic leachable substance. Mouse fibroblast cells (L929) are used in cytotoxicity experiments to investigate live cell reactions to a leachable substance from the material (Li *et al.* 2015).

Dental materials are in direct contact either with oral mucosa or dental tissue including the pulp tissue. Any leachable components from a dental material may

lead to adverse reactions on oral mucosa or pulp and through the permeable dentine (Moharamzadeh *et al.* 2009). A national survey carried out in the UK, on adverse reactions related to dental materials, showed that dental resins are the main cause of adverse reactions in dental technicians, and more than 12% of adverse reactions in patients are related to resin-based dental materials. Skin irritation, itching, cracking and dryness are examples of reported adverse effects of such exposure (Scott *et al.* 2004). As a result, it is compulsory to conduct toxicity tests on all new dental materials in order to identify and define safety thresholds (Niles *et al.* 2009). There are two main different types of biocompatibility tests, in-vitro and in-vivo tests used to assess the effects of resin-based materials' biocompatibility (Moharamzadeh *et al.* 2009).

In-vitro tests simulate biological reactions of the body in response to the materials. They are repeatable and relatively simple without any ethical issues (Hanks *et al*. 1996). In-vitro toxicity tests are used to assess the cell proliferation, growth rate, metabolic function, or other cellular function of the cells exposed to the material (Wataha 2001). Cell culture assays examine the biocompatibility of a material, or its extract, through the use of isolated cells in-vitro. It evaluates the toxicity or irritancy of materials and can screen materials prior to in-vivo tests.

11.1.1 DNA fluorometric assay

The DNA fluorometric assay is a reliable and simple endpoint test used for cell proliferation to determine cellular deoxyribonucleic acid (DNA) content of the viable cells. Fluorochrome bis-benzimidazole (Hoechst 33258) is used as the marker (Jones *et al.* 2001; Rengarajan *et al.* 2002).

Fluorochrome bis-benzimidazole binds to the cellular DNA, with a marked preference towards the adenosine-tyrosine sequence, in viable cells (Rage *et al*. 1990). This leads to a shift in the emission of spectrum and enhances fluorescence (Portugal and Waring 1988). The fluorochrome is in a high salt buffer, which dissociates the DNA and the chromatin, leading to improved exposure of DNA binding sites (Labarca and Paigen 1980). It should be mentioned that fluorescence-based nucleic acid quantification methods are more sensitive than absorbance-

based methods because the former is able to measure a lower level DNA (Rengarajan *et al.* 2002).

11.1.2 MTT assay

Mossman in 1983 introduced the colorimetric assay, called MTT (3-[4,5-dimethylthiazol-2-yl]-2,5- diphenyltetrazolium bromine; thiazolyl blue), which is based on the metabolically active cells. This method is able to measure a soluble tetrazolium salts conversion into an insoluble formazan precipitate.

MTT is a water soluble tetrazolium salt. It yields a yellow solution when dissolved in media or salt solution lacking phenol (Gerlier and Thomasset 1986). The dehydrogenase enzymes, found in active mitochondria in live cells, are able to convert the dissolved MTT to an insoluble purple formazan by cleavage of the tetrazolium ring (Figure 11.1). The electrons from the oxidised substrate, nicotinamide adenine dinucleotide- hydrogen (NADH) and nicotinamide adenine dinucleotide phosphate (NADPH), bind to the tetrazolium salts and are reduced at the cytochrome b and c sites of the mitochondrial electron transport system by succinate dehydrogenase activity. This reaction transforms the yellow salts to blue formazan crystals. Since the formazan crystals are impermeable to the cell membrane, they are accumulated in healthy cells. The formazan crystals would be dissolved in isopropanol or any organic solvent with the range of concentration determined by using spectrophotometer at the test and reference wavelengths of 550 and 620nm, respectively (Supino 1995). The absorbance reading, as a function of concentration of converted dye is correlated to the number of intact alive cells (Mosmann 1983). Cytotoxic compounds are able to damage and destroy cells, and thus decrease the reduction of MTT to formazan (Ulukaya *et al*. 2008).

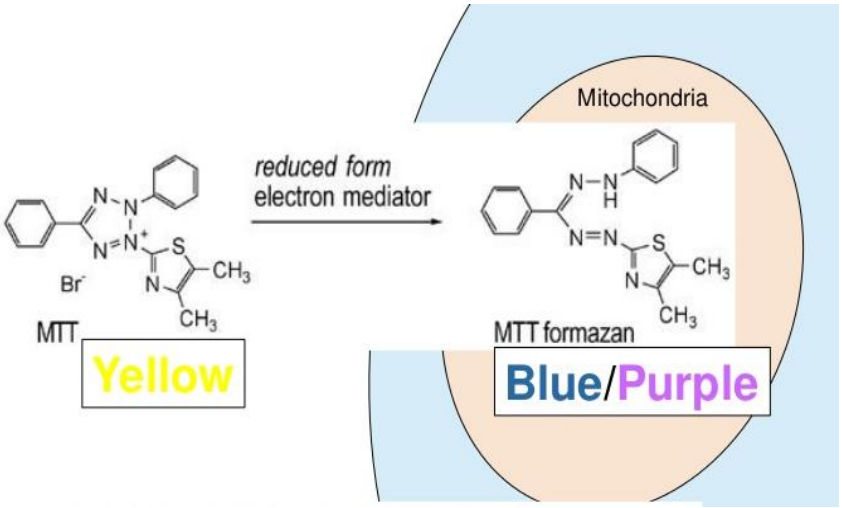

Figure 11.1 Colorimetric assay, MTT is able to convert the dissolved MTT (yellow) to an insoluble formazan (purple) in active mitochondria in live cells. (http://www.slideshare.net, accessed on 20/12/2016).

11.2 Aims and objectives

In this study, direct contact assays of MTT and DNA (deoxyribonucleic acid) were used to determine the cytotoxic effects of the specimens based on the international standard (ISO 10993-5:2009) (ISO 2009).

The aim of these two experiments were:

- ***DNA Fluorometric assay to investigate***:
  - whether the cells are growing over time by investigation on a plate including cells only (without specimen) on day 0, 5 and 10,
  - whether the vapour of resins has an effect on cell cytotoxicity by comparing between the cell columns in 96-plate including cells only (without specimen) and 96-plate including cells column adjacent to the columns of specimen,
  - whether the different curing time (10, 20, 30 and 40s) of specimen has an effect on cell cytotoxicity,
  - the cell cytotoxicity of different specimen on day 0, 5 and 10.

- ***MTT assay to examine***:

  - The cytotoxicity of different specimen on day 0, 5 and 10.

11.3 Materials and methods

11.3.1Pilot Study

The DNA and MTT experiments, as described in sections 11.3.2- 11.3.8, were carried out five times each as pilot study to improve the cell culture skills by the examiner prior to the actual experiments.

11.3.2 Preparation of plates with cell and samples' columns

96-well plates were prepared for each test (Figure 11.2). In all experiments, the peripheral rows were kept blank.

100µL of specimen were added to the relevant well using the multi-channel pipette (F1-ClipTip, ThermoFisher Scientific, UK). The resins were cured by a blue LED activation light at 400 mW/cm^2 for 40s (Demetron LC, Ser no 66004022, KERR corporation, Danbury). Then, the 96-well plates with the cured materials were sterilised by using ultraviolet for 20 minutes.

In the set of experiment to investigate the correlation between the curing time and cell cytotoxicity, different plates were allocated to the range of curing times including 10, 20, 30 and 40s.

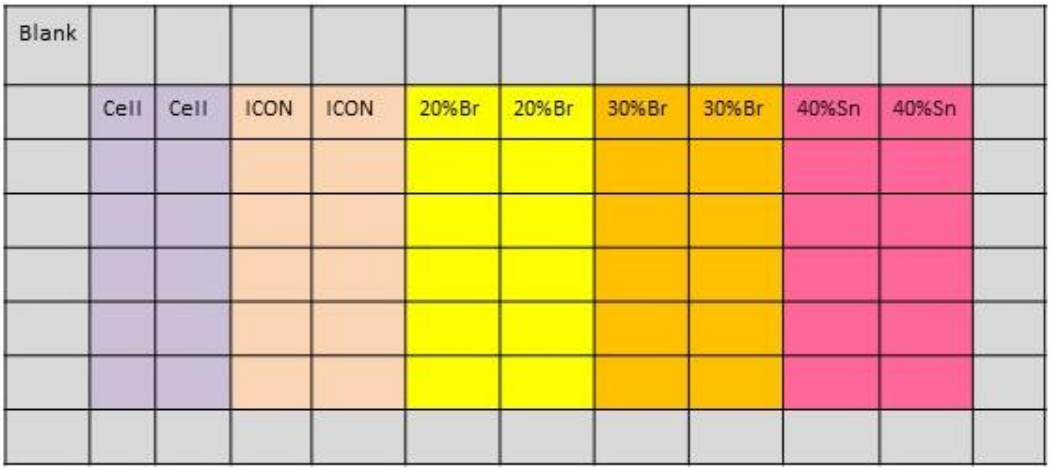

Figure 11.2 Schematic of 96-plate preparation for cell cytotoxicity tests in terms of the different specimens.

11.3.3 Preparation of plates with cell columns only

A 96-well plate with the presence of cell line (L929) without any specimen was prepared for each experiment. 100µl of cell line (L929) suspension (5000 cells/100µl) was added to two columns in the plate and all other wells were kept empty and considered as blank (Figure 11.3).

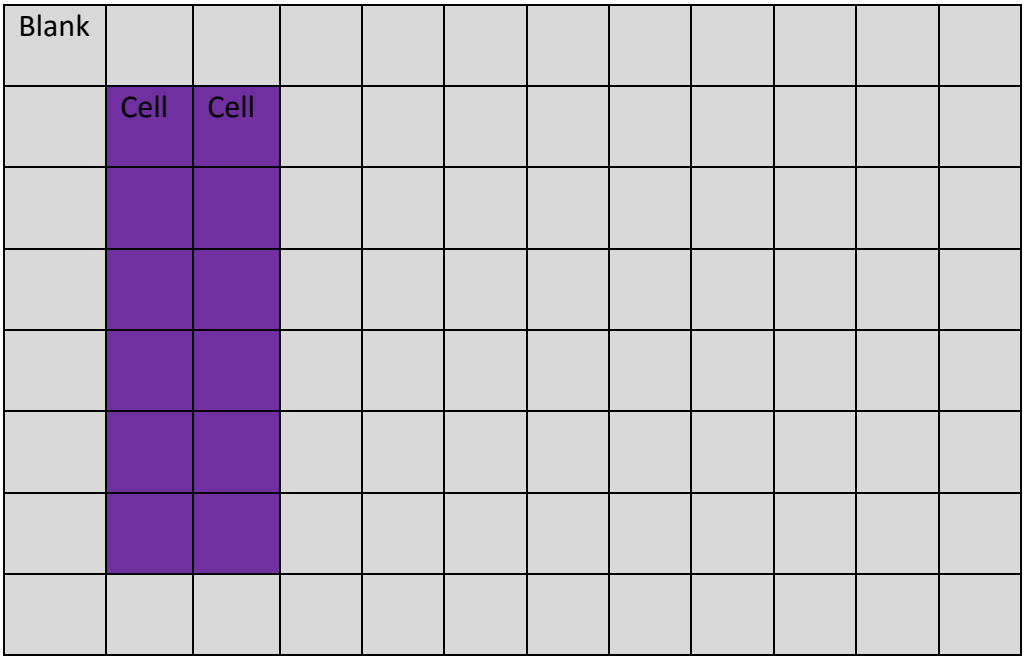

Figure 11.3 Schematic of 96-plate preparation for the plate with the presence of cells only.

11.3.4 Cell lines culture

The culture medium for cell growth was prepared using Dulbecco's Modified Eagle Media, fetal calf serum, L-glutamate and penicillin-streptomycin. For each 500mL of Dulbecco's Modified Eagle Media, 5mL of 5000 units/mL Penicillin, 5000µg/mL Streptomycin, 5mL of 200mM L-glutamate and 50mL of fetal calf serum were added. The culture medium was stored in refrigerator at 4°C.

Mouse L929 fibroblast cell lines (DPSCs, Lonza) were cultivated into two 75cm^2 flasks. 15mL of culture medium was added into each flask. The flasks were kept in an incubator for 3 days at 37°C $\pm$ 1°C with 95 % oxygen and 5% CO_2. This allowed the cell lines to multiply and grow in the flasks, until they reached at least 90% of confluency before the cytotoxic tests. The growth of the cells was examined under the light microscope every 3 days. The cells were sub-cultured into new flasks when the cell confluency reached 90%. The transferring process of cells from one flask to another at a new lower concentration is called passaging.

The culture medium in the flasks was removed by using vacuum suction. Then, the base of the flasks was washed twice with 10mL phosphate buffered saline (PBS). 1mL of trypsin/ Ethylene diamine tetra-acetic acid (EDTA) was next added to each flask and incubated in the incubator for 5 to 10 minutes at 37°C $\pm$ 1°C with 5% CO_2. Following the incubation, the flasks were placed under the microscope to check whether the cells are 'floating'. 10mL of culture media was added into the flasks to stop the trypsin/EDTA reaction and then, 2mL of cells in the culture media was taken and cultivated in a new flask followed by addition of 10mL of culture medium and placing in the incubator at 37°C $\pm$ 1°C with 5% CO_2 for 3 days.

All of the above- mentioned procedures were performed in a clean culture hood.

11.3.5 Microscopic evaluation of cells growth

Mouse L929 fibroblasts were cultivated in 75cm^2 flasks. 10mL of culture medium was added into each flask. The flasks were kept in an incubator for 2 to 3 days at 37°C $\pm$ 1°C with 95 % oxygen and 5% CO_2. This allowed the cell lines to multiply and grow in the flasks.

The growth of the cells was checked under the microscope on 0, 5 and 10 days to confirm the cell growth over experiment time.

11.3.6 Cell counting and passaging of cells into 96-well plates

After the standard trypsinisation and passaging of cells using trypsin/EDTA, 0.5ml of the culture medium containing cells was placed on the heamocytometer (Figure 11.4). The total number of cells in each grid (48 in total) was counted using a light microscope, and the numbers of cells/ml were determined. 5000 cells in 100µL of culture medium were seeded per well, except the peripheral rows which were filled with cell free medium, by using a multi-channel pipette (F1-ClipTip, ThermoFisher Scientific, UK) .

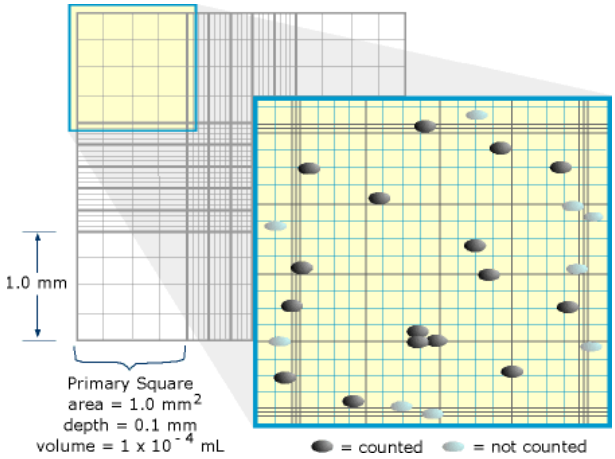

Figure 11.4 Schematic image showing how to use a haemocytometer to count the cell numbers (http://simulab.ltt.com.au/4/laboratory/studynotes/SNHaemo.htm, accessed on 21/12/2016).

11.3.7 DNA fluorometric assay

Two plates were prepared including one plate with only cell columns and the other one with columns of cells and materials. The 96-well plate was incubated at 37°C ± 1°C with 5% CO_2 for 24 hours. The growth of cells was checked under microscope and then, the culture medium in each well was discarded using vacuum suction in the clean culture hood. 100µL PBS was used to wash all the residual media for each cell twice. After gentle tapping, the PBS in the wells was discarded. The plates were frozen at -20°C ± 1°C for overnight and then defrost for one hour. 100µL of deionised water was added into each well using the multi-channel pipette (F1-

ClipTip, ThermoFisher Scientific, UK) and the plates were frozen at -20℃ ± 1℃ for one hour followed by thawing.

DNA solution was prepared by adding 400µL of fluorochrome (Hoechst 33258) per 20mL of TNE buffer (50 mm Tris–HCl (pH 7.4), 100 mM NaCl and 0.1 mm EDTA). 100µL of DNA solution was added into each well using a multi-channel pipette. Then, the reading carried out by using spectrophotometer at 460nm wavelength.

The test was repeated three times for each experiment.

11.3.8 MTT assay

Two plates were prepared including one plate with only cell columns and the other one with columns of cells and materials. MTT plates were incubated for 24 hours at 37℃ ± 1℃ with 5% CO_2. All media in the wells were discarded in the clean hood using vacuum suction. 50µL of 5mg/ml MTT reagent, obtained from the manufacturer were added into each well using a multi-channel pipette (F1-ClipTip, ThermoFisher Scientific, UK). Then, the plates were incubated for 4 hours at 37℃ ± 1℃ with 5% CO_2 followed by the MTT reagent removal from each well aseptically using vacuum suction. 100µL of Dimethyl sulfoxide (DMSO) was added into each well using a multi-channel pipette(F1-ClipTip, ThermoFisher Scientific, UK) to dissolve the insoluble formazan crystal in the cells and the concentration of the formazan crystal produced in each well was measured by means of absorbance, using the spectrophotometer (96-wellplate reader) at 570nm wavelength, with reference of 650nm wavelength.

The test was repeated three times.

11.3.9 Data Analysis

- ***DNA fluorometric assay***
    - To prove the cell growth over time, the cell morphology and the number of cells in the plates with the cell columns only (without specimen) were examined under light microscopy and bar graphs presenting the absorbance against the time (days) were plotted.

- The percentage viability of cells for DNA fluorometric assay was determined using the equation below (Equation 11.1):

Viability of cells (%)= [(d –e)/ (f –e)] x100 Equation 11.1

where:

d: Fluorescent value of eluates of test materials,

e: Fluorescent value of blank,

f: Fluorescent value of negative control.

Bar charts were used to represent the mean viability cells (%) against the different curing time for each specimen and also the mean viability cells (%) against the different specimen in 0,5 and 10 days.

Cytotoxicity feature of each specimen was rated based on cell viability relative to controls as:

- Not cytotoxic: >90% cell viability,
- Slightly cytotoxic: 60–90% cell viability,
- Moderately cytotoxic: 30–59% cell viability and
- Strongly cytotoxic: <30% cell viability (Dahl 2007).

- ***MTT assay***

For MTT assay, the percentage viability of cells was determined as (ISO 10993-5:2009, Yalcin *et al.,* 2013):

Equation 11.2

Viability of cells (%)= [(a –b)/ (c-b)] x100

Where:

a: Absorbance value of eluates of test materials,

b: Absorbance value of blank,

c: Absorbance value of negative control.

A bar chart was plotted the mean viability cells (%) in 0, 5 and 10 days for the different specimen.

Cytotoxicity feature of each sample was rated based on cell viability relative to controls as:

- Not cytotoxic: >90% cell viability,
- Slightly cytotoxic: 60–90% cell viability,
- Moderately cytotoxic: 30–59% cell viability and
- Strongly cytotoxic: <30% cell viability (Dahl 2007).

11.4 Results

11.4.1 Cell growth experiment

The growth of the cells was investigated by light microscopy (Figure 11.5). The number of cells increased from day 0 to day 10 and the cell shape changed from a circular shape to the fibroblast elongated shape. These results confirmed the cells are growing in the experimental period.

The data from DNA test in day 0, 5 and 10 days for the plates including cells only (without specimen) showed an increase in absorbance readings, meaning there was an increase in the number of cells over 10 days (Figure 11.6).

In the plates including cells and specimen, there was an increase in absorbance measurements over 10 days in cell columns; however, this number was lower for the cell columns in the plates including the material columns compared to the plates with cells only (without specimen) (Figure 11.7).

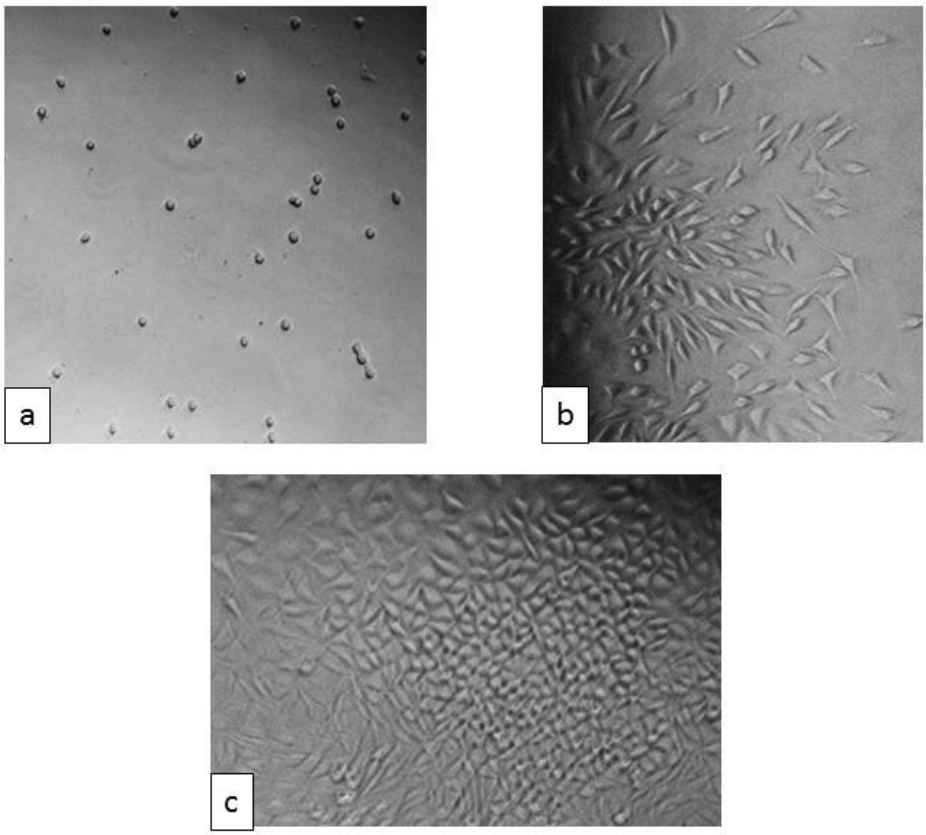

Figure 11.5 Images (10x10) showing an increase in the number of L929 cells and also a change from round shape to the fibroblast elongated shape in 10 days on the same plate with the cells' column only ((a) 0day, (b) 5days, (c) 10days).

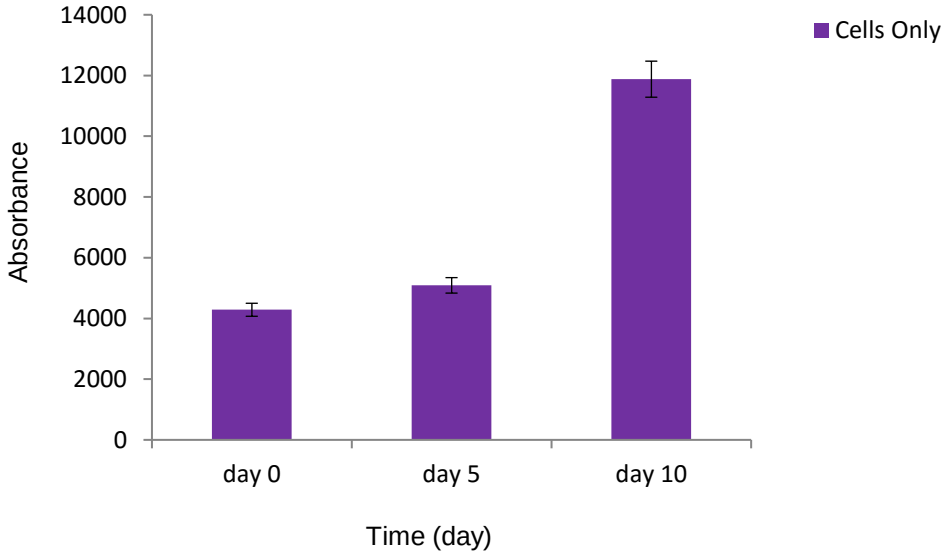

Figure 11.6 A graph bar with standard deviation (SD) showing an increase in DNA absorbance from day 0 to day 10, indicating the cells are growing.

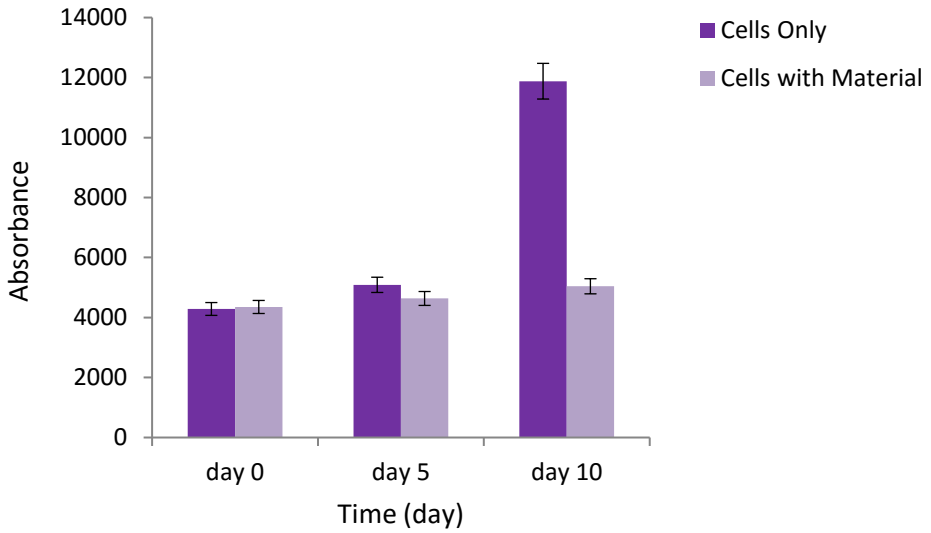

Figure 11.7 A graph bar with standard deviation (SD) showing an increase in absorbance in the DNA test, presenting the cell growth over 10 days of the experiment, in both plates with and without the presence of specimen.

11.4.2 Effect of curing time on cell cytotoxicity of the different materials

The mean cell viability of tin-methacrylate in ICON® resin was higher than bromine-methacrylate groups. The cell viability of all specimen increased with an increased curing time and there appeared to be a correlation between the curing time and mean cell viability for each specimen (Figure 11.8).

All resins including ICON® showed cell viability less than 30% of the control even for the longest curing time of 40s. Thus, they can be considered as strongly cytotoxic based on Dahl and colleagues' classification (Dahl 2007).

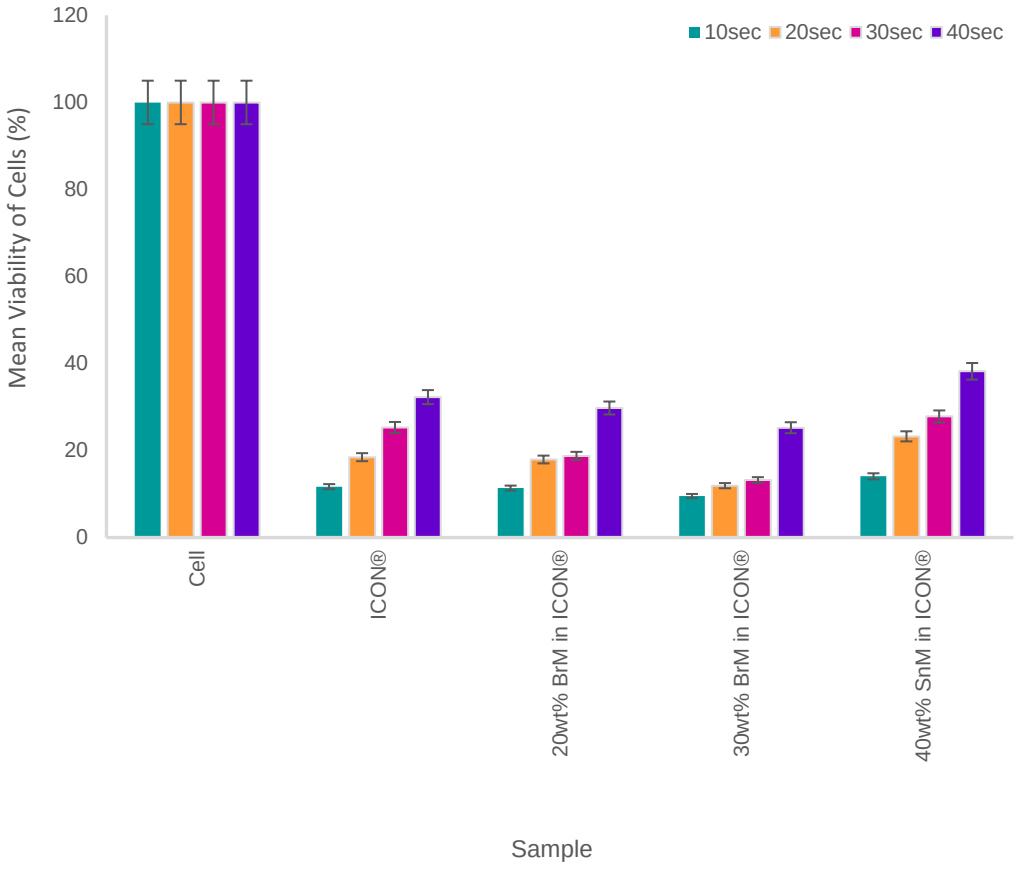

Figure 11.8 A graph bar with standard deviation (SD) showing the cell viability calculated from DNA fluorometric assay for the different curing times for each specimen. There was an increase in cell viability by an increase in curing time for all different materials.

11.4.3 Cytotoxicity of the different materials

11.4.3.1 DNA fluorometric assay

All materials showed a negative effect on the cell growth over 10 days. There was a negative correlation between the time and the cell viability over a 10- days experiment. 30wt% BrM in ICON® resin had the greatest effect to decrease the cell viability among all resins (Figure 11.9).

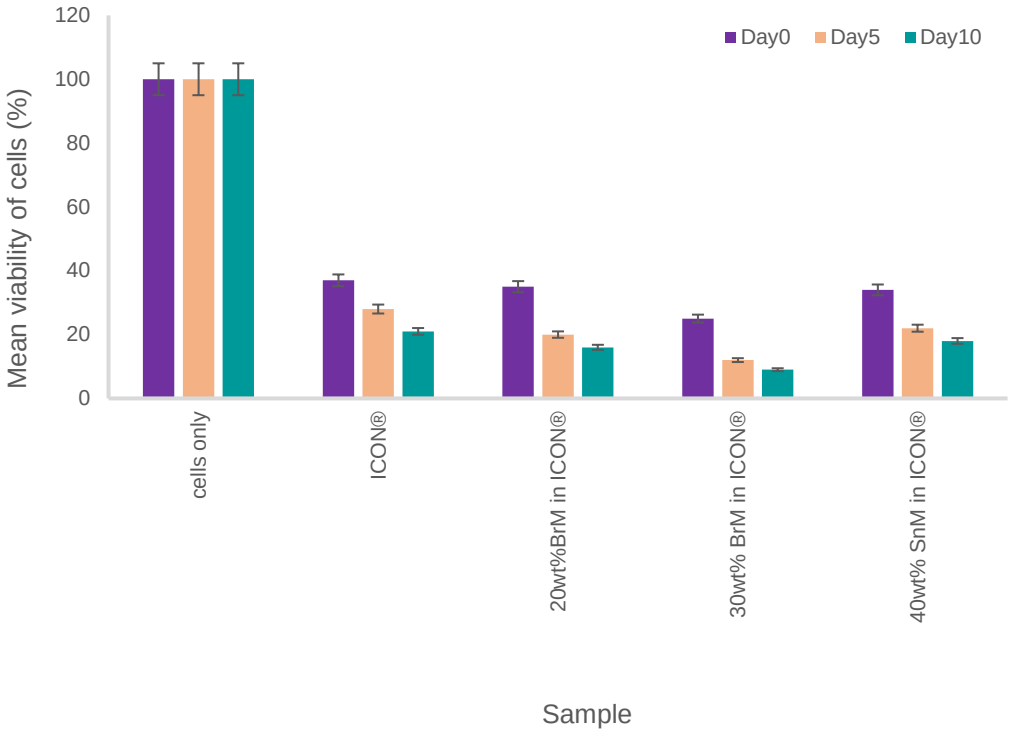

Figure 11.9 A graph bar with standard deviation (SD) showing the cell viability calculated from DNA fluorometric assay for the different resins as a function of time. There was a decrease in cell viability over time.

All specimen except 30wt% bromine-methacrylate in ICON® resin were moderately cytotoxic on day 0 and all specimens were strongly cytotoxic after 5 and 10 days. 30wt% bromine-methacrylate in ICON® resin was considered as strongly cytotoxic since day 0 (Table 11.1).

Table 11.1 The degree of the materials' cytotoxicity over a 10-days experiment.

	ICON®	**20wt%BrM in ICON®**	**30wt%BrM in ICON®**	**40wt%SnM in ICON®**
Day0	MC	MC	SC	MC
Day5	SC	SC	SC	SC
Day10	SC	SC	SC	SC

11.4.3.2 MTT assay

All materials showed a negative effect on the cell growth over 10 days. There was a decrease in cell viability measurements over a 10-days experiment (Figure 11.10).

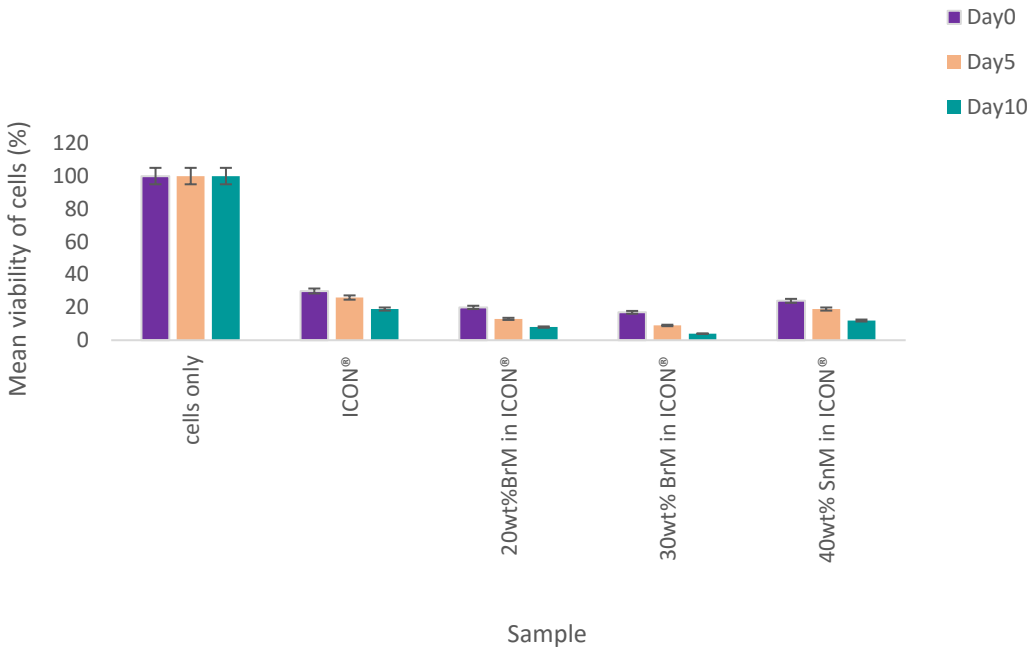

Figure 11.10 A graph bar with standard deviation (SD) showing the cell viability calculated from MTT assay for the different resins as a function of time. There was a

ICON® resin was moderately cytotoxic at day 0 while it was strongly cytotoxic by day 5 and day 10. All other specimen were strongly cytotoxic from day 0 based on the findings from MTT assay.

11.5 Discussion

In the current study, a material with more than 30% reduction of cell viability is considered as cytotoxic (ISO 10993-5) and the grade of its cytotoxicity is classified based on Dahl classification (Dahl 2007). DNA fluorometric assay results showed that all specimen except 30wt% BrM in ICON® are moderately cell cytotoxic at day 0 while the MTT findings showed all specimen are strongly cytotoxic at day 0 except ICON® resin which was moderately cytotoxic. This difference could be due to a possible difference in the sensitivity of the tests. The results of MTT assay depends on the mitochondrial activity of the cells and therefore, the results might not

represent the actual number of viable cells, as some cells can still survive without mitochondria activity and undergo the anaerobic respiration to generate Adenosine Triphosphate (ATP) (Gerlier and Thomasset 1986). DNA fluorometric assay is an highly accurate, sensitive and reliable test and could be used to test biocompatibility (Rage *et al.* 1990); however, it is still possible that DNA fluorometric assay measures the DNA belonging to the dead cells. Therefore, a combination of these two assays will give a better estimate of cytotoxicity of the materials and it is more desirable.

It has been claimed that the established cell lines provide more reproducible results in comparison with primary cells, and they are more suitable for screening purposes. In the current study, the L929 cells were used for cytotoxicity experiments. This cell line is commonly used to evaluate the cytotoxicity of root canal sealers (Pissiotis and Spangberg 1991). Although the L929 cells are popular in cytotoxicity tests, their suitability of use is often questioned. The key argument is that L929 cells might respond in a different way to toxic materials than the relevant target cells in human due to their heteroploid chromosome pattern (Kasten *et al.* 1982; Browne 1985). Moreover, the normal diploid cells are different with aneuploidy cell lines in terms of mitotic rate, density-dependent regulation of growth, and mitochondrial function and they show more tolerance to toxic products (Al-Nazhan and Spangberg 1990).

In the current study, the cells were growing more in the plates without the presence of material in comparison to the plates with the specimen. It was assumed that this could be possibly due to the vapour from the resin materials, which can have an adverse effect on the cell viability of the cells on the adjacent columns.

There are studies on the cytotoxicity of other resin-based dental materials. Huang and Chang (2002) reported a significant cell death ranging from 40 to 75% by resin composites compared to control (Huang and Chang 2002). Al-Hisayat *et al*. (2005) found almost 60% of reduction on the mitochondrial activity in the presence of flowable composite (Al-Hiyasat *et al*. 2005). Also, Wataha *et al*. (2003) reported a severe cytotoxic effect imposed by flowable composite towards the cell lines in-vitro (Wataha *et al.* 2003). Sadoh *et al*. (1999) had reported a generalised neuropathy in dental technicians after 14 years of exposure to methacrylate (Sadoh

et al. 1999). Data from a study by Eldeniz *et al*., (2007) showed a strong cytotoxicity of that root canal sealer, which consists of methyl methacrylate/ tributylborane (MMA/TBB) resin, partially oxidised tri-n-butylborane (TBBO) as a catalyst and 4-methacryloxyethyl trimellitate anhydride/methyl methacrylate (4-META/MMA) as monomer. They assumed that the toxic effect may be associated with the TBBO component of this sealer (Eldeniz *et al.* 2007).

A previous study showed that the resin monomer and photo-initiator could leach from resin composites and were cytotoxic to fibroblast cell lines (Geurtsen *et al*. 1998). We proposed that the cytotoxicity of our test materials can be either due to the leaching of the residual resin monomer, TEDGMA, Bis-GMA or photo-initiator camphorquinone from the resin infiltrate or the presence of either tin or bromine.

The mechanism of cytotoxicity of TEDGMA on the intracellular cells has been explained by different researchers including:

- Geurtsen and Leyhausen (2001) stated that TEDGMA has a 'hydrophilic' nature and tends to leach out into the aqueous environment such as the oral cavity (Geurtsen and Leyhausen 2001);
- Fujisawa *et al.* (1988) stated that TEDGMA can change the lipid layer of cell membrane, causing a change in the permeability of the cell membrane. Therefore, the monomer is able to migrate inside the cells, affect the intercellular target such as mitochondria and subsequently causing cell death and lysis (Fujisawa *et al*. 1988; Issa *et al.* 2004);
- Englemann *et al*., 2002 stated that TEGMA can interfere with intercellular glutathione activity. It forms TEDGMA-glutathione adducts leading to depletion of the glutathione concentration. This results in reduction in the detoxifying potency of the cells; therefore, increase the cytotoxic effects of TEDGMA (Engelmann *et al*. 2002).

Bowen (1965), provided a patent on Bis-GMA synthesis. He explained three different ways to make the resin while biologists considered several issues with

these methods in absence of a strict product policy. The three methods to product BIS-GMA and the relevant issues are (Bowen 1965):

- Methacrylate groups attach to hydroxy glyceryl groups, which, in turn, link to phenoxy groups. This method can produce the residuals of diglycidyl ether of a bisphenol in dental composites and cause allergic reactions,
- The same amount of sodium salt of bisphenol A with the reaction product of glycidyl methacrylate and anhydrous hydrochloric acid would condensate. The residuals from this method is able to induce estrogenic effects or allergic reactions,
- Bowen suggested to combine two moles of glycidyl methacrylate with one mole of bisphenol A. Furthermore, a tertiary amine was added to catalyse the addition of the phenolic hydroxyl groups to the epoxide groups. In this method, glycidyl methacrylate and bisphenol A are leading allergic and estrogenic effects, respectively.

Camphorquinone, as a photoinitiator, is not involved in the polymerised resin network and able to leach out over time after polymerisation, which contribute to the cytotoxicity (Geurtsen *et al.* 1998; Volk *et al*. 2009).

Zakaria (2014) examined the cytotoxicity of the ICON® and mixture of SnM and ICON® as part of his MClinDent project. He showed that the mixture of SnM in ICON® resin is cytotoxic and has a positive correlation with the wt% of SnM. Also, his data showed that the ICON® resin is cytotoxic. The results from this study in DNA and MTT assays for ICON® and the mixture of SnM in ICON® is similar to his finding. He used an indirect method for the cytotoxic experiments while in the current study a direct technique was used, which is a recommended technique to measure the cytotoxicity of a materials' extract by ISO 10993-5.

Although Conine *et al.,* (1975) stated that tin has potential cell cytotoxic effects (Conine *et al.* 1975), it does not have any toxic hazard on an acute or chronic basis at a concentration present in commercial formulation (Gleason *et al*. 1957). It

should be noted that the cytotoxicity of tin might be different from tin methacrylate.

There is no evidence in literatures to show the cell cytotoxicity of the bromine.

Many studies in the literature showing that the vast majority of dental materials are cytotoxic in-vitro. However, this does not mean that they are toxic in-vivo due to presence of biological barriers or insufficient time of contact between the material and underlying tissue (Wataha *et al.* 1994).

It should be kept in mind that the infiltrate resin application is to use on enamel, which is a non-vital tissue. Furthermore, a very small amount of the material is used, and the area in contact with vital tissue is small; therefore, its cytotoxic effect should be negligible.

11.6 Conclusion

All of the materials tested including ICON® were cytotoxic using the cell line tested. Among specimens, the mixture of BrM in ICON® resin is more cytotoxic in comparison with SnM in ICON® resin and 30wt% BrM in ICON® resin, is the most cell cytotoxic material regardless the curing time and time period of experiments. The vapour of resins might also be cell cytotoxic and there is a correlation between the curing time and the cell cytotoxicity of the specimen.

Chapter 12- Relative radiopacity and Infiltration Ability of 30wt% Bromine Methacrylate in ICON® Resin into Artificial White Spot Lesions

12.1 Introduction

Since the aetiology and development of natural occurred white spot lesions (WSLs) can be multi-factorial, and the structure of lesions is different from each other (Chapter 10), it is difficult to standardise the lesion to compare the effects of an intervention. Hence, an artificial lesion is commonly used as an analogue to investigate the process of de- and remineralisation (White 1987; Cate 1990, Margolis *et al*. 1999). There are three types of studies to examine mineral changes in enamel including demineralisation, remineralisation or pH cycling (Anderson *et al*. 1998; Anderson *et al*. 2004).

Demineralisation involves diffusion of acids into the enamel, reaction of the apatite lattice ions to the acid, and outward diffusion of the reactants. In order to develop an artificial WSL, the demineralising solution should demineralise the enamel partially leading to a softened enamel without forming a cavity. Previous studies showed that small differences in the degree of saturation with respect to enamel values found in plaque fluid can lead to a significant difference in the rate of enamel demineralisation in-vitro. Furthermore, the rates of demineralisation in lactic acid were greater than that in acetic and propionic acid (Margolis *et al.* 1999; Zhang *et al*. 2000).

For remineralisation, Backer Dirks (1966) showed that half of the white spot lesions observed in young individuals will disappear over the time. He attributed that this could possibly be due to the remineralising potential of saliva as the body natural remineralising solution (Dirks 1966). Exterkate *et al*. (1993) found that there is a significant difference in the remineralising ability of solutions having Ca:P in a ratio similar to plaque fluid compared to that of having a ratio representing hydroxyapatite (HA) stoichiometry (Exterkate *et al*. 1993).

In order to mimic the natural process of demineralisation and remineralisation in oral environment, pH cycling is used. This can be achieved by passing alternating demineralising and remineralising solutions along the enamel surface (Ten Cate and Duijsters 1982; White 1987; Anderson *et al.* 1998; Anderson *et al.* 2004; Lynch and Ten Cate 2006).

To create artificial white spot lesions, two main methods are commonly used, namely the static and dynamic methods. The static method refers to the experiments creating a lesion using a demineralising agent only, such as acid-gel system (Silverstone 1967), diphosphonate inhibitor system (Francis *et al*. 1969), and buffer system (Moreno and Zahradnik 1974). Wefel and Hareless (1984) found that the acid-gel system, out of the three artificial systems, was the best method to mimic natural white spot lesions. It produced the four classical zones of carious enamel under the polarised light microscope. Furthermore, the shape of the lesion was triangular in cross section and the lesion depth ranged from 250 to 300µm (Wefel and Harless 1984). Some other researchers found acetic acid as a good alternative to produce artificial WSLs (Featherstone 1983; Anderson *et al.* 2004; Elliott *et al.* 2005). Davis (2014) showed that the pH value of acetic acid has a crucial role to induce either an artificial carious lesion or an erosive lesion. She showed that 0.1M acetic acid at pH∼4.5 will induce the formation of a WSL whilst at pH ∼4, an erosive lesion will be formed instead (Davies 2014).

The dynamic method is where a cycle of de- and remineralisation solutions is used to induce an artificial WSL. The Featherstone laboratory (1989) originally designed pH-cycling model to generate artificial white spot lesion similar to the natural WSL in enamel (Featherstone 1983). This model has been used as an effective and reproducible method to assess the anti-caries potential of F containing oral care products over the past few decades. Data collected from this model was closely parallel to those of the Food and Drug Administration (FDA) required rat caries model, which is considered as the "Gold Standard." Furthermore, Lynch and colleagues (2007) used the acid-gel method, followed by remineralisation solutions, to generate an in-vitro WSL similar to that naturally (Lynch *et al*. 2007).

In the present study, artificial WSLs were created using both static and dynamic methods in order to investigate the change of radiopacities after resin infiltrations.

12.2 Aims and objectives

The aims of this part of the study were:

- To investigate and measure the penetration depth of 30wt%BrM-ICON® and ICON® resins into artificial WSLs;
- To investigate and quantify the change of radiopacities of the artificial WSL after application of 30wt%BrM-ICON® and ICON® resins.

12.3 Null Hypothesis

- There is no statistical significant change ($p \geq 0.05$) in the linear attenuation coefficients (LACs) of the artificial white spot lesions (static pathway) before and after 30wt%BrM-ICON® infiltration.
- There is no statistical significant change ($p \geq 0.05$) in the LACs of the artificial white spot lesions (static pathway) before and after ICON® infiltration.
- The increase in LAC in artificial WSLs (static pathway) after 30wt%BrM-ICON® is not significantly different ($p \geq 0.05$) to that of LACs after ICON® infiltration.
- There is no statistical significant change ($p \geq 0.05$) in the LACs of the artificial white spot lesions (dynamic pathway) before and after 30wt%BrM-ICON® infiltration.
- There is no statistical significant change ($p \geq 0.05$) in the LACs of the artificial white spot lesions (dynamic pathway) before and after ICON® infiltration.
- The increase in LAC in artificial WSLs (dynamic pathway) after 30wt%BrM-ICON® is not significantly different ($p \geq 0.05$) to that of LACs after ICON® infiltration.

12.4 Materials and methods

12.4.1 Sample selection and preparation

Extracted premolars teeth from the Royal London Hospital tooth bank (approval from Queen Mary Research Ethics Committee, QMREC 2011/99), stored in 70%

ethanol (Sigma-Aldrich, Gillingham, UK) were examined by eight examiners who were trained and familiar with the International Caries Detection and Assessment System (ICDAS) scoring system. The examination was carried out by cleaning the tooth by bristle brush (Henry Schein, London, UK) and slow handpiece (NSK Ltd, Stevenage, UK), drying the tooth with compressed air, and using a good light (A-dec 6300 Light Bulb 17V, 95W, Mercia Dental, UK) and ICDAS score was recorded for each tooth (Table1.12).

Table 12.1 Showing International Caries Detection and Assessment System (ICDAS) score (Pitts *et al*. 2014). Teeth with score 0 met the criteria and were selected.

Code	Criteria
0	Sound
1	First visual change in enamel (seen only after air drying or restricted to within the confines of a pit or fissure)
2	Distinct visual change in enamel
3	Localised enamel breakdown (without clinical visual signs of dentinal involvement)
4	Underlying dark shadow from dentine
5	Distinct cavity with visible dentine
6	Extensive distinct cavity with visible dentine

Twelve premolars with ICDAS score 0 were selected and painted with two layers of nail varnish (Number 7 'Colour Lock', Quick dry nail polish Boots, Nottingham, UK), to leave enamel windows approximately 2x2 mm^2 exposed on proximal, buccal and lingual surfaces. Teeth were divided into two groups, six teeth per group, randomly to create artificial WSLs via static and dynamic methods.

12.4.2 Static demineralisation with 0.1M acetic acid (pH 4.5)

The demineralising solution including 0.1M acetic acid (Sigma-Aldrich, Gillingham, UK), buffered to pH 4.5 with 1M sodium hydroxide (NaOH) (Sigma-Aldrich,

Gillingham, UK) was prepared. Each tooth was immersed in the 500ml solution for 60 hours to demineralise the exposed enamel in the windows of each tooth. Each tooth was kept in a separate beaker (Camlab Limited, Cambridge, UK), labelled and stirred at an arbitrary speed of 1 and room temperature (25°C±1℃) on the stirrer (Cole-Palmer, London, UK) (Figure 12.1).

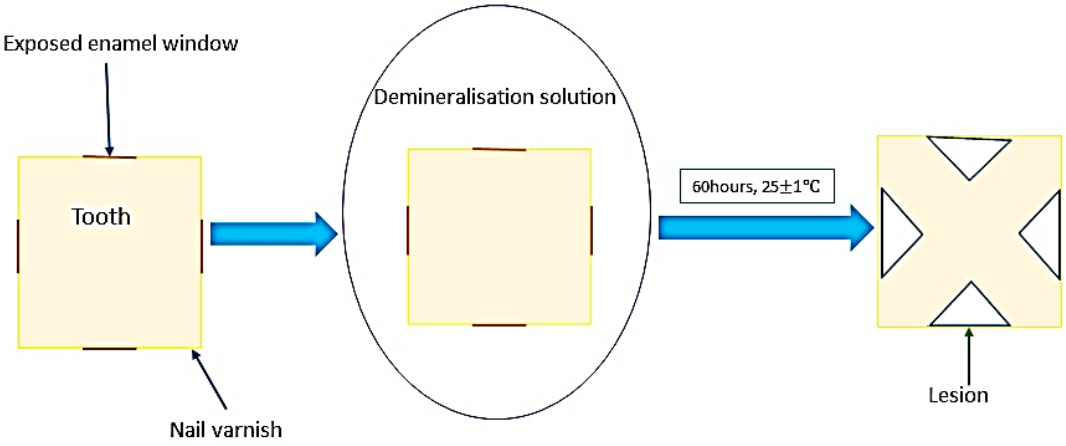

Figure 12.1 Schematic diagram showing static demineralisation by using 0.1M acetic acid (pH 4.5) solution.

12.4.3 Dynamic demineralisation with acid-gel system followed by the remineralising solution

Each exposed enamel window was covered with 8% methylcellulose (aqueous, 1,500 cP, 63 kDa, Sigma-Aldrich, Gillingham, UK) and was left in a fridge at 4°C to set overnight. Then, it was covered with an equal volume of 0.1M lactic acid (Sigma-Aldrich, Gillingham, UK), buffered to pH~4.6 with 1M potassium hydroxide (KOH) (Sigma-Aldrich, Gillingham, UK) and incubated at 37°C using an incubator (Model 56, BINDER GmbH, Tuttlingen, Germany) for 14 days. Each sample was then immersed in 500ml of in-vitro remineralising solution representing plaque fluid (PF) with the same composition and pH reported by Gao and colleagues (2011) for 192 hours at 37 °C using the incubator (Model 56, BINDER GmbH, Tuttlingen, Germany) (Gao *et al*. 2001). The remineralising solution included 20mM HEPES (4-(2-

hydroxyethyl)-1-piperazineethanesulfonic acid) (Sigma-Aldrich,Gillingham,UK), 1.5mM calcium chloride dehydrate (Sigma-Aldrich, Gillingham, UK), 0.9mM potassium dihydrogen orthophosphate (Sigma-Aldrich, Gillingham, UK) and 130 mM potassium chloride (Sigma-Aldrich, Gillingham, UK), pH adjusted to 7.0 using potassium hydroxide (Sigma-Aldrich, Gillingham, UK) (Figure 12.2).

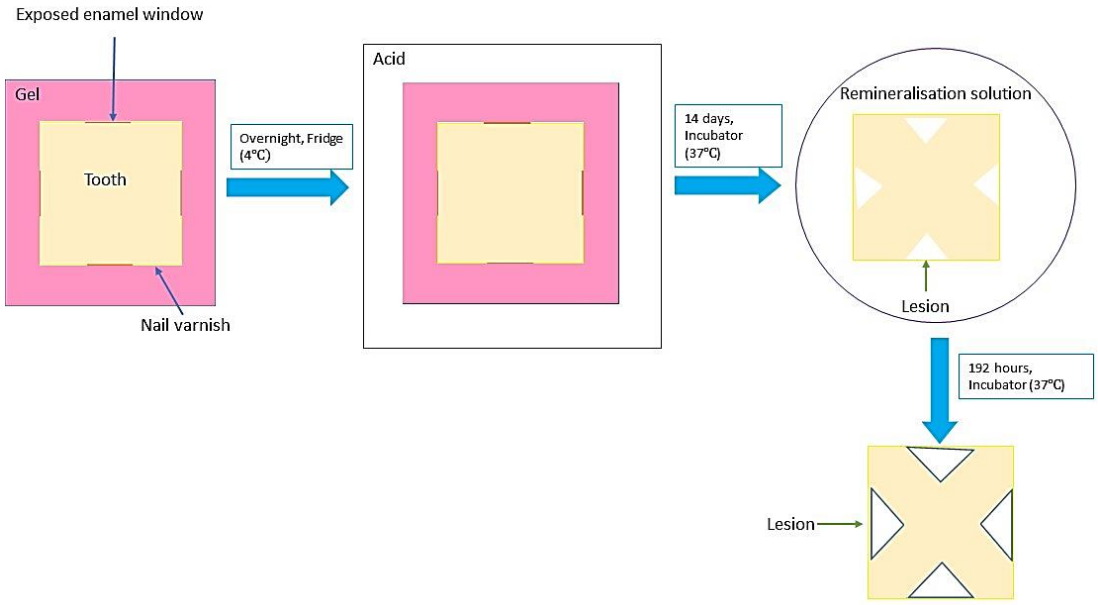

Figure 12.2 Schematic diagram showing dynamic demineralisation by acid-gel system followed by plaque fluid (PF) remineralisation solution. Yellow square is tooth with exposed enamel windows on different surfaces (orange line) in pink square (gel), white square is acid and circle shows the remineralisation solution.

12.4.4 Application of 30wt%BrM-ICON® resin and ICON® resin

For each tooth, one smooth surface and one proximal surface was allocated to one type of resin. Then, the resin material was applied as manufacturer's instruction as follows:

- The surface of the lesion was cleaned with a bristle brush (Henry Schein, London, UK) and slow handpiece (NSK Ltd, Stevenage, UK);
- ICON®-etch was applied for 2 minutes on the white spot lesion using an etch applicator (DMG, Hamburg, Germany);

- The etch was rinsed off with water for 30 seconds and dried with water-free and oil-free air for 15 seconds;
- ICON®-dry was applied for 30 seconds (DMG, Hamburg, Germany), and then dried with oil-free air;
- The relevant material was applied on the surface using a micro-brush (Dental Directory, UK) and waiting for 3 minutes and cured by a blue LED activation light in direct contact with the lesion at 400 mW/cm^2 for 40s (Demetron LC, Ser no 66004022, KERR corporation, Danbury);
- The second layer of resin material was applied on the surface of the lesion and waiting for 1minute and cured by a blue LED activation light in direct contact with the lesion at 400 mW/cm^2 for 40s (Demetron LC, Ser no 66004022, KERR corporation, Danbury).

12.4.5 X-ray microtomography (XMT)

The XMT was carried out after demineralisation, remineralisation and application of materials. Two teeth were inserted into a tube and stabilised with wax and cotton wool. The tube was filled with distilled water and 0.01% thymol (Sigma-Aldrich, Gillingham, UK). Each tube including two samples was scanned using an accelerating potential of 70kV and the current of 0.215 mA using the scanning system described in section 10.4.4. 1125 projections were taken in each complete scan, which took approximately 16 hours per tube.

12.4.6 Data Analysis

Tomview software and Tomalign software were used to align the XMT images and Image J™ (Image Processing and Analysis in Java, National Institute of Health, Bethesda, Maryland, USA) was used to analyse the data as described in section 10.4.6.

- ***Relative Radiopacity***

Aligned XMT images saved in Image J format and then, imported into Image J™ (Image Processing and Analysis in Java, National Institute of Health, Bethesda,

Maryland, USA). The numbers of the first and the last slice showing each lesion were recorded and their difference was calculated in order to find out the number of slices including each lesion. A criterion was set to include one slice in every ten slices into the calculation. For each slice, three line profiles were drawn through the lesion: the first line was at the centre of the lesion, the other two lines were at half the distance between the first central line and the margins of the lesions on either side of the lesions. By using Image J™, it was possible to superimpose the line profile of the first scan on the second scan. Then, their LAC differences were calculated. The LAC difference for static demineralisation was calculated between the post-infiltration and aligned post-demineralisation XMT images while this value was calculated between aligned post-infiltration and aligned post-remineralisation XMT images for dynamic demineralisation group. Paired t-tests were used to investigate whether the differences were significant at p value <0.05. Independent t-test was used to investigate the global increase in radiodensities.

- ***Penetration Depth***

The subtraction software was used to visualise the changes after each step in 3D. Furthermore, the lesion depth (LD), the penetration depth (PD) and penetration potential (PP) was calculated as described in section 10.4.6 in the subtracted XMT images.

An example of data can be found in Appendix C.

12.5 Results

12.5.1 Static demineralisation method

Post-static demineralised, post-infiltration with 30wt%BrM-ICON® or ICON® resins and subtracted XMT images for the six teeth are shown in Figures 12.3-12.14. It could be observed from the subtracted XMT images that there was an increase in radiopacity, except for sample 1 and a lesion in sample 5, for 30wt%BrM-ICON® resin infiltrated lesions. In all the ICON® infiltrated lesions, there was a decrease in radiopacity (shown as black). This can be shown clearly in mean LAC graphs for each lesion (Figure 12.15, Tables 12.2 and 3). For the ICON® infiltrated lesions, there was

a significant decrease (p<0.05) in LAC in 8 out of the 12 lesions. For 30wt%BrM-ICON® infiltrated lesions, 5 lesions had significant increases in radiopacity (p<0.05), whilst 6 lesions had significant decreases (p<0.05) and there was no significant changes in one lesion, DS4a, (p>0.05).

Combining all the lesions together, there was a highly significant decrease (p<0.001) of LAC after ICON® infiltration whilst there was a highly significant increase (p<0.001) of LAC after 30wt%BrM-ICON® infiltration (Figure 12.16). The increase of LAC after 30wt%BrM-ICON® infiltration was significantly higher (p<0.001) than that after ICON® infiltration.

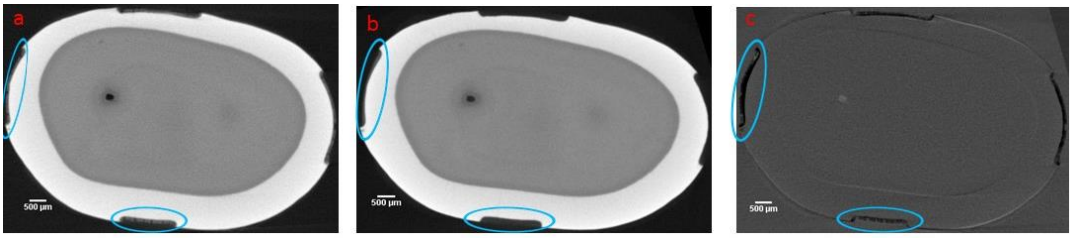

Figure 12.3 Sample DS1- XMT images showing of artificial white spot lesions produced by static demineralisation pathway: (a) before, (b) after infiltration of 30wt%BrM-ICON®, (Blue circle) and, (c) subtracted XMT image. The scale bar is 500µm.

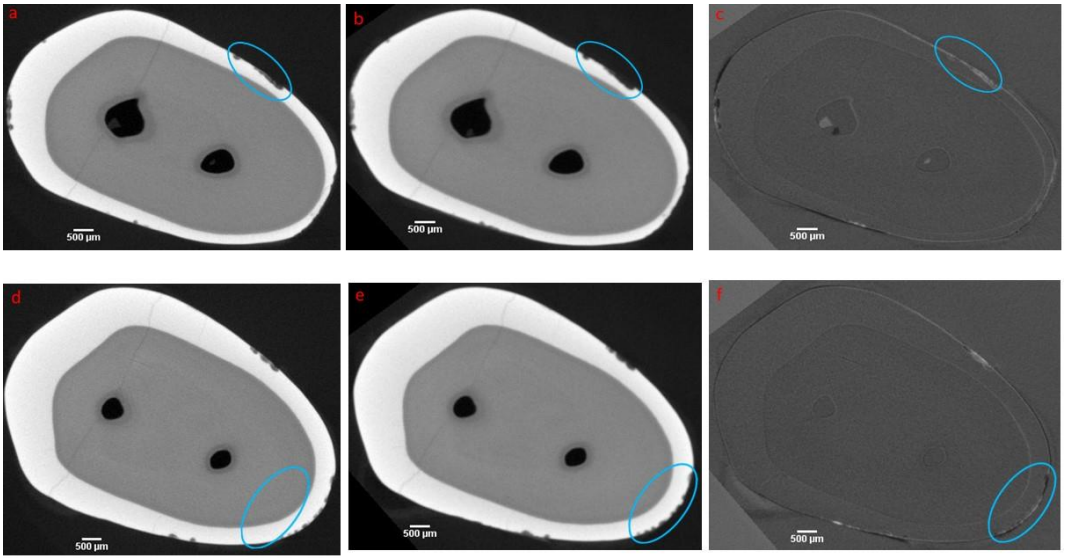

Figure 12.4 Sample DS2 -XMT images of artificial white spot lesions produced by static demineralisation pathway (a,d) before, (b,e) after infiltration of 30wt%BrM-ICON®, (c,f) subtracted XMT images. The scale bar is 500µm.

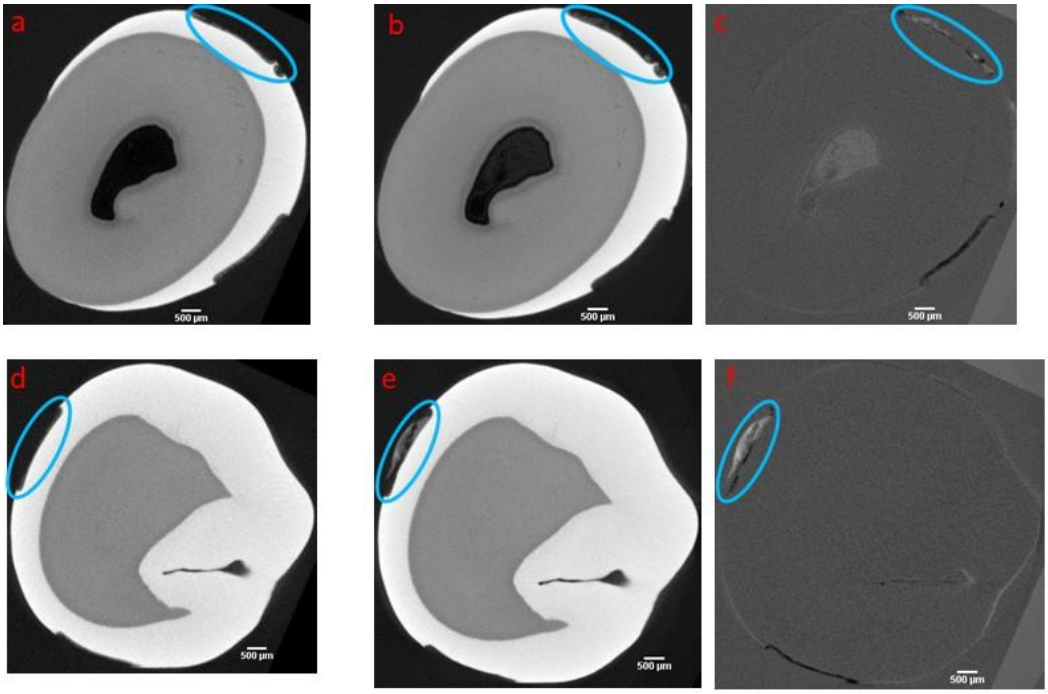

Figure 12.5 Sample DS3 - XMT images of artificial white spot lesions produced by static demineralisation pathway. (a,d) before, (b,e) after infiltration of 30wt%BrM-ICON®, (c,f)subtracted XMT image. The scale bar is 500µm.

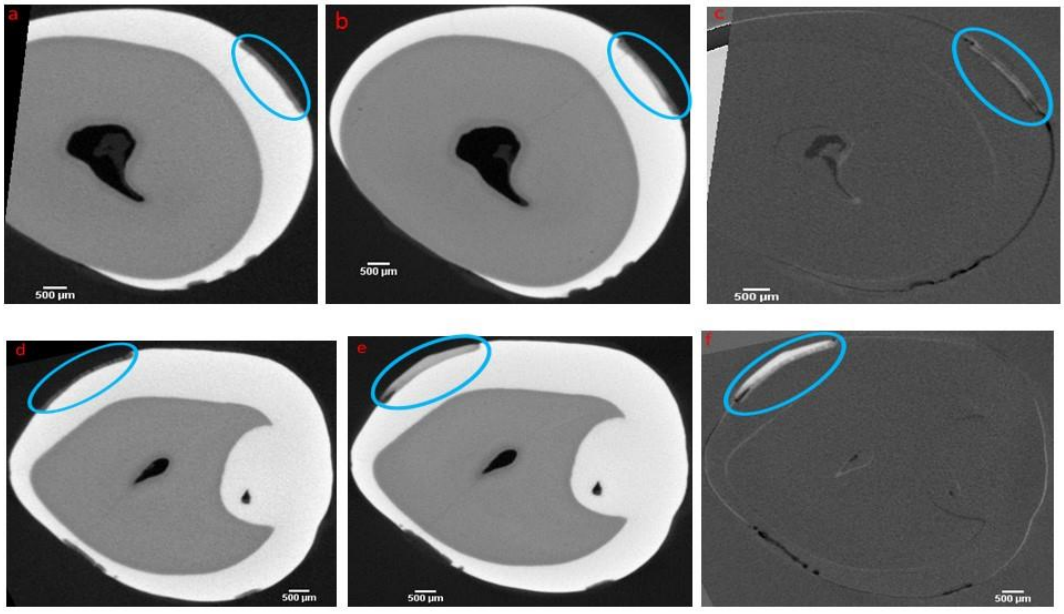

Figure 12.6 sample DS4 - XMT images of artificial white spot lesions produced by static demineralisation pathway. (a,d) before, (b,e) after infiltration of 30wt%BrM-ICON®, (c,f) subtracted XMT image. The scale bar is 500µm.

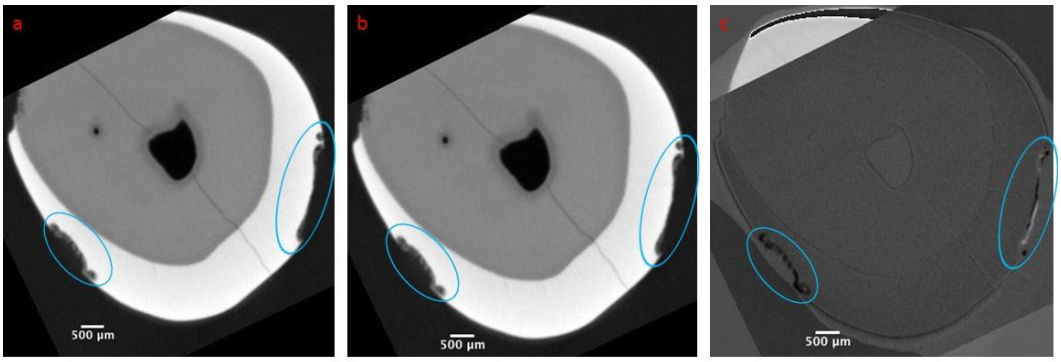

Figure 12.7 Sample DS5 - XMT images showing of artificial white spot lesions produced by static demineralisation pathway. (a) before, (b) after infiltration of 30wt%BrM-ICON®, (c) subtracted XMT image. The scale bar is 500µm.

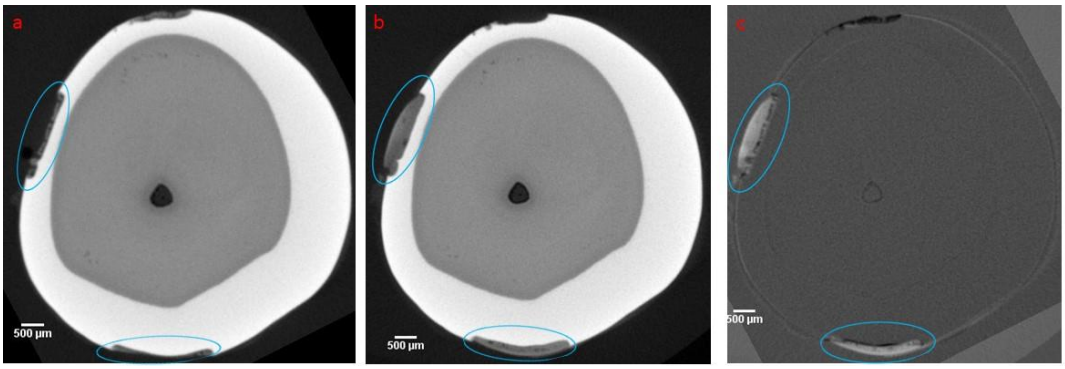

Figure 12.8 Sample DS6 - XMT images showing infiltration of artificial white spot lesions produced by static demineralisation pathway (a) before, (b) after infiltration of 30wt% 30BrM-ICON®, (c) subtracted XMT image. The scale bar is 500µm.

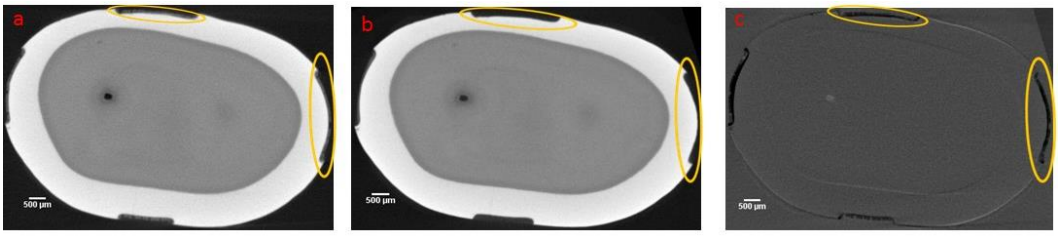

Figure 12.9 Sample DS1 - XMT images of artificial white spot lesions produced by static demineralisation pathway. (a,d) before, (b,e) after infiltration of ICON®, (c,f) subtracted XMT image. The scale bar is 500µm.

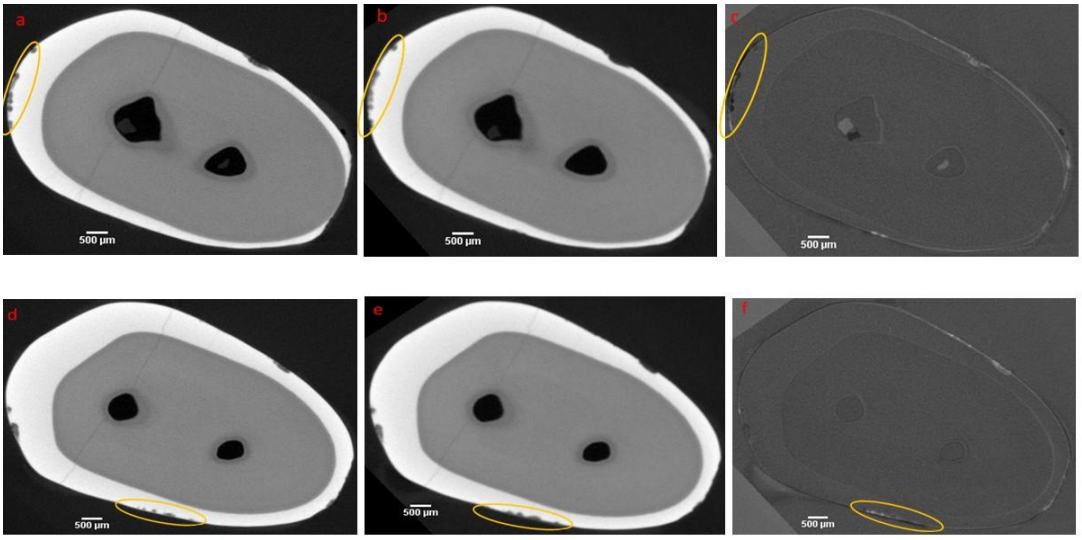

Figure 12.10 Sample DS2 - XMT images of artificial white spot lesions produced by static demineralisation pathway. (a,d) before, (b,e) after infiltration of ICON®, (c,f) subtracted XMT image. The scale bar is 500µm.

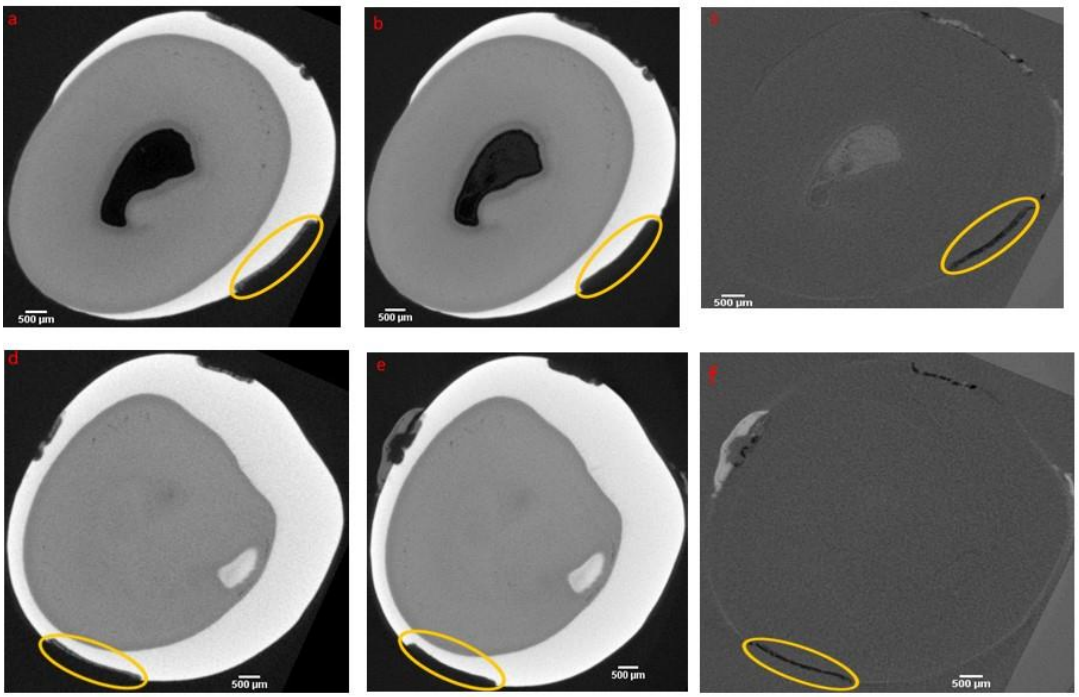

Figure 12.11 Sample DS3 - XMT images of artificial white spot lesions produced by static demineralisation pathway. (a,d) before, (b,e) after infiltration of ICON®, (c,f) subtracted XMT image. The scale bar is 500µm.

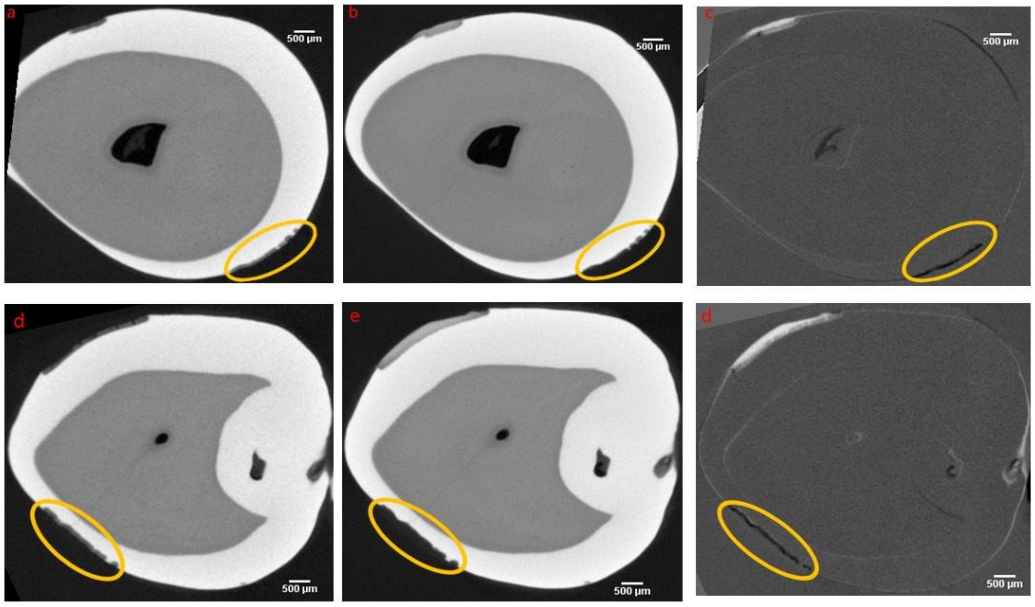

Figure 12.12 Sample DS4 - XMT images of artificial white spot lesions produced by static demineralisation pathway. (a,d) before, (b,e) after infiltration of ICON®, (c,f) subtracted XMT image. The scale bar is 500µm.

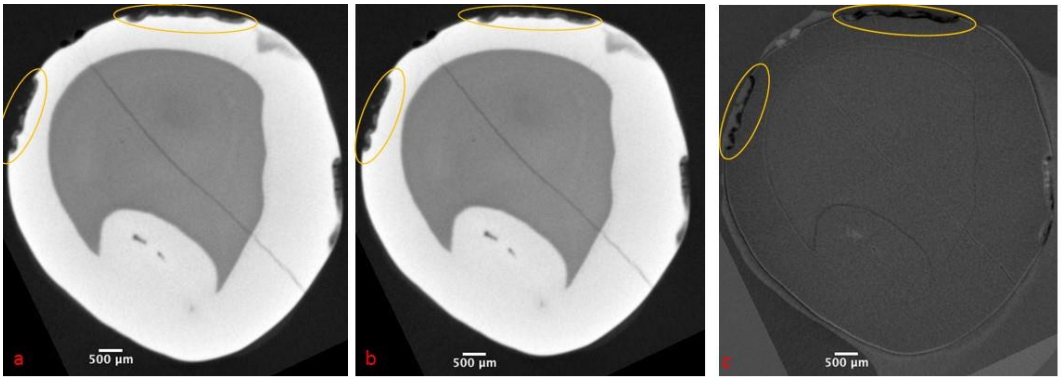

Figure 12.13 Sample DS5 - XMT images of artificial white spot lesions produced by static demineralisation pathway. (a,d) before, (b,e) after infiltration of ICON®, (c,f) subtracted XMT image. The scale bar is 500µm.

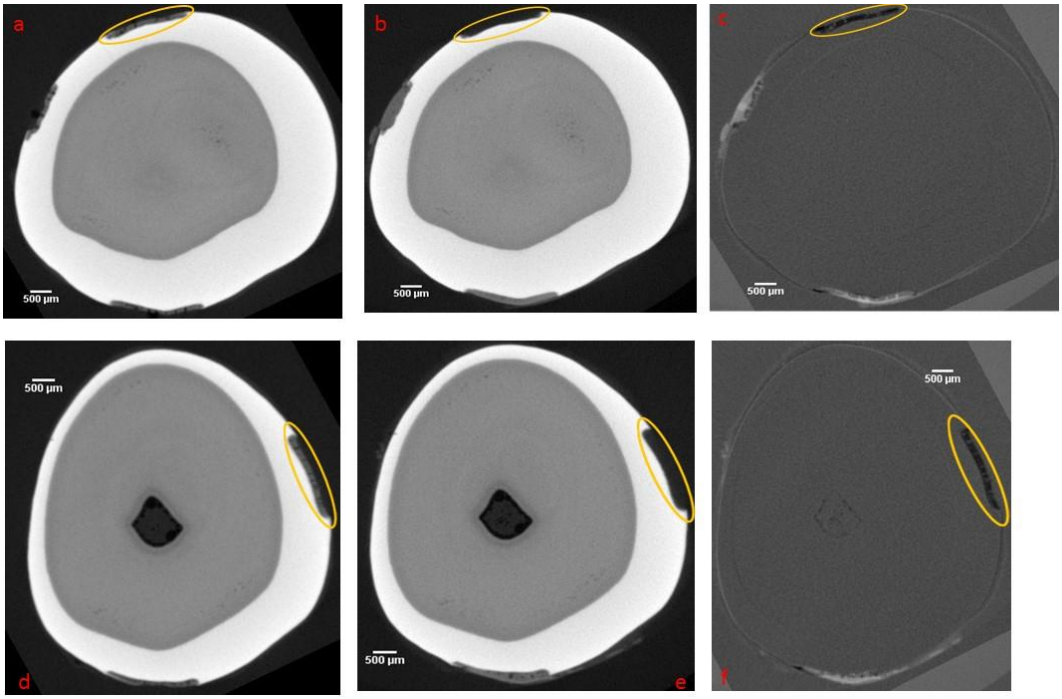

Figure 12.14 Sample DS6- XMT images of artificial white spot lesions produced by static demineralisation pathway. (a,d) before, (b,e) after infiltration of ICON®, (c,f) subtracted XMT image. The scale bar is 500µm.

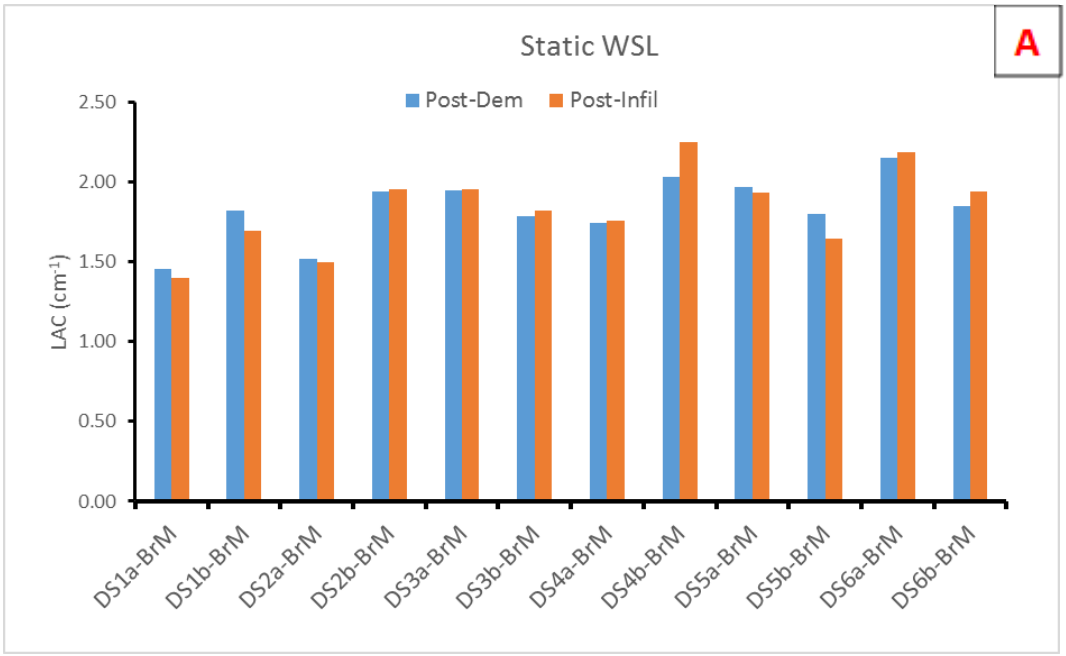

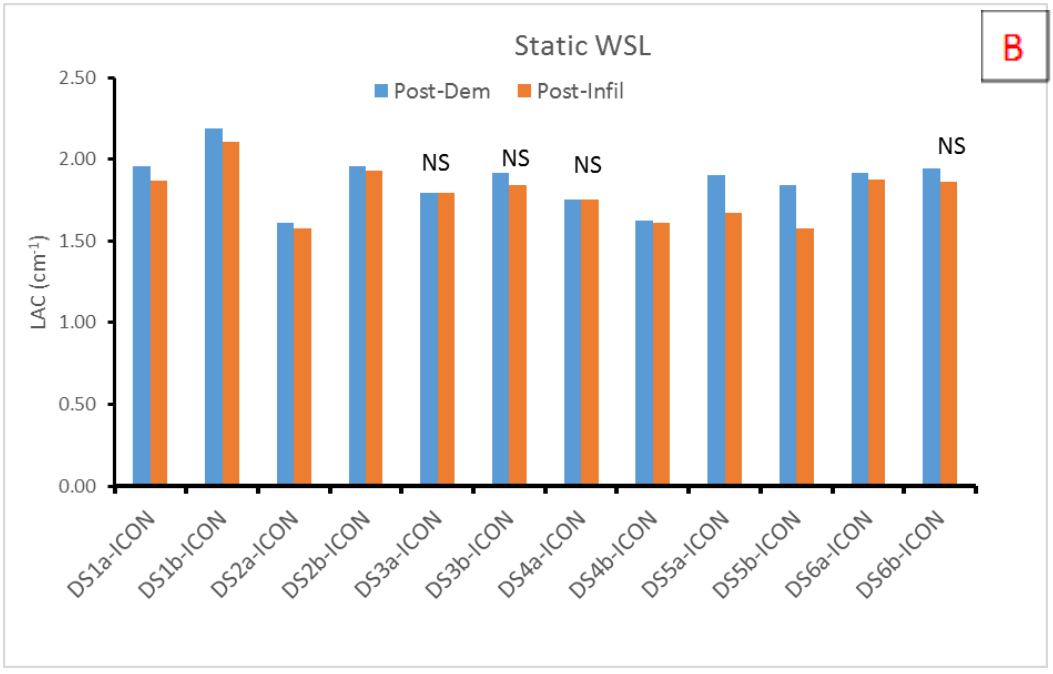

Figure 12.15 Mean LAC of the artificial WSL (static pathway) before and after infiltration with 30wt%BrM in ICON® (A), and ICON® (B) resins. NS – the difference is not significant.

Table 12.2 The mean LACs (standard deviation) for each lesion before and after infiltration with 30wt%BrM in ICON®. *p*-value <0.05 was statistically significant.

Specimen	Post-Dem LAC (sd) cm^{-1}	Post-30wt%BrM+ICON® LAC (sd) cm^{-1}	t-Test (*p* value)
DS1a-BrM	1.45(o.44)	1.39(0.43)	<0.001
DS1b-BrM	1.82(0.23)	1.69(0.26)	<0.001
DS2a-BrM	1.51(o.12)	1.49(0.16)	<0.001
DS2b-BrM	1.93(0.11)	1.95(0.10)	<0.001
DS3a-BrM	1.94(0.27)	1.95(0.27)	<0.001
DS3b-BrM	1.78(0.24)	1.82(0.26)	<0.001
DS4a-BrM	1.74(0.41)	1.75(0.4)	0.08
DS4b-BrM	2.02(0.37)	2.24(0.66)	<0.001
DS5a-BrM	1.94(0.40)	1.90(0.40)	<0.001
DS5b-BrM	1.79(0.61)	1.63(0.62)	<0.001
DS6a-BrM	2.20(0.14)	1.63(0.15)	<0.001
DS6b-BrM	1.82(0.39)	1.91(0.30)	<0.001

Table 12.3 The mean LACs (standard deviation) for each lesion before and after infiltration with ICON®. The *p*-value is from paired t-test comparing the means of the LACs.

Specimen	Post-Dem LAC (sd) cm^{-1}	Post-ICON® LAC (sd) cm^{-1}	t-Test (*p* value)
DS1a-ICON®	1.96 (0.52)	1.87(0.52)	<0.001
DS1b-ICON®	2.18(0.14)	2.11(0.15)	<0.001
DS2a-ICON®	1.60 (0.41)	1.57(0.40)	<0.01
DS2b-ICON®	1.95(0.13)	1.93(0.14)	<0.05
DS3a-ICON®	1.79(0.52)	1.79(0.52)	0.09
DS3b-ICON®	1.91(0.25)	1.84(0.26)	0.47
DS4a-ICON®	1.75(0.14)	1.75(0.14)	0.84
DS4b-ICON®	1.62(0.23)	1.61(0.23)	<0.001
DS5a-ICON®	1.90(0.15)	1.67(0.13)	<0.001
DS5b-ICON®	1.84(0.42)	1.57(0.45)	<0.001
DS6a-ICON®	1.91(0.12)	1.87(0.13)	<0.001
DS6b-ICON®	1.94(0.45)	1.86(0.49)	0.09

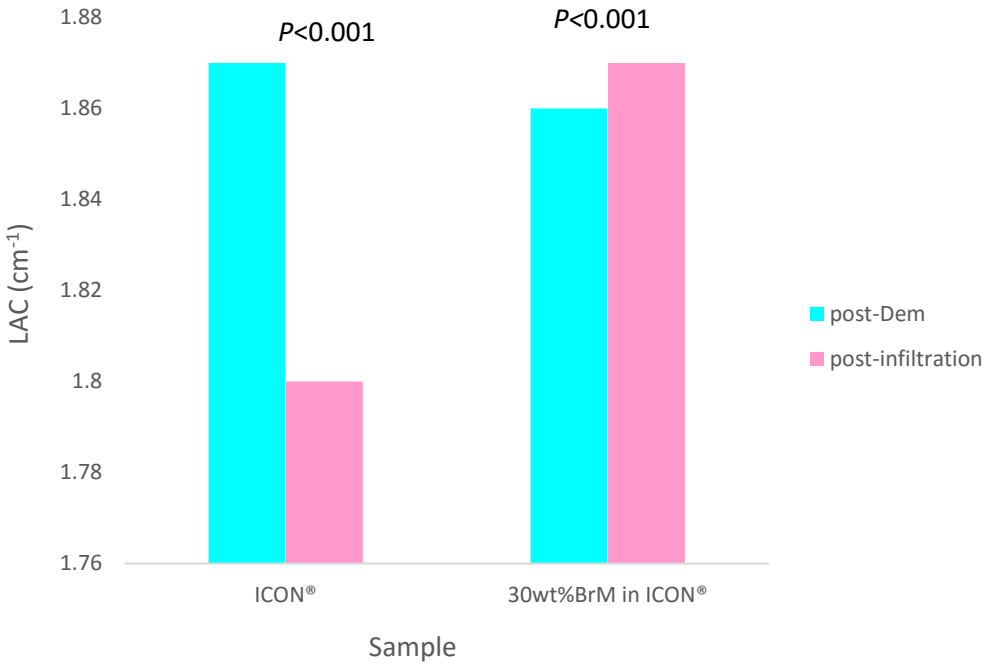

Figure 12.16 Global mean LACs of the artificial WSL (static pathway) before and after infiltration with either ICON® or 30wt%BrM in ICON® resins. The *p*-value was calculated from independent t-test.

12.5.2 Dynamic demineralisation method

Representative XMT images for the six teeth with artificial white spot lesion produced by dynamic demineralisation (cycles of de- and re-mineralisation) and infiltrated with either 30wt%BrM-ICON® or ICON® resin are shown in Figures 12.17-12.36. Generally, there was an increase of radiodensity of the lesion after remineralisation compared to the initial post-demineralised lesions (except for DD5 and DD6). For the lesions infiltrated with 30wt%BrM-ICON®, there was no particular trend in the change of radiodensities. For instance, in DD1 (Figure 12.17), there was a clear increase after 30wt%BrM-ICON® infiltration. However, in DD4 (Figure 12.22), there was a slightly increase in radiodensity in the right lesion whereas there was a decrease in radiodensity in the top lesion. After ICON® infiltration, there was a decrease in radiodensity in the post-remineralised WSLs. In Figure 12.37 and Tables 12.4-12.5, the mean LAC per lesion was calculated, most post-remineralised lesions had significant increase ($p<0.05$) in LACs, except DS-5a lesion in 30wt%BrM-ICON® group and DD-5 and DD-6a lesions in ICON® group.

For 30wt%BrM-ICON® infiltrated lesions, 4 lesions had significant increases in radiopacity (p<0.05), whilst 5 lesions had significant decreases (p<0.05) and there was a decrease in LACs of three lesions with no statistical significant changes (p>0.05).

For post-ICON® infiltrations, there was a significant decrease in LACs except DS-5b and DS-6a with no statistically significant decrease.

When the global means for all the lesions were taken (Figure 12.38), the was a significant increase in LACs after remineralisation, and a significant decrease after ICON® infiltrations. Although there was a decrease in LAC after 30wt%BrM-ICON® infiltration, the decrease was not significant (p>0.05). The LACs in WLS after 30wt%BrM-ICON® infiltration was significantly higher than that after ICON® infiltration (p<0.001).

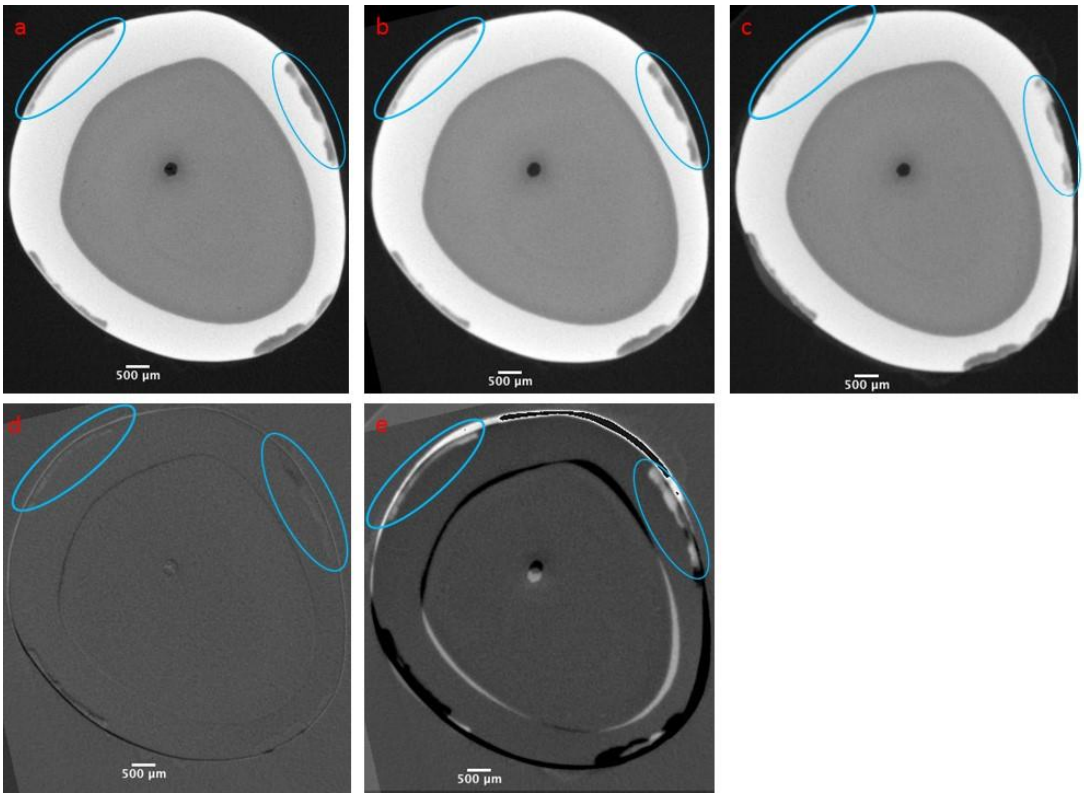

Figure 12.17 Sample DD1- XMT images of artificial white spot lesions (blue circle) produced by dynamic demineralisation pathway. (a) before, (b) after remineralisation, (c) after infiltration of 30wt%BrM-ICON®, (d) subtracted XMT image between post-demineralisation and post-remineralisation, (e) subtracted XMT image after infiltration of 30wt%BrM-ICON® in post-remineralised lesion. The scale bar is 500µm.

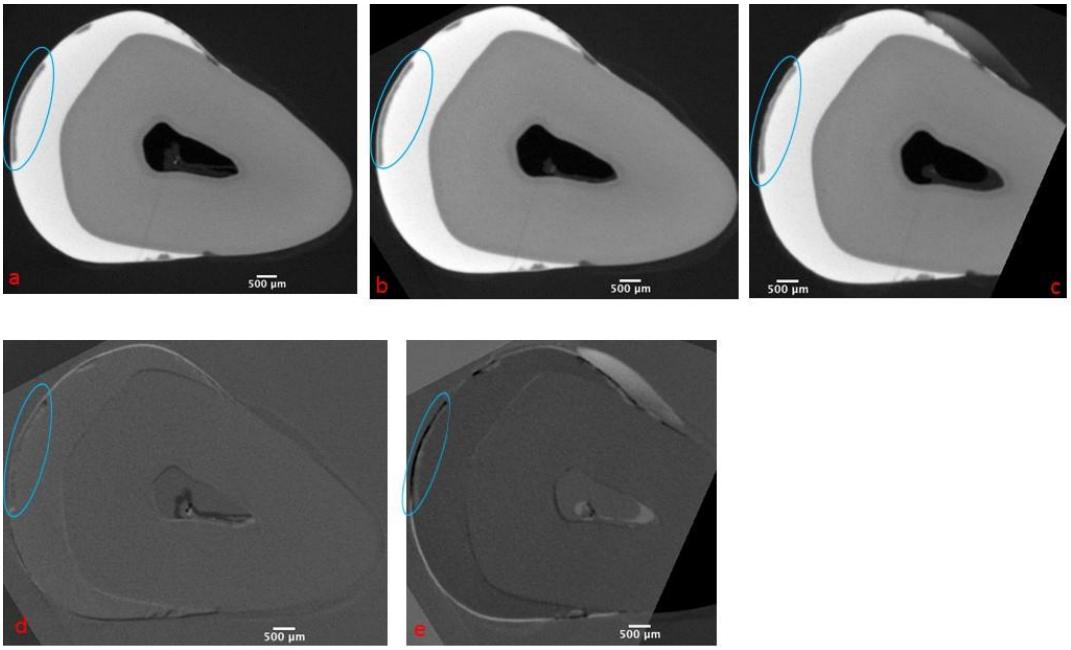

Figure 12.18 Sample DD2a- XMT images of artificial white spot lesions (blue circle) produced by dynamic demineralisation pathway. (a) before, (b) after remineralisation, (c) after infiltration of 30wt%BrM-ICON®, (d) subtracted XMT image between post-demineralisation and post-remineralisation, (e) subtracted XMT image after infiltration of 30wt%BrM-ICON® in post-remineralised lesion. The scale bar is 500µm.

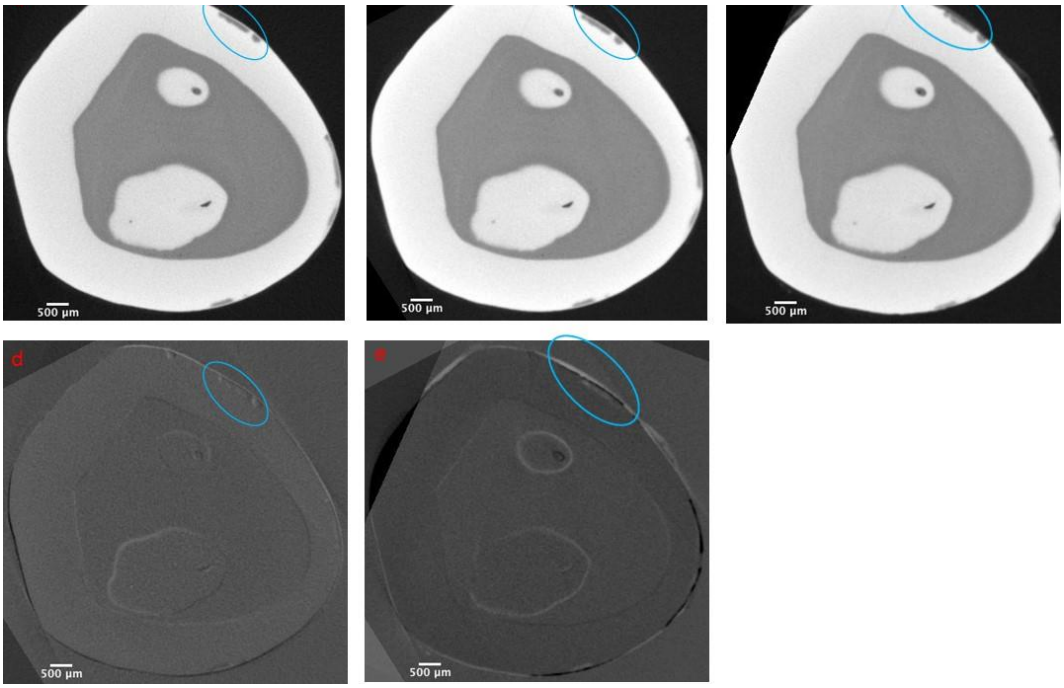

Figure 12.19 Sample DD2b- XMT images of artificial white spot lesions (blue circle) produced by dynamic demineralisation pathway. (a) before, (b) after remineralisation, (c) after infiltration of 30wt%BrM-ICON®, (d) subtracted XMT image between post-demineralisation and post-remineralisation, (e) subtracted XMT image after infiltration of 30wt%BrM-ICON® in post-remineralised lesion. The scale bar is 500µm.

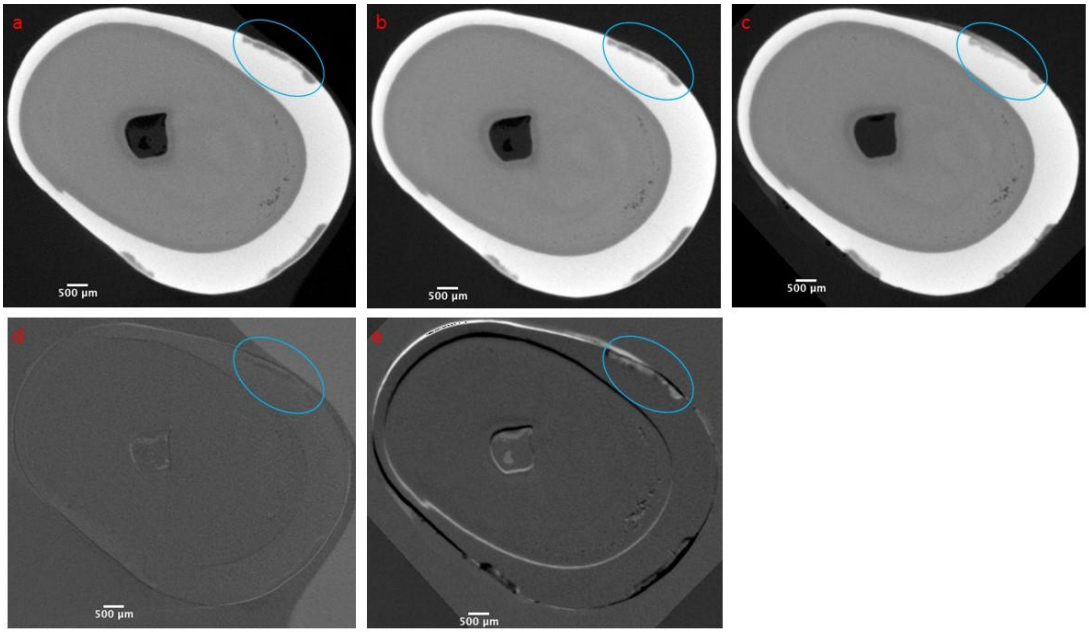

Figure 12.20 Sample DD3a- XMT images of artificial white spot lesions (blue circle) produced by dynamic demineralisation pathway. (a) before, (b) after remineralisation, (c) after infiltration of 30wt%BrM-ICON®, (d) subtracted XMT image between post-demineralisation and post-remineralisation, (e) subtracted XMT image after infiltration of 30wt%BrM-ICON® in post-remineralised lesion. The scale bar is 500µm.

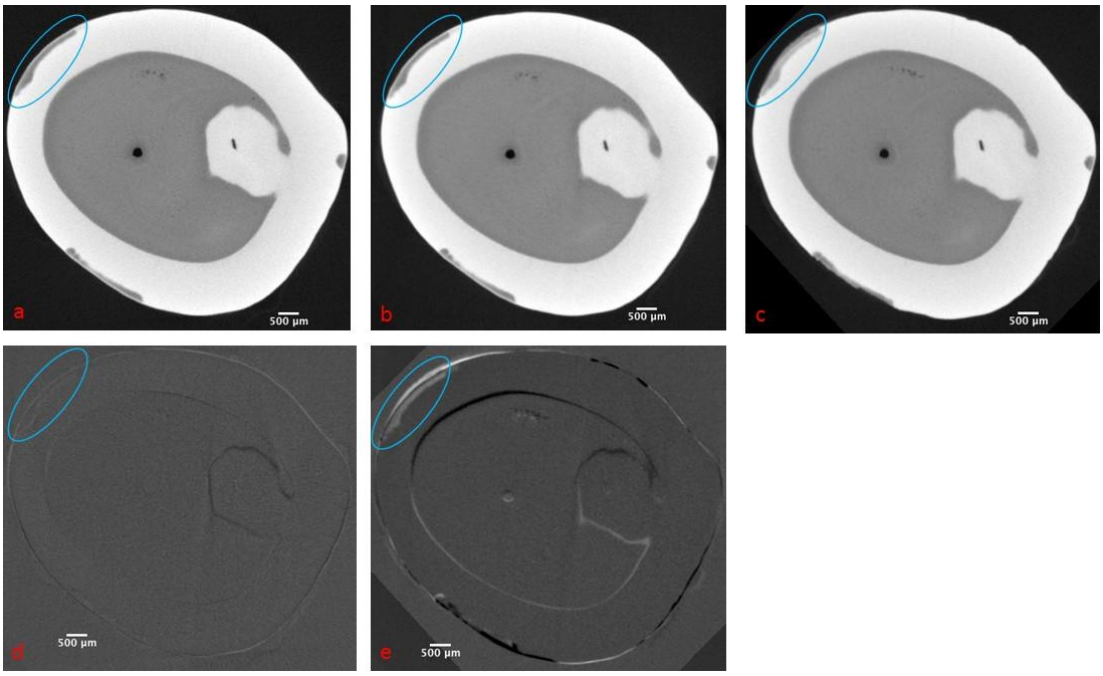

Figure 12.21 Sample DD3b- XMT images of artificial white spot lesions (blue circle) produced by dynamic demineralisation pathway. (a) before, (b) after remineralisation, (c) after infiltration of 30wt%BrM-ICON®, (d) subtracted XMT image between post-demineralisation and post-remineralisation, (e) subtracted XMT image after infiltration of 30wt%BrM-ICON® in post-remineralised lesion. The scale bar is 500µm.

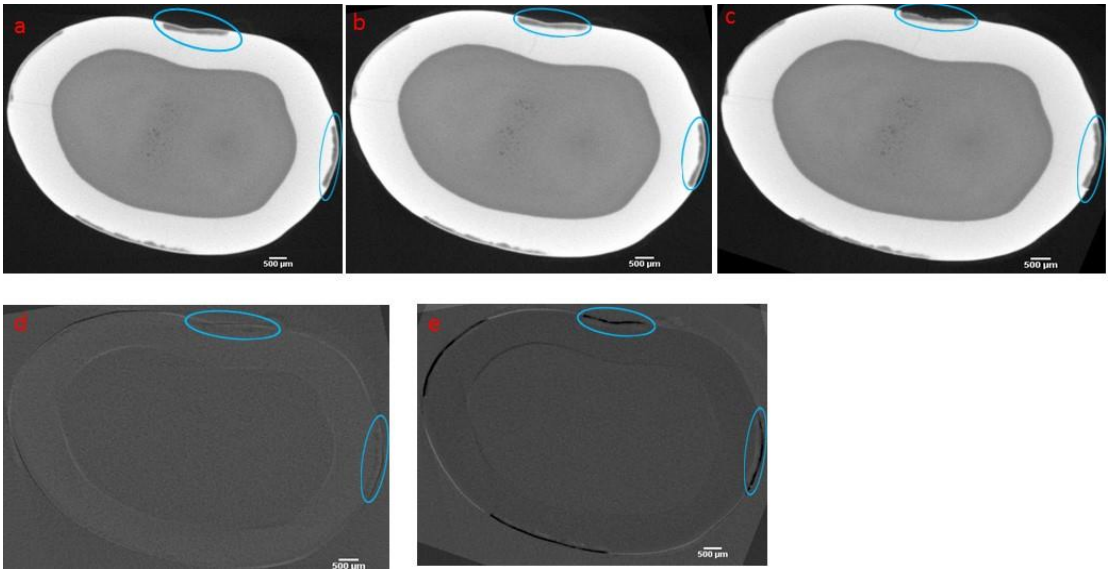

Figure 12.22 Sample DD4- XMT images of artificial white spot lesions (blue circle) produced by dynamic demineralisation pathway. (a) before, (b) after remineralisation, (c) after infiltration of 30wt%BrM-ICON®, (d) subtracted XMT image between post-demineralisation and post-remineralisation, (e) subtracted XMT image after infiltration of 30wt%BrM-ICON® in post-remineralised lesion. The scale bar is 500µm.

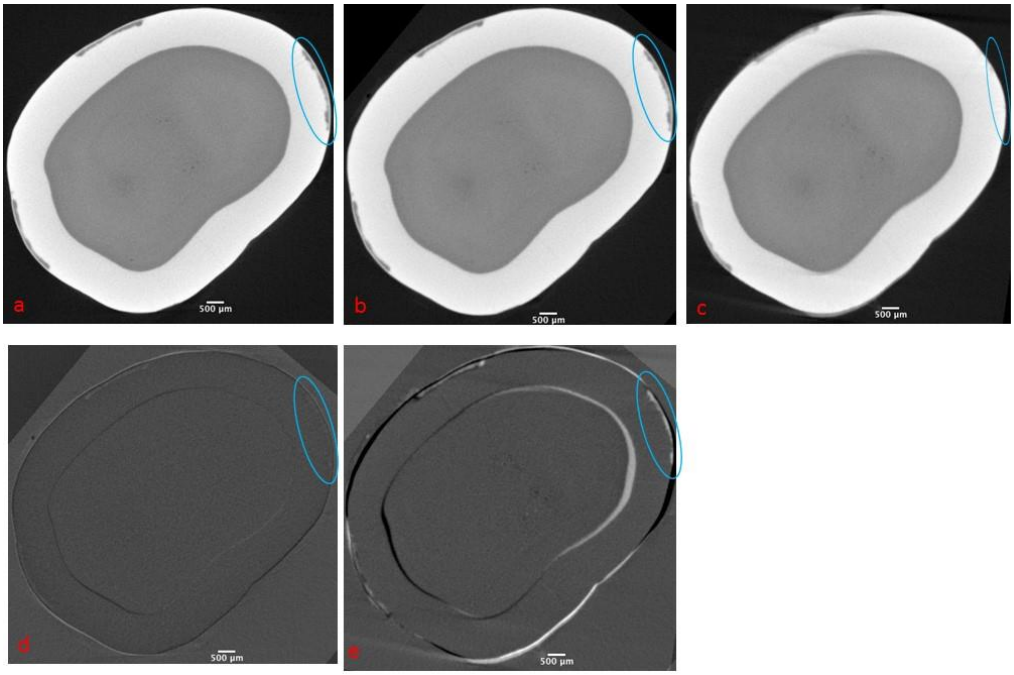

Figure 12.23 Sample DD5a- XMT images of artificial white spot lesions (blue circle) produced by dynamic demineralisation pathway. (a) before, (b) after remineralisation, (c) after infiltration of 30BrM-ICON®, (d) subtracted XMT image between post-demineralisation and post-remineralisation, (e) subtracted XMT image after infiltration of 30wt%BrM-ICON® in post-remineralised lesion. The scale bar is 500µm.

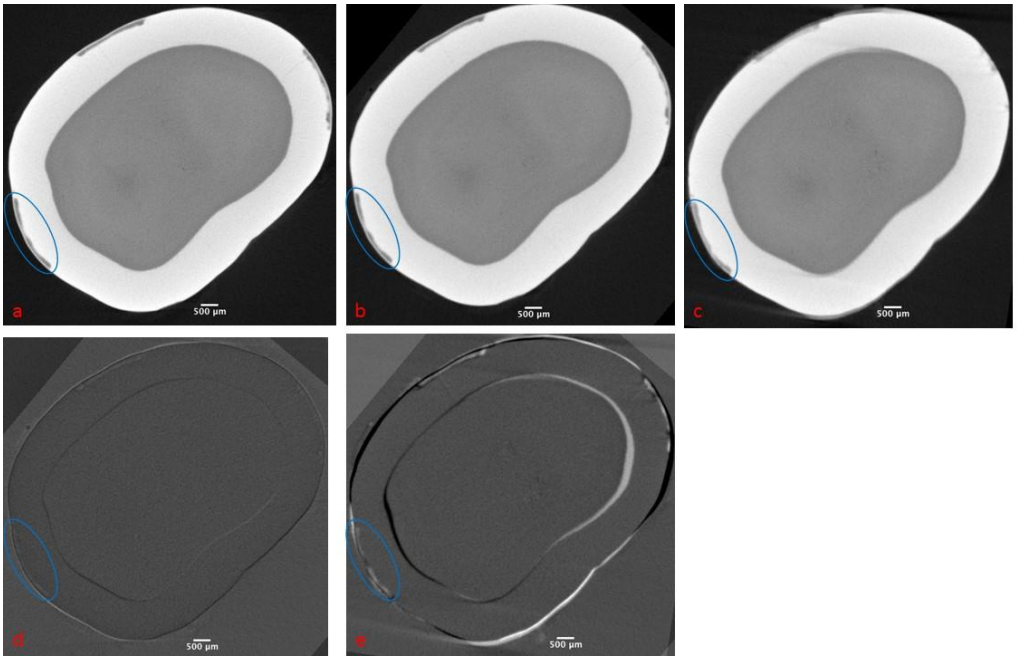

Figure 12.24 Sample DD5b-BrM - XMT images of artificial white spot lesions (blue circle) produced by dynamic demineralisation pathway. (a) before, (b) after remineralisation, (c) after infiltration of 30BrM-ICON®, (d) subtracted XMT image between post-demineralisation and post-remineralisation, (e) subtracted XMT image after infiltration of 30wt%BrM-ICON® in post-remineralised lesion. The scale bar is 500µm.

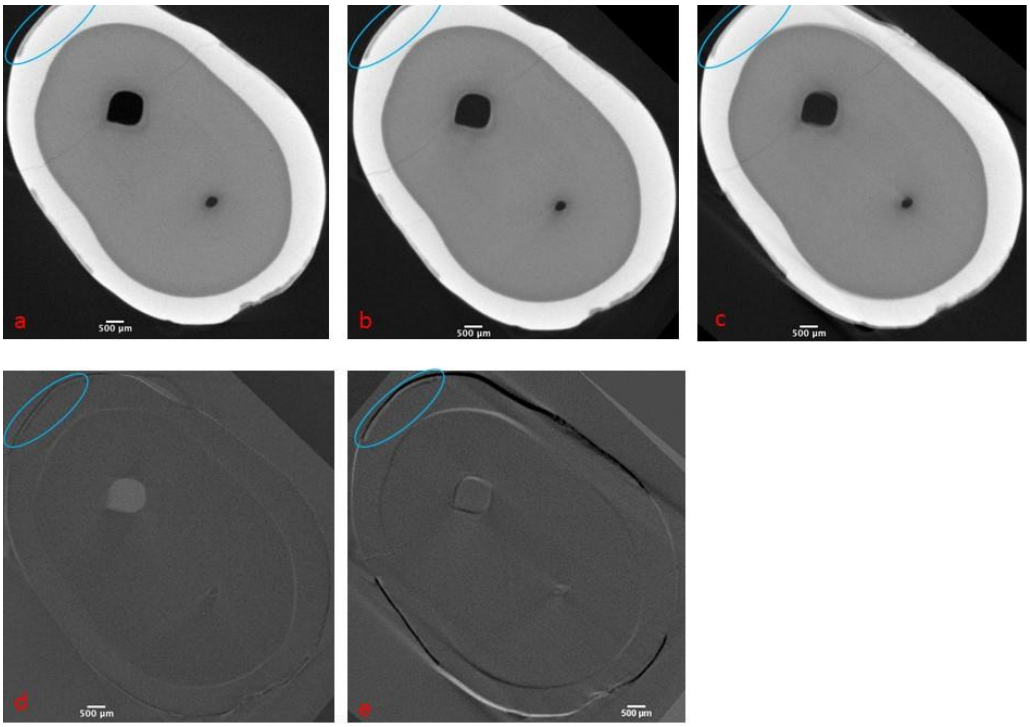

Figure 12.25 Sample DD6a- XMT images of artificial white spot lesions (blue circle) produced by dynamic demineralisation pathway. (a) before, (b) after remineralisation, (c) after infiltration of 30wt%BrM-ICON®, (d) subtracted XMT image between post-demineralisation and post-remineralisation, (e) subtracted XMT image after infiltration of 30wt%BrM-ICON® in post-remineralised lesion. The scale bar is 500µm.

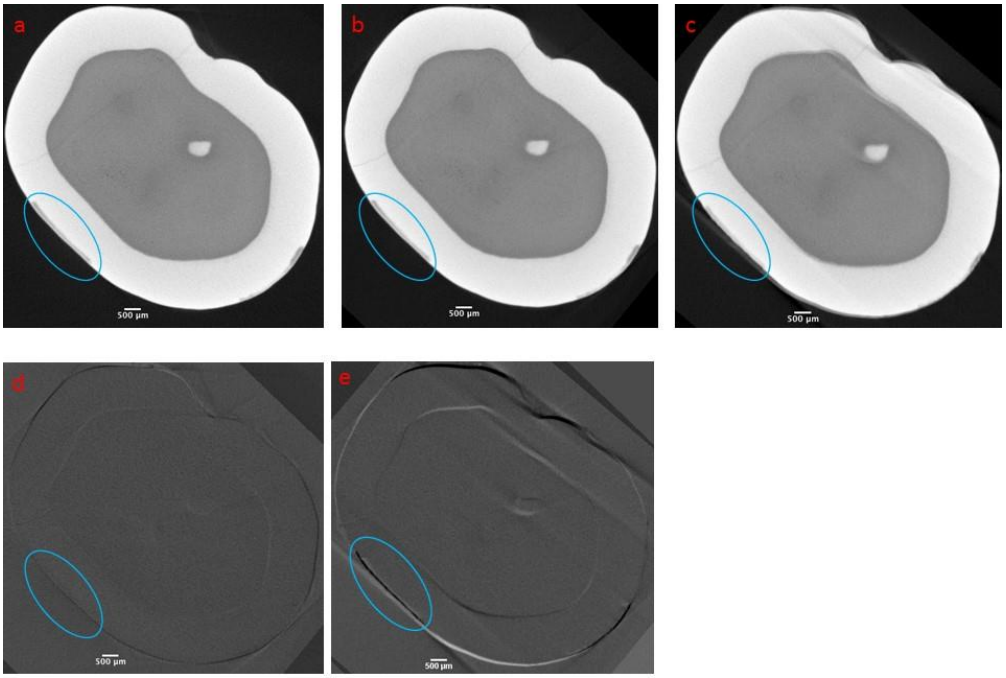

Figure 12.26 Sample DD6b- XMT images showing infiltration in artificial white spot lesions produced by dynamic demineralisation pathway (sample-6, Lesion- 2): (a) before, (b) after remineralisation, (c) after infiltration of 30wt%BrM-ICON®, (d) subtracted XMT image showing remineralisation, (e) subtracted XMT image showing infiltration of 30wt%BrM-ICON®. The scale bar is 500µm.

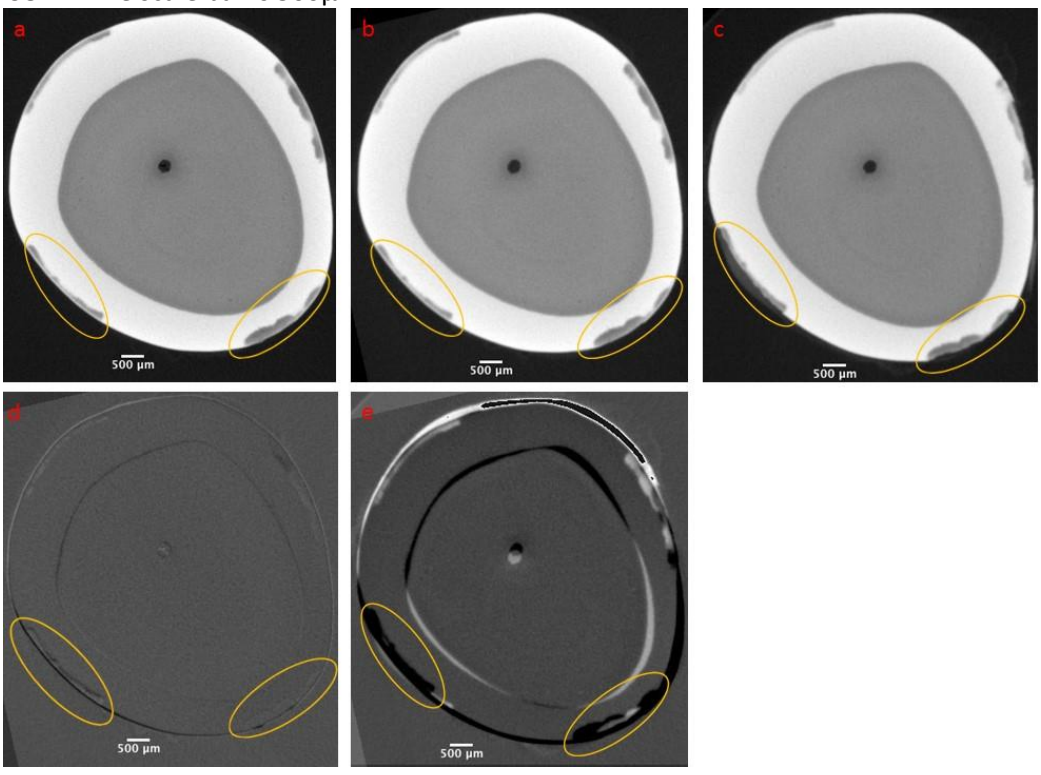

Figure 12.27 Sample DD1- XMT images of artificial white spot lesions (yellow circle) produced by dynamic demineralisation pathway. (a) before, (b) after remineralisation, (c) after infiltration of ICON®, (d) subtracted XMT image between post-demineralisation and post-remineralisation, (e) subtracted XMT image after infiltration of ICON® in post-remineralised lesion. The scale bar is 500µm.

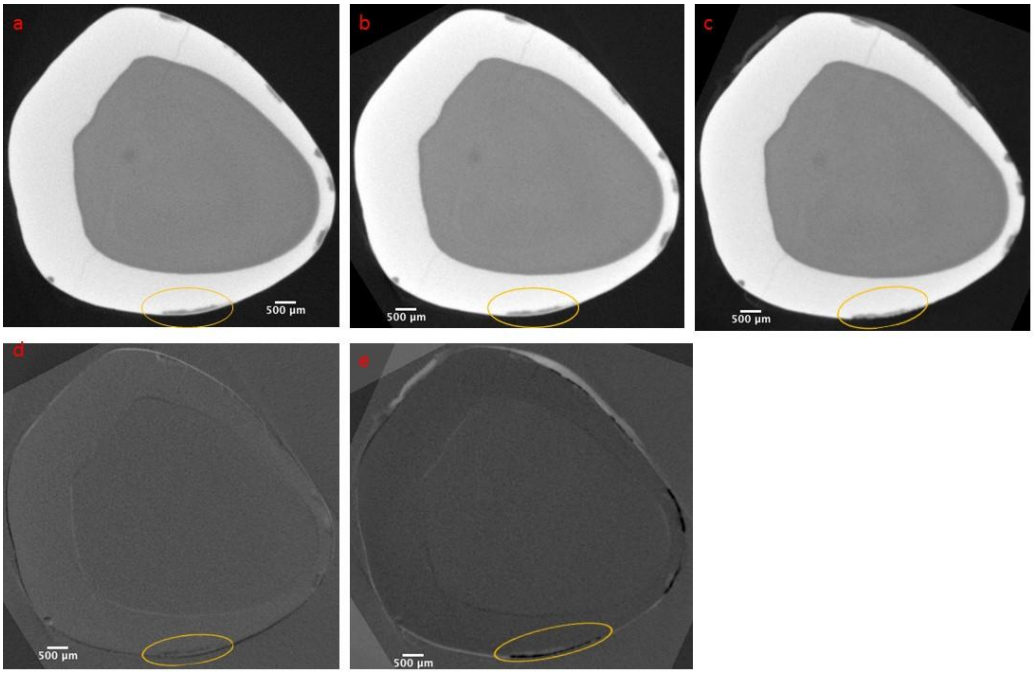

Figure 12.28 Sample DD2a- XMT images of artificial white spot lesions (blue circle) produced by dynamic demineralisation pathway. (a) before, (b) after remineralisation, (c) after infiltration of ICON®, (d) subtracted XMT image between post-demineralisation and post-remineralisation, (e) subtracted XMT image after infiltration of ICON® in post-remineralised show the lesion. The scale bar is 500µm.

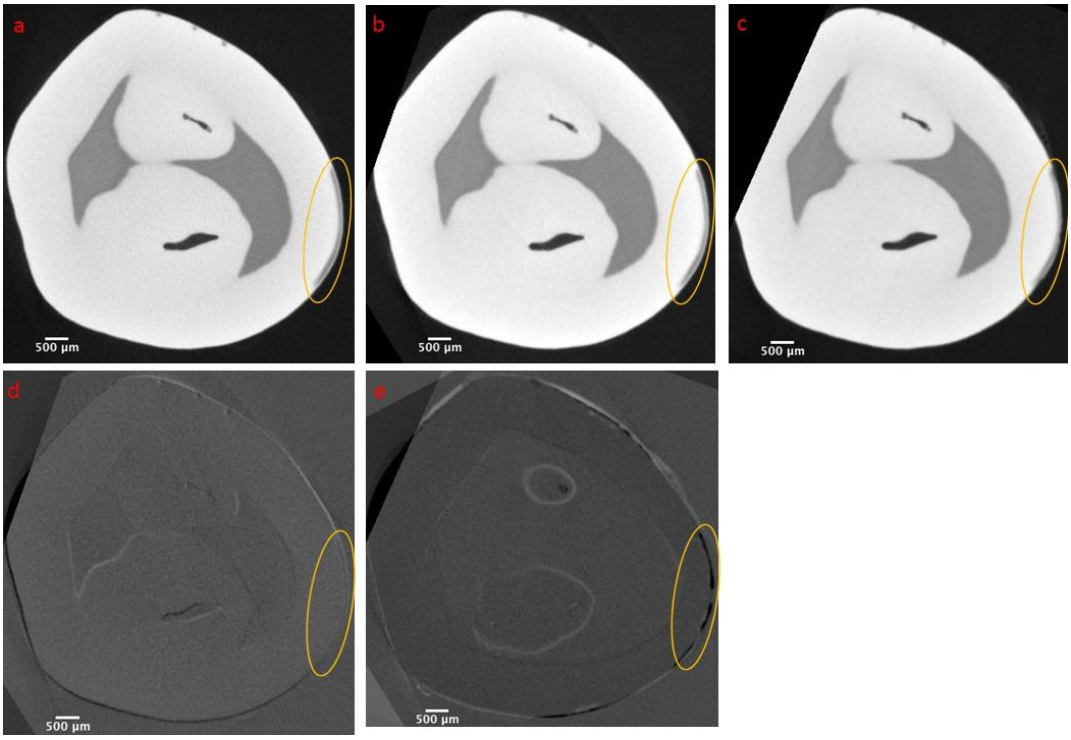

Figure 12.29 Sample DD2b- XMT images of artificial white spot lesions (yellow circle) produced by dynamic demineralisation pathway. (a) before, (b) after remineralisation, (c) after infiltration of ICON®, (d) subtracted XMT image between post-demineralisation and post-remineralisation, (e) subtracted XMT image after infiltration of ICON® in post-remineralised show the lesion. The scale bar is 500µm.

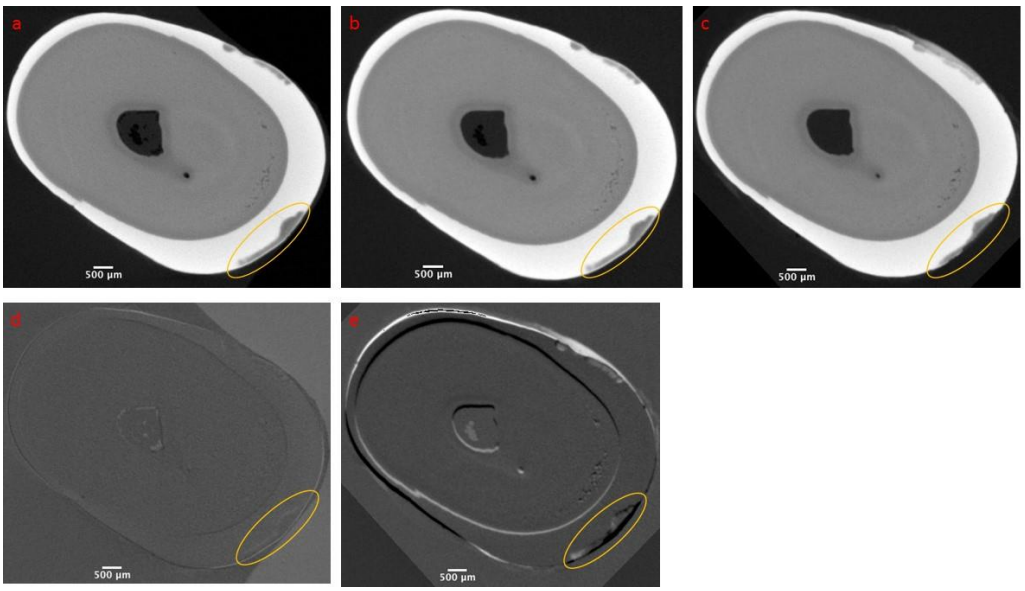

Figure 12.30 Sample DD3a- XMT images of artificial white spot lesions (yellow circle) produced by dynamic demineralisation pathway. (a) before, (b) after remineralisation, (c) after infiltration of ICON®, (d) subtracted XMT image between post-demineralisation and post-remineralisation, (e) subtracted XMT image after infiltration of ICON® in post-remineralised show the lesion. The scale bar is 500µm.

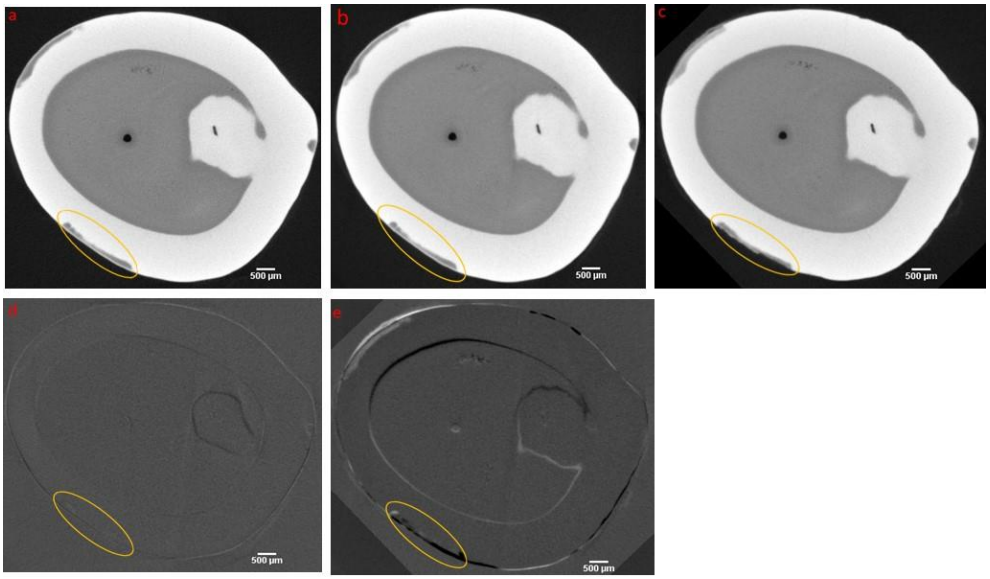

Figure 12.31 Sample DD3b- XMT images of artificial white spot lesions (yellow circle) produced by dynamic demineralisation pathway. (a) before, (b) after remineralisation, (c) after infiltration of ICON®, (d) subtracted XMT image between post-demineralisation and post-remineralisation, (e) subtracted XMT image after infiltration of ICON® in post-remineralised show the lesion. The scale bar is 500µm.

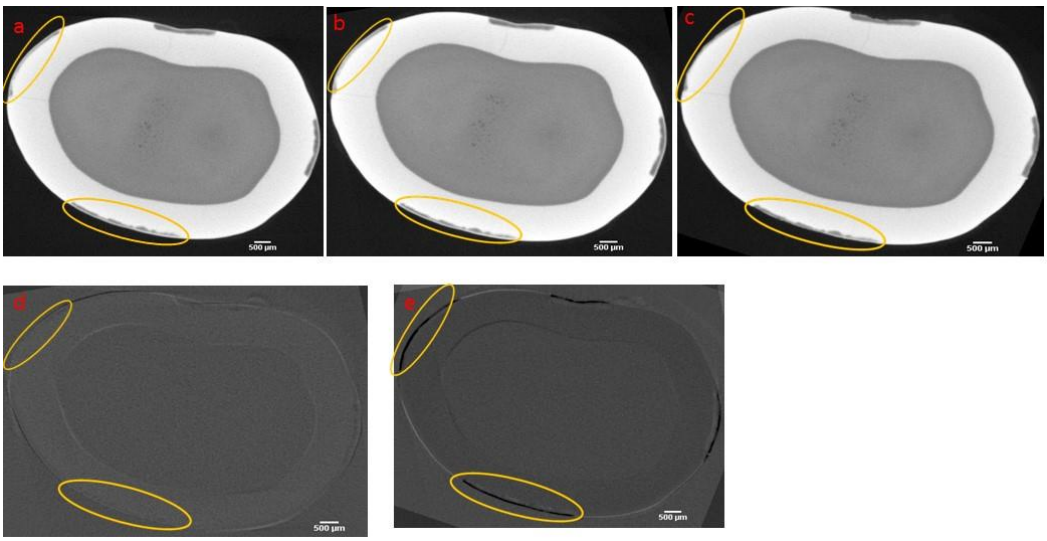

Figure 12.32 Sample DD4- XMT images of artificial white spot lesions (yellow circle) produced by dynamic demineralisation pathway. (a) before, (b) after remineralisation, (c) after infiltration of ICON®, (d) subtracted XMT image between post-demineralisation and post-remineralisation, (e) subtracted XMT image after infiltration of ICON® in post-remineralised show the lesion. The scale bar is 500µm.

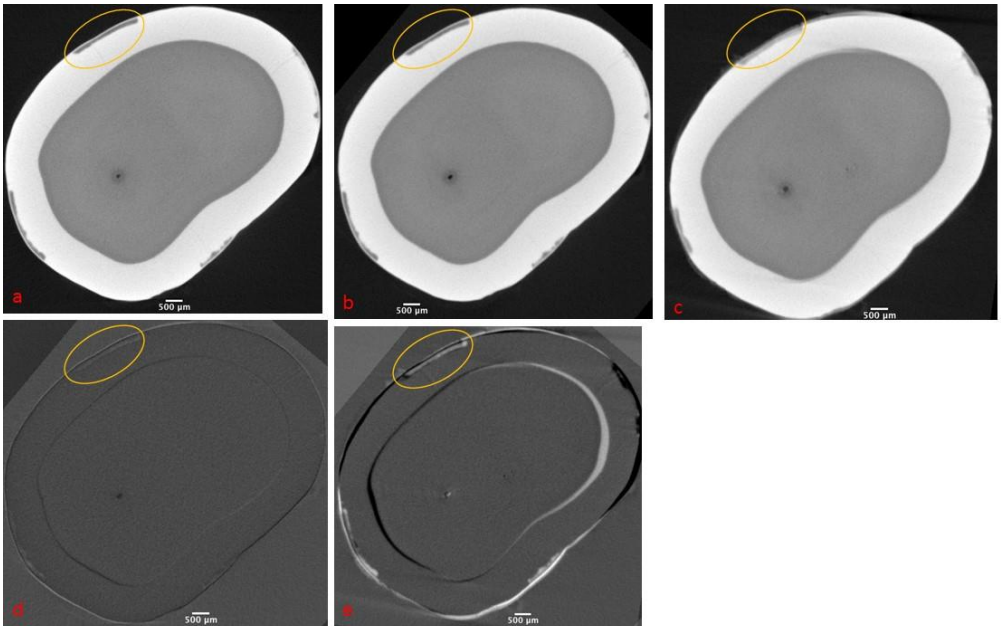

Figure 12.33 Sample DD5a- XMT images of artificial white spot lesions (yellow circle) produced by dynamic demineralisation pathway. (a) before, (b) after remineralisation, (c) after infiltration of ICON®, (d) subtracted XMT image between post-demineralisation and post-remineralisation, (e) subtracted XMT image after infiltration of ICON® in post-remineralised show the lesion. The scale bar is 500µm.

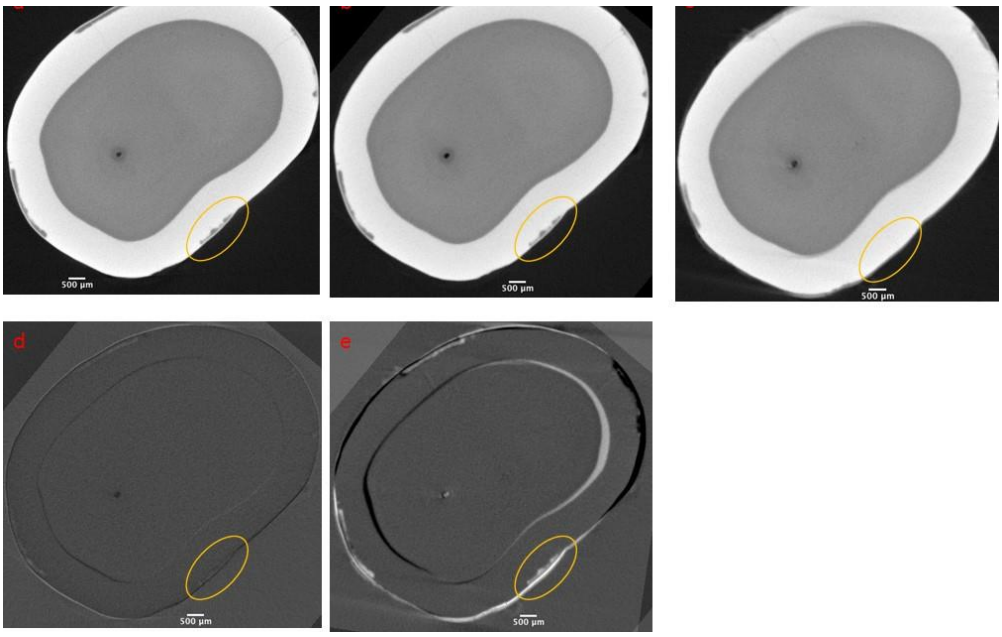

Figure 12.34 Sample DD5b- XMT images of artificial white spot lesions (yellow circle) produced by dynamic demineralisation pathway. (a) before, (b) after remineralisation, (c) after infiltration of ICON®, (d) subtracted XMT image between post-demineralisation and post-remineralisation, (e) subtracted XMT image after infiltration of ICON® in post-remineralisation, (e) subtracted XMT image showing infiltration of ICON®. The scale bar is 500µm.

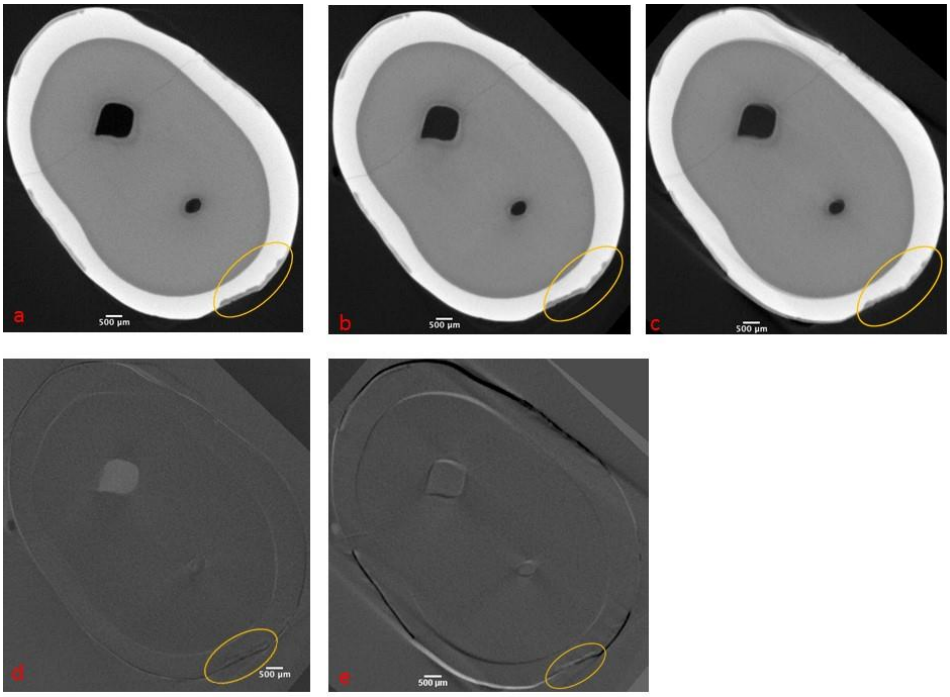

Figure 12.35 Sample DD6a- XMT images of artificial white spot lesions (yellow circle) produced by dynamic demineralisation pathway. (a) before, (b) after remineralisation, (c) after infiltration of ICON®, (d) subtracted XMT image between post-demineralisation and post-remineralisation, (e) subtracted XMT image after infiltration of ICON® in post-remineralised lesion. The scale bar is 500µm.

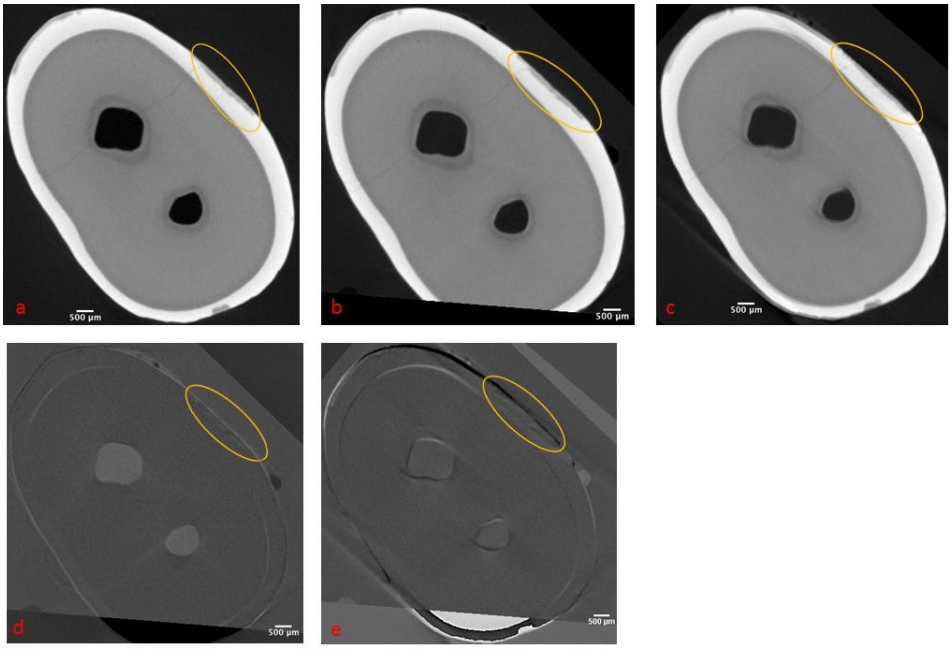

Figure 12.36 Sample DD6b- XMT images of artificial white spot lesions (yellow circle) produced by dynamic demineralisation pathway. (a) before, (b) after remineralisation, (c) after infiltration of ICON®, (d) subtracted XMT image between post-demineralisation and post-remineralisation, (e) subtracted XMT image after infiltration of ICON® in post-remineralised lesion. The scale bar is 500µm.

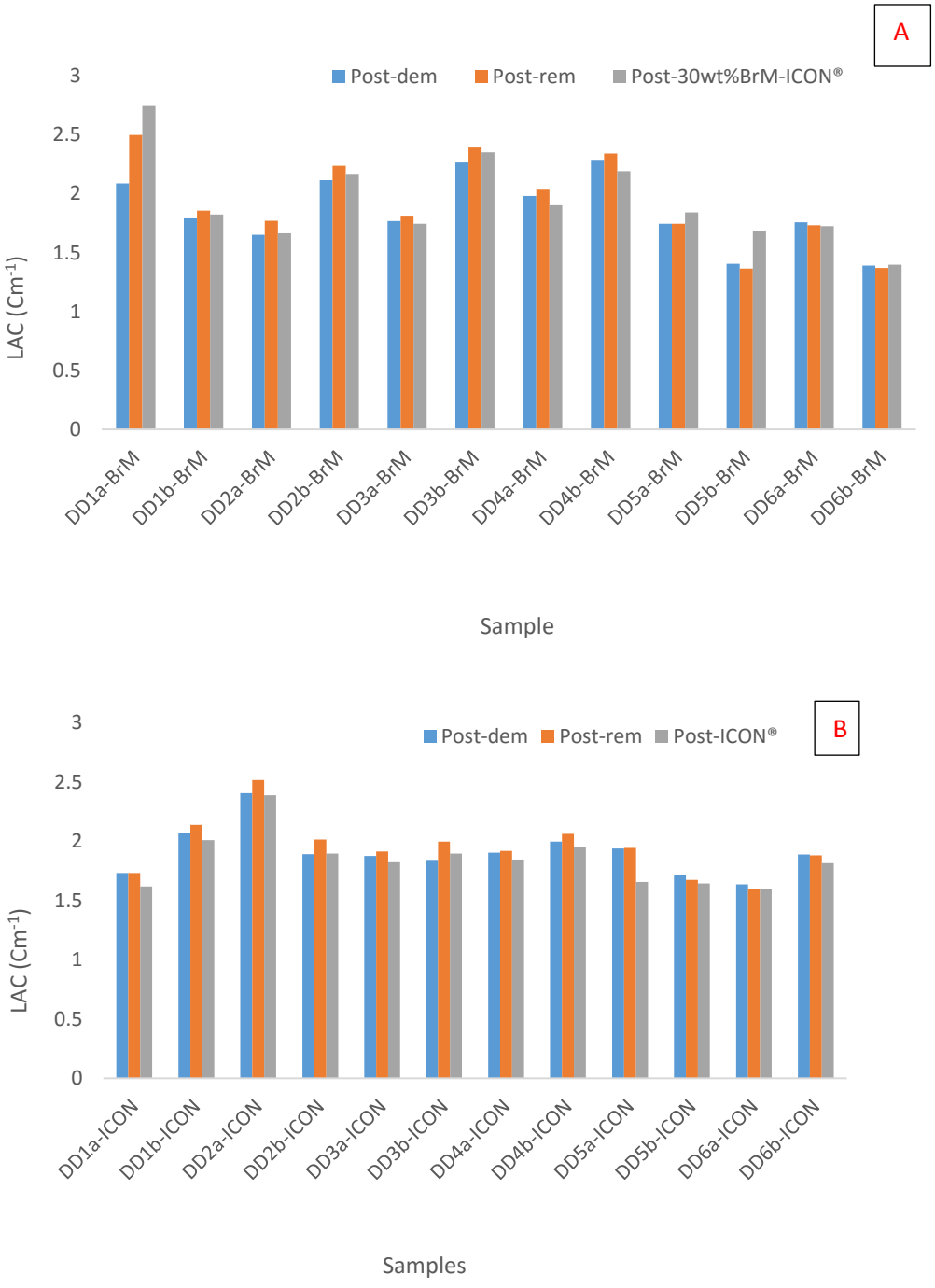

Figure 12.37 Mean LAC of the artificial WSL produced with dynamic demineralisation after de- and remineralisation and post-infiltration with 30wt% BrM in ICON® (A), and ICON® (B).

Table 12.4 The mean LACs (standard deviation) for each WSL lesion created by dynamic remineralisation before and after infiltration with 30wt%BrM-ICON®. $p<0.05$ was statistically significant.

Specimen	Post-Dem LAC(sd) cm^{-1}	Post-Rem LAC(sd) cm^{-1}	Post-30BrM+ICON LAC (sd) cm^{-1}	t-test Post-Rem (*p*-value)	t-test Post - 30BrM+ICON® (*p*-value)
DD1a-BrM	2.09	2.50	2.75	<0.001	<0.001
DD1b-BrM	1.79	1.86	1.82	<0.001	0.08
DD2a-BrM	1.65	1.77	1.66	<0.001	<0.001
DD2b-BrM	2.12	2.24	2.17	<0.001	<0.001
DD3a-BrM	1.77	1.81	1.74	<0.001	<0.001
DD3b-BrM	2.27	2.39	2.35	<0.001	0.20
DD4a-BrM	1.98	2.04	1.90	<0.001	<0.001
DD4b-BrM	2.29	2.34	2.19	<0.001	<0.001
DD5a-BrM	1.75	1.74	1.84	0.70	<0.001
DD5b-BrM	1.40	1.37	1.68	<0.001	<0.001
DD6a-BrM	1.76	1.73	1.72	<0.001	0.50
DD6b-BrM	1.39	1.37	1.40	<0.001	<0.001

Table 12.5 Mean LAC per WSL lesion after dynamic demineralisation and infiltrated with ICON®. $p<0.05$ was statistically significant.

Specimen	Post-Dem LAC (sd) cm^{-1}	Post-Rem LAC (sd) cm^{-1}	Post-ICON LAC (sd) cm^{-1}	t-test Post-Rem	t-test Post-ICON®
DD1a-ICON®	1.73	1.73	1.62	<0.001	<0.001
DD1b-ICON®	2.07	2.14	2.01	<0.001	<0.001
DD2a-ICON®	2.41	2.52	2.39	<0.001	<0.001
DD2b-ICON®	1.89	2.01	1.90	<0.001	<0.001
DD3a-ICON®	1.88	1.91	1.82	<0.001	<0.001
DD3b-ICON®	1.84	2.00	1.90	<0.001	<0.001
DD4a-ICON®	1.90	1.92	1.84	<0.001	<0.001
DD4b-ICON®	2.00	2.06	1.95	<0.001	<0.001
DD5a-ICON®	1.94	1.94	1.66	0.29	<0.001
DD5b-ICON®	1.72	1.67	1.65	0.17	0.31
DD6a-ICON®	1.64	1.60	1.59	0.001	0.32
DD6b-ICON®	1.89	1.88	1.82	<0.001	<0.001

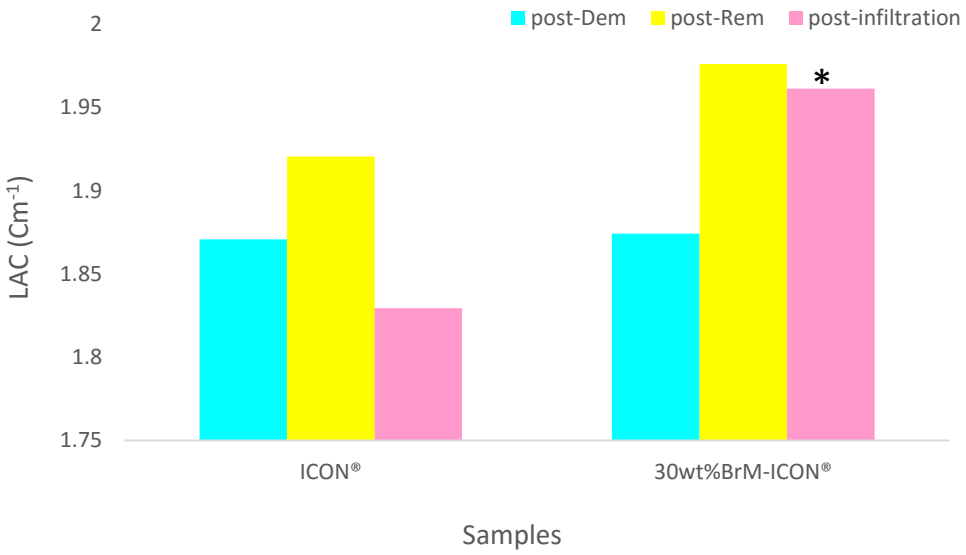

Figure 12.38 Global mean LACs of the artificial WSL after de- and remineralisation and after infiltration with ICON® or 30wt%BrM-ICON® resins. * denoted that the changes in LACs was not significant between post-remineralisation (post-Rem) and post-infiltration ($p>0.05$).

12.5.3 Penetration potential

The penetrations of 30wt%BrM-ICON®resin into the lesion depth was 85% and 96% in static and dynamic induced artificial white spot lesions, respectively. The penetration depth of the ICON® resin could not be calculated as this material is radiolucent and cannot be detected on XMT images (Table 12.6).

Table 12.6 The means of lesion depth, penetration depth and penetration potential of 30wt%BrM-ICON® into static and dynamic induced artificial white spot lesions.

	Number of lesions	Lesion Depth(µ)	Penetration Depth(µ)	Penetration Potential%
Static Demineralisation	12	27.0	23.1	85
Dynamic Demineralisation	12	87.2	83.7	96

12.6 Discussion

Since natural WSLs presented complex structure in Chapter 10, artificial induced WSLs can be used as a simplified model to investigate new concepts. In this experiment, two techniques including static and dynamic were used to create artificial WSLs. The static demineralisation method is a simple method but it does not simulate natural oral environment. The dynamic method has an added remineralisation step. The latter does simulate the actual de- and remineralisation cycles in the oral environment leading to create a lesion with a highly mineralised surface layer that mimics the natural WSL (Wefel and Harless 1984; Anderson *et al.* 2004; Elliott *et al.* 2005; Davies 2014).

Although the white spot lesions were produced in the same lab under the same condition by the same investigator, artificial white spot lesions showed a wide variation in size and shape with the different methods, with different teeth and also, with different surfaces of the same tooth. The current results were similar to the previous researchers' finding on variations in artificial WSLs (Paris *et al*. 2007, Meyer-Lueckel and Paris 2010). The following reasons might explain the variety in size and shape of artificial white spot lesions in this experiment. As previously mentioned, the teeth were collected from the anonymous tooth bank at Royal London Hospital and there was therefore no record of the relevant patients' data including their age or the reason of the extraction. It is assumed that the most common reasons to extract a tooth with ICDAS scoring 0 is either orthodontic reasons or periodontal disease. It should be mentioned that the mineral content of the tooth might be different from one individual to another as their oral environment and de- and remineralisation cycles vary. Previous studies have shown that fluoride accumulates in the enamel surface and converts the hydroxyapatite to fluorapatite with a lower solubility that is more resistant to demineralisation. Thus, it is expected to have a higher fluoride content in enamel if the individual is using the fluoridated toothpaste twice a day compared to someone with poor oral hygiene and irregular brushing habits with fluoridated toothpaste. Moreover, brushing with fluoridated toothpaste most likely could be a helpful method to clean the smooth surfaces of the tooth rather than proximal areas leading to a higher

fluoride content of enamel in smooth surfaces compared to the proximal areas and possibly resulting in a difference in solubility rate of the enamel on different surfaces of the tooth (Brudevold *et al*. 1956; Isaac *et al*. 1958; DePaola *et al*. 1975).

In chapter eight (Sections 8.5.3.2 and 8.5.3.4), it was shown that the radiopacity of the ICON® resin is equivalent to 0.27mm Al thickness while the value is 1.65mm Al thickness for the 30wt%BrM-ICON® resin. Therefore, it is assumed that the LAC should increase after infiltration of both materials and this value should be higher for 30wt%BrM-ICON®. However, the results showed that there was a significant decrease in LAC after the ICON® infiltration in artificial WSLs created by either the static or dynamic methods. This could be possibly attributed to the manufacturer's protocol that 15% of HCl was used to remove the surface layer before infiltration. The XMT images showed that the reductions of LACs were not confined to the surface but through the depth of the lesion. This finding was not reported before as previous studies only used histological examination to investigate penetration depth (Meyer-Lueckel and Paris 2010) or dental radiographs for caries progression after infiltration (Paris and Meyer-Lueckel 2010). Furthermore, there was a reduction of LAC in 30wt%BrM-ICON® group; however, the higher radiopacity of BrM has almost restored the radiodensity of the lesion before infiltration. This supports that the 30wt%BrM-ICON® has infiltrated well within the lesions produced by either static or dynamic demineralisation. Although in some lesions, the radiopacities of the radiopaque resin can be seen clearly, in some lesions, the penetration is not as noticeable.

It is interesting to note that even in this controlled experiments, there are notable differences in radiopacities among different lesions of the same tooth and also, in different areas of the same lesion. This shows that the enamel's reaction to demineralisation, and subsequent infiltration is not only tooth specific, but also site specific (Neel *et al.* 2016).

The penetration depth for 30wt%BrM in ICON® was 86% and 96% in static and dynamic groups, respectively. This finding is interesting as one would assume that the penetration depth would be high in the static group because there is no surface layer to inhibit its penetration. This shows that the complexity of the porous

structures in WSLs needs further investigation in order to ascertain the dynamic effect of de- and re-mineralising processes in enamel. With regard to ICON® alone, due to its lack of radiopacity, its penetration depth could not be measured with XMT.

12.7 Conclusion

The following null hypothesis were rejected:

- There is no statistical significant change ($p \geq 0.05$) in the linear attenuation coefficients (LACs) of the artificial white spot lesions (static pathway) before and after 30wt%BrM-ICON® infiltration (Figure 12.16).
- There is no statistical significant change ($p \geq 0.05$) in the LACs of the artificial white spot lesions (static pathway) before and after ICON® infiltration (Figure 12.16).
- The increase in LAC in artificial WSLs (static pathway) after 30wt%BrM-ICON® is not significantly different ($p \geq 0.05$) to that of LACs after ICON® infiltration (Figure 12.16).
- There is no statistical significant change ($p \geq 0.05$) in the LACs of the artificial white spot lesions (dynamic pathway) before and after ICON® infiltration (Figure 12.38).
- The increase in LAC in artificial WSLs (dynamic pathway) after 30wt%BrM-ICON® is not significantly different ($p \geq 0.05$) to that of LACs after ICON® infiltration (Figure 12.38).

The following null hypothesis were failed to be rejected:

- There is no statistical significant change ($p \geq 0.05$) in the LACs of the artificial white spot lesions (dynamic pathway) before and after 30wt%BrM-ICON® infiltration(Figure 12.38).

The 30wt%BrM-ICON® resin is relatively radiopaque material and it is able to infiltrate into the artificial white spot lesion.

Chapter 13- SEM Study of Enamel Surface Change during the Infiltration Procedure

13.1 Introduction

In the current study, the experimental radiopaque resins including 20 and 30wt% bromine-methacrylate (BrM) and 40wt% tin-methacrylate (SnM) in ICON® resin were radiopaque and had a suitable penetration ability. Although the radiopacity of the infiltrated materials into WSLs could not be detected clinically, the subtracted digital radiographs were able to detect the radiopaque infiltrant resins. Furthermore, the penetration depth of the radiopaque resins varied in different teeth and even in different areas of the same lesion. Based on these findings, we believe that it is useful to understand and address the barrier(s) to full penetration of the experimental radiopaque resins prior to increasing their radiopacity. Therefore, this study was to examine the surface topography, following each step of resin infiltration application, using scanning electron microscopy (SEM).

13.1.1 Scanning Electron Microscopy (SEM)

The electron microscope was developed when the wavelength became the limiting factor in optical microscopy. Electrons with much shorter wavelengths could provide an image with a much higher resolution.

SEM is a technique to study the surface topography and determine the chemical composition of the specimen by using a unique medium for imaging. Firstly, a high voltage applied to the electrons will accelerate them in a high energy beam, with a short wavelength with the ability to image a small specimen; then, the image will be produced. The spatial resolution of electron microscopes is higher and is typically between 1-10nm. The reason is the use of electrons and magnifying lenses instead of light and conventional glass lenses.

Electrons of adjustable energy are generated by heating up a cathode using a high voltage. The cathode is made typically from a tungsten filament. The generated electrons are moving towards the anode, condensed by the condenser lenses and then directed towards the probe-forming lens, which focuses the beam on the sample (Figure 13.1) (Reimer 2000). When the electron beam hits the surface of the specimen and interacts, it forms a pear-shaped volume, known as interaction volume, in a sample surface including most of the scattered signals (Figure 13.2). This interaction volume determines the image properties in the SEM images and

can be increased by increasing the accelerating voltage. Samples with a higher atomic number will result in a reduction in the volume size. The produced signals will be then detected, amplified and produce a pixel intensity of the image on the screen and finally a sequentially formed image (Egerton 2005).

SEM images can be produced by using either the secondary electrons (SE) or the backscattered electron (BSE) signals. This depends on the specimen properties and the purpose of the experiment.

The secondary electrons are generated by the energy of incident beam and then escape from the outer shell of the atoms. Only those electrons, because of their low energy (ranging between 0 and 30eV), which are closer to the surface, could escape and be detected to produce SEM images. Therefore, the image in SE mode describes the specimen surface morphology.

On the other hand, the inelastic scattering of the incident beam which has an energy close to the primary beam (15-30keV), can be deflected back from the solid specimen. This BSE mode is useful to describe the bulk properties as most electrons will escape from the deeper part of the material surface (Figure 13.3). The number of back scattered electrons (BSE) can be used to determine the mineral density of the material because they are dependent on the mean atomic number of the specimen (Egerton 2005).

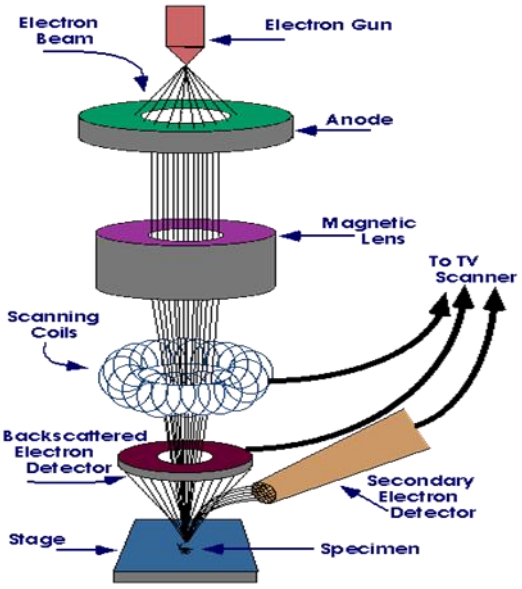

Figure 13.1 Schematic picture showing the principle of scanning electron microscopy (SEM) (http://www.purdue.edu, accessed on 07/06/2016).

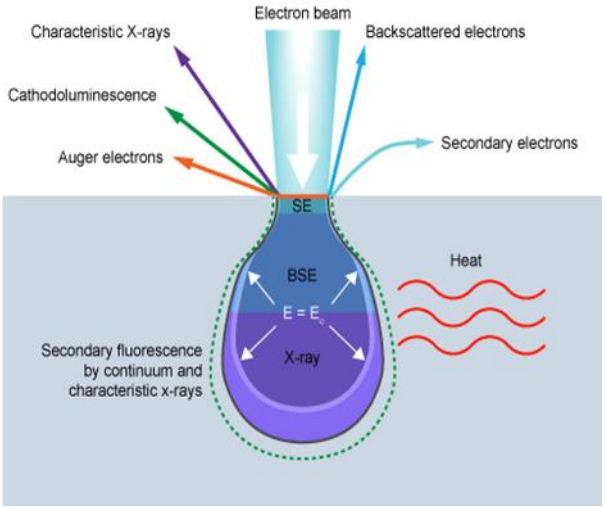

Figure 13.2 Schematic diagram showing the interaction volume and the types of scattered signals (http://www.ammrf.org.au, accessed on 07/06/2016).

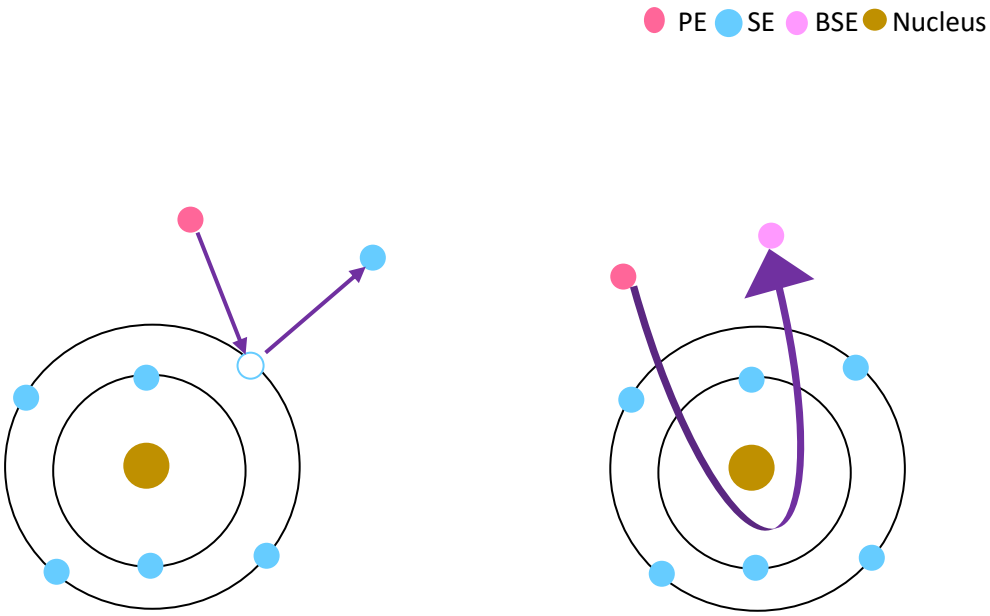

Figure 13.3 Schematic presenting the definition of primary electron (PE), secondary electron (SE) and backscatter electron (BSE).

A characteristic X-ray is a signal, produced by the interaction between the incident beams and the electron from atoms in the sample. It leads to the inner shell electron escape from its position followed by the outer shell electron occupation. The characteristic X-ray of each element will be detected and separated from each other by an energy- dispersive detector. Then, it will transform into an energy spectrum and will be analysed by its software to determine the sample elements' concentration. Energy Dispersive X-ray (EDX) Spectroscopy is a useful technique to analyse the elemental or the chemical characterisation of a sample in the scanned area (Velayudhan 2013).

SEM uses vacuum conditions and electrons to form an image; therefore, special sample preparation is required. Firstly, samples should be completely dried because the water would vaporise in the vacuum. Sputter coating was used to apply a thin layer of gold or carbon in order to coat non-conductive materials (non-metal materials). This prevents the charging of the sample with the electron beam. Charging results in image or scanning artefacts because the deflection of the primary beam is away from the sample.

13.2 Aims and objectives

The aim of this pilot study was to investigate the barrier(s) preventing penetration of infiltrant resins using BSE spectroscopy backscatter electron imaging after each of the following steps:

- Early enamel caries lesion on the tooth,
- Sodium hypochlorite (NaOCl) application,
- Etch the surface of lesion with 15% Hydrochloric acid (HCl) (4.1 molarity) for 2min,
- Application of the experimental radiopaque resins based on the manufacturer's instruction.

It should be noted that sodium hypochlorite application is not part of ICON® manufacturer's instruction; however, it has been added to the pilot study due to the presence of contamination on the surface of the teeth samples before treatment.

13.3 Materials and Methods

13.3.1 Sample Selection

Extracted premolars and molars teeth from Royal London Hospital tooth bank (approval from Queen Mary Research Ethics Committee, QMREC 2011/99), stored in 70% ethanol (Sigma-Aldrich, Gillingham, UK) were examined visually for white spot lesion in proximal surfaces by the current investigators. The examination was carried out by cleaning the tooth by bristle brush (Henry Schein, London, UK) and slow handpiece (NSK Ltd, Stevenage, UK), drying the tooth with compressed air, and using a good light (A-dec 6300 Light Bulb 17V, 95W, Mercia Dental, UK). Three teeth were selected and divided into three groups randomly. Each group was located to one type of experimental resin (Table 13.1).

Table 13.1 Teeth allocation for experimental resin infiltration.

Name of material	Identification (FDI Tooth Number)
20%wt BrM in ICON®	Br20 (35)
30%wt BrM in ICON®	Br30 (25)
40%wt SnM in ICON®	Sn40 (18)

13.3.2 Backscatter electron (BSE) imaging

Four BSE images were taken from WSL at 1nA and 20kV using a scanning electron microscopy (ZEISS, Oberkochen, Germany) for each tooth after each of the following steps: 1) An initial image before any treatment; 2) The specimen was immersed in sodium hypochlorite (NaOCl)(Sigma-Aldrich, Gillingham, UK) for 30 minutes at room temperature (25±1 °C), rinsed with distilled water for 30s and dried using the oil-free air; 3) 15% hydrochloric acid (HCl) gel etchant with 4.1 molarity (ICON®-etch, DMG, Hamburg, Germany) was applied on the WSL for 2 minutes, rinsed with distilled water for 30s, and dried using the oil-free air for 15s; 4) Ethanol (ICON®-dry, DMG, Hamburg, Germany) was applied on the lesion for 30s followed by drying with a compressed air. Then, the first layer of allocated experimental resin was applied on the lesion and after 3 minutes, it was light-cured using a blue LED activation light at 400 mW/cm^2 for 40s (Demetron LC, Ser no 66004022, KERR corporation, Danbury) on direct contact with the lesion. Then, the second layer of infiltrant resin was applied and light cured after 1 minute as described previously. The tooth sectioned from the middle of the WSLs using a cutting machine (Microslice 2, Malvern Instruments, Malvern, UK). A small notch was made about 3mm on the right side of the area of the interest by a fast handpiece (PANA-MAX, NSK, Japan) and then the cross section was polished with 200, 500 and 2000 grit SiC papers (Sigma-Aldrich, Gillingham, UK). Samples were ultra-sonicated for 5 minutes

using QS25 ultrasonic bath (Medisave, Weymouth, UK). Then, the final BSE image was taken.

13.3.3 Data Analysis

The BSE images were observed by examiners qualitatively. The final BSE image of each tooth was transferred to Image J™ (Image Processing and Analysis in Java, National Institute of Health, Bethesda, Maryland, USA) and penetration depth (PD) was measured at 10 different areas of the cross section of the lesion. Penetration depth was defined as the distance from the enamel surface to the deepest point of resin presence.

13.4 Results

All samples showed lots of debris on the surface at the start point. The vast majority of debris was removed followed the application of NaOCl (Figure 13.4- 13.6). Following the HCl application, some parts of tooth surface were eroded and some remained intact resulting in a scooping pattern on the tooth surface. Furthermore, it was noticed that some etchant gel remained attached on the tooth surface after etch-rinse step (Figure 13.7). After application of the resin, there was interface between the resin and the surface of the WSL, with little resin penetration~ 2-10µm (Figure 13.8).

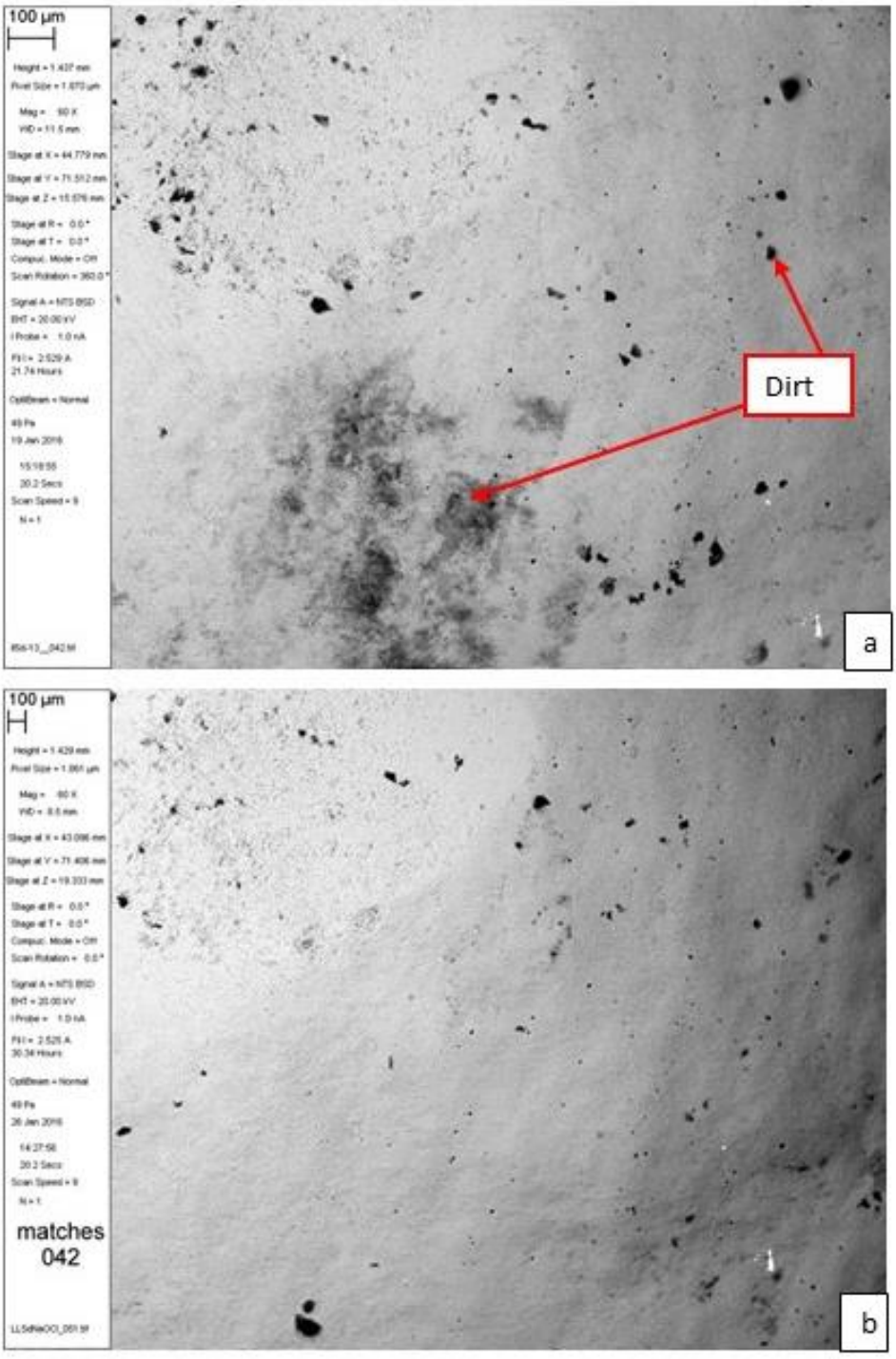

Figure 13.4 BSE images of tooth Br20 (a) before and, (b) after application of NaOCl.

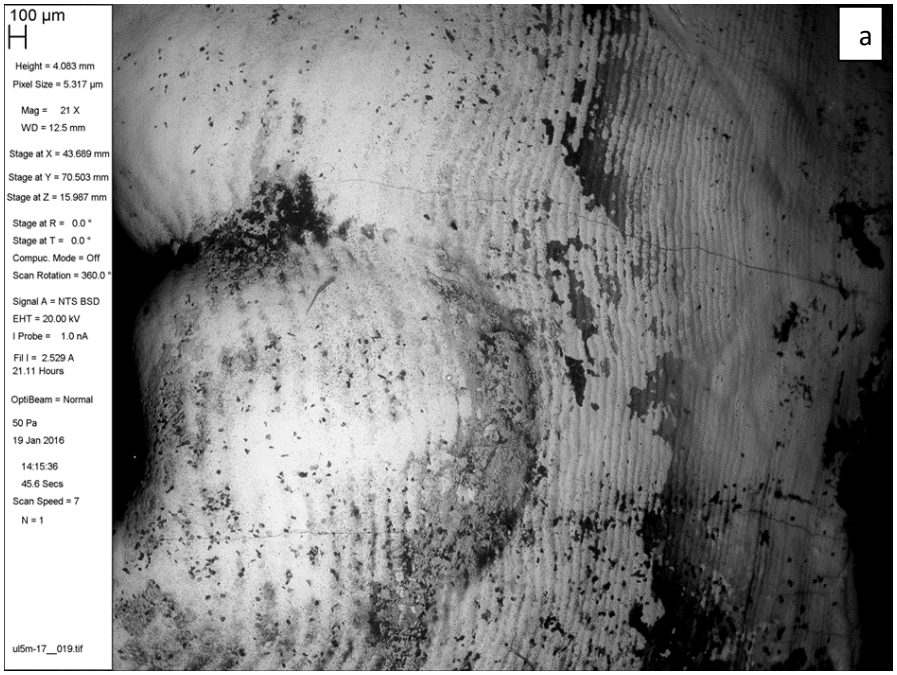

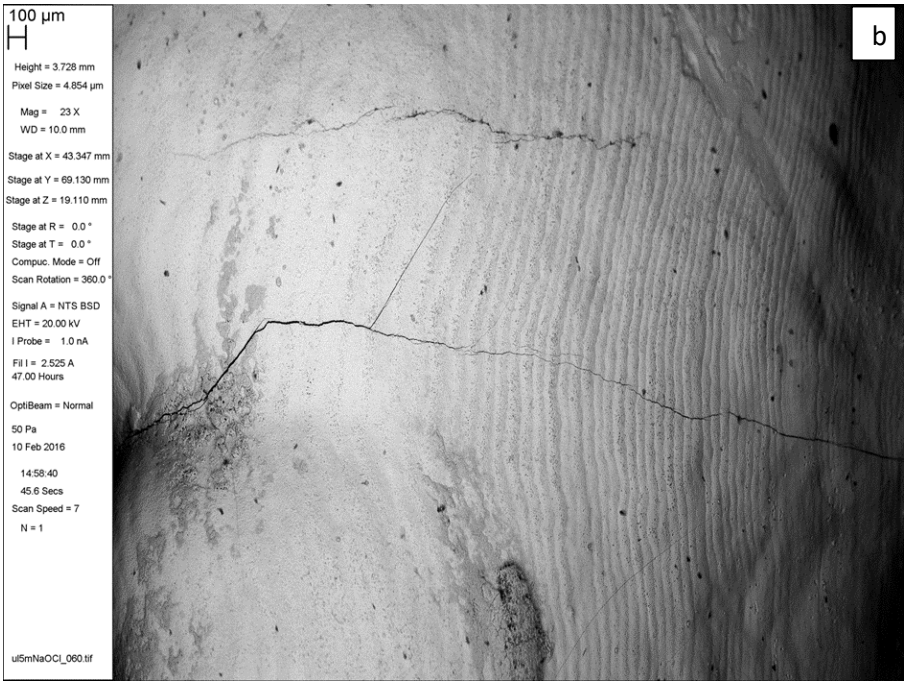

Figure 13.5 BSE images of tooth Br30 (a) before and, (b) after application of NaOCl.

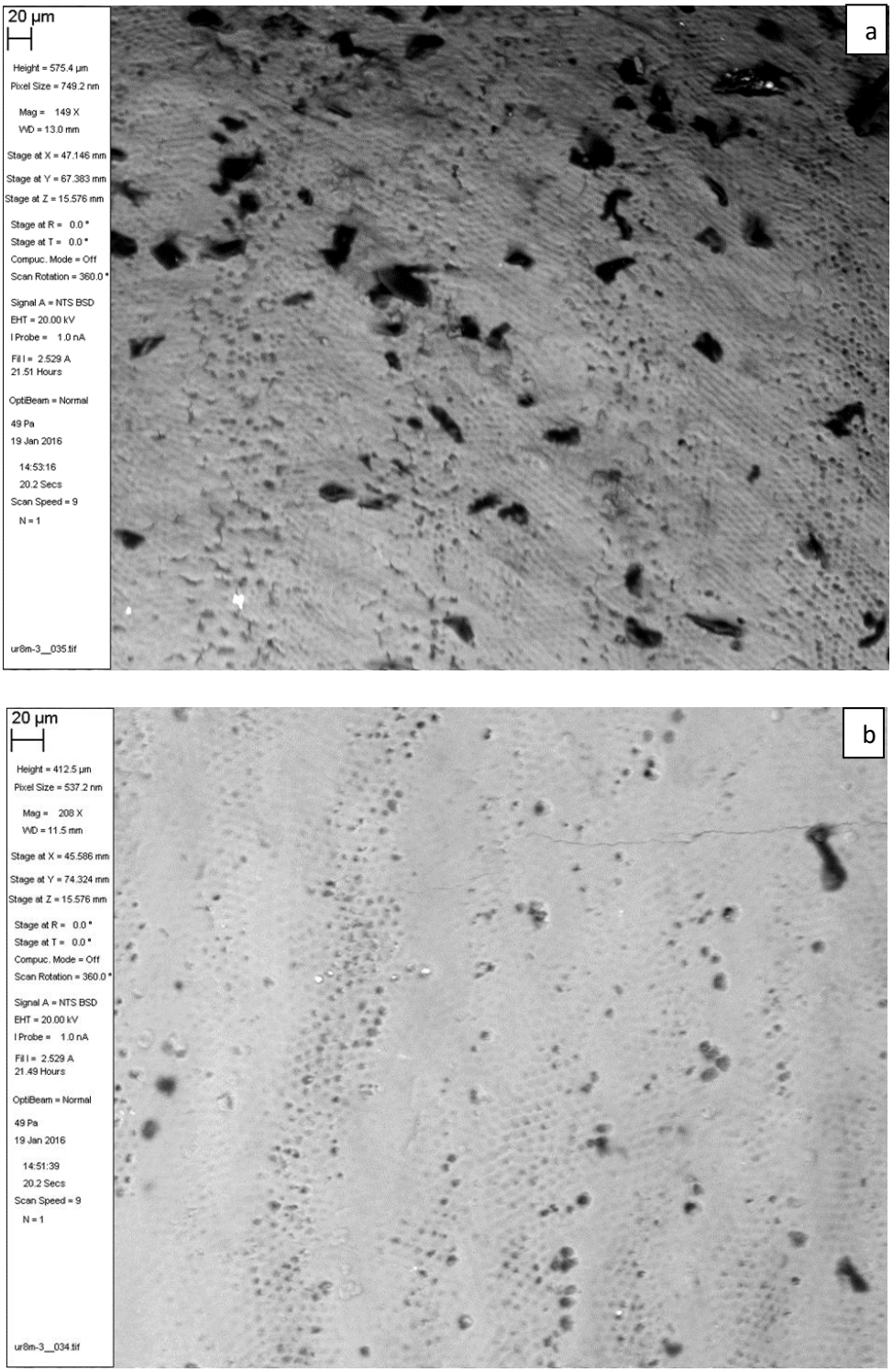

Figure 13.6 BSE images of tooth Sn40 (a) before and, (b) after application of NaOCl.

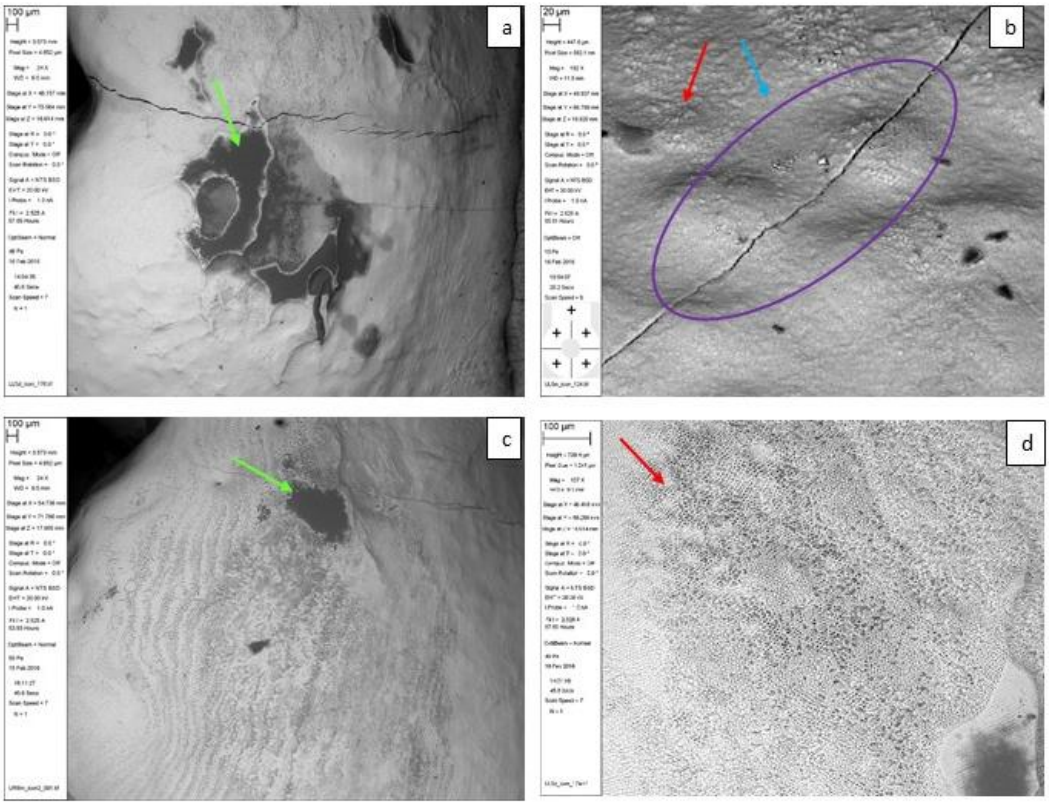

Figure 13.7 BSE image of samples (a) Br20 (b) Br30 and (c) Sn40 (d) normal enamel after etching with 15% HCl for 2 min and rinsed with distilled water for 30s. Some parts of tooth remained intact (blue arrow) while some parts were etched (red arrow). Purple oval (b) shows a scooping etch pattern. The green arrows (a,c) show the possible remained etchant gel on the surface.

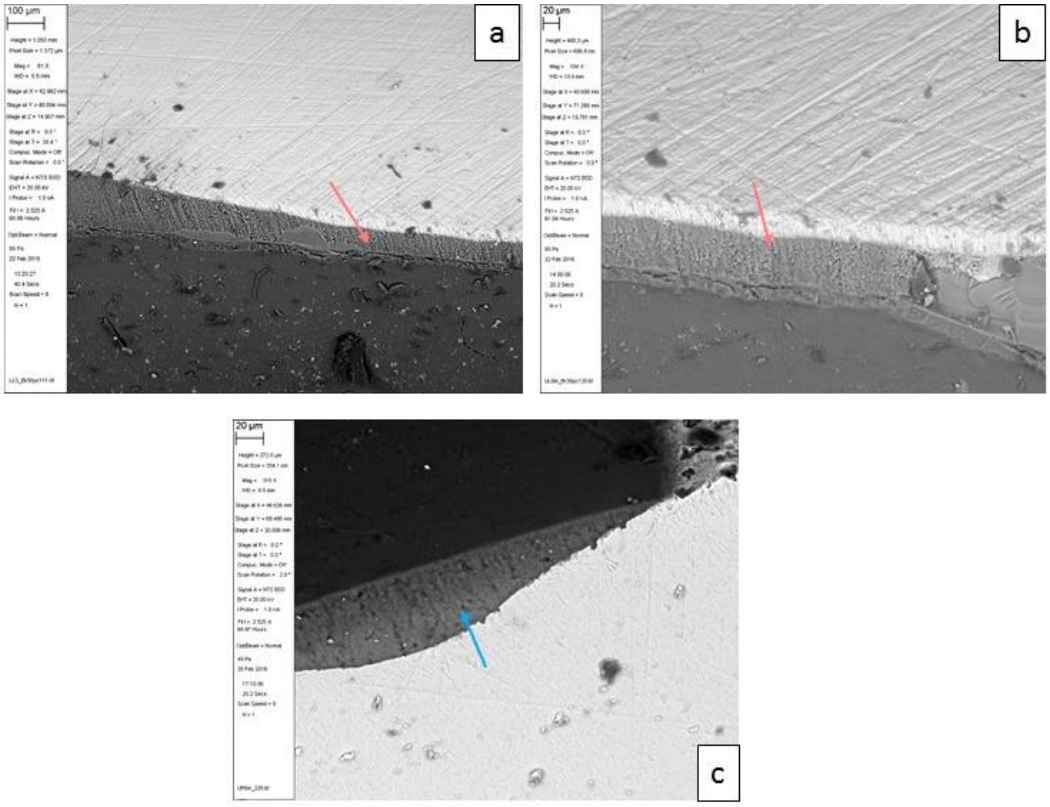

Figure 13.8 BSE images showing the interface (pink arrow) of ICON® resin containing (a) 20wt% bromine-methacrylate (b) 30wt% bromine-methacrylate and, (c) 40wt% tin-methacrylate with WSL (blue arrow).

13.5 Discussion

In the current study, the samples were cleaned by soaking in NaOCl to remove the debris from the tooth surface, which was detected by the first BSE image. Sodium hypochlorite is a common solution proteins in the root canal and requires dental dam application clinically (Siqueira *et al.* 2000).

A white spot lesion has a hypermineralised surface layer and a demineralised sub-surface body (Al 1956). It is crucial to remove the hypermineralised surface layer before resin infiltration in order to infiltrate the resin into the lesion. A previous study showed that 15% HCl for 90-120s is helpful to remove this surface layer in order to open the pore system inside the WSLs for the resin to infiltrate (Meyer-Lueckel *et al.* 2007). In the current study, BSE images showed that the mineralised surface of the lesion was not removed completely. Some areas of the tooth surface were etched while the other parts were remained intact leading to a scooping

pattern. The reason for this pattern of etching is not clear. Hence, the remained intact layers could hinder penetration of the infiltrant resin into the lesion. Furthermore, the BSE images showed that there was etchant gel remaining on the tooth surface despite vigorous rinsing with distilled water rinse. The former version of the acidic etchant was in the form of solution. Because the solution tends to run over the intended area and may cause damage to healthy tooth structure, the gel form was subsequently developed. The latter gel is thixotropic and easy to dispense over the lesion only and avoids contamination of the adjacent healthy tooth structure. This gel component is usually a colloidal silica sol, which is microfine particles of silicon dioxide in water. The silicon dioxide is poorly soluble and its solubility in water strongly depends on its crystalline form as a function of temperature, which peaks around 340°C (Jia and Jin 2004). In a clinical situation where the WSL is on proximal surface, it would be more difficult to remove the etching gel because of restricted access. This could inhibit the resin infiltration into the WSL.

13.6 Conclusion

This in-vitro pilot study shows that the HCl does not provide a uniform removal of the surface layer. Furthermore, irrigation alone might not be able to remove the etching gel on the surface, thus mechanical removal may be needed to remove the gel in a clinical situation, especially in an area where access is restricted. These factors may hamper full penetration of the resin. In an area where the enamel layer was removed, the resin penetration depth is comparable to the etched depth on the enamel surface.

General Discussion, Conclusion and Future Work

Chapter 14- General Discussion, Conclusion and Future Work

14.1 General discussion

14.1.1 Characterisation of WSL

The initial enamel carious lesion is the result of mineral loss due to demineralisation without loss of the surface layer. The milky white opaque appearance of the WSL is an optical phenomenon caused by the porosity due to a difference in the refractive index of the normal enamel and the air filled pores when the lesion is dried. The treatment options for these lesions has historically included prevention, remineralisation to preserve the lesion surface and tooth structure, or to remove and replace the affected lesion with restorations (Brantley *et al.* 1995; Kidd and Fejerskov 2004). Some believe that the former preventive option is very subjective and requires high patient compliance, whereas others believe that the restorative option will weaken the tooth structure and need more frequent replacement (Dorri *et al*., 2015). Recently, resin infiltration was introduced as a minimally invasive technique that potentially could arrest caries progression with less than ideal patient compliance on prevention. This concept requires the resin to infiltrate and obturate the pores in the WSL. However, in the literature review, no clear description of the pores in WSLs was found. Although there are studies reporting lower mineral density in WSL, no conclusive information was provided regarding the pore size and pore structure in the white spot lesion.

In the present study, two methods, Brunauer–Emmett–Teller (BET) and Focussed Ion Beam-Scanning Electron Microscope (FIB-SEM), were used in an attempt to characterise the pore size and structure in WSLs. BET results were inconclusive because it requires a much larger sample size, which is usually much larger than the size of a WSL. FIB-SEM techniques are useful in showing up the spaces within the prismatic cores. However, 3D rendering can only be carried out using selected well-aligned slices as the samples tend to move during the scanning. Nevertheless, it can be concluded that the caries demineralisation process follow a tunnel pattern within the prismatic core in the advancing region, as shown by previous researchers (Huang *et al*. 2010). These authors also show the loss of inter-prismatic enamel structure due to severe demineralisation in the body of WSL, a feature that was observed in the FIB-SEM images in the surface region in the present study. Hence,

although FIB-SEM cannot be used to determine the pore sizes unless the specimen movement can be controlled and minimised, it has the potential to show the shape and connectivity of the pores. We believe that if the pores are defined as space within enamel, their size could be as small as the enamel crystallite, 24x48nm based on the findings of a previous study (Yanagisawa and Miake 2003).

14.1.2 Development of radiopaque resin

Although the infiltration concept to seal up the pores in the WSLs is an excellent management technique in minimally invasive (MI) dentistry, the radiolucent property in the commercially available material, ICON®, is a negative feature and it has not gained popularity with clinicians. The aim of the present study attempted to improve the radiopacity by incorporating either fillers or monomers.

Although our attempt to characterise the pore sizes using the above methods were not conclusive, the estimated pore size are within the range of the enamel crystallite size, 24x48nm, to 400-700nm. The latter was calculated from Mie scattering theory. In the former approach, two fillers were tried, namely nano-SrHA and SrBG. SrBG showed an increase in radiopacity of resin but did not reach the ISO-4049 standard. It also showed particle agglomeration. Nano-SrHA with nano-sized crystallites reached the ISO-4049 regarding radiopacity with a more even distribution in resin compared to SrBG. The former still agglomerated in ICON® resin even when the particles were functionalised with methacrylic acid to create charge separation. Furthermore, the needle-shaped nano-SrHA has width ~23nm and length ~73nm. Therefore, unless the filler particles are perfectly aligned, a factor that is impossible to control during the application, they would not be able to penetrate into the pores.

In addition, the low viscosity characteristics of the resin is essential to infiltrate into the lesion as the resin penetration mainly depends on capillary reaction. Incorporation of nano-SrHA or SrBG increases the viscosity of the resin dramatically. This leads to a further decrease of the infiltration ability of the resins.

Due to the above reasons, the approach of incorporating fillers in the resin to make it radiopaque was discarded.

The other pathway to make the ICON® resin radiopaque is to incorporate radiopaque monomers such as BrM and SnM. Bromine and tin provide a high radiopacity due to their high atomic numbers. The BrM could be added to the resin to the maximum of 30wt% as above this loading, the mixture had a soft texture after the curing whereas, SnM added to the resin up to 40wt% showed an acceptable radiopacity and was hard in texture after curing. The incorporation of radiopaque elements into ICON® resin discs reached the standard of an acceptable radiopacity value on the digital radiographs based on ISO-4049 standards. The results of radiopacity were similar to the results of the previous study by Patel (2013).

These resins were also shown to have low viscosity and contact angle (high wettability), which make them suitable to infiltrate into the lesion as it assumes a hydrophilic material is suitable to infiltrate into pores due to the presence of the water inside of the pores structure (Paris e*t al*. 2007).

In the current study, the infiltration ability was measured using XMT as this method can detect the material in 3D. The results showed the infiltration to the natural white spot lesion to some extent; however, the radiopacity of the infiltrated lesion was not sufficient in order to detect by digital radiographs clinically. It is because the radiopacity of the SnM and BrM, though above the ISO standard, is still lower than that of enamel.

The biocompatibility of the materials were examined and it was shown that all infiltrant resins including ICON® resin are cytotoxic. The results were similar to the previous study by Zakarias (2014).

To standardise the WSLs for investigations, artificial white spot lesions were used to compare the linear attenuation coefficient (LAC) difference and penetration depth between ICON® and 30wt%BrM-ICON®. The methods used to create artificial white spot lesions were either static, a continuous action of pure acid system, or dynamic, which is a de- and remineralisation system whereas natural white spot lesions are produced by repeated, intermittent and prolonged acid attacks with exposure to saliva and other substances of the oral environment. Although the dynamic pathway includes remineralisation, it is impossible for the in-vitro lesion to acquire organic

substances in the body or on the outer surface of the lesion, or both. Thus, it is assumed that there is a difference between in-vitro and in-vivo white spot lesions regarding to their structure. This might explain that the post-infiltration subtracted XMT images in artificial white spot lesions were shown to have visually detectable radiopacity and penetration of 30wt%BrM-ICON®, whereas in natural white spot lesions, enhancement of the contrast was required.

Based on the findings from this study, there is a need to increase the radiopacity of the material to a greater value and, ideally much greater than that of the enamel. However, it is necessary to assure that the material could be infiltrated fully into the depth of lesion, prior to increasing the radiopacity. Therefore, a pilot study was carried out to distinguish the exact barrier for resin infiltration for the experimental resins by taking BSE imaging after each step of the experimental resin application. The results show drawbacks for each step of application, which are considered as a barrier for complete infiltration of the resins. These barriers are:

- Parts of tooth surface might remain intact after etching and pores does not open to the environment. It is important to remove or perforate the intact surface layer prior to infiltration of the resin;
- The gel component of the etch might remain on the tooth surface and it is not feasible to remove it completely in the oral environment; therefore, the area underneath could not be infiltrated with the infiltrant resin;
- The infiltration of the resin is mostly an interface between the resin and the etched surface areas rather the complete infiltration of the resin into the depth of the lesion.

Furthermore, there is no information in the literature on what it is inside the pores and it is not clear how to clean the pores properly to use the maximum effect of capillary reaction and infiltrate the resin into the pores completely.

Finally, yet importantly, the literature stated that the intact surface layer is very similar to the normal enamel, which considers as one of the barriers for the successful infiltration. The manufacturer recommends the removal of the surface

intact layer in order to have full depth infiltration. This leads to a burning question whether it is beneficial to remove this layer to allow the resin to infiltrate into the lesion, which might not be successful, or it is better to maintain the intact surface layer and improve the other aspects of prevention. However, if a highly radiopaque infiltrant is developed and available, it can be used as a diagnostic material, i.e. if it can infiltrate without the use of hydrochloric acid (HCl), it will indicate the WSL does not have an intact protective layer and the infiltrants will obturate the pores and prevent further bacterial invasion and progression of the lesion. On the other hand, if there is no evidence of infiltration observed in radiographs, the surface layer is intact and further remineralisation can be enhanced by F or other remineralising agents.

14.1.3 Sample Size

A large sample size (n) is usually needed in order to have narrower confidence intervals and more reliable conclusions. Thus, “mega-trial” with 10,000 samples is the ideal in statistics for natural occurring conditions that are multifactorial and have large individual variations, such as the structures of natural WSL in the present study. However, the reality is sometimes different and the researcher will have to work with much smaller sample size due to limitations in budget, time, ethical constrains or the nature of research such as studies on animal species, rare illness (Rost, 1991). Hence, in laboratory studies, this may not be practical. To overcome this, laboratory studies tend to use standardised samples so that small sample sizes can be used. In most material research, a sample size of 5 is conventionally acceptable. Nevertheless, if n< 5, they might encounter with a low statistical power and incredulity about the relevant statistical test accuracy and ultimate inference from the resulting *p* value (Pashler and Harris, 2012). However, Winter (2013) showed that a paired t-test is feasible with extremely small sample size (n<5) if the within-pair correlation is high. They stated that a sample size of two could have the probability of a true positive of 4.7% and the probability of a false positive of 2.5% leading to 65% true effect if the data is statistically significant. In other words, the researchers should consider that a statistically significant finding is more likely to be a false positive in smaller sample size (De Winter, 2013).

In the current study, although the number of natural white spot lesions was small, the mineral concentration for each site within the lesion presented a wide distribution. Hence, it could be argued that each site was a specific sampling point. With the amount of 3D data, there were many sampling points using this definition. In Chapter 10, the line profiles, as the representative of samples, were taken to assess the changes of LAC at those specific sites. In the artificial lesions, as the mineral distribution of the lesion was less varied, the whole lesion was used as an independent sample and 12 lesions were used per group.

14.2 General Conclusion

The present study shows radiopaque methacrylates can be the used as components to increase the radiopacities of infiltrants for WSLs. The 30wt%BrM could be the material of choice. The application of 15% HCl to remove the surface layer before infiltration should be taken cautious as it may remove mineral from within the lesion as well as the surface layer.

14.3 Future work

Future studies might consider the following:

- ***Characterisation of WSL***
  - In order to visualise the micro-structure of WSL in 3D, better FIB-SEM set-up is required. For example:
    - A wider and deeper front trench should be used to prevent blockage of SEM beam,
    - The current should be reduced to minimise heating and expansion of the resin for better stability.
  - The pores in the white spot lesion are known to take up water. These pores could be imaged by small angle neutron scattering providing that they have dimensions less than 1 micron. The pore size characterisation would be facilitated by doing measurements in heavy water (D_2O), which has a larger

amount of the hydrogen isotope deuterium than normal, as well as conventional H_2O.

- ***Radiopaque infiltrant resins***

  - Mechanical properties including hardness, abrasion resistance and physical properties of radiopaque resins such as water uptake and permeability to acids, as these features are important to prevent the loss of the material on the surface of the lesion in clinical application.

  - Characterise residual monomers by extraction and high performance liquid chromatography (HPLC) in order to investigate the exact cause of the experimental resins cytotoxicity.

  - In order to increase the sample size of natural white spot lesions, it might be useful to create the lesions using the brackets on premolars before the extraction in extraction based fixed orthodontic cases (Aghoutan *et al*. 2015).

  - Artificial WSLs data in this study suggested that 15% HCl might have a significant effect on mineral loss at WSL site. In order to confirm the actual effect of 15% HCl the on mineral changes, it is beneficial to compare XMT sections after the WSL formation and after the application of the HCl on the lesion.

  - Saliva, the total volume of saliva secreted is 1–2L per 24 h, plays a key role in different physiological and biological processes including lubrication, cleansing, enzymatic digestion and maintenance of dental and mucosal integrity (Pedersen *et al.* 2002). It is evident that saliva secretion in oral environment could be helpful to remove any cytotoxic leachable products from the dental materials in the oral environment whilst cell culture plate is a closed system and the media is only change every 2-3 days. Therefore, the grade of cell cytotoxicity of the material in-vitro is higher compared to in-vivo. It might be beneficial to do cytotoxicity in the artificial mouth.

- The pores in WSL might be filled with a protein-like material from saliva, bacterial cells, or demineralised debris that could not be removed by washing and application of the alcohol before the application of the resins. Hence, in order to increase more uniform infiltration, a conditioning solution (e.g. hypochlorite) might be helpful to remove protein before infiltration. It is beneficial to design the experiments to compare the penetration depth and infiltration ability between two groups with and without using a conditioning solution such as sodium hypochlorite.

References

Aaseth, J., G. Boivin and O. Andersen (2012). "Osteoporosis and trace elements–an overview." Journal of Trace Elements in Medicine and Biology 26(2): 149-152.

Aghoutan, H., S. Alami, F. El Quars, S. Diouny and F. Bourzgui (2015). White Spots Lesions in Orthodontic Treatment and Fluoride—Clinical Evidence. Emerging Trends in Oral Health Sciences and Dentistry.

Ahmed, M., G. Davis and F. Wong (2012). "X-ray microtomography study to validate the efficacies of caries removal in primary molars by hand excavation and chemo-mechanical technique." Caries research 46(6): 561-567.

Ahovuo-Saloranta, A., H. Forss, T. Walsh, A. Hiiri, A. Nordblad, M. Mäkelä and H. V. Worthington (2013). "Sealants for preventing dental decay in the permanent teeth." The Cochrane Library.

Al-Hiyasat, A., H. Darmani and M. Milhem (2005). "Cytotoxicity evaluation of dental resin composites and their flowable derivatives." Clinical oral investigations 9(1): 21-25.

Al-Khateeb, S., R. Exterkate, B. Angmar-Månsson and B. ten Cate (2000). "Effect of acid-etching on remineralization of enamel white spot lesions." Acta Odontologica Scandinavica 58(1): 31-36.

Al-Nazhan, S. and L. Spangberg (1990). "Morphological cell changes due to chemical toxicity of a dental material: an electron microscopic study on human periodontal ligament fibroblasts and L929 cells." Journal of endodontics 16(3): 129-134.

Al, D. (1956). "Studies of the early lesion of enamel caries with transmitted light, polarised light and radiography." British Dental Journal 101: 289-297.

Allaker, R. (2010). "The use of nanoparticles to control oral biofilm formation." Journal of dental research 89(11): 1175-1186.

Allen, T. (2013). "Particle size measurement", 3rd Edition, Springer, England.

Anderson, P., Y. Ahmed, M. Patel, G. Davis and M. Braden (2006). "X-ray microtomographic studies of novel radio-opaque polymeric materials for dental applications." Materials science and technology 22(9): 1094-1097.

Anderson, P., F. Bollet-Quivogne, S. Dowker and J. Elliott (2004). "Demineralization in enamel and hydroxyapatite aggregates at increasing ionic strengths." Archives of oral biology 49(3): 199-207.

Anderson, P., M. Levinkind and J. Elliott (1998). "Scanning microradiographic studies of rates of in vitro demineralization in human and bovine dental enamel." Archives of Oral Biology 43(8): 649-656.

Andrade, E. d. C. (1952). "Viscosity of liquids." Proceedings of the Royal Society of London. Series A, Mathematical and Physical Sciences: 36-43.

Anwar, A. (2014). Continuous plastic flow synthesis and characterization of nanoscale bioceramics, UCL (University College London).

Ardu, S., N. V. Castioni, N. Benbachir-Hassani and I. Krejci (2007). "Minimally invasive treatment of white spot enamel lesions." Quintessence international 38(8): 633-636.

Arends, J. and J. Christoffersen (1986). "Invited review article: the nature of early caries lesions in enamel." Journal of Dental Research 65(1): 2-11.

Arnold, W., B. Haddad, K. Schaper, K. Hagemann, C. Lippold and G. Danesh (2015). "Enamel surface alterations after repeated conditioning with HCl." Head & face Medicine 11(1): 32.

Asmussen, E. (1977). "Penetration of restorative resins into acid etched enamel. I: Viscosity, surface tension and contact angle of restorative resin monomers." Acta Odontologica Scandinavica 35(4): 175-182.

Atkinson, M. E. and F. H. White (1992). Principles of anatomy and oral anatomy for dental students, Churchill Livingstone.

Atkinson, R. (1986). "Kinetics and mechanisms of the gas-phase reactions of the hydroxyl radical with organic compounds under atmospheric conditions." Chemical Reviews 86(1): 69-201.

Author, A. (1964). "International Union of Pure and Applied Chemistry." Proceedings of the Society for Analytical Chemistry 1(6): 73-74.

Bagramian, R. A., F. Garcia-Godoy and A. R. Volpe (2009). "The global increase in dental caries. A pending public health crisis." American Journal of Dentistry 22(1): 3-8.

Bakry, A. S., Y. Tamura, M. Otsuki, S. Kasugai, K. Ohya and J. Tagami (2011). "Cytotoxicity of 45S5 bioglass paste used for dentine hypersensitivity treatment." Journal of Dentistry 39(9): 599-603.

Balasundaram, G., M. Sato and T. J. Webster (2006). "Using hydroxyapatite nanoparticles and decreased crystallinity to promote osteoblast adhesion similar to functionalizing with RGD." Biomaterials 27(14): 2798-2805.

Banerjee, A. (2013). "Minimal intervention dentistry: part 7. Minimally invasive operative caries management: rationale and techniques." British Dental Journal 214(3): 107-111.

Banerjee, A., H. M. Pickard and T. F. Watson (2011). Pickard's manual of operative dentistry, Oxford University Press.

Beerens, M., M. Van Der Veen, H. Van Beek and J. Ten Cate (2010). "Effects of casein phosphopeptide amorphous calcium fluoride phosphate paste on white spot lesions

and dental plaque after orthodontic treatment: a 3-month follow-up." European Journal of Oral Sciences 118(6): 610-617.

Behbehani, M. and E. Zaatar (1999). "Bioactive glass in dentistry." Dental Update 6(4): 11-15.

Berkovitz, B., G. Holland and B. Moxham (2009). "Oral Anatomy, Histology and Embryology Mosby Elsevier." Edinburgh (Scotland).

Berry, H. M. (1983). "Cervical burnout and Mach band: two shadows of doubt in radiologic interpretation of carious lesions." The Journal of the American Dental Association 106(5): 622-625.

Bigi, A., E. Boanini, C. Capuccini and M. Gazzano (2007). "Strontium-substituted hydroxyapatite nanocrystals." Inorganic Chemical Acta 360(3): 1009-1016.

Billington, R., P. Hadley, J. Williams and G. Pearson (2001). "Kinetics of fluoride release from zinc oxide-based cements." Biomaterials 22(18): 2507-2513.

Bishara, S. E. and A. W. Ostby (2008). White spot lesions: formation, prevention, and treatment. Seminars in Orthodontics, Elsevier.

Botelho, M. A., R. A. dos Santos, J. G. Martins, C. O. Carvalho, M. C. Paz, C. Azenha, R. S. Ruela, D. B. Queiroz, W. S. Ruela and G. Marinho (2009). "Comparative effect of an essential oil mouthrinse on plaque, gingivitis and salivary Streptococcus mutans levels: a double blind randomized study." Phytotherapy Research 23(9): 1214-1219.

Bourne, M. (2002). Food texture and viscosity: concept and measurement, Academic press.

Bowen, R. L. (1965). Method of preparing a monomer having phenoxy and methacrylate groups linked by hydroxy glyceryl groups, Google Patents.

Boyde, A. (1989). Enamel. Teeth, Springer: 309-473.

Brantley, C. F., J. D. Bader, D. A. Shugars and S. P. Nesbit (1995). "Does the cycle of rerestoration lead to larger restorations?" The Journal of the American Dental Association 126(10): 1407-1413.

Browne, R. (1985). "In vitro cytotoxicity testing of dental restorative materials." CRC Critical Reviews in Biocompatibility 1: 85-110.

Brudevold, F., D. E. Gardner and F. A. Smith (1956). "The distribution of fluoride in human enamel." Journal of Dental Research 35(3): 420-429.

Buonocore, M. (1972). "Adhesives for pit and fissure caries control." Dental clinics of North America 16(4): 693.

Buonocore, M. and A. Gwinnett (1967). "Chemical, polarized light, and microradiographic study of the effects of various toothpastes on" white spot" formation in vitro." Journal of Oral Therapeutics and Pharmacology 3(5): 321.

Burwell, A., L. Litkowski and D. Greenspan (2009). "Calcium sodium phosphosilicate (NovaMin®): remineralization potential." Advances in Dental Research 21(1): 35-39.

Bushberg, J. T. and J. M. Boone (2011). The essential physics of medical imaging, Lippincott Williams & Wilkins.

Bushby, A. J., K. M. P'ng, R. D. Young, C. Pinali, C. Knupp and A. J. Quantock (2011). "Imaging three-dimensional tissue architectures by focused ion beam scanning electron microscopy." Nature Protocols 6(6): 845-858.

Cai, Y., Y. Liu, W. Yan, Q. Hu, J. Tao, M. Zhang, Z. Shi and R. Tang (2007). "Role of hydroxyapatite nanoparticle size in bone cell proliferation." Journal of Materials Chemistry 17(36): 3780-3787.

Carton, J., R. Daly and P. Ramani (2007). Clinical pathology, Oxford University Press, USA.

Carvalho-Junior, J., L. Correr-Sobrinho, A. Correr, M. Sinhoreti, S. Consani and M. Sousa-Neto (2007). "Radiopacity of root filling materials using digital radiography." International Endodontic Journal 40(7): 514-520.

Cate, J. T. (1990). "In vitro studies on the effects of fluoride on de-and remineralization." Journal of Dental Research 69(2_suppl): 614-619.

Chan, D., H. Titus, K.-H. Chung, H. Dixon, S. Wellinghoff and H. Rawls (1999). "Radiopacity of tantalum oxide nanoparticle filled resins." Dental Materials 15(3): 219-222.

Chaudhry, A. A., H. Yan, K. Gong, F. Inam, G. Viola, M. J. Reece, J. B. Goodall, I. ur Rehman, F. K. McNeil-Watson and J. C. Corbett (2011). "High-strength nanograined and translucent hydroxyapatite monoliths via continuous hydrothermal synthesis and optimized spark plasma sintering." Acta Biomaterialia 7(2): 791-799.

Chen, F., Z.-C. Wang and C.-J. Lin (2002). "Preparation and characterization of nano-sized hydroxyapatite particles and hydroxyapatite/chitosan nano-composite for use in biomedical materials." Materials letters 57(4): 858-861.

Chen, L., Q. Yu, Y. Wang and H. Li (2011). "BisGMA/TEGDMA dental composite containing high aspect-ratio hydroxyapatite nanofibers." Dental Materials 27(11): 1187-1195.

Clementino-Luedemann, T. N. R. and Kunzelmann K.-H. (2006). "Mineral concentration of natural human teeth by a commercial micro-CT." Dental materials Journal 25(1): 113-119.

Cochrane, N., P. Anderson, G. Davis, G. Adams, M. Stacey and E. Reynolds (2012). "An X-ray microtomographic study of natural white-spot enamel lesions." Journal of Dental Research 91(2): 185-191.

Cochrane, N. and E. Reynolds (2012). "Calcium phosphopeptides—mechanisms of action and evidence for clinical efficacy." Advances in Dental Research 24(2): 41-47.

Conine, D. L., M. Yum, R. C. Martz, G. K. Stookey, J. C. Muhler and R. B. Forney (1975). "Toxicity of sodium pentafluorostannite, a new anticariogenic agent. I. Comparison of the acute toxicity of sodium pentafluorostannite, sodium fluoride, and stannous chloride in mice and/or rats." Toxicology and Applied Pharmacology 33(1): 21-26.

Council on Dental Materials, I. and Equipment (1981). "The desirability of using radiopaque plastics in dentistry: a status report." The Journal of the American Dental Association 102(3): 347-349.

Craig, R. G., D. Welker, J. Rothaut, K. G. Krumbholz, K. P. Stefan, K. Dermann, H. J. Rehberg, G. Franz, K. M. Lehmann and M. Borchert (2000). Dental materials, Wiley Online Library.

Curzon, M. and P. Spector (1981). "Effect of using different strontium salts on dental caries in the rat." Caries Research 15(4): 296-301.

Cushing, B. L., V. L. Kolesnichenko and C. J. O'Connor (2004). "Recent advances in the liquid-phase syntheses of inorganic nanoparticles." Chemical Reviews 104: 3893-3946.

D'Onofrio, A., N. Kent, S. Shahdad and R. Hill (2016). "Development of novel strontium containing bioactive glass based calcium phosphate cement." Dental Materials 32(6): 703-712.

Da Silva, R. C., A. C. C. Zuanon, D. M. P. Spolidorio and J. A. D. B. Campos (2007). "Antibacterial activity of four glass ionomer cements used in atraumatic restorative treatment." Journal of Materials Science: Materials in Medicine 18(9): 1859-1862.

Dabnun, M. A., M. Hashmi and M. El-Baradie (2005). "Surface roughness prediction model by design of experiments for turning machinable glass–ceramic (Macor)." Journal of Materials Processing Technology 164: 1289-1293.

Dahl, J. E. (2007). "Potential of dental adhesives to induce mucosal irritation evaluated by the HET–CAM method." Acta Odontologica Scandinavica 65(5): 275-283.

Darling, A. (1961). "The Selective Attack of Caries on the Dental Enamel: Charles Tomes Lecture delivered at the Royal College of Surgeons of England on 21st July 1961." Annals of the Royal College of Surgeons of England 29(6): 354.

Dave, R., R. Gupta, R. Pfeffer, S. Sundaresan and M. S. Tomassone (2006). Deagglomeration and mixing of nanoparticles. NSF Science and Engineering Grantees Conference.

Davies, J. A. (2014). An X-ray Microtomography Study of the Effect of an Experimental Statherin-like Peptide on Demineralisation and Remineralisation of Enamel, Queen Mary University of London.

Davis, G. R., A. N. Evershed and D. Mills (2013). "Quantitative high contrast X-ray microtomography for dental research." Journal of Dentistry 41(5): 475-482.

Davis, G. R. and F. S. Wong (1996). "X-ray microtomography of bones and teeth." Physiological Measurement 17(3): 121.

Davy, K. W. and B. E. Causton (1982). "Radio-opaque denture base: a new acrylic co-polymer." Journal of Dentistry 10(3): 254-264.

De Winter, J. C. (2013). "Using the Student's t-test with extremely small sample sizes." Practical Assessment, Research & Evaluation 18(10).

Delaviz, Y., Z. X. Zhang, I. Cabasso and J. Smid (1989). Novel Homogeneous X-Ray Contrast Polymer Salt Composites. Integration of Fundamental Polymer Science and Technology—3, Springer: 279-283.

Deng, D. M., M. J. Buijs and J. M. Ten Cate (2004). "The effects of substratum on the pH response of Streptococcus mutans biofilms and on the susceptibility to 0.2% chlorhexidine." European Journal of Oral Sciences 112(1): 42-47.

DePaola, P., F. Brudevold, R. Aasenden, E. Moreno, H. Englander, Y. Bakhos, F. Bookstein and J. Warram (1975). "A pilot study of the relationship between caries experience and surface enamel fluoride in man." Archives of Oral Biology 20(12): 859-864.

Dettre, R. H. and R. E. Johnson Jr (1964). Contact angle hysteresis, ACS Publications.

DeWald, J. and J. Ferracane (1987). "A comparison of four modes of evaluating depth of cure of light-activated composites." Journal of Dental Research 66(3): 727-730.

Dibdin, G. and D. Poole (1982). "Surface area and pore size analysis for human enamel and dentine by water vapour sorption." Archives of Oral Biology 27(3): 235-241.

Dirks, O. B. (1966). "Posteruptive changes in dental enamel." Journal of Dental Research 45(3): 503-511.

Dorozhkin, S. V. (2012). "Dissolution mechanism of calcium apatites in acids: A review of literature." World Journal of Methodology 2(1): 1.

Dorri, M., S. M. Dunne, T. Walsh and F. Schwendicke (2015). "Micro-invasive interventions for managing proximal dental decay in primary and permanent teeth." The Cochrane Library.

Dowker, S., P. Anderson, J. Elliott and X. Gao (1999). "Crystal chemistry and dissolution of calcium phosphate in dental enamel." Mineralogical Magazine 63(6): 791-791.

Doyle, W. M. (1992). "Principles and applications of Fourier transform infrared (FTIR) process analysis." Process control and quality 2: 50.

Dubinin, M. (1960). "The potential theory of adsorption of gases and vapors for adsorbents with energetically nonuniform surfaces." Chemical Reviews 60(2): 235-241.

Egerton, R. F. (2005). Physical principles of electron microscopy, Springer.

Eggerath, J., T. Kremniczky, P. Gaengler and W. Arnold (2011). "EDX-element analysis of the in vitro effect of fluoride oral hygiene tablets on artificial caries lesion formation and remineralization in human enamel." The Open Dentistry Journal 5: 84.

Eldeniz, A., K. Mustafa, D. Ørstavik and J. Dahl (2007). "Cytotoxicity of new resin-, calcium hydroxide-and silicone-based root canal sealers on fibroblasts derived from human gingiva and L929 cell lines." International Endodontic Journal 40(5): 329-337.

Elliott, J. (1997). Structure, crystal chemistry and density of enamel apatites. Ciba Foundation Symposium 205-Dental Enamel, Wiley Online Library.

Elliott, J., F. Bollet-Quivogne, P. Anderson, S. Dowker, R. Wilson and G. Davis (2005). "Acidic demineralization of apatites studied by scanning X-ray microradiography and microtomography." Mineralogical Magazine 69(5): 643-652.

Elliott, J. and S. Dover (1982). "X-ray microtomography." Journal of Microscopy 126(2): 211-213.

Engelmann, J., G. Leyhausen, D. Leibfritz and W. Geurtsen (2002). "Effect of TEGDMA on the intracellular glutathione concentration of human gingival fibroblasts." Journal of Biomedical Materials Research 63(6): 746-751.

Espelid, I., A. Tveit, R. Erickson, S. Keck and E. Glasspoole (1991). "Radiopacity of restorations and detection of secondary caries." Dental Materials 7(2): 114-117.

Exterkate, R., J. Damen and J. Ten Cate (1993). "A single-section model for enamel de-and remineralization studies. 1. The effects of different Ca/P ratios in remineralization solutions." Journal of Dental Research 72(12): 1599-1603.

Faghihnejad, A. and H. Zeng (2013). "Interaction mechanism between hydrophobic and hydrophilic surfaces: Using polystyrene and mica as a model system." Langmuir 29(40): 12443-12451.

Featherstone, J. (1983). "Remineralisation of artificial carious lesions in vivo and in vitro." Demineralisation and Remineralisation of the Teeth: 89-110.

Featherstone, J. (2008). "Dental caries: a dynamic disease process." Australian Dental Journal 53(3): 286-291.

Featherstone, J. and S. Doméjean (2012). "Minimal intervention dentistry: part 1. From'compulsive'restorative dentistry to rational therapeutic strategies." British Dental Journal 213(9): 441-445.

Featherstone, J., J. Duncan and T. Cutress (1979). "A mechanism for dental caries based on chemical processes and diffusion phenomena during in-vitro caries simulation on human tooth enamel." Archives of Oral Biology 24(2): 101-112.

Featherstone, J. D. (1999). "Prevention and reversal of dental caries: role of low level fluoride." Community Dentistry and Oral Epidemiology 27(1): 31-40.

Feilzer, A. and B. Dauvillier (2003). "Effect of TEGDMA/BisGMA ratio on stress development and viscoelastic properties of experimental two-paste composites." Journal of Dental Research 82(10): 824-828.

Fejerskov, O., J. Tencate, M. Larsen and E. Pearce (2003). "Chemical interactions between the tooth and oral fluids." Dental Caries 2: 49-60.

Ferracane, J. L. (1985). "Correlation between hardness and degree of conversion during the setting reaction of unfilled dental restorative resins." Dental Materials 1(1): 11-14.

Ferraz, M., F. Monteiro and C. Manuel (2004). "Hydroxyapatite nanoparticles: a review of preparation methodologies." Journal of Applied Biomaterials and Biomechanics 2(2): 74-80.

Fincham, A., J. Moradian-Oldak and J. Simmer (1999). "The structural biology of the developing dental enamel matrix." Journal of Structural Biology 126(3): 270-299.

Fisher, J., S. Johnston, N. Hewson, W. Dijk, E. Reich, J. L. Eiselé and D. Bourgeois (2012). "FDI Global Caries Initiative; implementing a paradigm shift in dental practice and the global policy context." International Dental Journal 62(4): 169-174.

Forsten, L. (1994). "Flouride Release of Glass Ionomers." Journal of Esthetic and Restorative Dentistry 6(5): 216-222.

Foster, J. and V. B. Ahir (1976). Denture bases of X-ray opaque polymers, Google Patents.

Francis, M. D., R. Graham, G. Russell and H. Fleisch (1969). "Diphosphonates inhibit formation of calcium phosphate crystals in vitro and pathological calcification in vivo." Science 165(3899): 1264-1266.

Fredholm, Y. C., N. Karpukhina, R. V. Law and R. G. Hill (2010). "Strontium containing bioactive glasses: glass structure and physical properties." Journal of Non-Crystalline Solids 356(44): 2546-2551.

Fujisawa, S., Y. Kadoma and Y. Komoda (1988). "1H and 13C NMR studies of the interaction of eugenol, phenol, and triethyleneglycol dimethacrylate with phospholipid liposomes as a model system for odontoblast membranes." Journal of Dental Research 67(11): 1438-1441.

Fultz, B. and J. M. Howe (2012). Transmission electron microscopy and diffractometry of materials, Springer Science & Business Media.

Gao, X., Y. Fan, R. Kent Jr, J. Van Houte and H. Margolis (2001). "Association of caries activity with the composition of dental plaque fluid." Journal of Dental Research 80(9): 1834-1839.

Gentleman, E., Y. C. Fredholm, G. Jell, N. Lotfibakhshaiesh, M. D. O'Donnell, R. G. Hill and M. M. Stevens (2010). "The effects of strontium-substituted bioactive glasses on osteoblasts and osteoclasts in vitro." Biomaterials 31(14): 3949-3956.

Gerlier, D. and N. Thomasset (1986). "Use of MTT colorimetric assay to measure cell activation." Journal of Immunological Methods 94(1-2): 57-63.

Geurtsen, W., F. Lehmann, W. Spahl and G. Leyhausen (1998). "Cytotoxicity of 35 dental resin composite monomers/additives in permanent 3T3 and three human primary fibroblast cultures." Journal of Biomedical Materials Research Part A 41(3): 474-480.

Geurtsen, W. and G. Leyhausen (2001). "Concise review biomaterials & bioengineering: chemical-biological interactions of the resin monomer triethyleneglycol-dimethacrylate (TEGDMA)." Journal of Dental Research 80(12): 2046-2050.

Gjorgievska, E. and J. W. Nicholson (2011). "Prevention of enamel demineralization after tooth bleaching by bioactive glass incorporated into toothpaste." Australian Dental Journal 56(2): 193-200.

Gleason, M. N., R. E. Gosselin and H. C. Hodge (1957). "Clinical toxicology of commercial products." Williams and Wilkins Co., Baltimore, MD: 154.

González Cabrera, D., F. Douelle, Y. Younis, T.-S. Feng, C. Le Manach, A. T. Nchinda, L. J. Street, C. Scheurer, J. Kamber and K. L. White (2012). "Structure–Activity Relationship Studies of Orally Active Antimalarial 3, 5-Substituted 2-Aminopyridines." Journal of Medicinal Chemistry 55(24): 11022-11030.

Groeneveld, A. and J. Arends (1975). "Influence of pH and demineralization time on mineral content, thickness of surface layer and depth of artificial caries lesions." Caries Research 9(1): 36-44.

Güler, H., G. Gündoğmaz, F. Kurtuluş, G. Çelik and Ş. Gacanoğlu (2011). "Solid state synthesis of calcium borohydroxyapatite." Solid State Sciences 13(11): 1916-1920.

Guo, X. and P. Xiao (2006). "Effects of solvents on properties of nanocrystalline hydroxyapatite produced from hydrothermal process." Journal of the European Ceramic Society 26(15): 3383-3391.

Haghgoo, R., F. Abbasi and M. B. Rezvani (2011). "Evaluation of the effect of nanohydroxyapatite on erosive lesions of the enamel of permanent teeth following exposure to soft beer in vitro." Scientific Research and Essays 6(28): 5933-5936.

Haghgoo, R., M. B. Rezvani and M. S. Zeinabadi (2014). "Comparison of nano-hydroxyapatite and sodium fluoride mouthrinse for remineralization of incipient carious lesions." Journal of Dentistry (Tehran, Iran) 11(4): 406.

Hamilton, W., G. Judd and G. Ansell (1973). "Ultrastructure of human enamel specimens prepared by ion micromilling." Journal of Dental Research 52(4): 703-710.

Hanks, C. T., J. C. Wataha and Z. Sun (1996). "In vitro models of biocompatibility: a review." Dental Materials 12(3): 186-193.

Hannig, M. and C. Hannig (2010). "Nanomaterials in preventive dentistry." Nature Nanotechnology 5(8): 565-569.

Harris, R. K., E. D. Becker, S. M. Cabral de Menezes, R. Goodfellow and P. Granger (2002). "NMR nomenclature: nuclear spin properties and conventions for chemical shifts. IUPAC Recommendations 2001. International Union of Pure and Applied Chemistry. Physical Chemistry Division. Commission on Molecular Structure and Spectroscopy." Magnetic Resonance in Chemistry 40(7): 489-505.

He, Q. and J. Shi (2011). "Mesoporous silica nanoparticle based nano drug delivery systems: synthesis, controlled drug release and delivery, pharmacokinetics and biocompatibility." Journal of Materials Chemistry 21(16): 5845-5855.

Hench, L. L. (1998). "Bioactive materials: the potential for tissue regeneration." Journal of Biomedical Materials Research Part A 41(4): 511-518.

Hench, L. L. (2006). "The story of Bioglass®." Journal of Materials Science: Materials in Medicine 17(11): 967-978.

Hench, L. L. and Ö. Andersson (1993). Bioactive glasses. An introduction to bioceramics, World Scientific: 41-62.

Hench, L. L. and J. Wilson (1996). Introduction. Clinical performance of skeletal prostheses, Springer: 1-10.

Hill, R. G. and M. M. Stevens (2007). Bioactive glass, Google Patents.

Hilliard, C. (2010). NHS Dental Epidemiology Programme for England Oral Health Survey of 12 year old Children 2008/2009 Press, North West Public Health Observatory.

Hlady, V. and H. Füredi-Milhofer (1979). "Adsorption of human serum albumin on precipitated hydroxyapatite." Journal of Colloid and Interface Science 69(3): 460-468.

Hocking, L. and A. Rivers (1982). "The spreading of a drop by capillary action." Journal of Fluid Mechanics 121: 425-442.

Höland, W., V. Rheinberger, E. Apel, C. van't Hoen, M. Höland, A. Dommann, M. Obrecht, C. Mauth and U. Graf-Hausner (2006). "Clinical applications of glass-ceramics in dentistry." Journal of Materials Science: Materials in Medicine 17(11): 1037-1042.

Holmen, L., A. Thylstrup and J. Artun (1987). "Surface changes during the arrest of active enamel carious lesions in vivo: a scanning electron microscope study." Acta Odontologica Scandinavica 45(6): 383-390.

Holmen, L., A. Thylstrup, B. Øgaard and F. Kragh (1985). "A scanning electron microscopic study of progressive stages of enamel caries in vivo." Caries Research 19(4): 355-367.

Holzwarth, U. and N. Gibson (2011). "The Scherrer equation versus the'Debye-Scherrer equation'." Nature Nanotechnology 6(9): 534-534.

Horvath, S. (1980). "Cytotoxicity of drugs and diverse chemical agents to cell cultures." Toxicology 16(1): 59-66.

Huang, F.-M. and Y.-C. Chang (2002). "Cytotoxicity of resin-based restorative materials on human pulp cell cultures." Oral Surgery, Oral Medicine, Oral Pathology, Oral Radiology, and Endodontology 94(3): 361-365.

Huang, S., S. Gao, L. Cheng and H. Yu (2011). "Remineralization potential of nano-hydroxyapatite on initial enamel lesions: an in vitro study." Caries Research 45(5): 460-468.

Huang, S., S. Gao and H. Yu (2009). "Effect of nano-hydroxyapatite concentration on remineralization of initial enamel lesion in vitro." Biomedical Materials 4(3): 034104.

Huang, T. T., L.-H. He, M. A. Darendeliler and M. V. Swain (2010). "Correlation of mineral density and elastic modulus of natural enamel white spot lesions using X-ray microtomography and nanoindentation." Acta biomaterialia 6(12): 4553-4559.

Hubbell, J. H. and S. M. Seltzer (1995). Tables of x-ray mass attenuation coefficients and mass energy-absorption coefficients 1 keV to 20 MeV for elements Z= 1 to 92 and 48 additional substances of dosimetric interest, National Inst. of Standards and Technology-PL, Gaithersburg, MD (United States). Ionizing Radiation Div.

Hunt, C. and J. Navia (1975). "Pre-eruptive effects of Mo, B, Sr and F on dental caries in the rat." Archives of Oral Biology 20(8): 497-501.

Imperiano, M. T., H. J. Khoury, M. L. A. Pontual, M. A. J. R. Montes and M. M. F. da Silveira (2007). "Comparative radiopacity of four low-viscosity composites." Brazilian journal of Oral Sciences 6(20):1278-1282.

Ingram, G. and L. Silverstone (1981). "A chemical and histological study of artificial caries in human dental enamel in vitro." Caries Research 15(5): 393-398.

Irinoda, Y., Y. Matsumura, H. Kito, T. Nakano, T. Toyama, H. Nakagaki and T. Tsuchiya (2000). "Effect of sealant viscosity on the penetration of resin into etched human enamel." Operative Dentistry 25(4): 274-282.

Isaac, S., F. Brudevold, F. A. Smith and D. E. Gardner (1958). "Solubility rate and natural fluoride content of surface and subsurface enamel." Journal of Dental Research 37(2): 254-263.

ISO, B. (1999). "10993-5: Biological evaluation of medical devices." Tests for in vitro cytotoxicity.

ISO, E. (2009). "10993-5. Biological evaluation of medical devices-Part 5: Tests for in vitro cytotoxicity." Geneva: International Organization for Standardization.

Issa, Y., D. Watts, P. Brunton, C. Waters and A. Duxbury (2004). "Resin composite monomers alter MTT and LDH activity of human gingival fibroblasts in vitro." Dental Materials 20(1): 12-20.

Jallot, E., J. Lao, J.-M. Nedelec, J.-M. Sautier and J. Isaac (2008). Strontium doped bioactive glasses, Google Patents.

Jenkins, R. (2000). "X-Ray Techniques: Overview." Encyclopedia of analytical chemistry.

Jeong, S., S. Jang, K. N. Kim, H. Kwon, Y. D. Park and B. Kim (2006). Remineralization potential of new toothpaste containing nano-hydroxyapatite. Key Engineering Materials, Trans Tech Publ.

Jia, W. and S. Jin (2004). Dental acid etchant composition, Google Patents.

Jones, L. J., M. Gray, S. T. Yue, R. P. Haugland and V. L. Singer (2001). "Sensitive determination of cell number using the CyQUANT® cell proliferation assay." Journal of Immunological Methods 254(1): 85-98.

Jongebloed, W., I. Molenaar and J. Arends (1975). "Morphology and size-distribution of sound and acid-treated enamel crystallites." Calcified Tissue International 19(1): 109-123.

Joseph, M., I. Gedalia and A. Fuks (1977). "Effect of strontium and fluoride administration on caries resistance of hamster molars." Journal of Dental Research 56(8): 924-924.

Kaneko, K. (1994). "Determination of pore size and pore size distribution: 1. Adsorbents and catalysts." Journal of Membrane Science 96(1-2): 59-89.

Kasten, F. H., S. M. Felder, L. Gettleman and T. Alchediak (1982). "A model culture system with human gingival fibroblasts for evaluating the cytotoxicity of dental materials." In vitro 18(7): 650-660.

Kato, A. and N. Ohno (2009). "Construction of three-dimensional tooth model by micro-computed tomography and application for data sharing." Clinical Oral Investigations 13(1): 43-46.

Kay, M. I., R. Young and A. Posner (1964). "Crystal structure of hydroxyapatite." Nature 204: 1050.

Kerebel, B., G. Daculsi and L. Kerebel (1979). "Ultrastructural studies of enamel crystallites." Journal of Dental Research 58(2_suppl): 844-851.

Kestin, J., M. Sokolov and W. A. Wakeham (1978). "Viscosity of liquid water in the range− 8 C to 150 C." Journal of Physical and Chemical Reference Data 7(3): 941-948.

Kidd, E. and O. Fejerskov (2004). "What constitutes dental caries? Histopathology of carious enamel and dentin related to the action of cariogenic biofilms." Journal of Dental Research 83(suppl 1): C35-C38.

Kidd, E. and J. Van Amerongen (2003). "The role of operative treatment." Dental caries: The disease and its clinical management. Blackwell Munksgaard, Oxford: 245-250.

Kim, S., E. Y. KIM, T. S. JEONG and J. W. KIM (2011). "The evaluation of resin infiltration for masking labial enamel white spot lesions." International Journal of Paediatric Dentistry 21(4): 241-248.

Koumoulidis, G. C., A. P. Katsoulidis, A. K. Ladavos, P. J. Pomonis, C. C. Trapalis, A. T. Sdoukos and T. C. Vaimakis (2003). "Preparation of hydroxyapatite via microemulsion route." Journal of Colloid and Interface Science 259(2): 254-260.

Kumar, S. R. and R. Vijayalakshmi (2006). "Nanotechnology in dentistry." Indian Journal of Dental Research 17(2): 62-65.

Labarca, C. and K. Paigen (1980). "A simple, rapid, and sensitive DNA assay procedure." Analytical Biochemistry 102(2): 344-352.

Larsen, M. (1990). "Chemical events during tooth dissolution." Journal of Dental Research 69(2_suppl): 575-580.

Lee, J.-J., Y.-K. Lee, B.-J. Choi, J.-H. Lee, H.-J. Choi, H.-K. Son, J.-W. Hwang and S.-O. Kim (2010). "Physical properties of resin-reinforced glass ionomer cement modified with micro and nano-hydroxyapatite." Journal of Nanoscience and Nanotechnology 10(8): 5270-5276.

Li, L., H. Pan, J. Tao, X. Xu, C. Mao, X. Gu and R. Tang (2008). "Repair of enamel by using hydroxyapatite nanoparticles as the building blocks." Journal of Materials Chemistry 18(34): 4079-4084.

Li, W., J. Zhou and Y. Xu (2015). "Study of the in vitro cytotoxicity testing of medical devices (Review)." Biomedical Reports 3(5): 617-620.

Li, Z., W. Lam, C. Yang, B. Xu, G. Ni, S. Abbah, K. Cheung, K. Luk and W. Lu (2007). "Chemical composition, crystal size and lattice structural changes after incorporation of strontium into biomimetic apatite." Biomaterials 28(7): 1452-1460.

Lippert, F. and A. Hara (2012). "Strontium and caries: a long and complicated relationship." Caries Research 47(1): 34-49.

Lockyer, M., D. Holland and R. Dupree (1995). "NMR investigation of the structure of some bioactive and related glasses." Journal of Non-Crystalline Solids 188(3): 207-219.

Lowe, N., Auty J. and Robinson C.(1971). Changes in Protein of Mineralizing Enamel. Journal of Dental Research, American Association Dental Research 1619 DUKE ST, ALEXANDRIA, VA 22314.

Lowell, S., J. E. Shields, M. A. Thomas and M. Thommes (2012). Characterization of porous solids and powders: surface area, pore size and density, Springer Science & Business Media.

Lu, A. H., E. e. L. Salabas and F. Schüth (2007). "Magnetic nanoparticles: synthesis, protection, functionalization, and application." Angewandte Chemie International Edition 46(8): 1222-1244.

Lynch, R., U. Mony and J. Ten Cate (2007). "Effect of lesion characteristics and mineralising solution type on enamel remineralisation in vitro." Caries Research 41(4): 257-262.

Lynch, R. and J. Ten Cate (2006). "The effect of lesion characteristics at baseline on subsequent de-and remineralisation behaviour." Caries Research 40(6): 530-535.

Magne, P. (2007). "Efficient 3D finite element analysis of dental restorative procedures using micro-CT data." Dental Materials 23(5): 539-548.

Maiwald, H. and L. Geiger (1973). "Lokalapplikation von Fluorschutzlack zur Kariesprophylaxe in Kollektiven." Dtsch Stomat 23: 56-63.

Marghalani, H. Y. (2016). Resin-Based Dental Composite Materials. Handbook of Bioceramics and Biocomposites, Springer: 357-405.

Margolis, H., Y. Zhang, C. Lee, R. Kent Jr and E. Moreno (1999). "Kinetics of enamel demineralization in vitro." Journal of Dental Research 78(7): 1326-1335.

Marsh, P. (2004). "Dental plaque as a microbial biofilm." Caries Research 38(3): 204-211.

Martignon, S., K. Ekstrand, J. Gomez, J. Lara and A. Cortes (2012). "Infiltrating/sealing proximal caries lesions: a 3-year randomized clinical trial." Journal of Dental Research 91(3): 288-292.

Martignon, S., K. R. Ekstrand and R. Ellwood (2006). "Efficacy of sealing proximal early active lesions: an 18-month clinical study evaluated by conventional and subtraction radiography." Caries Research 40(5): 382-388.

McMillan, P. W. (1964). "Glass-ceramics."

Mellberg, J. and C. Nicholson (1974). "Fluoride uptake in vivo by deciduous enamel of children from neutral fluoride and APF mouthrinses." Caries Research 8(2): 148-154.

Meyer-Lueckel, H., K. Bitter and S. Paris (2012). "Randomized controlled clinical trial on proximal caries infiltration: three-year follow-up." Caries Research 46(6): 544-548.

Meyer-Lueckel, H. and S. Paris (2008). "Progression of artificial enamel caries lesions after infiltration with experimental light curing resins." Caries Research 42(2): 117-124.

Meyer-Lueckel, H. and S. Paris (2010). "Infiltration of natural caries lesions with experimental resins differing in penetration coefficients and ethanol addition." Caries Research 44(4): 408-414.

Meyer-Lueckel, H., S. Paris and A. Kielbassa (2007). "Surface layer erosion of natural caries lesions with phosphoric and hydrochloric acid gels in preparation for resin infiltration." Caries Research 41(3): 223-230.

Meyerowitz, C., P. Spector and M. Curzon (1979). "Pre-or post-eruptive effects of strontium alone or in combination with fluoride on dental caries in the rat." Caries Research 13(4): 203-210.

Miao, S., W. Weng, K. Cheng, P. Du, G. Shen, G. Han and S. Zhang (2005). "Sol–gel preparation of Zn-doped fluoridated hydroxyapatite films." Surface and Coatings Technology 198(1): 223-226.

Mizutani, R. and Y. Suzuki (2012). "X-ray microtomography in biology." Micron 43(2): 104-115.

Mohammed, N. R. (2014). Effects of zinc and fluoride on in vitro enamel demineralisation conditions relevant to dental caries, Queen Mary University of London.

Moharamzadeh, K., I. M. Brook and R. Van Noort (2009). "Biocompatibility of resin-based dental materials." Materials 2(2): 514-548.

Momose, A., T. Takeda, Y. Itai and K. Hirano (1996). "Phase–contrast X–ray computed tomography for observing biological soft tissues." Nature medicine 2(4): 473-475.

Moreno, E. and R. Zahradnik (1973). "The pore structure of human dental enamel." Archives of Oral Biology 18(8): 1063-1068.

Moreno, E. C. and R. Zahradnik (1974). "Chemistry of enamel subsurface demineralization in vitro." Journal of Dental Research 53(2): 226-235.

Mosmann, T. (1983). "Rapid colorimetric assay for cellular growth and survival: application to proliferation and cytotoxicity assays." Journal of Immunological Methods 65(1-2): 55-63.

Mueller, J., H. Meyer-Lueckel, S. Paris, W. Hopfenmuller and A. Kielbassa (2006). "Inhibition of lesion progression by the penetration of resins in vitro: influence of the application procedure." Operative Dentistry 31(3): 338-345.

Muñoz, M. A., L. A. Arana-Gordillo, G. M. Gomes, O. M. Gomes, N. H. C. Bombarda, A. Reis and A. D. Loguercio (2013). "Alternative esthetic management of fluorosis and hypoplasia stains: blending effect obtained with resin infiltration techniques." Journal of Esthetic and Restorative Dentistry 25(1): 32-39.

Murchison, D. F., D. G. Charlton and W. S. Moore (1999). "Comparative radiopacity of flowable resin composites." Quintessence International 30(3).

Najibfard, K., K. Ramalingam, I. Chedjieu and B. Amaechi (2011). "Remineralization of early caries by a nano-hydroxyapatite dentifrice." Journal of Clinical Dentistry 22(5): 139.

Nanci, A. (2007). Ten cate's oral histology-pageburst on vitalsource: development, structure, and function, Elsevier Health Sciences.

Neel, E. A. A., A. Aljabo, A. Strange, S. Ibrahim, M. Coathup, A. M. Young, L. Bozec and V. Mudera (2016). "Demineralization–remineralization dynamics in teeth and bone." International Journal of Nano-medicine 11: 4743.

Neeraj Malhotra, M. and M. Kundabala Mala (2010). "Light-curing considerations for Resin-based composite materials: A review Part I." Compendium 31(7).

Neffgen, S., S. Neander and D. Lübbers (2012). Radiopaque infiltrant, Google Patents.

Nesteruk, T. and Ł. Wiśniewski "Microtomography in Morphologival studies of small invertebrates." OL PAN, 2015, 12, 62–70. https://www.researchgate.net/publication/301689065.

Niles, A. L., R. A. Moravec and T. L. Riss (2009). "In vitro viability and cytotoxicity testing and same-well multi-parametric combinations for high throughput screening." Current Chemical Genomics 3(33): e41.

Nly, O. and Orm F. (2001). "Generation of 3-D finite element models of restored human teeth using micro-CT techniques." The International Journal of Prosthodontics 14(4): 311.

Novelline, R. A. and L. F. Squire (2004). Squire's fundamentals of radiology, La Editorial, UPR.

Nummikoski, P., T. Martinez, S. Matteson, W. McDavid and S. Dove (1992). "Digital subtraction radiography in artificial recurrent caries detection." Dentomaxillofacial Radiology 21(2): 59-64.

O'Brien, W. J. and G. Ryge (1965). "Wettability of poly-(methyl methacrylate) treated with silicon tetrachloride." The Journal of Prosthetic Dentistry 15(2): 304-308.

O'donnell, M., P. Candarlioglu, C. Miller, E. Gentleman and M. Stevens (2010). "Materials characterisation and cytotoxic assessment of strontium-substituted bioactive glasses for bone regeneration." Journal of Materials Chemistry 20(40): 8934-8941.

O'Donnell, M., Y. Fredholm, A. De Rouffignac and R. Hill (2008). "Structural analysis of a series of strontium-substituted apatites." Acta Biomaterialia 4(5): 1455-1464.

Olson, B. L., J. L. Mcdonald and G. K. Stookey (1978). "The effect of strontium and fluoride upon in vitro plaque and rat caries." Journal of Dental Research 57(9): 903-903.

Omelon, S. J. and M. D. Grynpas (2008). "Relationships between polyphosphate chemistry, biochemistry and apatite biomineralization." Chemical Reviews 108(11): 4694-4715.

Orchardson, R., L. Gangarosa, G. Holland, D. H. Pashley, H. Trowbridge, F. Ashley, I. Kleinberg and U. Zappa (1994). "Dentine hypersensitivity—into the 21st century." Archives of Oral Biology 39: S113-S119.

Paolinelis, G., A. Banerjee and T. F. Watson (2009). "An in vitro evaluation of the efficiency of an air-abrasion system using helium as a propellant." Dental Materials 25(11): 1442-1445.

Paris, S., K. Bitter, M. Naumann, C. E. Dörfer and H. Meyer-Lueckel (2011). "Resin infiltration of proximal caries lesions differing in ICDAS codes." European Journal of Oral Sciences 119(2): 182-186.

Paris, S., J. Lausch, T. Selje, C. Dörfer and H. Meyer-Lueckel (2014). "Comparison of sealant and infiltrant penetration into pit and fissure caries lesions in vitro." Journal of Dentistry 42(4): 432-438.

Paris, S. and H. Meyer-Lueckel (2009). "Masking of labial enamel white spot lesions by resin infiltration--A clinical report." Quintessence International 40(9).

Paris, S. and H. Meyer-Lueckel (2010). "Infiltrants inhibit progression of natural caries lesions in vitro." Journal of Dental Research 89(11): 1276-1280.

Paris, S. and H. Meyer-Lueckel (2010). "Inhibition of caries progression by resin infiltration in situ." Caries Research 44(1): 47-54.

Paris, S., H. Meyer-Lueckel, H. Cölfen and A. M. Kielbassa (2007). "Penetration coefficients of commercially available and experimental composites intended to infiltrate enamel carious lesions." Dental Materials 23(6): 742-748.

Paris, S., H. Meyer-Lueckel and A. Kielbassa (2007). "Resin infiltration of natural caries lesions." Journal of Dental Research 86(7): 662-666.

Pashler, H. and C. R. Harris (2012). "Is the replicability crisis overblown? Three arguments examined." Perspectives on Psychological Science 7(6): 531-536.

Patel, J 2013.”Development of a novel radiopaque infiltration resin for early enamel carious lesion”, MClinDent thesis, Queen Mary University of London. London, UK.

Pawlowska, J. and Z. Jego (1956). "Strontium chloride its importance in dentistry and prophylaxis." Czasop Stomatol 9: 353-361.

Pearce, E. and D. Nelson (1989). "Microstructural features of carious human enamel imaged with back-scattered electrons." Journal of Dental Research 68(2): 113-118.

Pearce, N. X., M. Addy and R. Newcombe (1994). "Dentine hypersensitivity: a clinical trial to compare 2 strontium densensitizing toothpastes with a conventional fluoride toothpaste." Journal of Periodontology 65(2): 113-119.

Pedersen, A., A. Bardow, S. B. Jensen and B. Nauntofte (2002). "Saliva and gastrointestinal functions of taste, mastication, swallowing and digestion." Oral Diseases 8(3): 117-129.

Pendrys, D. and J. Stamm (1990). "Relationship of total fluoride intake to beneficial effects and enamel fluorosis." Journal of Dental Research 69(2_suppl): 529-538.

Pepla, E., L. K. Besharat, G. Palaia, G. Tenore and G. Migliau (2014). "Nano-hydroxyapatite and its applications in preventive, restorative and regenerative dentistry: a review of literature." Annali di Stomatologia 5(3): 108.

Peters, O., A. Laib, P. Rüegsegger and F. Barbakow (2000). "Three-dimensional analysis of root canal geometry by high-resolution computed tomography." Journal of Dental Research 79(6): 1405-1409.

Petersen, P. E., D. Bourgeois, H. Ogawa, S. Estupinan-Day and C. Ndiaye (2005). "The global burden of oral diseases and risks to oral health." Bulletin of the World Health Organization 83(9): 661-669.

Phillips, J. (1983). "Realization of a Zachariasen glass." Solid state communications 47(3): 203-206.

Pirayesh, H. and J. A. Nychka (2013). "Sol–Gel Synthesis of Bioactive Glass-Ceramic 45S5 and its in vitro Dissolution and Mineralization Behavior." Journal of the American Ceramic Society 96(5): 1643-1650.

Pissiotis, E. and L. Spångberg (1991). "Toxicity of Pulpispad using four different cell types." International Endodontic Journal 24(5): 249-257.

Pitts, N. B., A. I. Ismail, S. Martignon, K. Ekstrand, G. Douglas and C. Longbottom (2014). "ICCMS™ guide for practitioners and educators." Online information. Available at: wwwicdasorg/uploads/ICCMS-Guide_Full_Guide_UKpdf (accessed February 2017).

Portugal, J. and M. J. Waring (1988). "Assignment of DNA binding sites for 4', 6-diamidine-2-phenylindole and bisbenzimide (Hoechst 33258). A comparative footprinting study." Biochimica et Biophysica Acta (BBA)-Gene Structure and Expression 949(2): 158-168.

Puvvada, N., P. K. Panigrahi and A. Pathak (2010). "Room temperature synthesis of highly hemocompatible hydroxyapatite, study of their physical properties and spectroscopic correlation of particle size." Nanoscale 2(12): 2631-2638.

Rage, R., J. Mitchen and G. Wilding (1990). "DNA fluorometric assay in 96-well tissue culture plates using Hoechst 33258 after cell lysis by freezing in distilled water." Analytical biochemistry 191(1): 31-34.

Rawls, H., J. Starr, F. Kasten, M. Murray, J. Smid and I. Cabasso (1990). "Radiopaque acrylic resins containing miscible heavy-metal compounds." Dental Materials 6(4): 250-255.

Reimer, L. (2000). Scanning electron microscopy: physics of image formation and microanalysis, IOP Publishing.

Rengarajan, K., S. M. Cristol, M. Mehta and J. M. Nickerson (2002). "Quantifying DNA concentrations using fluorometry: a comparison of fluorophores." Molecular Vision 8: 416-421.

Ricketts, D., K. Ekstrand, E. Kidd and T. Larsen (2002). "Relating visual and radiographic ranked scoring systems for occlusal caries detection to histological and microbiological evidence." Operative Dentistry 27(3): 231-237.

Ricketts, D., E. Kidd, P. Liepins and R. Wilson (1996). "Histological validation of electrical resistance measurements in the diagnosis of occlusal caries." CariesRresearch 30(2): 148-155.

Robinson, C., A. Hallsworth, J. Weatherell and W. Künzel (1976). "Arrest and control of carious lesions: a study based on preliminary experiments with resorcinol-formaldehyde resin." Journal of Dental Research 55(5): 812-818.

Robinson, C., J. Kirkham and R. Shore (1995). Dental enamel: formation to destruction, CRC.

Robinson, C., R. Shore, S. Brookes, S. Strafford, S. Wood and J. Kirkham (2000). "The chemistry of enamel caries." Critical Reviews in Oral Biology & Medicine 11(4): 481-495.

Romieu, G., X. Garric, S. Munier, M. Vert and P. Boudeville (2010). "Calcium–strontium mixed phosphate as novel injectable and radio-opaque hydraulic cement." Acta Biomaterialia 6(8): 3208-3215.

Rooney, E., G. Davies, J. Neville, M. Robinson, C. Perkins and M. Bellis (2010). "NHS dental epidemiology programme for England." Oral Health Survey of 12.

Rost, D. H. (1991). "Effect strength vs. statistical significance: a warning against the danger of small samples: a comment on Gefferth and Herskovits's article “Leisure activities as predictors of giftedness”." European Journal for High Ability 2(2): 236-243.

Sadoh, D., M. Sharief and R. Howard (1999). "Case Study: Occupational exposure to methyl methacrylate monomer induces generalised neuropathy in a dental technician." British Dental Journal 186(8): 380-381.

Saeri, M. R., A. Afshar, M. Ghorbani, N. Ehsani and C. C. Sorrell (2003). "The wet precipitation process of hydroxyapatite." Materials Letters 57(24): 4064-4069.

Salzedas, L. M. P., M. J. Q. Louzada and A. B. d. Oliveira Filho (2006). "Radiopacity of restorative materials using digital images." Journal of Applied Oral Science 14(2): 147-152.

Schäfer, F. (1989). "Evaluation of the anticaries benefit of fluoride toothpastes using an enamel insert model." Caries Research 23(2): 81-86.

Schmitt, J. and H.-C. Flemming (1998). "FTIR-spectroscopy in microbial and material analysis." International Biodeterioration & Biodegradation 41(1): 1-11.

Scott, A., W. Egner, D. Gawkrodger, P. Hatton, M. Sherriff, R. Van Noort, C. Yeoman and J. Grummitt (2004). "The national survey of adverse reactions to dental materials in the UK: a preliminary study by the UK Adverse Reactions Reporting Project." British Dental Journal 196(8): 471-477.

Scott, D. B., J. W. Simmelink and V. Nygaard (1974). "Structural aspects of dental caries." Journal of Dental Research 53(2): 165-178.

Setoyama, N., M. Ruike, T. Kasu, T. Suzuki and K. Kaneko (1993). "Surface characterization of microporous solids with helium adsorption and small angle x-ray scattering." Langmuir 9(10): 2612-2617.

Shelby, J. E. (2005). Introduction to glass science and technology, Royal Society of Chemistry.

Shellis, R. and A. Hallsworth (1987). "The use of scanning electron microscopy in studying enamel caries." Scanning Microscopy 1(3): 1109-1123.

Shen, P., D. J. Manton, N. J. Cochrane, G. D. Walker, Y. Yuan, C. Reynolds and E. C. Reynolds (2011). "Effect of added calcium phosphate on enamel remineralization by fluoride in a randomized controlled in situ trial." Journal of Dentistry 39(7): 518-525.

Shey, Z. and M. Oppenheim (1979). "A clinical evaluation of a radiopaque material in the restoration of anterior and posterior teeth." The Journal of the American Dental Association 98(4): 569-571.

Siddiqui, S. (2014). Crystallographic and Microstructural Studies of Dental Enamel using Synchrotron X-ray Diffraction and Complementary Techniques, Queen Mary University of London.

Siegel, S. (1956). "The case of two independent samples." Nonparametric statistics for the Behavioral Sciences: 127-136.

Silverstone, L. (1968). "The surface zone in caries and in caries-like lesions produced in vitro." British Dental Journal 125(4): 145-157.

Silverstone, L. (1973). "Structure of carious enamel, including the early lesion." Oral Sciences Reviews 3: 100.

Silverstone, L. M. (1967). "Observations on the dark zone in early enamel caries and artificial caries-like lesions." Caries Research 1(3): 261-274.

Simmer, J. and A. Fincham (1995). "Molecular mechanisms of dental enamel formation." Critical Reviews in Oral Biology & Medicine 6(2): 84-108.

Siqueira, J. F., I. N. Rôças, A. Favieri and K. C. Lima (2000). "Chemomechanical reduction of the bacterial population in the root canal after instrumentation and irrigation with 1%, 2.5%, and 5.25% sodium hypochlorite." Journal of Endodontics 26(6): 331-334.

Smid, J., I. Cabasso, A. Obligin and H. R. Rawls (1991). Novel radiopaque heavy metal polymer complexes, compositions of matter and articles prepared therefrom, Google Patents.

Smith, T. M., A. J. Olejniczak, P. Tafforeau, D. J. Reid, F. E. Grine and J.-J. Hublin (2006). "Molar crown thickness, volume, and development in South African Middle Stone Age humans: research letter." South African Journal of Science 102(11-12): 513-517.

Spitzer, D. and J. Ten Bosch (1975). "The absorption and scattering of light in bovine and human dental enamel." Calcified Tissue Research 17(2): 129-137.

Stamboulis, A., R. V. Law and R. G. Hill (2004). "Characterisation of commercial ionomer glasses using magic angle nuclear magnetic resonance (MAS-NMR)." Biomaterials 25(17): 3907-3913.

Standard, I. (2000). "ISO 4049 polymer based filling, restorative and luting materials." International Organization for Standardization: 1-27.

Supino, R. (1995). "MTT assays." In vitro toxicity testing protocols: 137-149.

Sutton, M. D. (2008). "Tomographic techniques for the study of exceptionally preserved fossils." Proceedings of the Royal Society of London B: Biological Sciences 275(1643): 1587-1593.

Swain, M. V. and J. Xue (2009). "State of the art of Micro-CT applications in dental research." International Journal of Oral Science 1(4): 177.

Syvitski, J. P. (2007). Principles, methods and application of particle size analysis, Cambridge University Press.

Takuma, S., H. Tohda, N. Tanaka and Kobayashi T. (1987). "Lattice defects in and carious dissolution of human enamel crystals." Journal of Electron Microscopy 36(6): 387-391.

Tellez, M., J. Gomez, S. Kaur, I. A. Pretty, R. Ellwood and A. I. Ismail (2013). "Non-surgical management methods of noncavitated carious lesions." Community Dentistry and Oral Epidemiology 41(1): 79-96.

Ten Cate, J. and P. Duijsters (1982). "Alternating demineralization and remineralization of artificial enamel lesions." Caries Research 16(3): 201-210.

Ten Cate, J. and P. Duijsters (1983). "Influence of fluoride in solution on tooth demineralization." Caries Research 17(3): 193-199.

Thanoo, B. C., M. Sunny and A. Jayakrisnnan (1991). "Tantalum-loaded polyurethane microspheres for particulate embolization: Preparation and properties." Biomaterials 12(5): 525-528.

Tong, L., M. Pang, N. Mok, N. King and S. Wei (1993). "The effects of etching, micro-abrasion, and bleaching on surface enamel." Journal of Dental Research 72(1): 67-71.

Tschoppe, P., D. L. Zandim, P. Martus and A. M. Kielbassa (2011). "Enamel and dentine remineralization by nano-hydroxyapatite toothpastes." Journal of Dentistry 39(6): 430-437.

Tsuge, T. (2009). "Radiopacity of conventional, resin-modified glass ionomer, and resin-based luting materials." Journal of Oral Science 51(2): 223-230.

Turnbull, D. (1969). "Under what conditions can a glass be formed?" Contemporary physics 10(5): 473-488.

Ulukaya, E., F. Ozdikicioglu, A. Y. Oral and M. Demirci (2008). "The MTT assay yields a relatively lower result of growth inhibition than the ATP assay depending on the chemotherapeutic drugs tested." Toxicology in vitro 22(1): 232-239.

van Dijken, J. W., K. R. Wing and I. E. Ruyter (1989). "An evaluation of the radiopacity of composite restorative materials used in Class I and Class II cavities." Acta Odontologica Scandinavica 47(6): 401-407.

Velayudhan, P. V. (2013). Studies of Leaching of Metals from Food Ceramics, University of Waikato.

Virdi, M. S. (2012). Oral Health Care-Pediatric, Research, Epidemiology and Clinical Practice, InTech.

Volk, J., C. Ziemann, G. Leyhausen and W. Geurtsen (2009). "Non-irradiated campherquinone induces DNA damage in human gingival fibroblasts."Dental Materials 25(12): 1556-1563.

Volkert, C. A. and A. M. Minor (2007). "Focused ion beam microscopy and micromachining." MRS bulletin 32(05): 389-399.

Vollenweider, M., T. J. Brunner, S. Knecht, R. N. Grass, M. Zehnder, T. Imfeld and W. J. Stark (2007). "Remineralization of human dentin using ultrafine bioactive glass particles." Acta Biomaterialia 3(6): 936-943.

Vrbic, V. and F. Brudevold (1970). "Fluoride uptake from treatment with different fluoride prophylaxis pastes and from the use of pastes containing a soluble aluminum salt followed by topical application." Caries Research 4(2): 158-167.

Warren, B. E., Ed. (1969). X-ray Diffraction, Addison-Wesley Pub. Co.

Wataha, J. C. (2001). "Principles of biocompatibility for dental practitioners." The Journal of Prosthetic Dentistry 86(2): 203-209.

Wataha, J. C., C. Hanks, S. Strawn and J. Fat (1994). "Cytotoxicity of components of resins and other dental restorative materials." Journal of Oral Rehabilitation 21(4): 453-462.

Wataha, J. C., P. E. Lockwood, S. Bouillaguet and M. Noda (2003). "In vitro biological response to core and flowable dental restorative materials." Dental Materials 19(1): 25-31.

Watts, D. and J. McCabe (1999). "Aluminium radiopacity standards for dentistry: an international survey." Journal of Dentistry 27(1): 73-78.

Weatherell, J., S. Weidmann and D. Eyre (1968). "Histological appearance and chemical composition of enamel protein from mature human molars." Caries Research 2(4): 281-293.

Wefel, J. and J. Harless (1984). "Comparison of artificial white spots by microradiography and polarized light microscopy." Journal of Dental Research 63(11): 1271-1275.

Wefel, J., M. Jensen, P. Triolo, R. Faller, M. Hogan and W. Bowman (1995). "De/remineralization from sodium fluoride dentifrices." American Journal of Dentistry 8(4): 217-220.

Weidmann, S., J. Weatherell and S. M. Hamm (1967). "Variations of enamel density in sections of human teeth." Archives of Oral Biology 12(1): 85-97.

White, D. (1987). "Reactivity of fluoride dentifrices with artificial caries." Caries Research 21(2): 126-140.

Williams, D. B. and C. B. Carter (1996). The transmission electron microscope. Transmission Electron Microscopy, Springer: 3-17.

Willmott, N., F. Wong and G. Davis (2007). "An X-ray microtomography study on the mineral concentration of carious dentine removed during cavity preparation in deciduous molars." Caries Research 41(2): 129-134.

Winter, A. (1957). "Glass formation." Journal of the American Ceramic Society 40(2): 54-58.

Wong, F., P. Anderson, H. Fan and G. Davis (2004). "X-ray microtomographic study of mineral concentration distribution in deciduous enamel." Archives of Oral Biology 49(11): 937-944.

Wong, F., N. Willmott and G. Davis (2006). "Dentinal carious lesion in three dimensions." International Journal of Paediatric Dentistry 16(6): 419-423.

Xiang, Y. and J. Du (2011). "Effect of strontium substitution on the structure of 45S5 bioglasses." Chemistry of Materials 23(11): 2703-2717.

Yanagisawa, T. and Y. Miake (2003). "High-resolution electron microscopy of enamel-crystal demineralization and remineralization in carious lesions." Journal of Electron Microscopy (Tokyo) 52(6): 605-613.

Yanagisawa, T. and Y. Miake (2003). "High-resolution electron microscopy of enamel-crystal demineralization and remineralization in carious lesions." Journal of Electron Microscopy 52(6): 605-613.

Yuan, Y. and T. R. Lee (2013). Contact angle and wetting properties. Surface science techniques, Springer: 3-34.

Zakarias, A 2014.'Biocompatibility of Novel Radiopaque Resin Infiltrant', MClinDent thesis, Queen Mary University of London. London, UK.

Zhang, X., P. Anderson, S. Dowker and J. Elliott (2000). "Optical profilometric study of changes in surface roughness of enamel during in vitro demineralization." Caries Research 34(2): 164-174.

Appendix

Appendix A

The following tables are showing the five times readings for the different materials and calculations of the relevant dynamic viscosity.

	Passing time(sec)	Q=0.0014/Time (l/sec)	8lq	3r4P	V(Pa)	v(mPa)
Water	3.5	0.0004	0.000224	1.89375E-07	0.000845424	0.845424
ICON®	28.1	4.98221E-05	2.79004E-05	1.89375E-07	0.006787548	6.787548
20%wt Br in Resin	26.5	5.28302E-05	2.95849E-05	1.89375E-07	0.006401068	6.401068
30%wt Br in Resin	34.5	4.05797E-05	2.27246E-05	1.89375E-07	0.008333466	8.333466
40% wt Sn in Resin	18.8	7.44681E-05	4.17021E-05	1.89375E-07	0.004541135	4.541135
				1.89375E-07		
Water	3.4	0.000411765	0.000230588	1.89375E-07	0.000821269	0.821269
ICON®	28.4	4.92958E-05	2.76056E-05	1.89375E-07	0.006860013	6.860013
20%wt Br in Resin	26.5	5.28302E-05	2.95849E-05	1.89375E-07	0.006401068	6.401068
30%wt Br in Resin	34.2	4.09357E-05	2.2924E-05	1.89375E-07	0.008261001	8.261001
40% wt Sn in Resin	18.8	7.44681E-05	4.17021E-05	1.89375E-07	0.004541135	4.541135
				1.89375E-07		
Water	3.5	0.0004	0.000224	1.89375E-07	0.000845424	0.845424
ICON®	28.3	4.947E-05	2.77032E-05	1.89375E-07	0.006835858	6.835858
20%wt Br in Resin	26.4	5.30303E-05	2.9697E-05	1.89375E-07	0.006376913	6.376913
30%wt Br in Resin	34.3	4.08168E-05	2.28571E-05	1.89375E-07	0.008285156	8.285156
40% wt Sn in Resin	19	7.36842E-05	4.12632E-05	1.89375E-07	0.004589445	4.589445
				1.89375E-07		
Water	3.5	0.0004	0.000224	1.89375E-07	0.000845424	0.845424
ICON®	28.3	4.947E-05	2.77032E-05	1.89375E-07	0.006835858	6.835858
20%wt Br in Resin	26.3	5.32319E-05	2.98099E-05	1.89375E-07	0.006352758	6.352758
30%wt Br in Resin	34.5	4.05797E-05	2.27246E-05	1.89375E-07	0.008333466	8.333466
40% wt Sn in Resin	18.9	7.40741E-05	4.14815E-05	1.89375E-07	0.00456529	4.56529
				1.89375E-07		
Water	3.4	0.000411765	0.000230588	1.89375E-07	0.000821269	0.821269
ICON®	28.5	4.91228E-05	2.75088E-05	1.89375E-07	0.006884168	6.884168
20%wt Br in Resin	26.5	5.28302E-05	2.95849E-05	1.89375E-07	0.006401068	6.401068
30%wt Br in Resin	34.4	4.06977E-05	2.27907E-05	1.89375E-07	0.008309311	8.309311
40% wt Sn in Resin	18.9	7.40741E-05	4.14815E-05	1.89375E-07	0.00456529	4.56529

	1	2	3	4	5	mean	sd	se
Water	0.845424	0.821269	0.845424	0.845424	0.821269	0.835762	0.011833	0.005306
ICON®	6.787548	6.860013	6.835858	6.835858	6.884168	6.840689	0.032045	0.01437
20%wt BrM in ICON® resin	6.401068	6.401068	6.376913	6.352758	6.401068	6.386575	0.019324	0.008665
30%wt BrM in ICON® resin	8.333466	8.261001	8.285156	8.333466	8.309311	8.30448	0.028169	0.012632
40%wt SnM in ICON® resin	4.541135	4.541135	4.589445	4.56529	4.56529	4.560459	0.018076	0.008106

* sd= standard deviation

**se=standard error

Appendix B

The following tables are showing the five times contact angle readings for the different materials between 10s and 180s and relevant calculations of mean, standard error, standard deviation and t-test. The fifth reading was excluded from further calculations due to an error in reading was noticed.

	10sec	60sec	120sec	180sec	
Water	37.1	36.4	36.2	36.2	
ICON®	41.1	38.4	37.2	36.4	
20%wt Br in Resin	38.8	35.1	34.6	34.1	
30%wt Br in Resin	31.2	29.8	27.9	27.1	
40% wt Sn in Resin	30.8	22.4	21.9	21.4	
Water	30.2	27.9	27.8	27.6	
ICON®	43.3	40.3	38.9	37.4	
20%wt Br in Resin	35.6	32.1	31.9	31.3	
30%wt Br in Resin	30.5	28.9	28.4	28.1	
40% wt Sn in Resin	29.7	21.5	20.9	20.4	
Water	32.6	30.1	29.6	29.4	
ICON®	44.4	41.1	40.6	40.1	
20%wt Br in Resin	35.8	32.9	31.9	31.6	
30%wt Br in Resin	31.9	28.6	27.9	27.4	
40% wt Sn in Resin	31.4	23.1	22.3	21.8	
Water	39.7	37.6	37.6	37.9	
ICON®	40.9	37.9	36.8	35.9	
20%wt Br in Resin	37.2	33.6	32.7	32.1	
30%wt Br in Resin	29.9	27.1	26.9	26.4	
40% wt Sn in Resin	31.6	23.2	22.6	22.1	
Water	49.2	49.2	49.2	49.2	
ICON®	39.1	39.1	39.1	39.1	not used in calculation
20%wt Br in Resin	49.2	49.2	49.2	49.2	
30%wt Br in Resin	46.4	46.4	46.4	46.4	
40% wt Sn in Resin	39.1	39.1	39.1	39.1	

*Mean

	10sec	60sec	120sec	180sec
Water	34.9	33	32.8	32.775
ICON®	42.425	39.425	38.375	37.45
20%wt Br in Resin	36.85	33.425	32.775	32.275
30%wt Br in Resin	30.875	28.6	27.775	27.25
40% wt Sn in Resin	30.875	22.55	21.925	21.425

*Standard Deviation

	10sec	60sec	120sec	180sec
Water	3.716853508	4.09695	4.178516	4.3637
ICON®	1.478808642	1.317906	1.507274	1.622498
20%wt Br in Resin	1.283549765	1.103121	1.103121	1.09173
30%wt Br in Resin	0.749583218	0.972111	0.544862	0.610328
40% wt Sn in Resin	0.739509973	0.680074	0.641775	0.641775

*Standard Error

	10sec	60sec	120sec	180sec
Water	1.858427	2.04847504	2.089258242	2.181849846
ICON®	0.739404	0.65895277	0.753637015	0.811249037
20%wt Br in Resin	0.641775	0.55156029	0.551560287	0.545865139
30%wt Br in Resin	0.374792	0.48605555	0.272431184	0.30516389
40% wt Sn in Resin	0.369755	0.34003676	0.320887441	0.320887441

*t-test

	10-60s	10 -120s	10 -180s	60 - 120s	60-180s	120-180s
Water	0.018712435	0.017649	0.023739	0.161162	0.353894	0.845976
ICON®	0.000149157	7.66E-05	0.000692	0.012308	0.014666	0.021607
20%wt BrM in Resin	0.000315382	0.000174	0.000199	0.039015	0.005109	0.005109
30%wt BrM in Resin	0.015931063	0.004268	0.004181	0.113766	0.061639	0.014631
40% wt SnM in Resin	4.1927E-07	8.27E-07	7.03E-07	0.00217	0.000381	0.000381

Appendix C

The following tables are an example of how to read LAC values by Image J™ for each line within one lesion. These tables are showing the LAC values for three different lines within one lesion. The red numbers are the slice number, each 10th slice within the white spot lesion. (a) and (b) mean before and after infiltration of the resin, respectively. The first column is the distance from the surface of the lesion (pixel).

Middle line-top lesion

		Middle line-Top lesion																							
Slice Number	70	70-a	70-b	80-a	80-b	90-a	90-b	100-a	100-b	110-a	110-b	120-a	120-b	130-a	130-b	140-a	140-b	150-a	150-b	160-a	160-b	170-a	170-b	180-a	180-b
	0	0.3733	0.0133	0.3333	0	0.36	0.0267	0.3333	0.0533	0.3333	0.0533	0.3867	0.0533	0.3467	0.0267	0.3467	0.0133	0.3333	0	0.2933	0.0133	0.36	0.0267	0.3333	0.0133
	1	0.32	0.0794	0.3468	0.0397	0.3597	0.0132	0.3332	0.0397	0.32	0.0268	0.3733	0.0663	0.3464	0.0397	0.36	0.0536	0.3206	0.0396	0.3731	0.0005	0.3335	0.0132	0.3465	0
	2	0.3069	0.0787	0.3469	0.0528	0.3728	0	0.3331	0.0264	0.3331	0	0.3467	0.0523	0.3203	0.0523	0.3731	0.0267	0.3205	0	0.3721	0.0008	0.3333	0.0003	0.3731	0.0392
	3	0.3452	0.0396	0.347	0.0267	0.36	0.0648	0.3459	0.0396	0.3459	0.0259	0.3333	0.0267	0.32	0.0004	0.3855	0	0.3596	0.0008	0.3459	0.0137	0.32	0.0008	0.3467	0.0518
	4	0.3713	0.039	0.36	0.0035	0.3733	0.0257	0.3462	0.0267	0.3195	0.0128	0.3462	0.0652	0.3323	0.0128	0.3723	0.0005	0.36	0.0133	0.3452	0.0128	0.3338	0	0.398	0.039
	5	0.3721	0.0254	0.3848	0.0419	0.3727	0.0152	0.3606	0.0013	0.3067	0.0133	0.3467	0.0267	0.3721	0.0254	0.3213	0.0006	0.3473	0.0127	0.3467	0	0.3473	0.0127	0.3727	0.014
	6	0.3348	0	0.3718	0.0526	0.3467	0.04	0.3615	0.0023	0.3474	0.0629	0.3341	0.0023	0.3733	0.003	0.3215	0.0133	0.3348	0.0267	0.3208	0.0259	0.3474	0.0377	0.3459	0.0289
	7	0.3475	0.0267	0.3716	0.0133	0.3467	0.0516	0.3609	0.0275	0.3849	0.0623	0.3458	0.0018	0.3858	0.0382	0.3333	0.0516	0.3351	0.0125	0.3342	0.0258	0.3618	0.0249	0.3209	0.0018
	8	0.358	0.0247	0.3723	0.038	0.36	0.037	0.3477	0.0533	0.3857	0.037	0.3477	0.003	0.3867	0.041	0.318	0.037	0.358	0.0267	0.3333	0.0257	0.3867	0.001	0.321	0.002
	9	0.3589	0	0.36	0.0377	0.3478	0	0.3478	0.0533	0.4088	0.061	0.3467	0.0133	0.3745	0.0522	0.3333	0	0.3433	0.0644	0.3311	0.0366	0.3955	0.0145	0.3211	0.0289
	10	0.3721	0	0.3613	0.0362	0.3358	0	0.3613	0.04	0.3696	0.0508	0.3346	0	0.3346	0.0242	0.3346	0.0242	0.3187	0.1029	0.3296	0.0483	0.3854	0.0025	0.3492	0.0146
	11	0.3494	0	0.3719	0.0147	0.3614	0.0119	0.3839	0.04	0.3494	0.0478	0.3494	0.0358	0.3333	0.0358	0.3467	0.0358	0.3439	0.0828	0.3292	0.0119	0.36	0.0147	0.3614	0.0281
	12	0.3482	0	0.3852	0.0045	0.3748	0.0118	0.3748	0.0015	0.3482	0.0236	0.3364	0.0355	0.3467	0.0355	0.357	0.0621	0.357	0.006	0.32	0.0118	0.323	0.0297	0.3748	0.0355
	13	0.3567	0.0182	0.3733	0.015	0.3766	0.0016	0.375	0	0.345	0.0585	0.3467	0.0601	0.3483	0.0468	0.3551	0.0351	0.3567	0.0166	0.2999	0.0117	0.3333	0.0199	0.3616	0
	14	0.3698	0.0204	0.36	0	0.4	0.0018	0.3884	0.0382	0.3494	0.0231	0.3547	0.081	0.3484	0.0267	0.3849	0.0782	0.3431	0.0249	0.3369	0.0382	0.3369	0.0631	0.3253	0.0018
	15	0.3714	0.0057	0.3371	0.0286	0.3771	0.0019	0.3752	0.0362	0.3162	0.0343	0.3333	0.0458	0.3371	0.0114	0.3677	0.0228	0.3086	0.0229	0.3581	0.061	0.3371	0.0381	0.3733	0.0114
	16	0.3733	0	0.3353	0.0307	0.3474	0.0247	0.362	0.034	0.3353	0.038	0.32	0.0626	0.3753	0.0113	0.3447	0.0194	0.2983	0.036	0.3733	0.0647	0.36	0.042	0.396	0
	17	0.3712	0.0112	0.36	0.0309	0.3776	0.0379	0.3733	0	0.3445	0.04	0.3333	0.0133	0.4181	0.0491	0.3424	0.0176	0.3312	0.0624	0.3397	0.0751	0.3755	0.0155	0.3712	0
	18	0.3756	0.0355	0.3688	0.0687	0.3489	0.0377	0.3711	0.0201	0.3223	0.0267	0.3776	0.04	0.4043	0.0443	0.3577	0.0201	0.3444	0.0579	0.3489	0.08	0.3444	0.0045	0.3424	0.0267
	19	0.3757	0.0133	0.3843	0.0547	0.3405	0.0048	0.3576	0.0424	0.3224	0.0219	0.3747	0.0314	0.4038	0.0048	0.3733	0.0314	0.3467	0.0605	0.3333	0.0557	0.3357	0.0109	0.3514	0.0314
	20	0.3358	0	0.4	0.0649	0.3567	0.0025	0.365	0.045	0.3575	0	0.3683	0.0133	0.3733	0.0075	0.3733	0.0425	0.3442	0.0692	0.3034	0.035	0.3542	0.0108	0.36	0.0775
	21	0.3626	0.0267	0.376	0.0481	0.3626	0.0321	0.3572	0.0158	0.3307	0.0053	0.4	0	0.384	0.0079	0.3733	0.0053	0.36	0.0507	0.3586	0.016	0.3626	0.0107	0.3626	0.0721
	22	0.3761	0.0584	0.36	0.0377	0.3494	0.0634	0.36	0.0272	0.3527	0.0194	0.395	0.0211	0.3972	0.0055	0.3867	0.0405	0.3683	0.0423	0.3356	0.0311	0.3522	0.0428	0.3678	0.0428
	23	0.3809	0.0533	0.3391	0.026	0.3733	0.0551	0.3525	0.0458	0.4047	0.0087	0.4133	0.0313	0.3867	0.0313	0.4018	0.0609	0.3971	0.0371	0.3247	0.0087	0.36	0.0771	0.3733	0.0209
	24	0.3909	0.0533	0.3691	0.0478	0.3673	0.037	0.3436	0.0667	0.3836	0.0357	0.4	0	0.3764	0.0576	0.3879	0.0503	0.3867	0	0.398	0	0.3836	0.003	0.3733	0.0206
	25	0.3867	0.0369	0.3796	0.0494	0.3631	0.0408	0.3498	0.0361	0.4376	0.0737	0.4031	0.0392	0.393	0.0502	0.4	0.0053	0.4235	0.0094	0.4369	0.0737	0.4345	0.0157	0.3569	0.0031
	26	0.3633	0.0186	0.3399	0.04	0.3499	0	0.3665	0.0367	0.4337	0.0433	0.4231	0.0533	0.3997	0.0367	0.4199	0.0299	0.4896	0.0634	0.64	0.0532	0.48	0.0433	0.3867	0.2033
	27	0.3569	0.0468	0.3234	0.0531	0.3867	0.0054	0.4094	0.0596	0.4133	0.0465	0.4409	0.0532	0.4369	0.0054	0.4567	0.0269	0.5809	0.0962	0.994	0.0634	0.7067	0.2131	0.5101	0.3501
	28	0.3769	0.0239	0.3769	0.033	0.5102	0.0035	0.4898	0.0392	0.4498	0.0463	0.5306	0.0561	0.4933	0.0141	0.5102	0.0176	0.6732	0.0565	1.7454	0.358	1.1326	0.7439	0.8372	0.4765
	29	0.3867	0.0376	0.4133	0.0327	0.8509	0.0291	0.6557	0.0206	0.5686	0	0.657	0.0654	0.617	0.0497	0.634	0.0764	0.8038	0.04	2.1979	0.9615	2.0473	1.8703	1.457	1.1746
	30	0.4075	0.0113	0.52	0	1.3311	0.0678	0.9316	0.0475	0.7304	0.0533	0.9104	0.0667	0.836	0.0782	0.8438	0.1307	1.0908	0.3064	2.2616	1.3509	2.9867	2.8591	2.442	2.4304

Middle line-top lesion

	31	0.4628	0.0384	0.7922	0	1.6728	0.0738	1.1389	0.1011	0.9067	0.08	1.1694	0.0517	1.145	0.095	1.0384	0.1389	1.4214	0.5918	2.4109	1.9566	3.2972	3.0478	3.1145	2.8995
	32	0.5346	0.0254	1.2893	0.0254	1.5935	0.2521	1.2081	0.0974	1.1733	0.0639	1.3067	0.1094	1.4161	0.3693	1.164	0.4226	1.7555	0.7806	2.6355	2.3477	3.324	3.0747	3.2614	3.0574
	33	0.7434	0.0575	1.7167	0.2042	1.5716	0.7814	1.2525	0.1283	1.3016	0.1117	1.6208	0.3117	1.6907	0.8459	1.2708	0.48	2.1636	1.2093	2.8655	2.6964	3.3108	3.0842	3.3108	3.0933
	34	1.2704	0.1376	1.8319	0.8886	1.9009	1.525	1.3733	0.3814	1.3809	0.3595	2.2171	0.7452	2.1223	0.9947	1.5009	0.6219	2.6888	2.0463	3.1052	2.9275	3.3062	3.0438	3.3114	3.0395
	35	2.1156	0.942	1.8713	1.3377	2.4884	2.3059	1.7332	0.8665	1.6575	0.7331	2.8487	1.657	2.724	1.8346	2.0796	1.0931	3.0884	2.7551	3.1999	3.0176	3.2933	3.0443	3.2891	3.0488
	36	2.804	2.1067	2.204	1.8068	3.0005	2.8229	2.4533	1.9733	2.2667	1.3291	3.1779	2.6941	3.1509	2.8445	2.7784	2.1701	3.2712	3.0043	3.2045	3.0757	3.2709	3.0667	3.2579	3.0933
	37	3.1194	2.7274	2.7733	2.5281	3.2233	3.0313	3.0487	2.8927	2.9467	2.4353	3.2667	2.934	3.222	2.9867	3.138	2.9253	3.2753	3.0034	3.1873	3.106	3.2474	3.0667	3.2059	3.026
	38	3.2571	2.9847	3.1067	2.9019	3.2858	3.0533	3.2581	3.0571	3.1952	2.9457	3.32	3.0201	3.2314	3.0752	3.2496	3.0191	3.2629	3.041	3.2048	3.0513	3.239	3.0629	3.1962	2.9857
	39	3.3333	3.1137	3.193	3.0057	3.3165	3.0498	3.2751	3.0702	3.24	3.0267	3.2982	3.0694	3.2098	3.1235	3.2533	3.0281	3.2582	3.0982	3.2302	3.047	3.247	3.073	3.2035	2.9951
	40	3.3499	3.0818	3.2883	3.0714	3.2951	3.0684	3.275	3.1165	3.2584	3.0599	3.2616	3.0584	3.1668	3.0901	3.2234	3.0601	3.24	3.0782	3.2433	3.0418	3.2033	3.0667	3.1751	2.9784

	41	3.3252	3.0946	3.3282	3.1209	3.2852	3.04	3.28	3.0748	3.2452	3.0489	3.2615	3.0564	3.2021	3.0197	3.2391	3.0348	3.2288	3.0318	3.1867	3.0421	3.1845	3.0452	3.1518	3.0206
	42	3.3172	3.1492	3.3042	3.0681	3.2775	3.0481	3.2694	3.0533	3.2533	3.0775	3.2081	3.0481	3.2106	3.0267	3.2081	2.9972	3.2133	3.0292	3.1839	3.0186	3.1975	3.0106	3.1358	3.0133
	43	3.2962	3.1146	3.2933	3.0958	3.2642	3.0187	3.2642	3.0108	3.2425	3.0216	3.2213	3.0454	3.2133	3.0425	3.1971	3.0483	3.1679	3.0371	3.1753	3.0484	3.1971	3.0158	3.1387	2.9762
	44	3.2911	3.0855	3.2833	3.0892	3.2377	3.0848	3.2533	3.0377	3.2244	3.0455	3.24	3.0234	3.2133	3.0377	3.16	3.0455	3.16	2.9857	3.1701	3.04	3.1567	2.9723	3.1034	2.9877
	45	3.3277	3.0647	3.2667	3.0933	3.2343	3.0517	3.2543	3.0507	3.2308	3.0268	3.1847	3.0533	3.181	3.017	3.162	3.0016	3.1753	2.941	3.2057	3.042	3.122	2.9487	3.1143	2.9503
	46	3.3182	3.0707	3.2591	3.0725	3.2684	3.0609	3.2075	3.0435	3.2136	3.004	3.164	3.0458	3.1426	3.0556	3.1675	3.0898	3.16	2.9489	3.1774	2.956	3.1182	2.9507	3.0951	2.9009
	47	3.3067	3.0741	3.2533	3.1126	3.2756	3.0977	3.1808	3.0533	3.2	3.0148	3.1436	2.9941	3.1392	3.0281	3.1792	3.0356	3.1526	2.9377	3.1392	2.9941	3.1467	2.9644	3.0326	2.8818
	48	3.2727	3.0581	3.2619	3.0667	3.234	3.0558	3.1796	3	3.2206	3.0086	3.1854	3.0146	3.16	3.0242	3.1225	2.9467	3.1587	2.96	3.1067	3.0073	3.1152	2.8896	3.0206	2.8314
	49	3.28	3.0555	3.2072	3.0533	3.1938	2.9938	3.1877	3.0298	3.2287	2.9956	3.2133	3.0062	3.1662	2.999	3.12	2.9405	3.16	2.9682	3.0872	2.961	3.0682	2.919	3.0558	2.8555
	50	3.2659	3.0648	3.2	3.0535	3.1937	2.9652	3.2008	3.0611	3.198	2.9819	3.1678	2.9985	3.1469	3.0287	3.1248	2.9764	3.1401	2.9819	3.1004	2.9348	3.0667	2.927	3.007	2.844

	51	3.2592	3.119	3.2336	3.0538	3.2128	2.9753	3.199	3	3.1664	3.0187	3.1664	2.9328	3.1467	2.9867	3.119	2.9808	3.1136	2.9072	3.0805	2.9003	3.0331	2.8938	2.9869	2.8192
	52	3.2199	3.1331	3.207	3.0755	3.1801	3.0126	3.1927	2.9937	3.1401	2.9537	3.1399	2.9758	3.1401	2.9396	3.0797	2.9205	3.0936	2.8805	3.0803	2.9328	3.04	2.9074	2.9001	2.7467
	53	3.2067	3.08	3.1933	3.02	3.1533	3.0333	3.16	3.0067	3.14	2.9753	3.1267	2.9867	3.1267	2.9333	3.0867	2.9067	3.1067	2.9067	3.08	2.9267	3	2.8467	2.7733	2.68
	54	3.1932	3.0257	3.1799	3.0667	3.1535	2.9726	3.1532	2.9799	3.16	2.9394	3.12	2.9753	3.0994	2.993	3.0853	2.9135	3.0865	2.9135	3.0199	2.8797	2.9935	2.8528	2.9328	2.4058
	55	3.1664	2.9936	3.16	2.9792	3.161	2.9857	3.1536	2.9526	3.1264	2.9328	3.1136	2.9826	3.0928	2.9805	3.0795	2.9062	3.0528	2.9067	2.9995	2.9403	2.9803	2.8459	2.1787	1.9847
	56	3.1718	2.9952	3.1263	2.9804	3.1411	2.993	3.1663	3.033	3.1004	2.953	3.0953	2.9726	3.0996	2.9411	3.0667	2.9192	3.0804	2.9004	3.033	2.9286	2.8996	2.7796	1.9263	1.7648
	57	3.1662	3.0605	3.1405	3.0062	3.1067	2.9733	3.1528	3.0133	3.1415	2.9867	3.0862	2.8943	3.0677	2.92	3.0462	2.8647	3.0605	2.8995	3.0257	2.8667	2.6667	2.6308	1.8052	1.6523
	58	3.1321	3.06	3.1394	2.9753	3.0921	2.92	3.1006	2.9806	3.126	2.9587	3.0853	2.9019	3.0606	2.8896	3.0521	2.8025	3.0279	2.8946	2.9721	2.8387	2.3648	2.2387	1.7235	1.646
	59	3.1259	2.9985	3.1423	2.9526	3.0844	2.9215	3.1082	2.9362	3.12	2.9392	3.1008	2.8918	3.0459	2.9215	3.0252	2.8756	3.0253	2.9023	2.8859	2.8267	2.0636	1.8888	1.68	1.6474
	60	3.1542	2.9776	3.16	2.9275	3.0631	2.9275	3.0951	2.9298	3.0951	2.8951	3.0591	2.92	3.0516	2.9177	3.0058	2.9142	3.0302	2.876	2.7298	2.7107	1.884	1.8191	1.7067	1.5925

Middle line-top lesion

	61	3.141	2.9923	3.1257	2.987	3.078	2.9717	3.0877	2.9503	3.0667	2.9087	3.0533	2.9026	3.0513	2.88	3.0343	2.8687	3.0077	2.842	2.4493	2.3919	1.798	1.6667	1.68	1.598
	62	3.1379	2.9811	3.0933	3.0234	3.1067	2.9801	3.0855	2.9233	3.0377	2.9346	3.0267	2.8755	3.0189	2.8855	3.0045	2.8501	2.9089	2.8156	2.1421	1.9542	1.7333	1.6355	1.6667	1.6023
	63	3.1225	2.9571	3.0825	3.0371	3.0933	2.9416	3.075	2.9787	3.0242	2.925	3.0321	2.8804	3	2.8854	2.9492	2.84	2.8187	2.7092	1.9175	1.7525	1.6854	1.6238	1.6904	1.5842
	64	3.1094	2.9867	3.1122	2.9597	3.0775	2.9306	3.0825	2.9494	3.04	2.9404	3.0292	2.8892	3.0028	2.8483	2.9572	2.8828	2.8319	2.5947	1.8186	1.6639	1.6961	1.6428	1.7414	1.6
	65	3.1015	2.9364	3.1424	2.967	3.0594	2.9488	3.0709	2.9333	3.043	2.9712	3.0155	2.8555	2.9652	2.8443	2.9467	2.8491	2.3355	2.24	1.7415	1.674	1.6994	1.6073	1.7579	1.6503
	66	3.0984	2.8883	3.115	2.9701	3.0616	3.0015	3.0367	2.9084	3.045	2.8933	3.0133	2.8284	2.9618	2.805	2.9016	2.8151	2.045	1.8782	1.6933	1.6418	1.7333	1.6483	1.7716	1.6068
	67	3.1418	2.903	3.1382	2.8533	3.0316	2.9667	3.0498	2.8898	3.0414	2.8533	3	2.8631	2.9818	2.7867	2.7831	2.713	1.9284	1.7586	1.6849	1.6582	1.7347	1.6435	1.7818	1.6084
	68	3.1114	2.9391	3.1306	2.882	3.0181	2.92	3.0629	2.9162	3.001	2.8725	2.9819	2.8913	2.9504	2.7952	2.5477	2.4516	1.7952	1.6629	1.7019	1.6314	1.7381	1.6267	1.7504	1.6513
	69	3.124	2.9386	3.0847	2.8847	3.018	2.9153	3.0093	2.8813	3.0047	2.8586	2.9953	2.8394	2.9113	2.7879	2.2146	1.9979	1.7067	1.618	1.698	1.64	1.7426	1.6753	1.7594	1.6481
	70	3.1243	2.9467	3.0667	2.9069	2.996	2.915	3.0136	2.8579	3.0088	2.8536	3.0133	2.8619	2.8491	2.7248	1.9381	1.7758	1.7286	1.6133	1.7021	1.636	1.7733	1.6752	1.7291	1.6621

	71	3.1199	2.92	3.0311	2.9776	3.04	2.8891	3.0044	2.8577	3.0177	2.8667	2.9823	2.8634	2.7243	2.6976	1.7777	1.6757	1.7157	1.6176	1.7112	1.5953	1.7823	1.6891	1.7867	1.6443
	72	3.0747	2.9338	3.0576	2.9467	3.0491	2.8933	2.9914	2.88	3.0304	2.8805	2.9691	2.8182	2.4571	2.3318	1.72	1.6443	1.7424	1.6395	1.7205	1.6488	1.7781	1.681	1.8096	1.6395
	73	3.0825	2.9467	3.0258	2.8892	3.0575	2.8616	2.96	2.8951	3.0391	2.8726	2.8975	2.7967	2.0708	1.9591	1.7309	1.6258	1.72	1.6492	1.7067	1.6901	1.7692	1.675	1.7742	1.6708
	74	3.0481	2.8966	3.004	2.8747	3.0521	2.8735	2.9733	2.8813	3.0081	2.8747	2.7374	2.7346	1.804	1.7761	1.7439	1.6201	1.6974	1.72	1.7333	1.6906	1.7698	1.6747	1.7733	1.6887
	75	3.0267	2.935	3.0189	2.8628	3.0117	2.9067	2.9639	2.8833	2.96	2.8611	2.485	2.4062	1.7372	1.7122	1.7561	1.6611	1.7122	1.6494	1.7589	1.7161	1.7717	1.705	1.7883	1.695
	76	3.0229	2.8991	3.0116	2.9009	3.0171	2.8189	2.9562	2.8211	2.9467	2.8838	2.1313	2.0098	1.6971	1.6418	1.7391	1.6742	1.7525	1.6629	1.7429	1.6742	1.7484	1.68	1.7907	1.7049
	77	3.04	2.9297	3.0121	2.8886	3.0303	2.8582	2.9733	2.8533	2.8582	2.8497	1.8679	1.7746	1.6873	1.6013	1.6873	1.6248	1.7394	1.663	1.7394	1.7176	1.766	1.686	1.7891	1.6787
	78	3.0196	2.9392	3.0063	2.8737	3.0161	2.8702	2.9369	2.8408	2.8808	2.8455	1.7843	1.6408	1.6969	1.6667	1.6906	1.6526	1.7157	1.6961	1.7761	1.68	1.7361	1.6926	1.7698	1.6569
	79	3.0233	2.9067	2.96	2.8567	3.0165	2.857	2.9268	2.8138	2.3265	2.2633	1.7203	1.6167	1.7166	1.6504	1.7299	1.713	1.7331	1.6735	1.7699	1.6834	1.7566	1.6633	1.7868	1.6633
	80	3.0433	2.8833	2.9331	2.8164	3.0234	2.8362	2.8931	2.8065	1.9867	1.8501	1.7532	1.6199	1.7736	1.6999	1.7501	1.7069	1.7369	1.72	1.7499	1.7369	1.7603	1.6699	1.7567	1.6634

	81	3.04	2.8761	2.9592	2.8698	2.9469	2.8557	2.7498	2.753	1.793	1.7678	1.7498	1.6965	1.7435	1.7028	1.7467	1.6863	1.7333	1.6933	1.7498	1.7028	1.7506	1.6909	1.7772	1.6698
	82	3.037	2.8787	2.9733	2.9079	2.9333	2.8727	2.5187	2.4865	1.7643	1.7316	1.686	1.6667	1.72	1.6516	1.7733	1.7424	1.7424	1.6667	1.763	1.683	1.7909	1.6667	1.8133	1.7109
	83	3.0609	2.9716	2.9716	2.898	2.9067	2.8325	2.1507	2.0203	1.7142	1.6667	1.6858	1.6983	1.7333	1.6789	1.76	1.7722	1.742	1.644	1.7762	1.6922	1.7867	1.6696	1.7942	1.7247
	84	3.1011	2.9366	2.955	2.84	2.8317	2.7605	1.8272	1.7205	1.7306	1.6745	1.7306	1.6722	1.7522	1.6438	1.7494	1.6589	1.7122	1.6483	1.7867	1.6639	1.7761	1.6561	1.7889	1.7384
	85	3.0533	2.9174	2.9653	2.8453	2.584	2.5707	1.7386	1.5918	1.7307	1.6079	1.7226	1.6747	1.7519	1.7146	1.7093	1.7253	1.6986	1.6881	1.7626	1.6933	1.7493	1.6426	1.7761	1.7093
	86	3.0375	2.9308	2.9567	2.8158	2.28	2.1067	1.6958	1.6292	1.6958	1.6425	1.7358	1.6425	1.7358	1.715	1.7308	1.7092	1.7467	1.6966	1.7575	1.6616	1.7358	1.6966	1.7796	1.7175
	87	3.0448	2.9224	2.9272	2.8	2	1.8557	1.6909	1.6291	1.7552	1.6167	1.7286	1.6519	1.72	1.7395	1.7491	1.7614	1.76	1.6909	1.7928	1.6776	1.7795	1.6776	1.7576	1.7005
	88	3.0443	2.9245	2.918	2.8088	1.9467	1.8023	1.6865	1.5756	1.7444	1.6536	1.7623	1.6913	1.7265	1.6357	1.7535	1.6755	1.7489	1.6933	1.8264	1.7288	1.7909	1.6624	1.7688	1.6735
	89	3.0091	2.9509	2.8976	2.8624	2.0645	1.7867	1.6491	1.6267	1.7488	1.6512	1.7952	1.6397	1.736	1.6634	1.7643	1.6288	1.7243	1.6667	1.7824	1.6997	1.7712	1.7062	1.8155	1.7067
	90	3.0226	2.9426	2.9281	2.874	2.2307	1.9668	1.68	1.6953	1.7353	1.6533	1.764	1.642	1.7426	1.7039	1.7733	1.724	1.7127	1.7107	1.758	1.7333	1.764	1.7353	1.798	1.7313

Middle line-top lesion

	91	3.0419	2.9123	2.9332	2.8648	2.5257	2.4114	1.7352	1.7104	1.7467	1.7067	1.7219	1.6704	1.7525	1.6914	1.7429	1.6971	1.7829	1.72	1.7733	1.7506	1.7486	1.7009	1.781	1.7981
	92	3.0533	2.9165	2.9502	2.8098	2.7365	2.6933	1.7084	1.673	1.7733	1.6719	1.7102	1.6986	1.7449	1.6533	1.6969	1.6782	1.7947	1.7218	1.8081	1.7165	1.8063	1.7653	1.7965	1.7253
	93	3.0517	2.88	2.9651	2.8419	2.8699	2.7932	1.6999	1.6767	1.7083	1.6182	1.7148	1.6966	1.7584	1.6699	1.7867	1.7001	1.7499	1.7048	1.7867	1.6433	1.8335	1.7633	1.7766	1.72
	94	3.0385	2.883	2.9852	2.8858	2.9245	2.8148	1.8533	1.7082	1.6564	1.5912	1.7615	1.6564	1.7452	1.7082	1.7718	1.723	1.726	1.6845	1.7764	1.6579	1.8236	1.7097	1.7897	1.7867
	95	3.0014	2.9039	3.0119	2.8708	2.9536	2.8308	2.0625	1.902	1.6083	1.6203	1.7733	1.6814	1.7053	1.6706	1.7361	1.7122	1.7242	1.6975	1.7789	1.675	1.8358	1.6947	1.8147	1.7494
	96	2.9746	2.9016	2.9987	2.8279	2.9358	2.8787	2.3404	2.2795	1.6558	1.6209	1.7454	1.6775	1.7696	1.6304	1.7492	1.6946	1.7371	1.7238	1.7733	1.6971	1.8133	1.7587	1.8	1.7238
	97	2.96	2.9033	2.9955	2.8556	2.9989	2.9078	2.6443	2.6187	1.6922	1.6133	1.7322	1.6777	1.7833	1.6468	1.7989	1.7044	1.7867	1.8122	1.7844	1.7555	1.8	1.76	1.7711	1.7467
	98	3	2.8913	2.959	2.8584	2.9907	2.919	2.8206	2.799	1.6657	1.5887	1.7436	1.643	1.7457	1.643	1.7743	1.644	1.8513	1.7753	1.7857	1.7457	1.8133	1.6984	1.798	1.8123
	99	3.0791	2.9333	2.9867	2.8586	2.9884	2.8826	2.9307	2.864	1.6649	1.6409	1.704	1.7014	1.7191	1.616	1.7218	1.6809	1.8516	1.7574	1.824	1.7067	1.7875	1.7742	1.8249	1.7858
	100	3.0392	2.9185	3.0392	2.8968	2.9608	2.9318	2.9733	2.8644	1.6918	1.7052	1.6792	1.6881	1.7318	1.6297	1.7185	1.7044	1.8133	1.7303	1.8118	1.7836	1.8023	1.7703	1.7985	1.7348

	101	2.9758	2.9448	3.0267	2.9213	2.974	2.8946	2.9733	2.8152	1.7594	1.6025	1.7333	1.7029	1.7842	1.6565	1.7454	1.684	1.774	1.6787	1.7987	1.7473	1.8019	1.7448	1.786	1.72
	102	2.9625	2.8948	2.9877	2.8938	2.9852	2.8405	2.9462	2.9072	1.8657	1.6543	1.6943	1.6667	1.7595	1.5902	1.7333	1.6943	1.7728	1.6538	1.7857	1.8	1.8015	1.7462	1.8138	1.7072
	103	3.0015	2.9696	2.9608	2.8933	2.973	2.8663	3.0118	2.92	2.0522	1.8252	1.653	1.613	1.6811	1.667	1.7459	1.6792	1.7733	1.7311	1.7859	1.7855	1.7874	1.7345	1.813	1.7733
	104	3.0538	3.0128	2.999	2.8808	2.9862	2.9062	3.0252	2.9462	2.2797	2.158	1.6795	1.6013	1.6938	1.6279	1.7197	1.6808	1.7469	1.7597	1.7864	1.7716	1.7808	1.7467	1.84	1.7733
	105	3.0531	2.9731	3.0392	2.9204	2.9999	2.8799	3.0127	2.9464	2.4835	2.5054	1.7064	1.6009	1.7201	1.6405	1.7199	1.7195	1.7068	1.7204	1.7333	1.7597	1.7469	1.7067	1.8008	1.7733
	106	3.0267	2.9733	3.04	2.8933	2.9867	2.9067	2.96	2.9067	2.6933	2.7067	1.6933	1.6667	1.7467	1.68	1.7467	1.68	1.7067	1.7467	1.7467	1.7467	1.72	1.7467	1.7867	1.7867
Average		2.219718	1.983951	2.208478	1.967339	2.190473	1.94143	2.038891	1.802742	1.888747	1.647907	1.861127	1.614136	1.816321	1.589806	1.74998	1.531779	1.759476	1.548021	1.781923	1.58798	1.766527	1.589953	1.701458	1.529577

Right line-top lesion

Right line - Top lesion

Slice Number	70	70-a	70-b	80-a	80-b	90-a	90-b	100-a	100-b	110-a	110-b	120-a	120-b	130-a	130-b	140-a	140-b	150-a	150-b	160-a	160-b	170-a	170-b	180-a	180-b
	0	0.32	0	0.36	0.0133	0.3467	0.0267	0.32	0.0133	0.3467	0	0.32	0.0133	0.36	0.0267	0.3467	0	0.3467	0	0.3467	0.0267	0.32	0	0.3333	0.0133
	1	0.339	0.0191	0.3143	0.0006	0.33	0.0598	0.3387	0.0005	0.3537	0.0204	0.3422	0.0072	0.3401	0.0837	0.3236	0.0189	0.3338	0.0038	0.3174	0.0427	0.3296	0.0104	0.3556	0.0003
	2	0.339	0.0257	0.3323	0.0115	0.3271	0.0336	0.3324	0.0115	0.3353	0.0086	0.3338	0.001	0.3457	0.0219	0.3252	0.0124	0.3333	0.0138	0.3195	0.0166	0.3452	0.0081	0.3462	0.0133
	3	0.3694	0.0243	0.3318	0.0029	0.3331	0.0276	0.3348	0.0124	0.3453	0.0011	0.3381	0	0.3299	0.0192	0.3299	0.0101	0.3214	0.0142	0.3296	0.0214	0.3467	0.0107	0.3505	0.0333
	4	0.3936	0.0264	0.3145	0.0009	0.2872	0.0141	0.3345	0.0109	0.3564	0.0017	0.3555	0	0.3317	0.0365	0.3225	0.0446	0.3176	0.0124	0.3556	0.0044	0.3688	0.0044	0.3563	0.0177
	5	0.3793	0.0303	0.3327	0.0082	0.2799	0.0053	0.3011	0.0127	0.3657	0.0016	0.3335	0	0.3589	0.018	0.3538	0.0391	0.2956	0.0015	0.3555	0.0045	0.3763	0.0061	0.3327	0.0398
	6	0.3603	0.0114	0.3461	0.033	0.2775	0.0017	0.2911	0.0433	0.3506	0.0147	0.3358	0.0338	0.3445	0.0111	0.3495	0.0125	0.3333	0.0105	0.35	0.0142	0.3456	0.0228	0.3189	0.027
	7	0.3482	0.0054	0.3505	0.0482	0.3071	0.0176	0.3111	0.0346	0.3529	0.0125	0.3653	0.0574	0.3356	0.006	0.3467	0.0028	0.3543	0.0436	0.3478	0.0328	0.3482	0.0078	0.2938	0.0061
	8	0.3499	0	0.364	0.0427	0.3411	0.0248	0.3397	0.0176	0.3683	0.0059	0.3605	0.0491	0.3448	0.0019	0.3467	0.0083	0.3485	0.0128	0.3342	0.0288	0.3451	0.0103	0.3237	0.0115
	9	0.3301	0.0108	0.3733	0.018	0.3504	0.0067	0.3521	0.0408	0.3625	0.0271	0.3566	0.0208	0.3704	0.018	0.3429	0.0188	0.345	0	0.3133	0.0195	0.3358	0.0214	0.3533	0.0113
	10	0.3188	0.0059	0.3659	0.0247	0.3603	0.0028	0.3308	0.0622	0.3572	0.0254	0.3806	0.0145	0.3823	0.013	0.3548	0.0189	0.3612	0.0028	0.3067	0.0211	0.32	0.0163	0.356	0.0015

11	0.3216	0.0022	0.3758	0.0383	0.3647	0.0003	0.32	0.069	0.3674	0.0254	0.3867	0.0286	0.3782	0.026	0.3652	0.0139	0.3735	0.0013	0.3081	0.042	0.3082	0.0183	0.3662	0
12	0.3134	0.0123	0.3532	0.0204	0.3484	0.0095	0.344	0.0538	0.3515	0.01	0.3705	0.0462	0.3612	0.0242	0.3414	0.0105	0.3489	0.0158	0.3401	0.0221	0.3106	0.0272	0.3745	0
13	0.3323	0.0247	0.3534	0.0086	0.3421	0.0121	0.3609	0.0425	0.3473	0.0111	0.3566	0.0234	0.3657	0.0299	0.3416	0.0032	0.3333	0.0178	0.3579	0.0162	0.3279	0.0206	0.3699	0
14	0.3585	0.0266	0.3602	0.0052	0.3434	0.0202	0.3617	0.0259	0.3583	0.0236	0.3352	0.0103	0.3718	0.0401	0.3534	0	0.3384	0.0307	0.3467	0.0264	0.3502	0.0236	0.3634	0.0035
15	0.3733	0.0201	0.3398	0.0064	0.3077	0.0326	0.3667	0.0004	0.3347	0.0327	0.3527	0.0126	0.3735	0.0212	0.3412	0.0004	0.3468	0.0333	0.3467	0.0139	0.3858	0.0202	0.3534	0.0001
16	0.3545	0.0235	0.3271	0.0247	0.3263	0.0177	0.3774	0.01	0.3386	0.0326	0.3674	0.0225	0.3775	0.0183	0.3296	0.0126	0.3563	0.0209	0.3487	0.0085	0.3786	0.0113	0.3488	0.0021
17	0.3218	0.0342	0.3447	0.0419	0.3463	0.0201	0.3475	0.0133	0.3666	0.021	0.3551	0.0158	0.3733	0.0325	0.346	0.006	0.3757	0.0145	0.3551	0.0146	0.3527	0.0158	0.3552	0
18	0.3064	0.0421	0.3743	0.0425	0.3361	0.032	0.3256	0.0245	0.3718	0.0298	0.3668	0.014	0.3774	0.0068	0.3616	0.0052	0.3851	0.0068	0.365	0.0047	0.3491	0.0109	0.3526	0
19	0.3141	0.0252	0.389	0.051	0.3367	0.0348	0.3496	0.0478	0.3767	0.0399	0.3874	0.0396	0.3796	0.0036	0.3778	0.0032	0.3665	0.0014	0.3614	0.0022	0.3418	0	0.3434	0
20	0.3439	0.0174	0.3961	0.0505	0.3341	0.0291	0.3572	0.0418	0.3876	0.0237	0.3853	0.0471	0.3741	0.0172	0.3814	0.0059	0.3532	0.0014	0.3588	0.0079	0.3485	0.0028	0.3276	0.004

21	0.3658	0.0075	0.4065	0.044	0.3319	0.0139	0.36	0.0463	0.4141	0.0241	0.3771	0.0511	0.3889	0.0252	0.3715	0.0169	0.3428	0.0145	0.3653	0.0112	0.3535	0.012	0.3382	0.0098
22	0.3617	0.0007	0.4031	0.0129	0.3508	0.0039	0.3651	0.0594	0.4251	0.0569	0.3772	0.1039	0.3812	0.0212	0.3667	0.0652	0.3168	0.0299	0.3793	0.0007	0.3542	0	0.3534	0
23	0.326	0.0012	0.399	0.0045	0.3812	0	0.3883	0.0337	0.4233	0.0717	0.384	0.1081	0.3802	0.0026	0.3636	0.0483	0.3313	0.0414	0.3715	0.0107	0.3517	0.0032	0.3406	0
24	0.3423	0.014	0.4047	0.017	0.3888	0	0.3879	0.0229	0.4242	0.0542	0.3789	0.0793	0.4009	0.0155	0.3715	0.0279	0.3883	0.0382	0.367	0.0344	0.3808	0.0329	0.3721	0
25	0.3766	0	0.388	0.0316	0.376	0	0.3926	0.0382	0.4217	0.0426	0.4076	0.0911	0.4126	0.0284	0.4019	0.0159	0.4088	0.0405	0.374	0.0469	0.4459	0.2206	0.4161	0.0075
26	0.3685	0	0.4274	0.0388	0.3614	0	0.4044	0.0649	0.4241	0.0376	0.4322	0.0771	0.4419	0.0388	0.4473	0.0206	0.4425	0.0405	0.4147	0.0912	0.5061	0.3916	0.5007	0.0712
27	0.3369	0	0.4272	0.0301	0.3762	0.0031	0.4462	0.0634	0.5406	0.0356	0.4858	0.0475	0.4736	0.0209	0.5019	0.049	0.4654	0.0506	0.4616	0.2501	0.7003	0.4403	0.7843	0.1787
28	0.3482	0.0005	0.4484	0.0141	0.4766	0.0135	0.5522	0.0477	0.753	0.0733	0.5901	0.0597	0.529	0.0211	0.5209	0.0668	0.4949	0.0539	0.5073	0.4147	0.9757	0.5332	1.2978	0.8618
29	0.4193	0.0097	0.5424	0.0362	0.6284	0.0366	0.7906	0.0763	1.0535	0.0534	0.7584	0.0532	0.5888	0.0696	0.5663	0.0769	0.566	0.1464	0.5463	0.476	1.1688	0.5701	2.1946	2.2258
30	0.5045	0.1679	0.6623	0.0388	0.8709	0.0905	1.2202	0.1317	1.2819	0.1677	0.9426	0.0645	0.7907	0.0787	0.7017	0.1811	0.715	0.3898	0.6112	0.5045	1.1764	0.65	3.02	2.9317

Right line-top lesion

	31	0.673	0.4654	0.8643	0.0955	1.2046	0.1966	1.5836	0.3899	1.2868	0.3626	1.0496	0.3122	1.0936	0.2502	0.9513	0.3794	0.9847	0.458	0.7541	0.5425	1.1369	0.7301	3.3086	3.0666
	32	1.1267	0.7875	1.1608	0.3387	1.6092	0.4543	1.9734	0.6489	1.3426	0.5123	1.1527	0.5326	1.3345	0.4683	1.2048	0.483	1.2214	0.4973	0.8618	0.6763	1.1423	0.932	3.3335	3.1216
	33	1.9336	1.7822	1.5037	0.6641	2.06	0.8997	2.4524	1.335	1.537	0.814	1.4385	0.7425	1.5252	0.5581	1.3661	0.5216	1.3543	0.5411	0.9952	0.8464	1.3582	1.1414	3.3373	3.1253
	34	2.7105	2.6904	1.8194	1.2672	2.473	1.6661	2.8302	2.2162	1.9816	1.4197	1.9279	1.2951	1.8411	0.7308	1.6522	0.6202	1.5885	0.64	1.2397	1.0406	1.8276	1.5131	3.2993	3.1099
	35	3.1637	3.0174	2.1375	1.798	2.754	2.3147	2.9967	2.715	2.5644	2.2201	2.563	2.3276	2.3982	1.5208	2.1753	1.0849	2.0075	1.1417	1.7641	1.4821	2.4872	2.2268	3.2923	3.0745
	36	3.3234	3.0989	2.4671	2.0421	2.9771	2.7178	3.0989	2.9369	2.9994	2.7506	3.0367	2.9279	2.9313	2.5251	2.7822	2.0878	2.6196	2.109	2.4787	2.2779	3.0124	2.7694	3.2996	3.0544
	37	3.3623	3.1364	2.8311	2.4723	3.1615	2.9434	3.1876	3.0545	3.1844	2.9783	3.2005	3.083	3.1742	2.9164	3.1103	2.7361	3.0355	2.7155	3.0103	2.8473	3.2193	2.934	3.2759	3.0763
	38	3.3471	3.1475	3.1323	2.8724	3.2612	3.005	3.2238	3.0797	3.2515	3.038	3.2313	3.0367	3.2177	2.9959	3.2122	2.957	3.1916	2.9257	3.1877	3.0081	3.2444	3.0139	3.262	3.0853
	39	3.3232	3.1436	3.278	3.0671	3.2735	3.0278	3.2543	3.0701	3.2512	3.0637	3.2322	3.0114	3.2285	3.0368	3.2275	3.0047	3.2325	3.009	3.2135	3.0004	3.2421	3.0421	3.2356	3.0379
	40	3.3131	3.1339	3.3118	3.1377	3.2603	3.0864	3.286	3.0756	3.2276	3.0893	3.2307	3.0236	3.2244	3.0228	3.2183	3.0294	3.2319	3.0447	3.2105	3.0325	3.2351	3.0303	3.2138	3.008

	41	3.3299	3.139	3.3015	3.1143	3.2641	3.0978	3.2835	3.0729	3.2063	3.0706	3.2342	3.0451	3.2133	2.9521	3.2058	3.011	3.2039	3.0965	3.2051	3.0627	3.2252	3.046	3.1931	3.0056
	42	3.3562	3.107	3.2569	3.0924	3.2426	3.0838	3.2633	3.0574	3.2314	3.0285	3.2291	3.0317	3.2281	2.9684	3.1901	2.9896	3.18	3.0705	3.2017	3.0367	3.22	3.0241	3.1898	2.9865
	43	3.3533	3.0833	3.23	3.0833	3.2167	3.08	3.27	3.0467	3.25	3.0233	3.2233	3.0233	3.2333	3.0333	3.18	2.9967	3.18	3.02	3.1967	3	3.2067	3.01	3.19	2.98
	44	3.3186	3.1005	3.2243	3.0592	3.2195	3.0514	3.2654	3.0312	3.2421	3.0231	3.2212	3.0347	3.2171	3.0359	3.1805	3.006	3.1971	2.9872	3.1757	2.9834	3.1695	3.0324	3.1743	2.9812
	45	3.2819	3.1246	3.222	3.0665	3.2151	3.0245	3.2225	3.0329	3.2288	3.0158	3.2156	3.0503	3.1795	3.0097	3.1653	3.046	3.2027	2.9983	3.1603	2.9875	3.1487	3.0626	3.1368	2.9684
	46	3.2655	3.0986	3.2276	3.0781	3.2109	3.0505	3.1947	3.0431	3.1938	3.0158	3.2133	3.0335	3.1734	2.9864	3.1506	3.0601	3.1514	3.0101	3.1584	2.998	3.1516	3.0507	3.103	2.9595
	47	3.2141	3.0489	3.2409	3.0944	3.2313	3.0659	3.186	3.0203	3.1642	3.0368	3.2182	2.9919	3.1676	2.9606	3.1407	2.998	3.1228	3.0072	3.1544	2.9819	3.1548	2.9966	3.1174	2.9626
	48	3.1817	3.0576	3.2194	3.0813	3.2309	3.0672	3.1711	3.0072	3.1619	3.0408	3.2036	2.9803	3.1367	2.9561	3.1668	3.016	3.1171	2.997	3.1613	2.9789	3.1224	2.9629	3.1496	2.9697
	49	3.21	3.0529	3.1899	3.0483	3.2086	3.0243	3.1471	3.0225	3.181	3.0204	3.2036	2.9735	3.165	2.97	3.168	2.9953	3.115	2.9961	3.1228	3.0185	3.1029	2.9612	3.1304	2.9637
	50	3.1946	3.0302	3.1662	3.0878	3.2254	3.0026	3.1516	3.0403	3.1468	2.9717	3.1841	2.9623	3.1694	2.9921	3.1504	2.9908	3.1075	2.9639	3.0967	2.9823	3.1023	2.9851	3.0648	2.9194

	51	3.1891	3.0867	3.1581	3.0976	3.2285	3.0097	3.1493	3.0208	3.1067	2.9743	3.1696	2.9782	3.1511	3.0195	3.1458	2.9588	3.1162	2.9798	3.0896	2.9285	3.1046	2.9403	3.0344	2.9155
	52	3.2127	3.0526	3.1436	3.0436	3.1947	3.0147	3.1301	3.0005	3.1266	3.0053	3.1573	2.9671	3.1264	3.0019	3.1288	3.0206	3.0978	2.9939	3.0798	2.9108	3.0868	2.9409	3.0509	2.9356
	53	3.2373	3.0453	3.121	3.0103	3.1547	3.0014	3.1217	3.002	3.1074	2.9973	3.1294	2.9876	3.1158	2.9697	3.0917	3.0187	3.1054	2.9477	3.0674	2.9604	3.0523	2.952	3.085	2.9354
	54	3.2234	3.0706	3.1121	3.0362	3.1437	2.9699	3.1245	3.0164	3.1184	2.9848	3.1328	2.9607	3.0964	2.9567	3.0889	2.9579	3.1124	2.9936	3.076	2.9551	3.0303	2.9309	3.0437	2.9046
	55	3.185	3.0722	3.1192	3.02	3.1304	2.9569	3.1464	3.0329	3.127	2.9642	3.1192	2.9384	3.1026	2.9797	3.0865	2.9851	3.0667	2.9886	3.0654	2.9599	3.034	2.9154	3.0048	2.8972
	56	3.1715	3.0027	3.1082	3.0012	3.0942	2.9498	3.1191	2.96	3.1439	2.934	3.133	3.0009	3.12	2.9627	3.0775	3.0597	3.0667	2.8858	3.037	2.9454	3.0521	2.9067	2.9609	2.8893
	57	3.1497	3.0499	3.1396	3.0104	3.1036	3.0104	3.0934	2.9764	3.0929	2.9174	3.1266	3.0099	3.1228	3.0028	3.0468	2.9893	3.0631	2.93	2.9867	2.9269	3.0232	2.9131	2.963	2.8099
	58	3.1271	3.0405	3.114	3.0326	3.1126	3.0326	3.093	2.9674	3.0543	2.9583	3.1136	2.9535	3.0878	2.9208	3.073	2.9217	3.0202	2.9335	2.9933	2.9261	3.0002	2.9003	2.9268	2.8199
	59	3.0923	2.9972	3.0998	2.9989	3.0896	2.9459	3.0984	2.9597	3.0478	2.9759	3.0598	2.8943	3.0778	2.9243	3.0449	2.8996	3.0656	2.9184	2.9928	2.9449	2.9898	2.8782	2.7587	2.7367
	60	3.0962	3.0017	3.0928	2.9655	3.0678	2.9461	3.057	2.9742	3.066	2.9954	3.0777	2.8963	3.0678	2.9085	3.0285	2.9428	3.0428	2.861	2.9877	2.9467	2.9377	2.8559	2.4828	2.4208

	61	3.1731	3.0169	3.0739	2.945	3.0776	2.9185	3.0919	2.9781	3.0672	2.9581	3.0763	2.9343	3.0434	2.9109	3.0388	2.9736	3.013	2.9174	2.9987	2.8762	2.8949	2.8141	2.1606	2.0023
	62	3.16	3.0969	3.0775	2.9123	3.1104	2.9045	3.1076	2.9642	3.0796	2.9622	3.0582	2.9407	3.0307	2.9209	3.0242	2.9123	3.0025	2.9132	2.984	2.8524	2.7334	2.7327	1.9053	1.7627
	63	3.1003	3.0245	3.0907	2.9551	3.08	2.9111	3.1053	2.9784	3.0728	2.9388	3.0519	2.8843	3.0392	2.8748	3.0247	2.8665	2.9786	2.8948	2.9465	2.8636	2.461	2.4429	1.7507	1.701
	64	3.0933	2.9882	3.1307	2.9755	3.0383	2.8991	3.1094	2.9652	3.0576	2.9156	3.0552	2.8949	3.0479	2.8516	3.0251	2.9111	2.9874	2.9189	2.875	2.8276	2.1425	2.0923	1.7282	1.6403
	65	3.1156	2.949	3.1216	2.9538	3.0489	2.9037	3.1057	2.9381	3.0389	2.9141	3.0352	2.8884	3.0138	2.9011	3.0238	2.9129	2.9834	2.879	2.721	2.7336	1.9056	1.8058	1.7111	1.6043
	66	3.1196	2.961	3.0854	2.9458	3.0691	2.9174	3.0798	2.9368	3.0321	2.9067	3.0303	2.9108	3.0146	2.8839	3.0135	2.8986	2.9448	2.8574	2.4552	2.4123	1.7844	1.7149	1.7119	1.6241
	67	3.105	3.0114	3.0586	2.9417	3.0681	2.9046	3.0644	2.905	3.0202	2.8919	3.0081	2.9187	3.0184	2.8893	2.9699	2.8786	2.8577	2.7619	2.1388	2.0123	1.6981	1.6565	1.7345	1.6555
	68	3.0999	2.9473	3.0338	2.9556	3.0527	2.9004	3.0596	2.9014	3.0201	2.8936	3.0087	2.8996	3.005	2.9206	2.9519	2.8651	2.6924	2.6337	1.8847	1.756	1.644	1.6499	1.7274	1.6425
	69	3.1115	2.9905	3.0128	2.9415	3.0546	2.9142	3.0489	2.9312	3.0262	2.9016	2.9864	2.873	2.9866	2.9082	2.94	2.8567	2.4262	2.3463	1.7879	1.6798	1.6564	1.668	1.7419	1.6247
	70	3.1189	2.9558	3.0298	2.9392	3.0599	2.8998	3.0357	2.9573	3.0275	2.9552	2.9846	2.849	2.975	2.8437	2.8721	2.8082	2.1276	1.9945	1.7335	1.6686	1.6879	1.6439	1.7616	1.6407

Right line-top lesion

	71	3.1267	2.9315	3.0671	2.9464	3.0522	2.8942	3.0126	2.9309	3.0001	2.9577	2.9927	2.8477	2.9386	2.8146	2.7165	2.6695	1.9236	1.7911	1.6998	1.6751	1.6867	1.6126	1.766	1.6802
	72	3.1221	2.9102	3.0636	2.9331	3.0366	2.9133	2.9932	2.8854	2.9718	2.9036	2.9477	2.8448	2.8755	2.8202	2.4545	2.3391	1.8008	1.7135	1.7079	1.6813	1.6979	1.6412	1.7514	1.7029
	73	3.1041	2.9229	3.0498	2.9037	3.0244	2.9038	3.0019	2.8895	2.9972	2.9074	2.9374	2.8543	2.7878	2.7211	2.1311	1.9641	1.7208	1.6927	1.7127	1.712	1.7063	1.6952	1.761	1.7006
	74	3.0961	2.9532	3.069	2.8832	3.0299	2.8744	3.036	2.903	3.0384	2.9077	2.9646	2.8833	2.6037	2.5524	1.8896	1.7688	1.6716	1.6544	1.7206	1.7436	1.719	1.7188	1.7716	1.6595
	75	3.0736	2.9576	3.0724	2.8971	3.0502	2.8634	3.0465	2.8831	3.013	2.8657	2.914	2.8717	2.2927	2.2105	1.768	1.6957	1.68	1.6085	1.7369	1.7176	1.7443	1.7018	1.7471	1.6437
	76	3.0685	2.9405	3.0532	2.9423	3.0282	2.8768	3.0309	2.876	2.9703	2.8548	2.7845	2.7882	2.0005	1.8651	1.714	1.675	1.7155	1.6475	1.7348	1.6819	1.7768	1.6822	1.7094	1.6772
	77	3.0726	2.9229	3.0346	2.9371	2.9912	2.8524	3.0158	2.8833	2.9533	2.8561	2.5584	2.5082	1.8423	1.7169	1.7239	1.6808	1.738	1.6808	1.7338	1.6681	1.7958	1.6533	1.7264	1.6932
	78	3.0392	2.8675	2.9966	2.9291	2.9485	2.8643	2.9792	2.889	2.9227	2.8194	2.2424	2.0899	1.792	1.6477	1.7365	1.6451	1.7664	1.6896	1.7549	1.6957	1.7835	1.6591	1.7413	1.6949
	79	3.0115	2.8617	2.9912	2.9054	2.9331	2.8688	2.9565	2.8783	2.8378	2.7722	1.9543	1.8348	1.7782	1.6586	1.7448	1.6247	1.781	1.7133	1.7755	1.6557	1.7566	1.6796	1.7285	1.6637
	80	3.0214	2.8927	3.004	2.8772	2.9886	2.8812	2.9381	2.8608	2.6397	2.6042	1.7983	1.7078	1.77	1.6816	1.7876	1.6901	1.7678	1.7	1.78	1.6775	1.7194	1.7114	1.7537	1.689

Left line-top lesion

		Left line- Top lesion																							
Slice Number	70	70-a	70-b	80-a	80-b	90-a	90-b	100-a	100-b	110-a	110-b	120-a	120-b	130-a	130-b	140-a	140-b	150-a	150-b	160-a	160-b	170-a	170-b	180-a	180-b
	0	0.3467	0	0.3333	0	0.3467	0	0.32	0.0267	0.32	0.0267	0.36	0	0.36	0.04	0.3333	0	0.3467	0.04	0.36	0.0133	0.36	0.0133	0.36	0
	1	0.3467	0	0.3467	0.0267	0.3733	0	0.3067	0	0.3333	0.0133	0.3733	0	0.3733	0.0533	0.36	0	0.3067	0.0267	0.36	0.04	0.36	0.0133	0.3733	0
	2	0.3333	0.0267	0.3467	0	0.36	0	0.3467	0	0.36	0.0133	0.3467	0.0267	0.3867	0.0267	0.36	0	0.3467	0	0.36	0.04	0.36	0	0.3467	0
	3	0.32	0.0267	0.3333	0	0.3867	0	0.36	0	0.3733	0.0267	0.3467	0.0133	0.36	0.0133	0.3467	0	0.32	0	0.3467	0.0133	0.36	0	0.3467	0
	4	0.3067	0	0.3333	0	0.3733	0	0.3467	0	0.32	0.0133	0.3333	0	0.3333	0	0.32	0.0267	0.3467	0.0267	0.36	0.0133	0.3733	0	0.3333	0
	5	0.3333	0	0.32	0	0.36	0	0.3333	0	0.3333	0.0133	0.32	0.0667	0.3467	0	0.3333	0.0267	0.36	0.04	0.3333	0	0.3467	0.0267	0.3467	0
	6	0.3333	0	0.32	0	0.36	0	0.3467	0	0.3333	0.0133	0.3333	0.0667	0.3333	0	0.3333	0.0133	0.36	0	0.3333	0.0267	0.3467	0.04	0.3467	0
	7	0.3333	0	0.3333	0.0133	0.3467	0	0.36	0.0133	0.3333	0.0133	0.32	0.0667	0.3467	0.0133	0.32	0	0.32	0.0133	0.3467	0.0133	0.3333	0.0267	0.36	0
	8	0.3333	0.0533	0.3333	0	0.3733	0	0.3733	0.0533	0.3333	0.0533	0.36	0	0.3467	0.0267	0.3333	0.08	0.28	0.0267	0.3467	0	0.36	0.0667	0.3333	0.04
	9	0.32	0.0267	0.3067	0	0.36	0	0.3467	0.04	0.3333	0.0667	0.3333	0	0.3467	0.0267	0.3333	0.0267	0.2933	0.0133	0.3333	0	0.3867	0.0667	0.3333	0.04
	10	0.3467	0.04	0.3067	0	0.36	0	0.3467	0.0133	0.36	0.0533	0.3333	0.0133	0.3467	0.0133	0.3733	0	0.3333	0.0667	0.3333	0.0133	0.3867	0.0133	0.3867	0.0133
	11	0.36	0.0667	0.3467	0	0.3467	0	0.36	0.0267	0.3467	0.0267	0.32	0	0.36	0.04	0.36	0.0133	0.32	0.04	0.3467	0.0533	0.3733	0	0.3733	0.0133
	12	0.3467	0.04	0.3733	0	0.3333	0	0.3333	0.0133	0.3467	0.0267	0.28	0.0133	0.3733	0.0667	0.36	0.0667	0.36	0.04	0.3467	0.04	0.36	0	0.3867	0.0133
	13	0.3067	0.0267	0.36	0	0.32	0.0133	0.3333	0	0.36	0.04	0.3467	0.0533	0.4	0.04	0.3867	0.04	0.3733	0.0267	0.36	0.0667	0.36	0	0.3867	0
	14	0.36	0.0267	0.3733	0.0533	0.3067	0.0133	0.3467	0.0133	0.36	0.0267	0.3867	0.0933	0.3733	0.04	0.36	0.0133	0.32	0.04	0.36	0.0533	0.36	0	0.36	0.0667
	15	0.3333	0.0133	0.3467	0.0133	0.3067	0.0133	0.36	0.04	0.36	0.0133	0.4	0.0667	0.3467	0.0267	0.3867	0.0267	0.36	0.0933	0.3467	0.04	0.3467	0.0133	0.3733	0.0533
	16	0.32	0	0.3467	0	0.3333	0.04	0.32	0.0533	0.36	0	0.3733	0.0133	0.3867	0.0133	0.3867	0.08	0.36	0.0533	0.36	0.04	0.3733	0.0267	0.36	0.0133
	17	0.3467	0.0133	0.3333	0	0.3333	0.0667	0.3067	0.04	0.3333	0	0.3867	0.0133	0.36	0	0.4	0	0.3867	0.0267	0.36	0.0133	0.4133	0.0667	0.3867	0.0133
	18	0.36	0	0.3867	0.0133	0.3733	0.0267	0.3333	0.0267	0.3467	0.04	0.3867	0	0.36	0.0133	0.44	0.0133	0.4133	0.0533	0.3467	0.04	0.4	0.0667	0.4133	0.08
	19	0.3467	0	0.3867	0.0133	0.3867	0	0.3467	0.0533	0.36	0.08	0.4667	0.0133	0.4	0.0533	0.4	0.0267	0.4	0	0.3867	0.0133	0.4	0.08	0.4	0.0667
	20	0.32	0.0133	0.36	0	0.4	0.04	0.3867	0.04	0.4533	0.0933	0.68	0.0667	0.4267	0.0667	0.3733	0.0667	0.3867	0	0.4267	0	0.4	0.1467	0.44	0.0667

Left line-top lesion

	21	0.3333	0	0.32	0	0.4133	0.0533	0.3733	0.0267	0.64	0.0933	1.2667	0.2133	0.4933	0.0533	0.4	0.0267	0.44	0.0133	0.5733	0.0533	0.5067	0.1733	0.5867	0.16
	22	0.3733	0	0.36	0.0533	0.4	0.08	0.4267	0.04	1.0667	0.1067	2.24	0.8933	0.64	0.0533	0.5467	0.0133	0.48	0.04	0.7867	0.0533	0.76	0.2	0.9067	0.5733
	23	0.4	0	0.4133	0.0667	0.3867	0.08	0.5867	0.04	1.6	0.0667	2.6533	1.6933	0.88	0.0267	0.7067	0.16	0.56	0.04	1.3067	0.2667	1.2267	0.5733	1.6	1.4267
	24	0.4	0.0267	0.4133	0.0667	0.4267	0.0933	0.88	0.0667	1.6133	0.36	2.8933	2.3333	1.0933	0.2267	1	0.7333	0.72	0.0933	1.72	0.5867	2.2133	1.8933	2.6	2.5333
	25	0.36	0.0667	0.4133	0.04	0.44	0.0533	1.1733	0.0933	1.5733	0.9733	3.0267	2.64	1.16	0.5467	1.3067	0.8933	0.9333	0.3333	1.7733	0.9467	3.0667	2.8267	3.12	2.9333
	26	0.4	0.0667	0.4133	0.0533	0.5067	0.0533	1.2	0.1067	1.9067	1.5733	3.16	2.84	1.28	0.6133	1.6267	1.0667	1.0933	0.4267	1.9733	1.4533	3.2933	3	3.28	3.0267
	27	0.44	0.08	0.4533	0.0933	0.6	0.1067	1.1333	0.2133	2.4667	2.2133	3.2133	2.96	1.48	0.6533	2.1067	1.8	1.1867	0.4933	2.3467	1.8667	3.3333	3.0133	3.2933	3.0267
	28	0.44	0.0933	0.4533	0.08	0.6667	0.12	1.0933	0.44	2.9867	2.8	3.24	2.9867	1.8267	1.0933	2.7733	2.64	1.4	0.6133	2.68	2.36	3.3333	3.0267	3.2667	3.0267
	29	0.4533	0.08	0.5333	0.0533	0.8267	0.16	1.2133	0.7333	3.2267	2.9067	3.24	3.08	2.44	2.04	3.1467	2.9467	1.7733	1.1067	3.0267	2.7867	3.28	3.0933	3.28	3.0133
	30	0.4533	0.0533	0.56	0.08	1	0.3867	1.5733	1.1733	3.3067	3	3.2667	3.0667	3.0667	2.84	3.28	2.96	2.3333	2.0133	3.24	2.9467	3.24	3.1067	3.2667	2.9867

	31	0.48	0.0267	0.64	0.1733	1.08	0.5467	2.2267	1.9733	3.3067	3.0133	3.2667	3.0667	3.24	3.0533	3.2933	3.0533	2.8933	2.7467	3.28	3.0133	3.24	3.04	3.2533	2.9867
	32	0.5333	0.1333	0.7733	0.4	1.0933	0.6267	2.7333	2.6133	3.3333	3.0933	3.2533	3.1067	3.28	3.0533	3.28	3.1067	3.1867	2.9867	3.2267	3.0533	3.2267	2.9867	3.2	2.9867
	33	0.6667	0.3733	1	0.5067	1.1733	0.7467	3.04	2.88	3.32	3.0667	3.28	3.0533	3.2933	3.0533	3.2667	3.0533	3.2	2.9867	3.2133	3.0133	3.1733	3	3.2	2.9333
	34	0.88	0.4533	1.12	0.6133	1.44	1	3.2	3.04	3.3333	3.1333	3.24	3.0933	3.2533	3.08	3.2533	3	3.2533	3	3.2	3.0133	3.2267	2.96	3.2	2.96
	35	1.2	0.48	1.1733	0.64	2	1.6267	3.2533	3.12	3.32	3.0667	3.2267	3.12	3.2533	3.1333	3.24	2.9867	3.2533	3.0133	3.1733	3.0267	3.2133	3	3.1733	2.9867
	36	1.28	0.6133	1.28	0.7067	2.7333	2.4667	3.2933	3.1067	3.3067	3.0267	3.2533	3.0933	3.24	3.04	3.24	3.0133	3.2133	2.9867	3.16	3.0267	3.1867	3	3.1467	2.9867
	37	1.2667	0.6533	1.5733	1	3.1733	2.96	3.2933	3.04	3.28	3.0133	3.24	3.04	3.2133	3.0133	3.2133	2.9733	3.1733	3	3.2	2.9867	3.1467	2.9733	3.1467	2.9467
	38	1.28	0.7333	2.1333	1.7867	3.28	3.0267	3.24	3.08	3.2667	3.0267	3.2133	3.0133	3.1733	3.0133	3.1733	3.0133	3.16	2.9733	3.1733	2.9733	3.1067	2.96	3.1333	2.9067
	39	1.48	0.9467	2.8	2.7333	3.2667	2.9867	3.1867	3.08	3.24	3.04	3.1733	3.0267	3.1733	2.9867	3.1867	3.0133	3.2133	2.9867	3.12	3.04	3.12	2.96	3.12	2.92
	40	2.1067	1.68	3.1333	3.0667	3.2533	2.9867	3.1867	3.1067	3.2533	3.0267	3.1467	3.0267	3.2133	2.9867	3.1867	3.04	3.2133	2.9867	3.1067	2.9867	3.0667	2.9333	3.0933	2.9067

	41	2.7467	2.5867	3.2267	3.0267	3.2933	3.0133	3.2	3	3.2533	3	3.1333	3.0267	3.2133	2.9867	3.1467	3.04	3.1733	3	3.0933	2.96	3.0667	2.9067	3.0667	2.8667
	42	3.1067	3.0533	3.2667	3.08	3.2667	3.0667	3.2	3.0267	3.24	3.0267	3.1733	2.9867	3.1867	2.9333	3.1333	3	3.0933	2.9467	3.08	2.9467	3.08	2.8933	2.96	2.84
	43	3.2267	3.12	3.24	3.0133	3.24	3	3.1867	3.0133	3.2533	2.9733	3.2	3	3.1867	2.9467	3.16	2.9733	3.0933	2.9467	3.0667	2.92	3.0933	2.8533	2.88	2.7867
	44	3.2	3.0667	3.2	3.0267	3.2267	3	3.1733	3.0533	3.1867	3.04	3.1733	3	3.16	2.92	3.12	2.92	3.0933	3.0133	3.0667	2.9067	3.04	2.88	2.6133	2.5867
	45	3.2133	3.0533	3.2	3.0533	3.1867	3	3.2	3.08	3.1333	2.9867	3.1733	2.9733	3.12	2.8933	3.0667	2.9067	3.0667	2.9733	3.08	2.8667	3.0133	2.8667	2.28	2.12
	46	3.2	3.04	3.1867	3.04	3.16	3	3.1733	3.0533	3.1333	3.0133	3.1333	2.9733	3.1067	2.88	3.0533	2.96	3.08	2.92	3.0667	2.9067	2.9733	2.8667	2	1.8
	47	3.2133	3.0533	3.2133	3.0267	3.1733	2.9733	3.1467	2.9867	3.1333	3	3.1467	2.9733	3.0667	2.9867	3.04	2.9733	3.08	2.8933	3.04	2.9067	2.92	2.8	1.8	1.7067
	48	3.24	3.04	3.2	2.9867	3.16	2.9867	3.16	2.9333	3.1333	2.9867	3.12	2.9467	3.0533	2.9733	3.1067	2.92	3.04	2.88	3.0133	2.8933	2.76	2.6933	1.7467	1.68
	49	3.28	3.04	3.1867	2.9733	3.1467	3.0267	3.12	2.9467	3.1467	2.9333	3.12	2.9733	3.0667	2.92	3.0667	2.9333	3.0267	2.9467	3	2.8933	2.4267	2.3333	1.7067	1.6133
	50	3.2533	3.0133	3.1867	2.9733	3.1067	2.9867	3.12	2.96	3.1333	2.9733	3.12	2.9333	3.0667	2.8933	3.0533	2.9067	3.0133	2.9333	2.9733	2.8	2.0933	1.92	1.6667	1.5467

	51	3.24	3.0133	3.1867	3.08	3.1067	2.9467	3.1333	2.96	3.12	2.96	3.08	2.9467	3.0933	2.9467	3.0533	2.8133	2.9733	2.88	2.8667	2.6933	1.8533	1.7867	1.6933	1.5467
	52	3.2	2.9733	3.1733	3.0933	3.12	2.9333	3.1467	2.9467	3.12	2.92	3.08	2.96	3.08	2.8933	3.0533	2.88	3.0267	2.8533	2.64	2.5733	1.76	1.7333	1.6933	1.5733
	53	3.1733	3	3.16	2.9467	3.1333	2.92	3.12	2.9333	3.0933	2.9067	3.0933	2.9333	3.0667	2.8933	3.0267	2.88	2.9733	2.84	2.2933	2.1467	1.7067	1.6133	1.6667	1.5733
	54	3.2	3.0533	3.1067	2.96	3.12	2.9067	3.0667	2.9467	3.1067	2.8933	3.08	2.9467	3.0933	2.8533	3.04	2.92	2.8933	2.8533	2.0133	1.8533	1.68	1.6133	1.7333	1.6
	55	3.1733	3.04	3.1067	2.92	3.1067	2.9333	3.0267	2.9067	3.0533	2.92	3.0667	2.92	3.0667	2.8667	3.0267	2.8533	2.76	2.7733	1.8	1.7467	1.7067	1.6133	1.7333	1.6133
	56	3.12	3.04	3.0933	2.9067	3.1467	2.8933	3.04	2.92	3.04	2.92	3.0533	2.9333	3.0533	2.8933	2.9867	2.8667	2.5733	2.5333	1.72	1.6533	1.72	1.5867	1.7467	1.6133
	57	3.1467	3.04	3.0933	2.9467	3.0533	2.96	3.0533	2.9333	3.0133	2.8667	3.04	2.8933	3.0533	2.9067	2.9467	2.84	2.2133	2.0933	1.6933	1.5867	1.7067	1.6267	1.7733	1.68
	58	3.16	2.9733	3.08	2.9067	3.08	2.96	3.1067	2.96	3	2.9067	3.0267	2.9067	3.0267	2.8667	2.88	2.8133	1.92	1.8	1.6667	1.6133	1.7067	1.6533	1.7467	1.7067
	59	3.12	2.96	3.12	2.9067	3.0933	2.9467	3.0667	2.96	3.0133	2.8933	3	2.9067	3	2.8667	2.7067	2.7067	1.76	1.6933	1.72	1.6	1.72	1.6667	1.76	1.72
	60	3.16	3	3.1067	2.88	3.0533	2.9067	2.9867	2.9333	3.04	2.9067	2.9867	2.8933	2.9867	2.8133	2.44	2.32	1.7067	1.6133	1.7867	1.6133	1.7467	1.6267	1.76	1.6533

Left line-top lesion

	61	3.1733	2.9867	3.0667	2.8533	3.04	2.8667	3.04	2.8933	3.0533	2.8667	2.9733	2.88	2.9333	2.7867	2.1333	1.9067	1.68	1.68	1.7733	1.6133	1.72	1.64	1.7867	1.6267
	62	3.16	3	3.0267	2.8933	3.0667	2.8533	3.04	2.8267	3.0533	2.8533	2.9733	2.8533	2.84	2.7733	1.9467	1.6933	1.7333	1.5867	1.7867	1.6133	1.72	1.6133	1.8	1.6533
	63	3.1333	2.9733	3.08	2.88	3.04	2.8667	3.0267	2.8133	3.04	2.8533	2.9467	2.8667	2.6533	2.6267	1.7867	1.6	1.7467	1.5733	1.76	1.64	1.7733	1.6933	1.76	1.6533
	64	3.0267	2.9333	3.08	2.84	3.0133	2.8933	3.0133	2.88	3.0133	2.9067	2.9467	2.8133	2.3733	2.16	1.6933	1.6133	1.76	1.6667	1.7467	1.6	1.76	1.68	1.7467	1.68
	65	3.0667	2.9067	3.0667	2.88	3.0267	2.8667	3.04	2.88	3	2.8133	2.92	2.8133	1.9733	1.8533	1.64	1.6533	1.76	1.6533	1.72	1.64	1.68	1.6667	1.7467	1.6933
	66	3.0533	2.8933	3.0667	2.8667	3.0667	2.9067	3.0267	2.88	2.96	2.8267	2.8533	2.7467	1.8133	1.64	1.6267	1.64	1.7333	1.6	1.7333	1.6667	1.7333	1.68	1.76	1.7333
	67	3.04	2.96	3.0533	2.9333	3.04	2.9067	2.9867	2.8533	2.96	2.8133	2.6	2.56	1.7333	1.6133	1.6933	1.6267	1.7333	1.6	1.7333	1.6	1.7867	1.6667	1.7467	1.7467
	68	3.04	2.92	3.0267	3	3.04	2.8533	2.96	2.88	2.9333	2.7867	2.28	2.1333	1.7067	1.64	1.7333	1.6133	1.7067	1.64	1.7333	1.6267	1.76	1.6533	1.7333	1.7067
	69	3.04	2.92	3.0133	2.9867	3.0267	2.88	2.9867	2.88	2.8	2.76	1.9733	1.84	1.7067	1.7067	1.7333	1.6133	1.7067	1.68	1.76	1.6667	1.72	1.6267	1.72	1.7067
	70	3.0533	2.9067	2.9733	2.8933	3	2.8667	2.9067	2.9067	2.6133	2.64	1.8133	1.7467	1.6933	1.6267	1.7467	1.7067	1.72	1.7067	1.7467	1.6933	1.72	1.6667	1.76	1.72
	71	3.0533	2.8533	2.96	2.88	2.9733	2.8933	2.92	2.88	2.2933	2.24	1.8	1.6667	1.72	1.6267	1.7867	1.7067	1.72	1.6933	1.7733	1.6267	1.7333	1.64	1.7467	1.6267
	72	3.0267	2.84	3	2.8533	2.9733	2.8533	2.8933	2.8133	1.96	1.84	1.7467	1.6133	1.6933	1.6133	1.76	1.6667	1.76	1.6667	1.76	1.6133	1.7867	1.68	1.72	1.68
	73	3.04	2.9067	2.9867	2.8933	2.9733	2.76	2.8	2.7467	1.76	1.6667	1.7467	1.6133	1.72	1.64	1.7733	1.7067	1.7333	1.68	1.7467	1.7333	1.7867	1.72	1.76	1.6933
	74	3.0533	2.92	2.9867	2.8533	2.96	2.7867	2.6	2.5467	1.7333	1.64	1.7333	1.6533	1.7333	1.6667	1.7067	1.72	1.7333	1.6667	1.7333	1.72	1.7467	1.7333	1.7467	1.6667
	75	3.04	2.9333	2.9867	2.84	2.9333	2.76	2.2933	2.1333	1.72	1.64	1.7333	1.7467	1.7067	1.68	1.7333	1.68	1.76	1.6933	1.6933	1.6533	1.76	1.68	1.7333	1.6667
	76	3.0267	2.9333	2.96	2.88	2.96	2.7467	1.96	1.8	1.6933	1.5733	1.7333	1.6667	1.7733	1.64	1.76	1.6533	1.76	1.6267	1.7333	1.6667	1.8	1.7067	1.76	1.6667
	77	3.0133	2.9467	2.96	2.88	2.8667	2.7867	1.76	1.64	1.6933	1.6133	1.7067	1.6933	1.76	1.6933	1.7067	1.6933	1.7333	1.6533	1.76	1.6533	1.7733	1.68	1.8	1.7067
	78	3.0267	2.9067	3.0267	2.8133	2.72	2.6667	1.7333	1.6933	1.7067	1.6667	1.7333	1.68	1.76	1.6933	1.72	1.7067	1.7467	1.68	1.76	1.6933	1.72	1.68	1.7867	1.72
	79	3.0267	2.8933	2.9867	2.7733	2.4267	2.36	1.7333	1.6267	1.7067	1.6667	1.7467	1.6133	1.7733	1.6933	1.7467	1.6667	1.76	1.64	1.7333	1.68	1.8	1.72	1.7733	1.7733
	80	3.0133	2.84	2.9733	2.84	2.0533	1.92	1.6667	1.6	1.7333	1.68	1.7333	1.6533	1.7467	1.64	1.7467	1.6667	1.7333	1.6267	1.7733	1.6933	1.7733	1.6667	1.7867	1.7067
	81	2.9867	2.9067	2.9733	2.7733	1.76	1.76	1.7067	1.6533	1.72	1.7067	1.7067	1.6933	1.7333	1.6667	1.7333	1.6267	1.7467	1.6267	1.7867	1.72	1.7867	1.68	1.7733	1.6667
	82	3.0133	2.9467	2.8267	2.7333	1.76	1.7067	1.72	1.72	1.72	1.68	1.72	1.6267	1.7467	1.6933	1.7467	1.64	1.7733	1.6933	1.7867	1.68	1.8	1.7067	1.7733	1.72
	83	3	2.8667	2.72	2.6933	1.76	1.5733	1.76	1.7333	1.7467	1.6533	1.7333	1.6267	1.7067	1.6933	1.72	1.68	1.7467	1.72	1.7733	1.72	1.8	1.72	1.7733	1.72
	84	3	2.8667	2.5733	2.5333	1.72	1.5333	1.7733	1.7333	1.7867	1.64	1.7467	1.7067	1.7333	1.7067	1.7467	1.6667	1.7333	1.7333	1.8	1.72	1.7333	1.6533	1.76	1.7333
	85	3.0133	2.8267	2.5067	2.3467	1.6933	1.6	1.76	1.72	1.76	1.68	1.7467	1.6667	1.7067	1.72	1.72	1.68	1.7467	1.68	1.76	1.72	1.7333	1.6267	1.7867	1.6933
	86	3.0133	2.8	2.5733	2.44	1.7067	1.6933	1.76	1.72	1.76	1.6667	1.7467	1.6933	1.7333	1.72	1.76	1.8133	1.7867	1.64	1.7733	1.6667	1.7733	1.6533	1.7733	1.7333
	87	3	2.8533	2.72	2.6533	1.7333	1.6533	1.7733	1.6933	1.76	1.6	1.7533	1.68	1.7867	1.6533	1.7733	1.6933	1.7467	1.64	1.7867	1.68	1.7867	1.72	1.76	1.72
Average		1.906665	1.653786	1.928333	1.679541	1.919394	1.665307	1.983941	1.750299	2.076509	1.832424	2.114847	1.892118	1.898483	1.660602	1.867124	1.667878	1.733328	1.51818	1.782273	1.557573	1.783638	1.59288	1.729699	1.549397

Appendix D

Research Communications

Moeinian, M; Wong, F; Hill, R (October 2014) "Development of a radiopaque infiltration resin for early enamel carious lesion". ADM Conference, Bologna, Italy.

Moeinian, M; Wong, F; Hill, R (October 2014) "Strontium Bioactive Glass, Strontium Hydroxyapatite and Barium Sulphate Resins Radio-opacity". William Harvey Day, Barts and The London School of Medicine & Dentistry, UK.

Moeinian, M; Wong, F; Hill, R (March 2015) "Strontium Bioactive Glass, Strontium Hydroxyapatite and Barium Sulphate Resins Radio-opacity". IADR Conference, Boston, USA.

Moeinian, M; Wong, F; Hill, R (July 2015) "Development of radio-opaque resin for white spot lesion". IAPD Conference, Glassgow, UK.

Moeinian, M; Wong, F; Hill, R (September 2015) "Characterization of White Spot Lesion Using Focused Ion Beam- Scanning Electron Microscopy". BSODR conference, Cardif, UK (2015).

**MINTIG Travel Award*

Moeinian, M; Wong, F; Hill, R (October 2015) "Development of radio-opaque resin for white spot lesion". William Harvey Day, Barts and The London School of Medicine & Dentistry, UK.

Moeinian, M; Wong, F; Hill, R (May 2016) "Development of radio-opaque resin for white spot lesion". BSPD Conference, Leeds, UK.

Moeinian, M; Wong, F; Hill, R (June 2016) "Analysis of White Spot Lesions Using Scanning Electron Microscopy ". IADR Conference, Seoul, South Korea.

**Poster Session Chair*

Moeinian, M (June 2016) "Micro-invasive caries treatment with resin infiltration". The Dental Channel, Live webinar.